Detailed studies of white dwarf binaries and their orbital periods.

by

Madelon Catherina Petra Bours

Thesis

submitted to the University of Warwick for the degree of

Doctor of Philosophy

Department of Physics

July 2015

THE UNIVERSITY OF

WARWICK

Contents

Chapter 5 Eclipse timing of white dwarf binaries   **82**

Chapter 6 Testing the planetary models of HU Aqr   **107**

⋆ ⋆ ⋆

List of Figures

★ ★ ★

List of Tables

★ ★ ★

Acknowledgements

After an intense period of nearly four years, the end is near. With this acknowledgement I write the last few words of my PhD thesis. It has been a wonderful time, in which I learned a tremendous number of things, both on an academic and on a personal level.

First of all, I am grateful to Tom Marsh for teaching and motivating me throughout these years, and for taking me on as a student in the first place. I would also like to express my thanks to all the other academics, post-docs and students that are part of the Astronomy & Astrophysics group of the University of Warwick, or were so during the last four years. They made me feel welcome and were always willing to answer questions.

For funding my time in England, my thanks go to the Midlands Physics Alliance Graduate School. I also want to convey my gratitude to the people who made it possible for me to travel all over the world to visit conferences and the telescopes I used to observe the stars that are presented in this thesis.

Speciale dank gaat uit naar mijn familie, mijn vrienden van 't Grupke en mijn Nijmeegse vrienden en collega's die mij door de vele jaren van studeren en leren heen hebben gesteund en zonder wie dit proefschrift niet tot stand zou zijn gekomen.

Zu guter Letzt, meinen Dank an Andreas, weil du immer für mich da bist, selbst wenn wir in unterschiedlichen Ländern sind. You are my moon and stars in this universe.

$$\star \, \star \, \star$$

Declarations

This thesis is submitted to the University of Warwick in support of my application for the degree of Doctor of Philosophy. It has been composed by myself and has not been submitted in any previous application for any degree.

The work presented was carried out by the author except in the cases outlined below:

* ⋆ Chapter 3: the Reflex reduction of the raw VLT+X-Shooter data was performed by C.M. Copperwheat. All subsequent analyses using these wavelength calibrated spectra were performed by the author herself.

* ⋆ Chapter 4: the observations and measurement of the parallax of SDSS J1257+5428 were done by J.R. Thorstensen.

* ⋆ The observations were obtained with help of a team of observers, including the UL-TRACAM and ULTRASPEC teams.

Parts of this thesis have previously been published by the author as follows:

* ⋆ Chapter 3: Bours et al. 2014a, MNRAS 438, 3399; *Precise parameters for both white dwarfs in the eclipsing binary CSS 41177.*

* ⋆ Chapter 3: Bours et al. 2015a, MNRAS 448, 601; *HST+COS spectra of the double white dwarf CSS 41177 place the secondary inside the pulsational instability strip.*

* ⋆ Chapter 4: Bours et al. 2015b, MNRAS 450, 3966; *A double white dwarf with a paradoxical origin?*

* ⋆ Chapter 6: Bours et al. 2014b, MNRAS 445, 1924; *Testing the planetary models of HU Aquarii.*

★ ★ ★

Abstract

Roughly two-thirds of all stars are locked in binary or higher-multiple systems. Given that over 97% of all stars also end their lives as white dwarfs, it is not surprising that more and more white dwarfs are being found as part of binary systems. A general introduction to white dwarfs and binary stars is presented in Chapter 1 and the techniques used throughout this thesis are presented in Chapter 2.

Then, Chapters 3 and 4 present detailed studies of two close double white dwarf binaries. The first, CSS 41177, is also an eclipsing binary, which allows for detailed measurements of the white dwarf masses and radii. With the help of statistical analyses of far-ultraviolet spectroscopy from the Hubble Space Telescope, I also determine the effective temperatures and surface gravities of both stars. For the second binary, SDSS J1257+5428, previous publications were inconclusive, and therefore prompted the far-ultraviolet HST observations featured in this thesis. Using these data, I present a detailed analysis of the system and the still paradoxical results which indicate that the more massive of the two white dwarfs is younger rather than older than its lower-mass white dwarf companion.

In Chapter 5 I detail the observations and aims of my eclipse timing programme, set up to measure apparent and/or real variations in the orbital periods of close white dwarf binaries. With more than 600 high-speed eclipse light curves, spread over more than 70 targets, I try to find general trends and hints of the underlying cause of such variations. Chapter 6 then presents a detailed study of the eclipsing semi-detached white dwarf + M-dwarf binary HU Aqr, which is part of the timing programme. In fact, it is one of the most controversial targets in this programme, since none of the theoretical explanations fit the large-scale eclipse timing variations observed in this binary.

Finally, I end with a concluding summary in Chapter 7.

★ ★ ★

Abbreviations

BD	Brown Dwarf
BJD	Barycentric Julian Date
BMJD	Barycentric Modified Julian Date
CCD	Charge-Coupled Device
C/O	Carbon/Oxygen
COS	Cosmic Origins Spectrograph
CRTS	Catalina Realtime Transient Survey
CSS	Catalina Sky Survey
CV	Cataclysmic Variable
dM	M-dwarf
dof	degrees of freedom
DT	Danish Telescope
DFOSC	Danish Faint Object Spectrograph and Camera
ELM	Extremely Low-Mass
EMCCD ...	Electron-Multiplying Charge-Coupled Device
ESO	European Southern Observatory
FUV	far-ultraviolet
FWHM	Full-Width at Half Maximum
GB	Giant Branch
GMOS	Gemini Multi-Object Spectrograph
H	Hydrogen
HAWK-I ...	High-Acuity Wide-field K-band Imager
HB	Horizontal Branch
He	Helium
HJD	Heliocentric Julian Date
HMJD	Heliocentric Modified Julian Date
HRD	Hertzsprung-Russell Diagram
HST	Hubble Space Telescope
IFMR	Initial-Final Mass Relation
IMF	Initial Mass Function
INT	Isaac Newton Telescope
ISAAC	Infrared Spectrometer And Array Camera
JD	Julian Date
LT	Liverpool Telescope
MAMA	Multi-Anode Multichannel Array
MCMC	Markov chain Monte Carlo
mCV	Magnetic Cataclysmic Variable
MJD	Modified Julian Date
MS	Main Sequence
NIR	near-infrared
NTT	New Technology Telescope

NUV	near-ultraviolet
O/Ne	Oxygen/Neon
PTF	Palomar Transient Factory
RG	Red Giant
RMS	Root Mean Square
SDSS	Sloan Digital Sky Survey
SED	Spectral Energy Distribution
SOAR	Southern Astrophysical Research
SOI	SOAR telescope Optical Imager
SofI	Son of ISAAC
STIS	Space Telescope Imaging Spectrograph
SWARMS ..	Sloan White dwArf Radial velocity Mining Survey
TAI	Temps Atomique International
TDB	Barycentric Dynamical Time
TNO	Thai National Observatory
TNT	Thai National Telescope
TT	Terrestrial Time
UTC	Coordinated Universal Time
UV	ultraviolet
UVB	ultraviolet-blue
VIS	visible
VLT	Very Large Telescope
WD	White Dwarf
WFC	Wide Field Camera
WHT	William Herschel Telescope
ZAMS	Zero-Age Main Sequence

★ ★ ★

Chapter 1

Introduction

1.1 Introduction

The common thread that links the research presented in this thesis is the white dwarf population that exists in close binary systems. White dwarfs are compact objects and the remnants of stellar evolution for over 97% of all stars. Through the correlation between the progenitor star's initial mass and the white dwarf's final mass (Weidemann, 2000), they trace the initial stellar distribution, and contain a history of the evolution of their progenitor stars. With the use of cooling models, temperature measurements of the oldest white dwarfs provide useful and independent age estimates when found in, for example, binary stars, globular clusters (Hansen et al., 2004, 2013) and Galactic populations such as the disc (Wood, 1992) and halo. Comparing observed magnitudes with absolute magnitudes derived from models that match the observed flux at all wavelengths also provide distance estimates to systems such as globular clusters (Woodley et al., 2012; Renzini et al., 1996).

White dwarfs also feature as the most likely candidates for supernova Type Ia progenitors (Nomoto, 1982; Iben & Tutukov, 1984; Whelan & Iben, 1973). The theory that the stars need to reach a specific mass before detonating as a Type Ia supernova forms the basis of the idea that light curves of these supernovae consistently produce a certain peak luminosity and can therefore be scaled to a standard (Phillips, 1993; Leibundgut et al., 1991). This characteristic makes it relatively easy to measure distances to observed supernovae Type Ia, which is why they can be used as standard candles in cosmology (Perlmutter et al., 1999; Riess et al., 1998). In addition, white dwarfs are prominent in accreting binaries such as cataclysmic variables (Warner, 2003; Hellier, 2001) and AM CVn binaries (Breedt et al., 2012; Kilic et al., 2014b), which experience the same mass-transfer related processes as, for example, active galactic nuclei. Besides the fact that these semi-detached white dwarf binaries are numerous, the significantly smaller scale associated with them means that phenomena such as accretion disks and variability develop on much shorter time scales, and are therefore more accessible for study. Furthermore, double white dwarfs are potential progenitors of single hot sdB/sdO stars (Heber, 2009), R CrB stars and extreme helium stars (Webbink, 1984), as well as supernovae Type .Ia (Bildsten et al., 2007).

Despite the abundance and importance of white dwarfs, many detailed aspects of the physics governing them have yet to be determined accurately. Chapter 1 gives an introduction to the topic of white dwarf stars and summarises what is known so far, both for single white dwarfs as well as for white dwarfs in detached and semi-detached close binary sys-

tems. The rest of this thesis aims to expand that knowledge further. It has proven difficult to measure fundamental parameters such as white dwarf masses and radii directly, without using theoretical mass – radius relations, therefore leaving the empirical basis for such theoretical calculations relatively uncertain (Schmidt, 1996). However, as is demonstrated in Chapter 3 for CSS 41177, combining high time-resolution photometry and spectroscopy of white dwarfs in eclipsing binary stars enables high precision in determining both masses and radii (see also Bours et al., 2014a). This chapter also includes an analysis of the effective temperatures and surface gravities of the two white dwarfs, through fits of the spectral energy distribution covering far-ultraviolet to optical wavelengths (Bours et al., 2015a). A similar approach is used in Chapter 4 for the non-eclipsing double white dwarf binary SDSS J1257+5428, for which the results surprisingly suggest that the extremely low-mass white dwarf in this binary is much older than the high-mass white dwarf. This is in direct contradiction with the generally accepted theory of stellar evolution that massive stars evolve faster than low-mass stars, leading to the conclusion that this binary is somewhat of a mystery (see also Bours et al., 2015b).

The emphasis then moves away from detailed parameter studies, as Chapter 5 introduces a large programme for which more than 600 white dwarf eclipse observations were obtained, covering a wide variety of close binaries. Through precise timing of the white dwarf eclipses the aim of this programme is to discover the underlying cause of variations in eclipse arrival times as observed in an ever increasing number of these binaries. By searching for correlations between the amplitudes of such variations and characteristics of the binaries such as the orbital period, the stellar spectral types and the size of the stars relative to the binary separation, I hope to discover the foundation of this behaviour. A complicating factor that is also discussed in this context is the duration of the eclipse observations, since this differs for different binaries in the programme. Following this, Chapter 6 provides a detailed look at one of the binaries in this programme, namely HU Aqr (see also Bours et al., 2014b). This semi-detached system is currently a topic of much debate, as it shows extreme variations which have previously been speculated to be the result of several planets orbiting this close binary. My data contradict this theory, but given the extreme behaviour this binary has shown throughout the years I am unable to produce a satisfactory alternative explanation.

Finally, this thesis closes with a few general conclusions in Chapter 7.

1.2   End points of stellar evolution

All stars begin their lives in molecular clouds. Such interstellar clouds, or parts of them, may be taken out of hydrostatic equilibrium by collisions with other clouds or by shock waves resulting from a nearby supernova explosion. If the mass of a cloud or fragment exceeds the so-called Jeans mass (Jeans, 1902), it will proceed to collapse. The Jeans mass spans a range of values, depending on the temperature and particle density of the environment, and therefore this process forms the basis of the formation of galaxies, stellar clusters as well as individual stars. For the latter, once enough angular momentum is

lost to form a cloud fragment that is bound by self-gravity and has become opaque to its own radiation, a protostar is born. If its mass is below the lower stellar mass-limit of about 0.08 $M_\odot$, the core will never be able to reach the critical density and temperature that allow fusion of hydrogen into helium. Therefore, such low-mass objects will never become stars, instead simply cooling away into oblivion. Such objects have been observed, both directly and through their influence on brighter binary companions (Rebolo et al., 1995; Maxted et al., 2006; Littlefair et al., 2014), and are known as brown dwarfs (BD). If instead the mass of the collapsed cloud fragment exceeds the minimum stellar mass limit, hydrogen fusion does ignite in the core. Once the energy generated by this nuclear fusion dominates and the energy that was generated during the gravitational collapse is mostly lost, a star is officially born. In the path of stellar evolution, the star emerges at the so-called zero-age main-sequence (ZAMS). In large populations, the distribution of ZAMS masses is described by the initial mass function (IMF), a power law which dictates that low-mass stars far outnumber their high-mass counterparts (Salpeter, 1955; Kroupa et al., 2013). The mass of an individual star, which is the main parameter determining its subsequent evolution, depends on the conditions in the cloud from which it forms, such as the mass of the cloud fragments and the metallicity of the cloud.

For all single stars, as well as for those stars in multiple systems wide enough for the stars to evolve independently and not influence each other except through gravitational forces, the core will continue to fuse hydrogen into helium until it is almost fully depleted of hydrogen. This main-sequence (MS) phase lasts for most of the star's lifetime (Hurley et al., 2000). Given the lower central temperature and pressure, the duration of this phase is longer for low-mass stars than it is for high-mass stars. Fig. 1.1 shows a Hertzsprung-Russell diagram with a distribution of MS stars in a large population such as our own Galaxy, and Fig. 1.2 shows a schematic summary of stellar evolution. When the core of a star becomes depleted of hydrogen it generates less and less energy, thereby destroying the hydrostatic equilibrium and initiating contraction of the core. This causes the central density and temperature to increase while hydrogen burning continues in a shell surrounding the core which moves outwards as it burns through the available fuel. While the core contracts, the density and temperature decrease in the outer envelope due to conservation of gravitational and thermal energy, and the star expands to roughly 100 times its former size. Depending on the star's ZAMS mass, its core either becomes hot and dense enough to start fusing helium and move onto the giant branch in the Hertzsprung-Russell diagram (Figs 1.1; 1.2), or it is not. A star that has a helium core and fuses hydrogen in a layer surrounding the core is defined as a red giant star (RG).

For stars with a ZAMS mass of $\sim$ 0.1 - 0.7 $M_\odot$, helium is never ignited (Kippenhahn & Weigert, 1990, Chapter 33). The envelope of the star is lost and returned to the interstellar medium, and the stellar remnant left is the helium core: a helium (He) white dwarf with a mass $\lesssim$ 0.4 $M_\odot$. However, MS lifetimes increase with decreasing ZAMS mass and the lifetimes for He white dwarf progenitors still exceed the age of our Galaxy. Therefore no He white dwarfs have formed yet naturally, without binary or other interactions that force
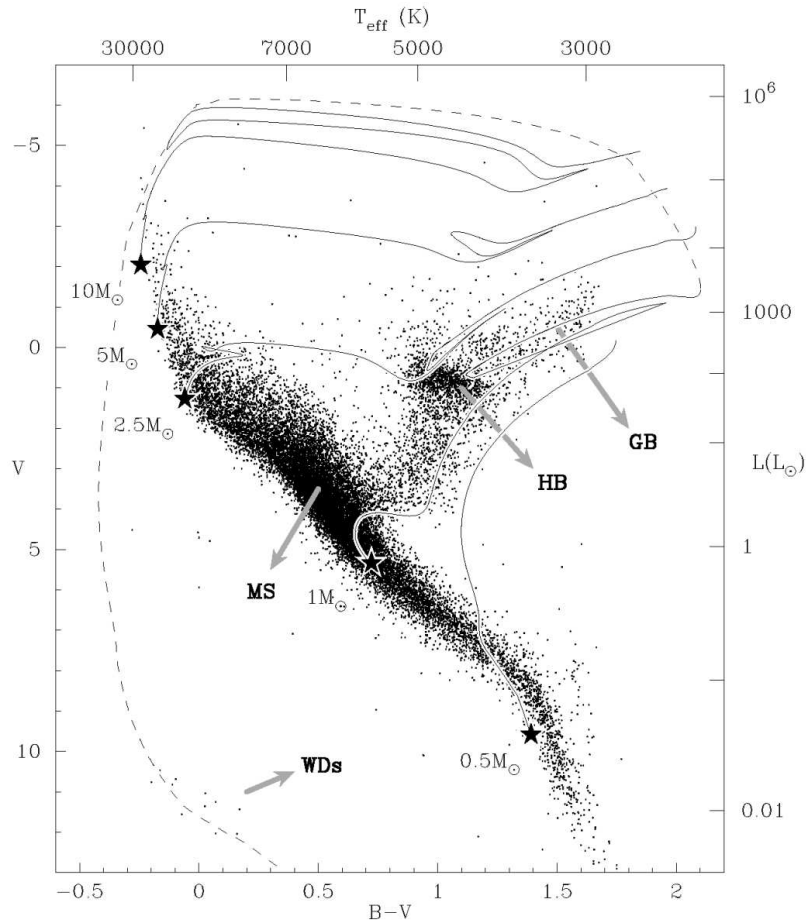
Figure 1.1: Hertzsprung Russell Diagram, based on Hipparcos data and showing the B-V colour, V-band magnitude, effective temperature and luminosity of 20546 nearby stars, with the main-sequence (MS; bottom right to top left), the horizontal branch (HB), giant branch (GB) and white dwarfs (WDs) indicated by the corresponding abbreviations at the end of the arrows. The solid lines show theoretical evolutionary tracks for a 0.5 $M_\odot$, 1 $M_\odot$, 2.5 $M_\odot$, 5 $M_\odot$ and 10 $M_\odot$ star up to the end of the asymptotic giant branch. The dashed line shows the subsequent evolution of the 1 $M_\odot$ star into a white dwarf. Courtesy of Marc van der Sluys.

an early termination of core-hydrogen burning and ejection of the envelope. This latter evolutionary path is discussed in more detail later (see also Chapter 4).

For ZAMS masses exceeding ~ 0.7 $M_\odot$, the core will become dense and hot enough for nuclear fusion of helium to take place, converting this element primarily into carbon and halting the core contraction. At the same time, hydrogen fusion continues in the shell separating the core from the outer envelope. The star has now reached another stable configuration, but because there is less energy to gain from helium fusion than from hydrogen fusion and because the luminosity of the star is higher, this horizontal branch (HB) phase will last roughly 10 times shorter than the MS phase. Once the core is depleted of helium and consists of a carbon/oxygen mixture, it will contract further while the envelope expands once more. In the meantime, the hydrogen burning shell has moved outwards, consuming hydrogen as it moves along and leaving a helium layer behind. Near the core, the bottom of this layer will ignite and undergo helium fusion. The star is now in the asymptotic giant branch phase and experiences double shell burning, and again one
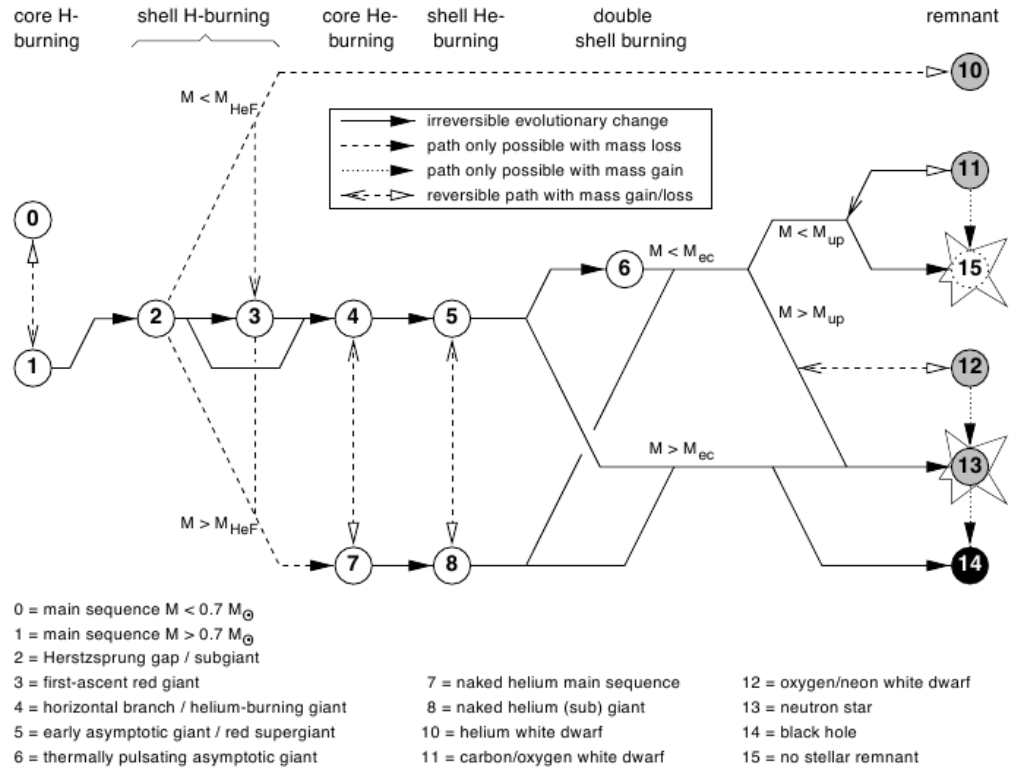
Figure 1.2: Schematic representation of the different stellar evolutionary phases. Critical points depend on the whether the star is massive enough to cross the threshold for a core helium flash (M_{HeF}), the maximum mass of a star ending its life as a white dwarf (M_{up}) and the mass required for electron capture to turn the remnant in a neutron star or even a black hole (M_{ec}). Solid lines indicate irreversible evolutionary steps, while dashed and dotted lines may also indicate steps that could be reversible, for example through mass loss or mass gain. Figure from Hurley et al. (2000).

of two scenarios can occur. For ZAMS masses of ~ 0.7 - 8 $M_{\odot}$ the contraction of the star's core is not sufficient to reach conditions necessary for carbon fusion and so it will keep contracting and start to cool. By this route, a carbon/oxygen (C/O) white dwarf of ~ 0.5 - 1.2 $M_{\odot}$ is formed.

For ZAMS masses exceeding ~ 8 $M_{\odot}$ the core is able to fuse carbon as well, after which it either cools down as a 1.2 - 1.4 $M_{\odot}$ oxygen/neon (O/Ne) white dwarf, or continues nuclear fusion of heavier elements. In the latter scenario, the star will end its life once the core collapses into a neutron star or, if the ZAMS mass exceeds ~ 40 $M_{\odot}$, a black hole. See Fig. 1.2 for these stellar evolutionary paths.

The exact ZAMS mass boundaries that result in the different end products are still uncertain and remain a topic of ongoing research (see for example Fig. 5 in Doherty et al., 2014). However, given the steepness of the IMF, more than 97% of all stars will end their lives as slowly cooling white dwarfs.

Contrary to MS or RG stars, white dwarfs do not experience nuclear fusion, and therefore do not resist gravitational collapse through radiative pressures. Instead, it is the presence of an electron degenerate gas that ensures a stable configuration. In the contracting

stellar core of the pre-white dwarf star the electrons are pushed ever closer together until quantum-mechanical interactions become important. According to the Pauli exclusion principle only two electrons, with opposite spins, can occupy the same quantum-mechanical state at a given time. When multiple electrons are pushed together nonetheless, they will start to fill higher energy levels, thereby generating an outward pressure. When this degeneracy pressure equals the gravitational pressure the white dwarf has reached a stable configuration. However, as explained in more detail in the next section, in the relativistic limit the relation between energy and momentum changes and from the corresponding change in the equation of state it follows that a maximum mass exists for white dwarfs. If this limit is exceeded, degeneracy pressure will not be able to keep the star from gravitationally collapsing and forming a neutron star (in turn supported by neutron degeneracy pressure). This famous limit was predicted in the early 1930's, is set near 1.4 $M_\odot$, and is called the Chandrasekhar mass M_{Ch} (Chandrasekhar, 1931).

1.3 General properties

1.3.1 Temperatures & surface gravities

White dwarfs emerging from the planetary nebulae that are the expelled outer layers of their progenitor stars are extremely hot due to the gravitational energy released during contraction of the pre-white dwarf star's core. In their interiors, a number of processes involving electroweak interactions generate large quantities of neutrinos. These quickly escape from the white dwarf, taking energy with them, and initiating the cooling of the star. At some point the neutrino luminosity decreases to below the photon luminosity and thermal cooling takes over (Fontaine et al., 2001). The radiated luminosity of the white dwarf causes a decrease in temperature of the star, while energy released by a small amount of accompanying contraction is sufficient to sustain the degenerate nature of the electron gas (Koester, 2013). For this reason, the evolution of white dwarfs is often simply referred to as cooling.

As the white dwarf approaches lower temperatures, elements in the outer layers start to recombine, thereby increasing the opacity of those layers. Although the helium and hydrogen layers are expected to be thin, close to 10^{-2} and 10^{-4} of the white dwarf mass respectively (Althaus et al., 2013; Wood, 1995), they regulate the energy outflow due to their opaque nature and therefore play an essential role in the white dwarf cooling process. The steep temperature gradient from the core to the surface leads to the formation of bulk convective motions in the envelope. The bottom of this convective zone will reach ever deeper as the white dwarf cools further, until it touches the outer boundary of the isothermal core (Althaus et al., 2010). This so-called convective coupling speeds up the cooling significantly, since the core's energy can now effectively be transported to the outer atmosphere where it is radiated away. A second important process that occurs as the white dwarf cools is crystallisation. When the ionic matter in the white dwarf's core has cooled sufficiently it will experience a first-order phase transition and become a solid. This process
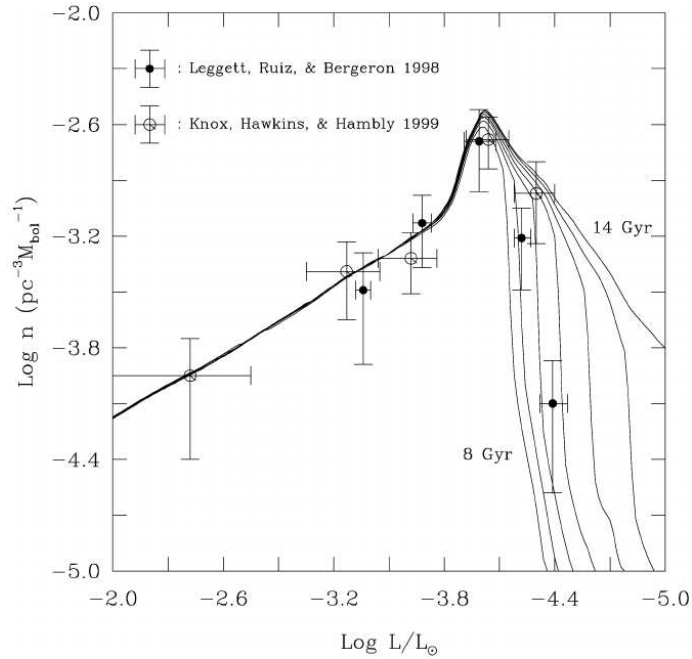
Figure 1.3: Comparison of the observational luminosity function of local white dwarfs and theoretical calculations for the Galactic disk for different ages. Figure from Fontaine et al. (2001), using data from Leggett et al. (1998) and Knox et al. (1999).

is accompanied by a release of latent heat and consequently slows down the cooling. When and in which order these two processes occur depends mainly on the mass of the white dwarf (Fontaine et al., 2001). Irrespective of the order in which these processes occur, the white dwarf will eventually be a crystallised, very low-temperature degenerate remnant, referred to as a black dwarf.

The monotonic decrease of temperature as a function of age is a unique and very useful aspect of white dwarf stars. It means that they can be used as independent age estimators of the population they are in, including the local neighbourhood, open clusters, or the Galactic disc and halo (Renzini et al., 1996; Hansen et al., 2004, 2013; Wood, 1992). This branch of astronomy, where the main aim is deriving ages, is called cosmochronology. For accurate measurements with white dwarfs it is necessary to precisely compute theoretical white dwarf cooling rates in order to link the measured temperature (or luminosity) to the star's age. White dwarfs in the Solar neighbourhood can be individually targeted and studied (Bergeron et al., 2001), but this becomes more difficult when analysing stars in distant clusters (Richer et al., 1997, 1998, 2008). In such cases, and for other large samples, it is useful to create both a theoretical and observational luminosity function. The former is calculated by assuming a certain star formation rate for a synthetic sample of stars, which are then evolved using detailed stellar evolution calculations and later white dwarf cooling models. The resulting theoretical luminosity function can then be compared with observed numbers of white dwarfs with a given magnitude per volume element, as is illustrated in Fig. 1.3 (see also Wood, 1992). Since the current-day luminosity function depends on the star formation history, knowing more about the latter can help constrain
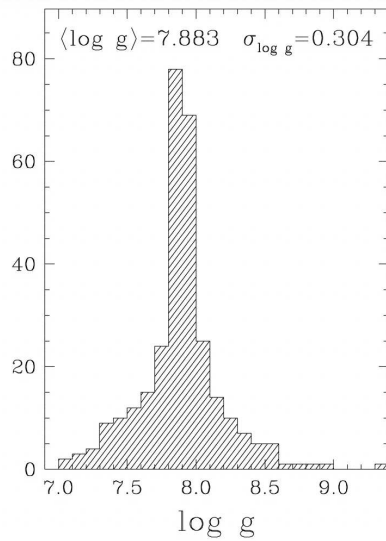
Figure 1.4: Histogram of surface gravities (log g) of a spectroscopic sample from the Palomar Green Survey consisting of 298 white dwarfs with effective temperatures T_{eff} > 13000 K and with hydrogen-rich atmospheres (Liebert et al., 2005).

the former. This can be done through, for example, studies of complete, volume limited white dwarf samples, combined with initial – final mass relations and white dwarf cooling times (Tremblay et al., 2014).

Besides temperature, the most important parameter describing a white dwarf is the surface gravity, log g, typically expressed as a logarithm with g in cgs units of cm/s^2 (so for the Earth log $g_\oplus \simeq 3$). The bulk of white dwarf stars have a surface gravity close to log $g \simeq 8$ (Fig. 1.4; Liebert et al., 2005; Gianninas et al., 2006; Kleinman et al., 2013). These represent by far the largest group of white dwarf remnants, those with C/O cores. We will see more about masses and white dwarfs with different core compositions in Sect. 1.3.2.

For a given combination of effective white dwarf temperature T_{eff}, surface gravity log g and chemical composition of hydrogen, helium and heavier elements, XYZ respectively, accurate models can be calculated that describe a white dwarf's atmosphere. These model atmospheres can then be used to calculate the emitted radiation at different wavelengths, and therefore to create model spectra (Bergeron et al., 1991; Koester, 2010; Tremblay et al., 2013b). Observed spectra of white dwarfs can then be compared to grids of such model spectra (usually the composition XYZ is fixed), and from the best fit one finds the star's effective temperature and surface gravity. The exact composition of the white dwarf's core as well as the thickness of the multi-layered atmosphere is not unimportant, as these influence both the temperature and surface gravity. Note that a white dwarf's temperature and surface gravity cannot be measured directly, therefore requiring them to be derived by comparison to physical models as just described. Hence this approach does not only rely on high-quality spectroscopic data, but also on a proper theoretical understanding of the relevant physics of white dwarf structures and cooling processes.

Fitting model spectra to spectroscopic data generally focuses on the Balmer absorption lines, which are present in the spectra of most white dwarfs. Because distances to stars are unknown, or at the very least uncertain, the measured flux does not constrain the white dwarf temperature. Also the slope of the spectrum's continuum alone is insufficient to constrain the star's temperature, because it is influenced by the amount of reddening due

to dust along the line of sight towards the target. Instead it is the shape and width of the hydrogen absorption lines that are sensitive to both temperature and surface gravity, allowing determination of both these parameters by fitting the line profiles (Bergeron et al., 1991; Gianninas et al., 2011; Giammichele et al., 2012).

Note that until recently the models included a 1-dimensional mixing-length theory to approximate convective motion. The latest models are based on 3-dimensional calculations instead (Tremblay et al., 2013a), and revealed that the former 1D approximation overpredicted surface gravities and, to a lesser extent, effective temperatures when these atmospheric parameters were deduced through Balmer line fitting. Tremblay et al. (2013b) provided analytical formulae with which parameter values from fits with 1D models can be corrected to the more accurate values that would result from fits with 3D model spectra.

As white dwarfs cool, they reach a combination of effective temperature and surface gravity, dependent on their chemical composition, at which they experience pulsational instabilities. These are mainly driven by changes in the opacities of the different elements that are present. Four empirical classes of white dwarf pulsators are known, separated by the composition of their core and/or atmosphere: the hot pre-white dwarfs (PG 1159 or DOV stars, McGraw et al. 1979), white dwarfs with helium-rich atmospheres (V777 Her or DBV, see for example Winget et al. 1982; Provencal et al. 2009; Østensen et al. 2011), those with carbon-rich atmospheres (DQV, see Montgomery et al. 2008; Dufour et al. 2008) and white dwarfs with hydrogen-rich atmospheres (ZZ Ceti or DAVs, see Landolt 1968; Gianninas et al. 2011). The latter are by far the largest known group of pulsating white dwarfs.

The time scale of radial pulsations is set by the dynamical time scale, which is only a few seconds for white dwarfs. The observed pulsations have periods on the order of a few minutes to tens of minutes (see for example Gianninas et al., 2006; Hermes et al., 2013c,d), therefore consistent with non-radial g-mode pulsations, so called because the dominant restoring force is gravity. Another group of pulsations is also thought to exist, the non-radial p-mode pulsations, where the restoring force is due to pressure. However, oscillations with typical p-mode periods and amplitudes have not yet been observed, partly due to the fact that they are likely to occur on time scales of only a few seconds, as well as with significantly lower amplitudes than the g-mode pulsations (Winget & Kepler, 2008).

For white dwarfs with hydrogen-rich atmospheres, the observed g-mode pulsations are driven by ionisation of hydrogen. This requires a certain combination of surface gravity and effective temperature, which is why there is a relatively well-defined instability strip in this parameter space. Empirically, this strip occurs at an effective temperature close to $T_{eff} = 12000$ K for high-mass white dwarfs ($\log g \sim 8$) and slants to $T_{eff} = 9500$ K for extremely low-mass white dwarfs ($\log g \sim 6.5$) (Gianninas et al., 2014a). This agrees reasonably well with theoretical calculations (Van Grootel et al., 2012, 2013). Whether the strip is continuous or not, whether it covers the full range of surface gravities, and whether or not the strip is pure and contains only pulsating white dwarfs has yet to be determined. Fig. 1.5 shows the current observational knowledge. Note that asteroseismology, the study
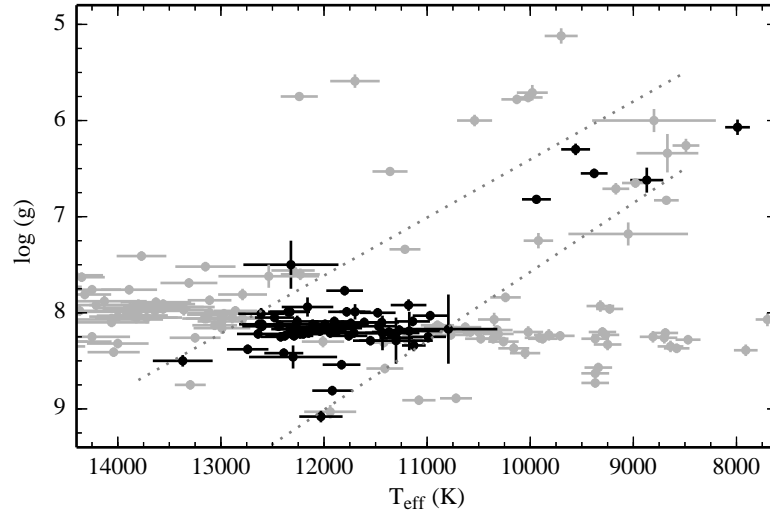
Figure 1.5: ZZ Ceti diagram, showing the position of the instability strip for white dwarfs with hydrogen-rich atmospheres as a function of surface gravity and effective temperature of those stars. Shown in black are confirmed pulsating white dwarfs (Gianninas et al., 2011, 2014a; Greiss et al., 2014; Hermes et al., 2011, 2013a, 2014b; Pyrzas et al., 2015) and in grey non-pulsating white dwarfs (Bours et al., 2014a, 2015a; Gianninas et al., 2011, 2014a; Hermes et al., 2013c,d; Steinfadt et al., 2012). The dotted lines follow the empirical instability strip as in Gianninas et al. (2014a).

of pulsating stars (Aerts et al., 2010), is a very powerful tool that can be used to probe the interior of stars, and to determine masses and bulk compositions (Winget & Kepler, 2008).

1.3.2   Masses & radii

The internal structure of a star as a function of its radius can be approximately described by a polytrope with index n. The polytropic equation describes the density profile of the star, and hence the pressure profile via the equation of state which links these two variables such that $P \propto \rho^{1+\frac{1}{n}}$. This assumption results in the Lane-Emden equation for describing a gaseous sphere:

$$\frac{1}{\xi^2}\frac{d}{d\xi}\left(\xi^2\frac{d\theta}{d\xi}\right) = -\theta^n \,, \tag{1.1}$$

where ξ is a dimensionless variable representing the stellar radius and θ is a dimensionless variable relating the density to the central density through $\rho = \rho_c\theta^n$. Stars that are dense enough to be dominated by non-relativistic electron degeneracy pressure, such as white dwarfs, can be accurately described by a polytrope with index $n = 3/2$. For this index, the solution of the Lane-Emden equation reduces to a mass – radius relation where

$$R \propto M^{-1/3} \tag{1.2}$$

(see for example Prialnik, 2000; Kippenhahn & Weigert, 1990). This explains one of the key characteristics of white dwarfs, namely that those with higher masses have smaller radii. In the extreme case where the electron degenerate gas is fully relativistic, the star is

better described by a polytrope with index $n = 3$. In this solution, the mass is independent of the radius, and it can therefore be used to derive an absolute upper mass limit for white dwarf stars. Using appropriate numbers, this results in the Chandrasekhar mass limit of $M_{\mathrm{Ch}} \simeq 1.4 \, \mathrm{M_\odot}$ (Chandrasekhar, 1931).

The inverse relationship in Eq. 1.2 between a white dwarf's mass and radius has been known for a long time, but determining exact mass – radius relations has turned out to be much more complicated, and is still work in progress (Wood, 1995; Benvenuto & Althaus, 1998; Althaus et al., 2013). Part of the complexity can be explained by the fact that the relations differ for white dwarfs with different core compositions. In addition they are sensitive to the star's temperature, because a white dwarf with a non-zero temperature becomes 'bloated' due to thermal pressure, which particularly influences the outer non-degenerate layers of the star. For testing and improving theoretical mass – radius relations, empirical data is essential, but it is not always easy to measure the relevant parameters.

Besides using asteroseismological tools on those white dwarfs that measurably pulsate, detailed studies can be performed on white dwarfs in resolved binary systems. Using these nearby, wide binaries, masses can be derived from the visible orbital motion as projected on the plane of the sky and radii can be derived from parallax observations and knowledge of effective temperatures from spectroscopic observations (Provencal et al., 2002, 1998; Holberg et al., 1998; Shipman et al., 1997). Knowledge of the distance to the white dwarf allows one to use the observed flux to calculate the flux emitted at the white dwarf's surface, which depends upon the star's temperature and radius. Note that this approach is independent of any mass – radius relation, but still relies on model spectra to obtain a temperature by fitting spectroscopic data.

Masses and radii can also be derived for white dwarfs in unresolved binaries, although in order to get proper parameter constraints these binaries then need to show certain spectral features as well as show eclipses from the Earth's point of view (see for example Chapter 3; Bours et al., 2014a; Parsons et al., 2010a, 2012a; Maxted et al., 2004; O'Brien et al., 2001). For such binaries, masses can be derived by measuring the radial velocity amplitudes K_1 and K_2 of the stars through phase-resolved spectroscopy. This requires accurate spectroscopy, ideally covering at least a full orbital cycle, as well as the presence of deep, sharp line cores originating in both stars from which the radial velocities can be measured. The radial velocity amplitudes of the stars are linked to the mass ratio $q = K_1/K_2 = M_2/M_1$, and, when the orbital inclination with respect to the plane of the sky i is known as well, the individual masses can be determined through

$$\frac{2\pi}{P_{\mathrm{orb}}} \, a \sin(i) = K_1 + K_2 \tag{1.3}$$

and the use of Kepler's third law given by

$$\frac{a^3}{G(M_1 + M_2)} = \frac{P_{\mathrm{orb}}^2}{4\pi^2} \, . \tag{1.4}$$

Generally the inclination i is not known beforehand. Removing the degeneracy between
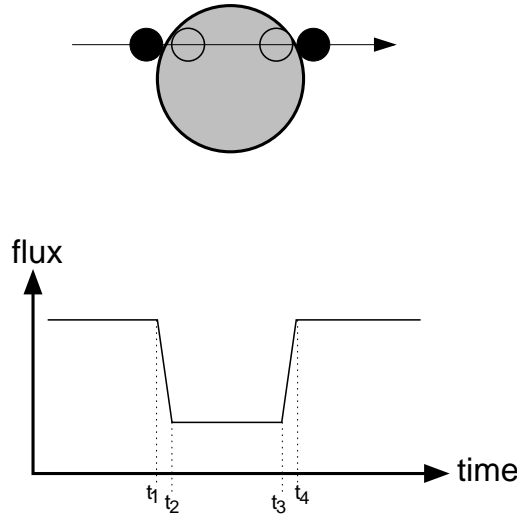
Figure 1.6: Schematic diagram of an eclipse, during which a white dwarf (small, black) gets obscured by a main-sequence star companion (large, grey). The total eclipse lasts from time t_1 to t_4, while the ingress and egress last from t_1 to t_2 and t_3 to t_4 respectively.

the masses and the orbital inclination can be achieved by combining the spectroscopic observations with high-speed photometric eclipse observations. These latter are also essential in deriving the stellar radii, which determine the duration of the ingress (t_2 - t_1) and egress (t_4 - t_3), as well as the duration of the entire eclipse (t_3 - $t_1 = t_4$ - t_2), see Fig. 1.6. At the third and fourth contact points, t_3 and t_4, the orbital phases ϕ_3 and ϕ_4 can be used to derive the relative radii of the two stars. Assuming that $R_2 > R_1$, the radii scaled by the orbital separation a are given by

$$\frac{R_1 + R_2}{a} = \sqrt{1 - \sin^2 i \cos^2 2\pi\phi_4}\,, \tag{1.5}$$

$$\frac{R_2 - R_1}{a} = \sqrt{1 - \sin^2 i \cos^2 2\pi\phi_3}\,, \tag{1.6}$$

although again the orbital inclination i plays a role. Combining the spectroscopic and photometric data sets removes the degeneracy introduced by the orbital inclination and therefore allows measurements of stellar masses and radii independently of theoretical mass – radius relations or model spectra. Although accurate, the observations are time consuming and this technique can only be applied to a limited number of stars, since they need to both have sharp spectral lines and show eclipses.

For larger sample sizes other approaches have proven more useful. This includes the one used by Liebert et al. (2005), who determined white dwarf masses by combining evolutionary models with temperatures and surface gravities obtained from fitting model spectra to spectroscopic data. Their distribution of masses for white dwarfs with temperatures $T_{\rm eff} > 13000$ K is shown in Fig. 1.7. The cooler white dwarfs are removed from this sample to avoid additional complexity due to the increasing importance of convection at these temperatures (Tassoul et al., 1990). The histogram shows a dominant, central component at a mass close to 0.6 $M_\odot$, corresponding to the bulk of the white dwarf remnants, namely those with C/O cores. There is also a sharp, smaller component at ~ 0.4 $M_\odot$, as well as a weak, broad contribution of white dwarfs with masses > 0.8 $M_\odot$. These sub-distributions correspond to the He core and O/Ne core white dwarfs respectively. Note that the sample
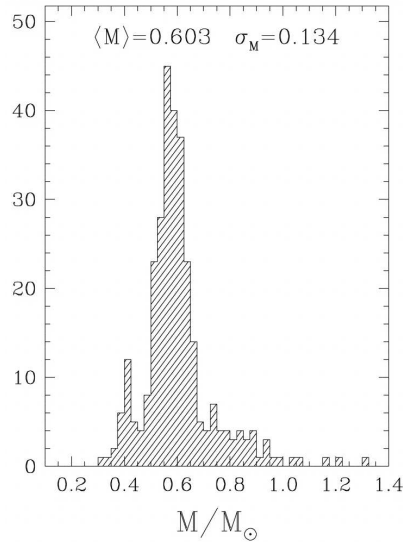
Figure 1.7: Histogram of masses of a spectroscopic sample from the Palomar Green Survey consisting of 298 white dwarfs with effective temperatures $T_{\text{eff}} > 13000$ K and with hydrogen-rich atmospheres (Liebert et al., 2005).

used to create this distribution is magnitude-limited, thereby creating a bias in favour of finding low-mass white dwarfs due to their larger radii and larger surface area. A mass distribution corrected for the volume searched should more accurately represent the true distribution, and does indeed show a more prominent component at higher white dwarf masses (see Liebert et al., 2005).

The results from this spectroscopic approach agree with the mean mass determined using the last of the four methods that can be used to measure white dwarf masses: through gravitational redshift measurements. This method relies on accurately measuring the wavelength of absorption lines in spectroscopic data of white dwarfs, most often those of the Balmer line series. The lines will be redshifted because the photons have had to emerge from the deep gravitational potential well of the white dwarf star itself. The measured shift in wavelength due to the gravitational redshift v_g therefore depends on the white dwarf's mass and radius, where

$$v_g = \frac{GM}{Rc} \, . \tag{1.7}$$

However, spectral features will also be redshifted or blueshifted if the white dwarf has a radial velocity with respect to the observer at Earth. Therefore this technique can only be applied to those white dwarfs for which the radial velocity is known: those in common-proper motion systems or in open clusters (Koester, 1987; Silvestri et al., 2005; Reid, 1996; Casewell et al., 2009). However, using a large sample of white dwarfs from the thin disk of our Galaxy, it can be assumed that the radial velocities cancel out on average, so that this statistical analysis results in a mean gravitational redshift and mean white dwarf mass (Falcon et al., 2010).

Note that both the spectroscopic and the gravitational redshift approach require the use of a theoretical mass – radius relation in order to determine both mass and radius for a given white dwarf. Therefore these do not provide independent tests of such relations. This has so far only been achieved through detailed studies of white dwarfs in close binary systems. However, if both the gravitational redshift and the surface gravity can be measured for a
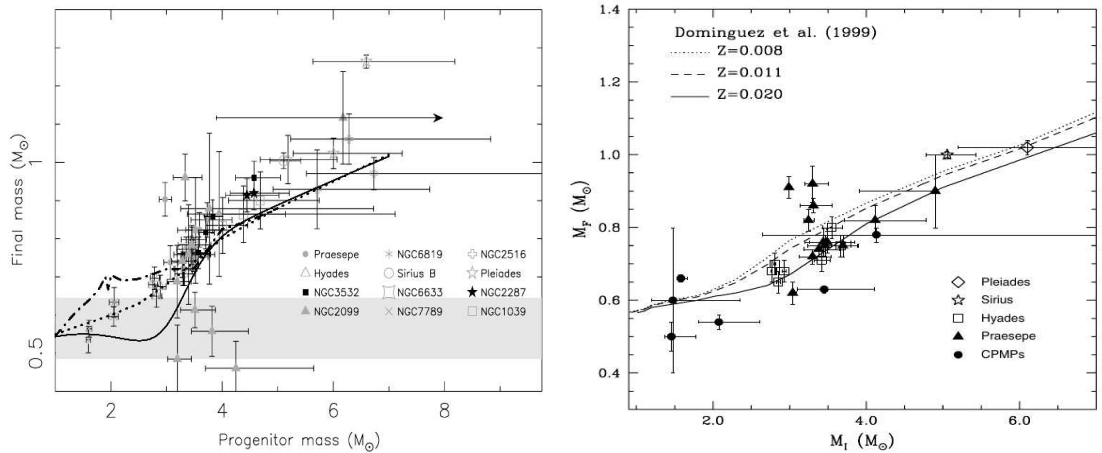
Figure 1.8: *Left:* initial – final mass measurements and theoretical relations from open clusters. Figure from Dobbie et al. (2009). *Right:* initial – final measurements from common proper motion pairs, and theoretical relations for different metallicities Z. Figure from Catalán et al. (2008b).

given white dwarf, the star's mass and radius can be determined independently (Holberg et al., 2012).

Knowing the mass of a white dwarf can reveal more information about stellar evolution and the star formation history, but only if the white dwarf's final mass can be linked to the star's initial mass on the main-sequence (Dobbie et al., 2009; Tremblay et al., 2014). With the help of an initial – final mass relation, a population of white dwarfs can reveal the history of their progenitor stars, and, for example, provide valuable insights into the amount of mass returned to the interstellar medium (see for example Kalirai et al., 2009). The large number of different processes that a star may experience during its lifetime, such as when thermal pulses occur, the opacity of different stellar layers at different times, mass-loss laws, stellar rotation, magnetic fields, etcetera, complicates theoretical evolutionary calculations (Weidemann, 2000). By using open star clusters with white dwarf members such as the Hyades cluster, and the turn-off mass of their main-sequence stars, the initial – final mass relation can be calibrated (Richer et al., 1997; Weidemann, 1977). Besides open clusters, also common proper motion pairs with one white dwarf and one non-degenerate star can be used. The total age and the initial metallicity of the binary may be determined from the non-degenerate companion, and can then be used to determine the main-sequence lifetime of the white dwarf progenitor, in combination with the white dwarf mass and derived cooling time (Catalán et al., 2008b). The measured relation between final white dwarf mass and inferred initial ZAMS mass follows the general theoretical calculations (Fig. 1.8). The ever-decreasing uncertainties and scatter present in the measured white dwarf masses will facilitate more detailed conclusions regarding the more subtle differences in the various theoretical calculations (Dobbie et al., 2009). For more information on how stellar metallicity influences the initial – final mass relation, see Meng et al. (2008).
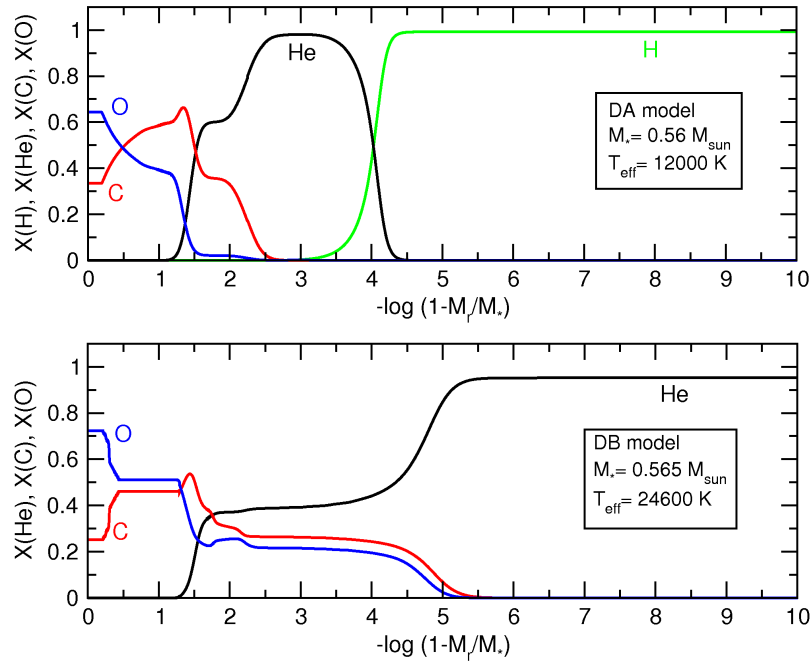
Figure 1.9: Cross-section showing the relative fractions X of oxygen (O), carbon (C), helium (He) and hydrogen (H) in a DA (*top panel*) and DB (*bottom panel*) white dwarf with a carbon/oxygen core of mass $M_\star$ and temperature T_{eff} as given in the legends (Althaus et al., 2010). The horizontal axes indicate the mass fraction (in the form of $-\log(1-M_r/M_\star)$) contained in the star beyond radius r. The centre of the white dwarf is at the left and the outer atmosphere is off the figures towards the right. The part of the atmosphere directly available to observations typically has a mass fraction $< 10^{-15}$, which corresponds to $-\log(1-M_r/M_\star) > 15$.

1.3.3   Chemical composition

The only method of truly probing a white dwarf's interior and determine its composition is through seismic analysis (see for example Aerts et al., 2010; Kawaler & Bradley, 1994; Costa et al., 2008; Córsico et al., 2012). However, since most white dwarfs do not pulsate, general assumptions about their composition have to be made. Depending on the mass, and hence the surface gravity, of the white dwarf, the core composition is either assumed to be He, a C/O mixture, or an O/Ne mixture for low-mass, canonical and high-mass white dwarfs respectively. The latter two are surrounded by both a helium and hydrogen layer, whereas the helium white dwarf's atmosphere is composed of a hydrogen layer only. Typical masses for these layers are 10^{-2} M_{WD} for the He layer, and 10^{-4} M_{WD} for the H layer (Althaus et al., 2013; Wood, 1995), although very low-mass white dwarfs can have substantially thicker hydrogen envelopes of $\sim 10^{-2}$ $M_\odot$ (Istrate et al., 2014b).

The high surface gravities typical of white dwarfs cause the chemical constituents in the stars to settle according to their elemental weights. This process occurs on time scales that are much shorter than the star's evolutionary time scales (Paquette et al., 1986; Koester, 2009). All heavy elements sink below the white dwarf's photosphere, while light elements such as helium and hydrogen form the upper layers of the atmosphere. Chemical profiles for canonical white dwarfs with a hydrogen-rich or helium-rich atmosphere are shown in Fig. 1.9. Note that the x-axes indicate the negative of the logarithmic mass-fraction, from
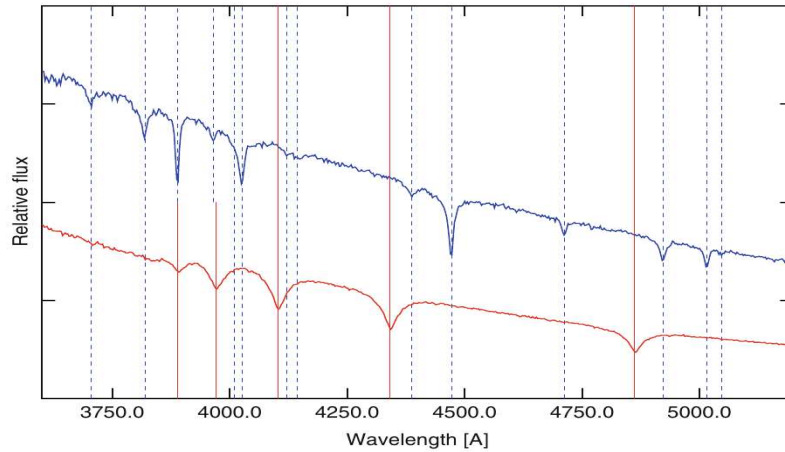
Figure 1.10: Spectrum of a DA (bottom) and DB (top) white dwarf, from the HST calibration database. Vertical lines indicate the positions of hydrogen (solid) and helium (dashed) spectral lines. Figure from Koester (2013).

the core of the white dwarf at 0 out to the outer envelope at 3 and above. Observationally, one can only see the photons emitted in a star's photosphere, which typically contains a mass fraction $\leq 10^{-15}$. This means that only the outermost layer of a white dwarf's atmosphere can be directly observed, and therefore it is these layers on which spectral sub-classification of white dwarfs is based.

In roughly 70% of all white dwarfs some amount of hydrogen is present and, barring any external supply of heavier elements, the photosphere will then be composed purely of hydrogen. In this case, the spectrum will show only hydrogen absorption lines and the star will be classified as a DA white dwarf. If all hydrogen has been lost during pre-white dwarf evolutionary phases, helium will make up the outer atmosphere, in which case the spectrum will show helium absorption lines and the star will be classified as a DB white dwarf. Spectra of a DA and DB white dwarf are shown in Fig 1.10.

With increasing amounts of spectroscopic data on white dwarfs, more categories are being discovered. A basic classification is listed in Table 1.1, and includes several subclasses besides the DA and DB white dwarfs. Among them are DC white dwarfs which show no deep absorption lines at all, DO white dwarfs that show strong HeII lines and weak HeI or H lines, DZ white dwarfs which show metal lines but no hydrogen or helium lines, and DQ white dwarfs which show carbon features. A combination of different spectral classes is also possible. For example, when a white dwarf has a hydrogen envelope enriched with metals, it will be classified as either a DAZ or DZA white dwarf, depending on whether the hydrogen spectral features are stronger than the metal features or vice versa. For pulsating white dwarfs a V is often added to the classification to indicate variability, although most spectral classes have additional names for the pulsating members based on their prototype, as mentioned before. Lastly, some white dwarfs contain a strong magnetic field, which can be seen through Zeeman splitting of the absorption lines. In these cases, the letter m or H can be added to the spectral classification. A few more less-populated classes exist, see

Table 1.1: White dwarf spectral classes.

classification	spectroscopic signature
DA	hydrogen lines, no HeI or metals present
DB	HeI lines, no hydrogen or metals present
DC	no lines deeper than 5% present
DO	strong HeII lines, some HeI or H may be present
DZ	metal lines only, no hydrogen or helium lines
DQ	carbon features present
PG 1159	hot white dwarfs: $T_{eff} \sim 140000$ K
V	photometric variability
m or H	magnetic

for example the review by Koester (2013) for more details.

1.4   Compact white dwarf binaries

Roughly two out of every three stars are part of a binary system, so that they will go through life with a nearby companion. If the binary separation is very large, the stars will never influence each other's evolution, not even when they evolve into giants or supergiant stars. For smaller separations however, the evolution of both stars is strongly dependent upon that separation because it determines the sphere of influence of the stars. In this thesis, it is the close white dwarf binaries that are of interest and so the focus lies on evolutionary paths towards and of these types of binaries.

Most binaries start their lives as two ZAMS stars. The more massive star (primary star with mass M_1) will burn through its fuel more quickly and will evolve off the MS first. Depending on its mass, and on the size it will reach, the star may fill its Roche lobe. The Roche geometry defines the gravitational potential in a frame that is corotating with the binary, as illustrated in Fig 1.11. The Roche lobe is the largest closed equipotential surface around an object. The Roche lobes of the two stars meet at Lagrange point L_1 where matter can transfer from being gravitationally bound to one star to being gravitationally bound to the other star. The equivalent radius R_L of a Roche lobe is defined by setting the Roche lobe's volume equal to a sphere occupying the same volume, and is given approximately by

$$\frac{R_L}{a} = \frac{0.49q^{2/3}}{0.6q^{2/3} + \ln(1 + q^{1/3})} \tag{1.8}$$

(Eggleton 1983, who updated the analytical approximation of Paczyński 1971), where a is the binary's semi-major axis and $q = M_2/M_1$ is the mass ratio.

To obtain this Roche potential several assumptions are made (see Paczyński, 1971, and references therein), with three of the most important ones following here. First, that the two objects are point masses. This is a reasonable assumption because even when they fill their Roche lobes, stars are very centrally concentrated. Second, that the binary orbit is circular. And third, that the stellar rotation is synchronised with the binary's orbital
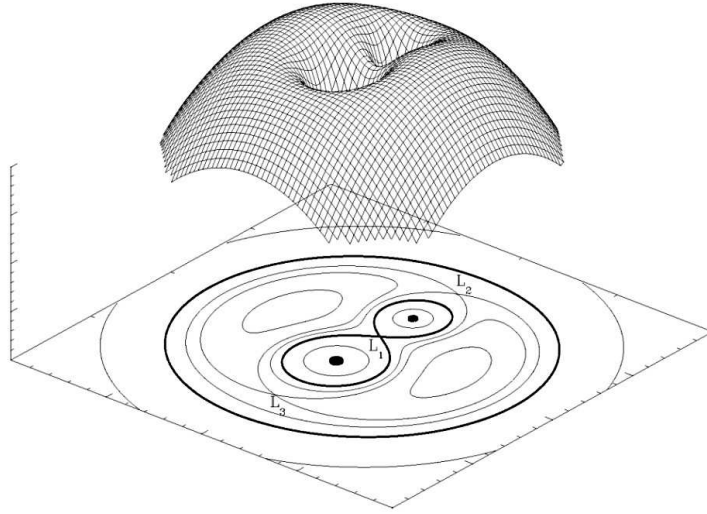
Figure 1.11: Representation of the Roche potential in a binary with a mass ratio $q = 2$ in three dimensions (top) and projected onto two dimensions (bottom). L_1, L_2 and L_3 are Lagrange points in which the gravitational forces of the two stars cancel each other. The thick solid black line that crosses L_1 shows the droplet shaped Roche lobes. Courtesy of Marc van der Sluys.

motion, so that the stars are tidally locked to each other and the binary orbit. These last two assumptions are not generally valid, but when stars are close to filling their Roche lobes, tidal interactions become strong enough to circularise and synchronise the orbit faster than the stars expand. Therefore, when a star reaches full Roche lobe size all three assumptions are usually satisfied.

In general, the evolution of the orbital separation of a close binary is governed by the following equation

$$\frac{\dot{a}}{a} = 2\frac{\dot{J}}{J} - 2\frac{\dot{M_1}}{M_1} - 2\frac{\dot{M_2}}{M_2} + \frac{\dot{M}}{M}\,, \tag{1.9}$$

with J the angular momentum, M_1 and M_2 the primary and secondary masses, $M = M_1 + M_2$ the total mass and the dots representing time derivatives. Angular momentum can be lost from the binary through one of two processes: the emission of gravitational waves, or the loss of matter that takes angular momentum with it. These processes play important roles in close binary evolution, as will become clear in more detail in Sect 1.5. Mass-loss of either star can occur when that star fills its Roche lobe, after which the subsequent mass transfer through the L_1 point to the secondary can either be stable or not. The stability depends strongly on the mass ratio q and on the reaction of the donor (primary) to the mass-loss as well as the reaction of the accretor (secondary) to mass-gain. In particular, the subsequent evolution of the binary depends on whether the donor expands faster or slower than its Roche lobe, thereby determining whether mass-transfer continues, and if so, whether it is stable on a dynamical time scale. Assuming the star fills its Roche lobe, the mass and radius of the donor then determine the amount by which the star exceeds its Roche lobe and hence the mass loss rate $\dot{M_1}$.

If mass transfer is stable, this phase can last for $\sim 10^9$ years, during which the secondary accretes (a fraction of) the transferred matter. For large $\dot{M_1}$ the Eddington limit is crossed,

and the secondary cannot accrete all the mass that is being transferred towards it, therefore resulting in a common envelope phase in which case the expanding envelope of the giant donor engulfs the secondary star completely. The classical common envelope prescription is based on conservation of energy, so that the envelope is expelled once a fraction α of the difference in orbital energy between the initial and final configuration of the binary equals the envelope's binding energy (Webbink, 1984; Tutukov & Yungelson, 1979; van den Heuvel, 1976; Paczyński, 1976):

$$E_{\mathrm{bind}} = \alpha \, \Delta E_{\mathrm{orb}} \, . \tag{1.10}$$

This can result in a large decrease of the binary's orbital separation, in order to gather the required energy to expel the envelope. Given the short orbital periods of the white dwarf + M-dwarf binaries discussed in this thesis, it is likely the case that most of them went through such a common envelope event. However, the existence of equal-mass double white dwarf binaries seems to challenge this mechanism: if the first common envelope phase, which followed the evolution of the primary into a giant, indeed caused the orbit to shrink significantly, there would not be enough space for the secondary star to evolve long enough as a giant in order to produce a core as massive as the primary white dwarf. Evolutionary models for these binaries introduced an alternative prescription for the first common envelope phase in such a binary. This alternative is based on conservation of angular momentum, in which the amount of decrease of the binary's orbital separation depends upon the fractional mass of the envelope m_{env} (Nelemans et al., 2000; Nelemans & Tout, 2005):

$$\frac{\Delta J}{J} = \gamma \, \frac{m_{\mathrm{env}}}{M_1 + M_2} \, . \tag{1.11}$$

The drawback of this model is that it has no solid physical interpretation, but is an empirically justified mathematical concept.

Exactly what happens during a common envelope event, and how and when common envelopes occur, is still somewhat unclear at the moment. This is partly due to a common envelope's short duration of only 100 – 1000 years, which makes it difficult to directly observe binaries in such a phase, assuming they are recognisable as such. A recent review on the subject of common envelope evolution can be found in Ivanova et al. (2013) and of the more comprehensive topic of close binary evolution in Postnov & Yungelson (2014).

1.4.1   Detached white dwarf + M-dwarf binaries

Many of the observational targets discussed in this thesis are close, detached white dwarfs + M-dwarf binaries. In order to form such a binary, the initially more massive star (the primary) must evolve into a white dwarf. While shedding its envelope, it is thought that the binary experiences an α common envelope event as described before, causing the orbit to shrink significantly and resulting in a close white dwarf binary. Because phases after the main-sequence last a relatively short amount of time, the secondary star is still on the main-sequence and will not have evolved significantly during the primary star's evolution. Even a small difference in ZAMS masses can therefore give rise to a white dwarf + main-
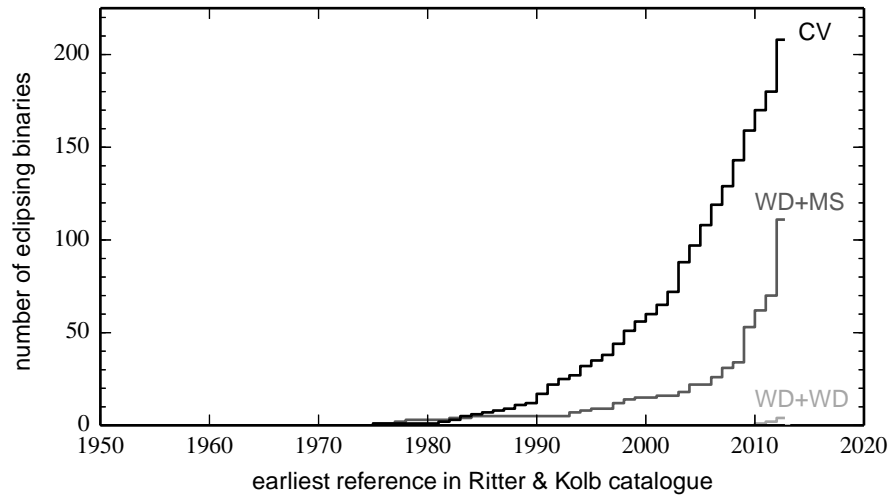
Figure 1.12: Number of known eclipsing detached and semi-detached white dwarf + main-sequence star binaries and eclipsing double white dwarf binaries (WD+MS, CV and WD+WD respectively). Data from Ritter & Kolb catalogue, edition 7.22, June 2014 (Ritter & Kolb, 2003).

sequence star (WD+MS) binary.

In particular, this thesis focuses on eclipsing white dwarf binaries, the numbers of which have increased dramatically in recent years, mainly due to large surveys such as the Sloan Digital Sky Survey (SDSS; York et al., 2000) and the Catalina Sky Survey (CSS; Drake et al., 2009). Fig. 1.12 shows the cumulative number of three subsets of known eclipsing white dwarf binaries from the Ritter & Kolb catalogue (Ritter & Kolb, 2003). In most binaries found so far in this eclipsing subset, the secondary star is a low-mass M-dwarf (dM) and typical orbital periods are between 2 hours and 2 days, with the majority closer to the lower boundary. The dominance of M-dwarf secondary stars, as well as the prevalence of short-period binaries, are partly due to observational selection effects. Stars with significantly earlier spectral types such as A, G and K stars are much brighter, and therefore more likely to outshine a white dwarf companion, making it more difficult to find such binaries, although some are known (Vennes et al., 1998; Burleigh & Barstow, 1999, 2000).

Although not the largest group, the detached binaries have the advantage of being simple systems because there are no varying elements in these binaries. Let us consider the light curves produced by an eclipsing WD+dM binary as seen from Earth. In these binaries, the orbital inclination i is close to $90°$, so that the binary is viewed almost exactly edge-on. Orbital phase $\phi = 0$ is defined at time T_0, as the moment at which the line of sight from Earth aligns with the line connecting the stellar centres while the white dwarf is farthest away from the observer and the M-dwarf is closest. Half an orbital period P_{orb} later the white dwarf is closest to the observer, and the orbital phase is equal to $\phi = 0.5$, etc.

In the simplest case, the white dwarf dominates the flux, and the M-dwarf is hardly visible. The resulting light curve will be flat at all orbital phases except for those during

which the white dwarf moves behind the M-dwarf and is being eclipsed. This is illustrated in the top panel of Fig. 1.13, where such a light curve is generated from a simple model.

When the M-dwarf is close to filling its Roche lobe, the star itself becomes distorted because it follows the gravitational equipotential surfaces (see 1.11). It takes on a droplet shape and therefore the star's projected surface area is larger when viewed from the side than when viewed from the front or back. As the binary stars orbit their common centre of mass, the variable fraction of surface area visible produces a modulation in the light curve with a period equal to half the orbital period. This so-called ellipsoidal modulation is illustrated in the middle panel of Fig. 1.13. Modelling a light curve of a binary that shows such a modulation of the M-dwarf can help determine the orbital period P_{orb} of the binary, as well as the radius of the M-dwarf relative to the semi-major axis of the binary: R_{dM}/a. However, if the binary is not eclipsing, one should be careful not to confuse ellipsoidal modulation with the so-called reflection effect.

The reflection effect occurs when the white dwarf is sufficiently hot and the orbital distance between the stars is small enough for the side of the M-dwarf facing the white dwarf to be strongly irradiated. The atmosphere of the M-dwarf reprocesses the photons and emits them at slightly redder wavelengths. This produces the reflection effect in the light curve, but note that technically speaking it is not reflection but reprocessing of the light that causes the observed effect. When the irradiated face of the M-dwarf is visible to the observer, the flux increases and when the cool back of the M-dwarf turns towards the observer the flux decreases, as is illustrated in the bottom panel of Fig. 1.13. This type of modulation occurs on the orbital period.

A given binary may exhibit either ellipsoidal modulation or the reflection effect, or both. Both the ellipsoidal modulation and the reflection effect are more pronounced in binaries with high orbital inclinations i, and may therefore be used to find such eclipsing binaries (Parsons et al., 2013b, 2015).

1.4.2   Semi-detached white dwarf + M-dwarf binaries

When the M-dwarf in detached WD+dM binaries starts evolving into a giant, or when the orbital period has decreased significantly due to the loss of angular momentum, the M-dwarf will start to fill its Roche lobe. At this point, the M-dwarf will lose matter through the L_1 Lagrange point, after which the matter becomes gravitationally bound to the white dwarf. However, because of the angular momentum it carries, the matter cannot directly accrete onto the white dwarf. Instead, assuming the white dwarf does not have a significant magnetic field, the material will pass the white dwarf by, will then fall back towards it again, and will hit material of the accretion stream at an earlier point. In this way an eccentric ring is formed around the white dwarf, which will become a circular ring and then spread into a disc, as illustrated in Fig. 1.14.

Such semi-detached white dwarf + low-mass main sequence star binaries are called cataclysmic variables (CVs; Warner, 2003; Hellier, 2001). This name is inspired by the often dramatic and significant changes in brightness that accompany the variable accretion
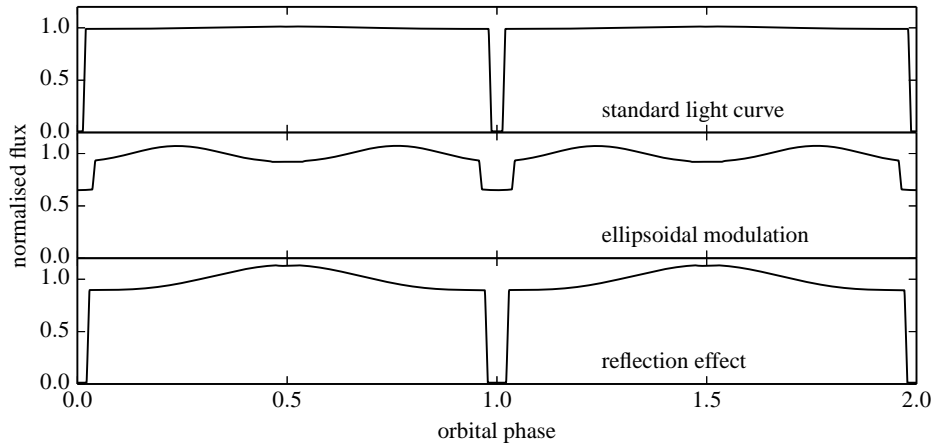
Figure 1.13: Model light curves of detached eclipsing WD+dM binaries with an inclination $i = 90°$. *Top:* simple detached binary. *Middle:* light curve showing ellipsoidal modulation, caused by Roche lobe distortion of the secondary star. *Bottom:* light curve showing the reflection effect, present in binaries with a hot white dwarf. Because the stars are locked in synchronous rotation, one side of the M-dwarf will be strongly irradiated, and will therefore emit additional reprocessed radiation.
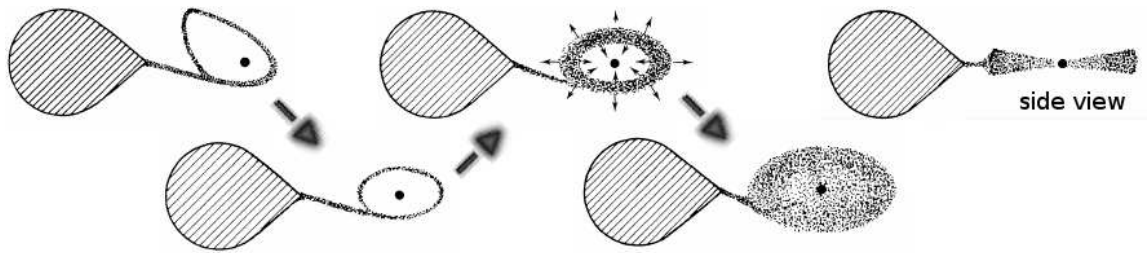
Figure 1.14: Schematic illustration of the four stages in the formation of an accretion disc in a cataclysmic variable. A Roche lobe filling companion (droplet shaped, shaded) loses matter through the inner Lagrangian point L_1 to a non-magnetic, degenerate object (black dot). The fifth figure shows a side view of the binary with a fully formed disc. Based on a figure from Verbunt (1982).

rates in these systems and the subsequent build-up and release processes controlling the accretion disc. The light curves of CVs are generally dominated by the bright accretion disc, and/or the hot spot where the accretion stream hits the disc.

The evolution of CVs is driven by angular momentum exchange between the two stars and angular momentum loss from the binary (see Eq. 1.9). The standard model includes as the dominant mechanism for angular momentum loss of long-period CVs ($P_{orb} \gtrsim 3$ hr) a process called magnetic braking, while the evolution of those at short orbital periods ($P_{orb} \lesssim 2$ hr) is dominated by gravitational wave radiation (see Rappaport et al., 1983; Howell et al., 2001; Knigge, 2006; Knigge et al., 2011, for more details). Both mechanisms will be discussed in more detail in the next section. Suffice it to say here that this model was developed to explain the famous period gap of cataclysmic variables. This period gap corresponds to a significant dearth of CVs in the period range 2 hr $\lesssim P_{orb} \lesssim 3$ hr compared to the number of systems at either side of this gap (Gänsicke et al., 2009; Ritter & Kolb, 2003). It is a key characteristic of the population of known cataclysmic variables,
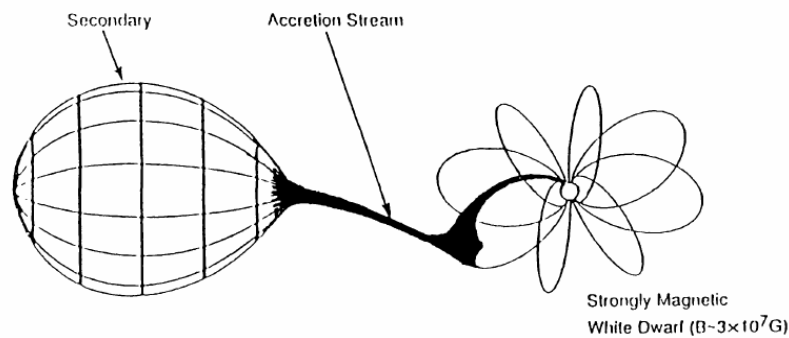
Figure 1.15: Schematic view of a polar, a cataclysmic variable with a strongly magnetic white dwarf, showing the donor star (left, marked secondary, generally a low-mass MS star), the accretion stream, and the accretor (right, magnetic white dwarf) (from Cropper, 1990).

and is believed to be related to the M-dwarf's (in)ability to produce a magnetic field and (dis)continue efficient angular momentum loss through a stellar wind.

Cataclysmic variables in which the white dwarf has a noticeable magnetic field also exist. These are divided into two categories, depending on the strength of this magnetic field. Those with field strengths above $\gtrsim$ 10 MG are called polars or AM Her type systems, after the class prototype (see Cropper 1990 for a review, and Warner 2003, Chapter 6). In polars, the accreting material does not get the chance to form an accretion disc because the magnetic field lines will guide the material away from the orbital plane and towards the white dwarf's magnetic pole, as illustrated in Fig. 1.15. In most polars the strong magnetic field causes the white dwarf to rotate synchronously with the orbit (Cropper, 1988), so that the same side is always turned towards the M-dwarf and the accretion stream. As in standard CVs, the accretion rate is variable, and so polars can be in high states or low states. During high accretion rates ($\sim 10^{-9}$ M$_\odot$/yr), the accreting pole or poles will dominate the light curve. On the other hand, during low accretion rates ($\sim 10^{-11}$ M$_\odot$/yr), the accreting pole(s) may hardly be visible at all. The difference between low and high states can be as large as several magnitudes (Bours et al., 2014b; Gänsicke et al., 1995).

Those CVs in which the white dwarf is magnetic, but not strongly enough to force synchronisation of the white dwarf to the binary orbit, fall into the category of intermediate polars (see Warner 2003, Chapter 7). Field strengths are typically in the range of $\sim$ 0.1 – 10 MG, and determine the type of accretion. The weaker fields are not able to force the flow of the accretion stream after it leaves the inner Lagrangian point, and therefore a disk is formed, as is the case in non-magnetic CVs, although the inner part of this disk is generally destroyed by the magnetic field. On the contrary, there are also intermediate polars in which the accretion stream is in fact magnetically confined, and accretion occurs on the white dwarf's magnetic pole, as in polars. The class of cataclysmic variables containing the intermediate polars therefore includes a wide variety of systems, and numerous types of accretion flows (Norton et al., 2008).

As for the detached binaries, the numbers of known CVs and magnetic CVs have also increased significantly with the arrival of large, all-sky surveys, see Fig. 1.12, and Breedt

et al. (2014); Drake et al. (2014a); Gänsicke et al. (2009); Szkody et al. (2002, part I-VII) for more details.

1.4.3   Detached double white dwarf binaries

The third and last type of binary of particular interest for this thesis includes the double white dwarfs, which are quite common as end products of binary evolution (Marsh et al., 1995; Toonen et al., 2014). Those with separations small enough to have experienced one or two common envelope phases are particularly interesting, as they are thought to be progenitors of supernovae Type Ia (Iben & Tutukov, 1984; Webbink, 1984), Type .Ia (Bildsten et al., 2007), R CrB stars (Webbink, 1984) and AM CVn systems (Breedt et al., 2012; Kilic et al., 2014b). In addition, mergers of Galactic double white dwarfs occur relatively frequently (Badenes & Maoz, 2012), and constitute the main source of the background gravitational wave signal at frequencies detectable from space (Nelemans et al., 2001; Hermes et al., 2012b).

In order to avoid an early merger before both white dwarfs have had a chance to form it may be necessary to avoid substantial shrinkage of the orbit during the evolution of the primary, more massive star into a white dwarf. This is where the γ prescription of the common-envelope phase becomes important. As mentioned before, in order to avoid the production of only unequal-mass double white dwarf binaries, the orbit of the binary after evolution of the primary star needs to be wide enough to allow the secondary star to evolve substantially as well. It needs to have enough space to expand while evolving and growing its core mass. Therefore the first mass-transfer phase cannot be described by a classical α common envelope, because this is generally paired with substantial shrinkage of the binary's orbit. A schematic diagram of the binary evolution in which the first common-envelope proceeds via the γ prescription is shown in Fig. 1.16. The specific binary in the figure evolves into a roughly equal-mass double white dwarf binary.

Currently there are five known double white dwarf binaries that are also eclipsing: NLTT 11748 (Steinfadt et al., 2010), CSS 41177 (Parsons et al., 2011a; Bours et al., 2014a), GALEX J171708.5+675712 (Vennes et al., 2011), SDSS J065133.33+284423.37 (Brown et al., 2011) and SDSS J075141.18-014120.9 (Kilic et al., 2014b). For these systems, masses can be determined from orbital velocities and radii from light curve analysis. Due to their eclipsing nature, the inclination of the system is strongly constrained, allowing for direct mass determinations as opposed to lower limits. In particular, CSS 41177 is the only one of the five binaries that is also a double-lined spectroscopic binary, allowing direct measurement of the stars' orbital velocities (Parsons et al., 2011a; Bours et al., 2014a) and therefore their masses without needing to assume a mass – radius relation. A detailed analysis of this system is presented in Chapter 3, based on Bours et al. (2014a) and Bours et al. (2015a).

WD 0136+768

Age (Gyr)	$M_1(M_\odot)$			$M_2(M_\odot)$	$P_{orb}(d)$
0.000	1.59			1.53	75.88
2.379	1.59			1.53	75.88
2.379	0.34			1.53	269.50
2.678	0.34			1.53	269.50
2.830	0.34			0.43	1.41

100$R_\odot$
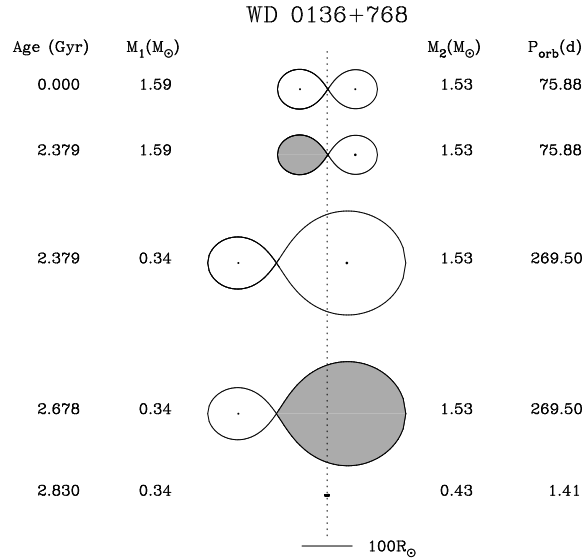
Figure 1.16: Schematic drawing of the binary evolution that resulted in the close double white dwarf binary WD 0136+768 (Maxted et al., 2002; van der Sluys et al., 2006). Starting with two ZAMS stars (top), the binary experiences a γ common-envelope phase as the primary star evolves and an α common-envelope as the secondary evolves. The final binary is a close double white dwarf binary with an orbital period of 1.41 days (bottom). Courtesy of Marc van der Sluys.

1.5 Orbital period variations: real & apparent

A substantial number of eclipsing white dwarf binaries that have been monitored for variations in their eclipse times do indeed show such changes. There are several processes that can lead to eclipse timing variations in close binaries. Eclipsing white dwarf binaries are particularly useful for studying this phenomenon, because the short and sharp features of a white dwarf eclipse are uniquely suited for precise timing. As seen earlier, the evolution of close white dwarf binaries is determined by the binary's angular momentum and the stellar masses, and by how these parameters change with time (see Eq. 1.9). The stellar masses can change through mass-transfer between the stars, or by mass-loss through a stellar wind, although the latter is usually very small compared to the star's mass. A binary's angular momentum can decrease through a mechanism called magnetic braking (Verbunt & Zwaan, 1981; Mestel, 1968; Huang, 1966), or through emission of gravitational wave radiation (Paczyński, 1967; Faulkner, 1971).

In addition, other processes may be at work that make it appear as if the binary is losing angular momentum, while this is in fact not the case. The two most popular theories include one now often referred to as Applegate's mechanism (Applegate 1992; Applegate & Patterson 1987, see also Lanza et al. 1998), and the presence of circumbinary planet-like or brown dwarf-like bodies of mass (see for example Marsh et al., 2014; Beuermann et al., 2013a; Beavers et al., 1986).

All four processes just mentioned are described in more detail below. Any of them may be measured in observational data of a binary if it is possible to measure a regular, unrelated phenomenon in that binary. This could be the eclipse of a white dwarf or neutron star (Wood & Forbes, 1963; Parsons et al., 2010b; Hermes et al., 2012b), the very regular

pulses that a magnetic neutron star emits (Wolszczan & Frail, 1992; Wolszczan, 1994), or pulsations of stars themselves (Mullally et al., 2008; Hermes et al., 2013b). Such a precise clock allows the observer to measure changes in the orbital or spin periods in the system. Generally, observational data would also allow one to distinguish between certain mechanisms through the time scale on which the phenomena occur. Both magnetic braking and gravitational wave emission are secular processes, evolving slowly and steadily and typically taking 10^8 - 10^9 years. Orbital period changes caused by Applegate's mechanism or apparent variations caused by circumbinary objects on the other hand typically take place on 10 - 100 year time scales.

1.5.1   Magnetic braking

A short-period WD+MS binary can lose angular momentum through a process called magnetic braking (Verbunt & Zwaan, 1981; Mestel, 1968; Huang, 1966). This occurs because the main-sequence star emits a stellar wind that flows away from the star along the magnetic field lines. Assuming a simple dipolar magnetic field, the wind is mainly emitted from the poles, as the field lines near the rotational equator are closed. Because the wind consists of ionised particles, it is forced by the magnetic field to corotate with the star out to the Alvén radius. When the matter decouples from the magnetic field, it takes some angular momentum with it, thereby decreasing the spin angular momentum of the star. This phenomenon has been measured indirectly by its effect on the rotation rate of single stars (Kraft, 1967; Schatzman, 1962). In close binaries the star rotates synchronously with the orbital motion, so that the star's spin period equals the binary's orbital period. Therefore the angular momentum that is carried away by the stellar wind is effectively removed from the binary's orbital angular momentum, causing the binary's orbit to decrease over time.

Magnetic braking is especially important in cataclysmic variable stars and their progenitors. These binaries have separations that are small enough for magnetic braking to drive the binaries closer together and thereby drive evolution of the ongoing mass-transfer and the binary itself (Knigge et al., 2011; Rappaport et al., 1983). Note that the efficiency of magnetic braking depends on the presence and strength of a magnetic field in the low-mass main-sequence star (Schreiber et al., 2010). Magnetic fields are thought to be generated by the presence of a tachocline, which marks the transition from a radiative core to a convective envelope, through the combination of the turbulent convective motion and differential rotation. Since main-sequence stars with spectral types later than about M3 are fully convective, cataclysmic variables with such M-dwarfs experience little magnetic braking (Rebassa-Mansergas et al., 2013). This transition from being partially to being fully convective, which occurs naturally when the M-dwarf has lost enough mass, causes the star to contract slightly so that it loses contact with its Roche lobe and the mass-transfer process is interrupted. In addition, the star is out of thermal equilibrium, because its thermal time scale exceeds the time scale of the mass-tranfer processes, causing the star to be larger than usual for its mass. Once mass transfer stops, the star is able to regain thermal equilibrium by shrinking. This is the cause of the orbital period gap at $2 - 3$ hrs al-

ready described in Sect. 1.4.2. The subsequent evolution of cataclysmic variables is mainly driven by gravitational wave emission, which also ensures that mass-transfer restarts once the secondary fills its Roche lobe again at shorter orbital periods.

1.5.2 Gravitational wave emission

When binaries have sufficiently short orbital periods, angular momentum loss through gravitational wave emission becomes efficient (Paczyński, 1967; Faulkner, 1971). As a result, the binary's period will continue to decrease until the two stars merge. The time scale on which a merger occurs can be calculated through

$$\tau_{\mathrm{m}} = 10^7 \, \frac{(M_1 + M_2)^{1/3}}{M_1 M_2} \, P^{8/3} \mathrm{yr} \,, \tag{1.12}$$

where the orbital period P_{orb} is in hours and the masses M_1 and M_2 are in Solar masses (Landau & Lifshitz, 1975; Marsh et al., 1995, Sect. 4.3). The merger occurs on shorter time scales for binaries with shorter orbital periods as well as for binaries with more massive stars.

The need for short periods and massive stars implies that gravitational wave emission is only important for short-period binaries that contain one or two compact objects. This includes cataclysmic variables at moments when magnetic braking is inefficient (Knigge et al., 2011), double white dwarf binaries which likely generate most of the low-frequency background gravitational wave emission (Nelemans et al., 2001), and of course neutron star and black hole binaries. The latter two categories may emit stronger gravitational wave signals, but are also much less numerous than binaries containing white dwarfs (see Nelemans et al., 2001, and references therein).

On account of ongoing accretion, gravitational wave emission in short-period CVs does not necessarily result in a merger of the white dwarf and main-sequence star. The mass-loss experienced by the main-sequence star will eventually reduce its mass so far that the core stops fusing hydrogen. At this point, close to 0.08 $\mathrm{M}_\odot$, the M-dwarf essentially becomes a degenerate brown dwarf. As is the case with white dwarfs, the brown dwarf's radius increases in response to mass-loss, the feedback of which results in an increase of the binary's orbital period. This behaviour explains another key characteristic of the period-distribution of cataclysmic variable stars, namely the period-minimum near 80 minutes (Gänsicke et al., 2009; Knigge et al., 2011).

1.5.3 Applegate's mechanism

A third way of changing a binary's orbital period is through coupling with variations in the magnetic field of the main-sequence star. Applegate & Patterson (1987) proposed that a star in a close binary may experience magnetic cycles, and that a change in the global topology of the magnetic field can result in a variable gravitational quadrupole moment. The accompanying changes in the shape of that star affect the gravitational attraction between the pair of stars, and therefore introduces variations in the orbital period of
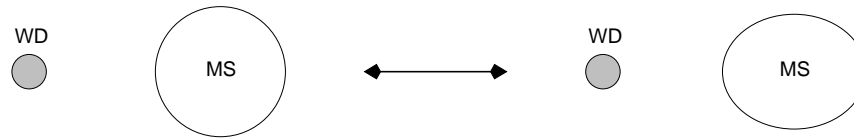
Figure 1.17: Schematic representation of Applegate's mechanism.

the binary. However, Marsh & Pringle (1990) showed that although a star would have sufficient amounts of energy available to produce such an effect, it still falls short by one or two orders of magnitude considering the short time scale on which orbital period variations have been observed in close binaries. Applegate (1992) then updated his earlier theoretical explanation and suggested that angular momentum can be redistributed between the core and the outer layers of a star by the turbulent motion in the convective region and the torques produced by the differential rotation. This also causes the star to deform and become oblate, as illustrated in Fig. 1.17, therefore changing its gravitational quadrupole moment. In turn, this couples to the binary's orbit, which subsequently changes the orbital period on the same quasi-periodic time scales as the magnetic activity cycles that drive the mechanism.

Note that no angular momentum is lost from the binary during this process, it is simply redistributed within the main-sequence star. Nonetheless, this requires energy. Since the orbital period variations are driven by the main-sequence star in the binary, the maximum amplitude of the variations is determined by the maximum amount of energy available in this star, which is equal to the total luminosity of the star. Generally, in close white dwarf binaries, the main-sequence companions are M- or K-dwarfs. The luminosity of these stars can be considered as their maximum energy budget available to drive the magnetic cycles, their physical distortions, and therefore the binary's orbital period variations. For certain binaries in which large variations of this kind have been observed, the energy budget is seemingly insufficient (Bours et al., 2014b; Brinkworth et al., 2006; Marsh & Pringle, 1990), and other explanations for the observed orbital period variations need to be considered. However, note that a modified version of Applegate's mechanism predicts that orbital period variations can be induced while only requiring a fraction of the energy of the original mechanism of Applegate (1992), see Lanza et al. (1998) and Lanza (2006). This may therefore still be a plausible explanation for the extreme orbital period variations observed in some binaries, and indeed may be the correct explanation for any kind of variation in the orbital periods of close binaries.

1.5.4 Circumbinary planets or brown dwarfs

A last possibility that could explain variations in observed 'clocks' such as white dwarf eclipse times is the presence of planet-like or brown dwarf-like bodies of mass in wide, circumbinary orbits around the close binary. These will be referred to as circumbinary planets or circumbinary brown dwarfs hereafter. The effect of such an additional unseen object is illustrated in Fig. 1.18. It is often quoted as the light travel time effect, because the third body causes the binary to periodically change its distance to a given observer,
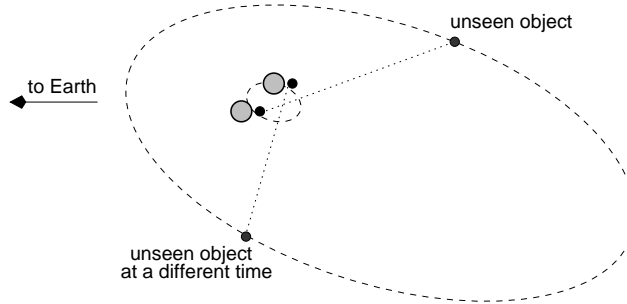
Figure 1.18: Schematic representation (not to scale) of an unseen, third body in a wide, circumbinary orbit around a close white dwarf + M-dwarf binary. The additional object's presence effects the observed times of eclipse of the white dwarf by its main-sequence companion as it forces the binary to move around the centre of mass between the binary and the unseen object. This causes the eclipses of the white dwarf to be observed slightly earlier or later by an observer at Earth, depending on the configuration and exact position of the binary at different times in this orbit.

thereby causing eclipses to be observed slightly advanced or delayed with respect to the expected eclipse time in a sinusoidal manner (Irwin, 1959).

No such circumbinary planet or brown dwarf has been directly observed as yet, but for one white dwarf + M-dwarf binary there is good indirect evidence of two such companions being present. This binary is NN Ser (Marsh et al., 2014; Beuermann et al., 2013a), for which the model predicts the presence of two planets with masses several times that of Jupiter and orbits of 8 and 15 years around the central binary. More observational data in the coming decade is necessary to conclusively confirm whether the current model correctly predicts future white dwarf eclipse times.

An additional complication of the hypothesis that circumbinary planets are present around white dwarf binaries lies in the dynamically stability of such systems if multiple planets are inferred. Multiple planets introduce multiple sinusoidal variations in the eclipse arrival times as observed at Earth. However, because any given signal can be fitted with a model that includes a sufficiently large number of sinusoids, any model that relies on several planets ($\gtrsim 3$) being present immediately introduces doubt about the validity of that model. One important clue in this regard is the dynamical stability of the proposed planetary system (see for example Hinse et al., 2012; Horner et al., 2012a; Wittenmyer et al., 2013), with the assumption that true planetary systems are stable on time scales of hundreds of megayears, if not on gigayear time scales.

1.6   Time scales used for timing periodic phenomena

Due to the Earth's motion around the Sun and the finite speed of light, measuring times from observations concerning stars, binaries, or other targets outside our Solar system has to be approached with caution. The exact time that a certain event is observed depends on the changing position of the observer in the Solar system, as well as the particular clock used to express the time. To be able to compare observations from different epochs nonetheless, the observed time can be converted to a number of time stamps (Eastman et al., 2010).

Rather then using the civil Gregorian calendar, times in astronomy are quoted with respect to the Julian calendar. Julian dates are expressed in decimal numbers, with the zeropoint at JD = 0 coinciding with noon Greenwich Mean Time on November 24, 4714 BC in the Gregorian calendar. By now, Julian date number have become quite long, and a more recent zeropoint is often used. The Modified Julian Date (MJD) starts counting at midnight November 17, 1858, so that MJD = JD - 2400000.5. To adjust to the reference frame of the Sun, rather than using the variable reference of Earth, one can also use Heliocentric Julian Date (HJD). To be even more precise, one can correct for the motion of the Sun around the barycentre of the Solar system, and use Barycentric Julian Dates (BJD). Both of these latter two can be expressed with respect to the more recent zeropoint, to obtain HMJD and BMJD.

The second important aspect regarding time stamping is the time standard used, which refers to the way a particular clock ticks (Eastman et al., 2010). As a time standard, Coordinated Universal Time (UTC) is most commonly used. However, this time system includes leap-seconds, which accumulate over the years, lead to jumps in the time scale, and can therefore make time comparisons tricky. When heliocentric and barycentric reference frames are used, a higher precision is often required. There are several alternatives to UTC, including, in order of increasing accuracy, International Atomic Time (TAI, from Temps Atomique International), Terrestrial Time (TT) and Barycentric Dynamical Time (TDB). TAI runs at nearly the same rate as UTC, but does not include leap seconds, and currently TAI = UTC + N, where $N = 35$ s until June 2015, when the next leap second will be introduced. TT includes an offset from TAI, which was introduced to retain continuity with its predecessor Ephemeris Time, so that TT = TAI + 32.184 s. TDB is a relativistic time standard in the reference frame of the Solar system barycentre, and is equal to TT corrected for time dilation and gravitational redshift caused by bodies in the solar system. TDB differs from TT by at most 3.4 ms. Therefore

$$TDB = UTC + N + 32.184 + (TDB - TT). \qquad (1.13)$$

To obtain the highest precision in this thesis, times are quoted in BMJD(TDB).

1.7   Conclusions

In this chapter I have introduced white dwarfs stars as the remnants of stellar evolution, and discussed their defining properties, including effective temperatures, surface gravities and the characteristic mass – radius relationship of these degenerate stars. I have also presented an overview of the main types of close binary stars in which white dwarfs can be found, and the key processes that drive the evolution and appearance of these systems. Finally, I have considered different reference frames and time standards, and justified the use of the BMJD(TDB) time stamp throughout this thesis.

★ ★ ★

Chapter 2

Observational, data reduction & statistical analysis techniques

2.1 Introduction

This chapter discusses a range of techniques on which the work presented throughout this thesis is based. First it focuses on the different instruments used for obtaining the observations discussed in later chapters. These instruments vary from ground-based optical photometers and spectrographs to satellite-based far-ultraviolet instruments. Although raw data from the different instruments are reduced using different pipelines, there are general concepts such as debiasing and flatfielding that apply to all data sets. These will also be explained and discussed in this chapter. The last part centres on statistical analysis techniques, in which both Monte Carlo and Markov-chain Monte Carlo techniques are discussed, which will later be used to statistically determine the values of model parameters. But first I begin with a description and discussion of charge-coupled devices, which form the basis of most astronomical instruments currently in use.

2.2 Charge-Coupled Devices

Charge-Coupled Devices (CCDs; Howell, 2006) have been in wide use in astronomy since shortly after their development in the early 1970s. One of the main attractions at the time was that CCDs were easier to use than the previously-used photographic plates and image photon counting systems (Jenkins, 1987). They are also more efficient in converting incoming photons into electronically readable charge (quantum efficiency). Since then, CCDs have improved significantly, which explains why they are currently the standard in astronomy throughout the wavelength range in which they are light-sensitive. Hampered by absorption in the Earth's atmosphere, from the ground CCDs are mostly used at the restricted wavelength range of $\lambda \sim 3000 - 11000$ Å. On board satellites however, they are also used at, for example, ultraviolet and X-ray wavelengths.

Briefly, CCDs work as follows. The main component is a photoactive layer, usually a silicon layer that can be p- or n-doped with boron or phosphorus. When incoming photons hit this layer, an electron-hole pair is created there. The voltage on the layer ensures that these pairs are separated and the electrons move towards the surface where they accumulate in potential wells, one for each pixel of the CCD. To minimise detection
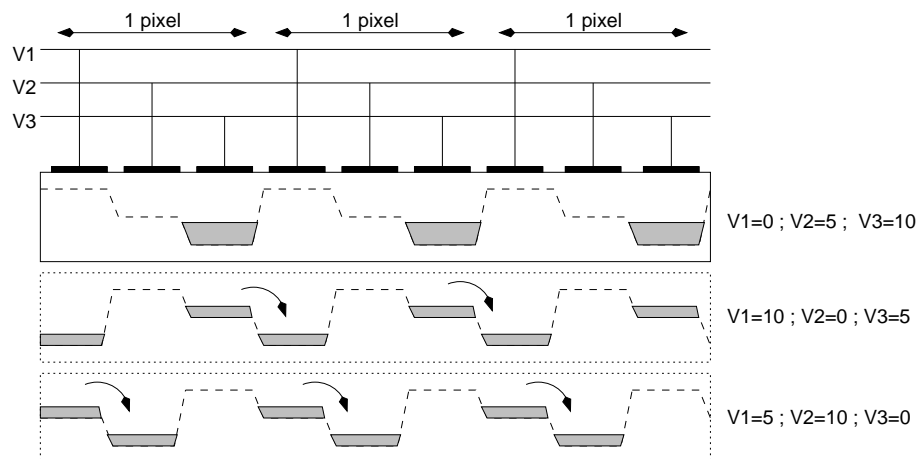
Figure 2.1: Schematic drawing of charge transfer in a CCD operating in a three-phase mode. The voltages are shown at three stages during the clocking cycle. After one full cycle, the charge in a pixel has been transferred to a neighbouring pixel. Based on a figure from Howell (2006).

of electrons that are thermally generated (called dark current), CCDs are usually cooled and operated at temperatures well below room temperature. After the full exposure time has elapsed, well-orchestrated voltage changes force the charges to move from well to well, thereby transferring the charges to the point where they can be read out. This moving of charge packages is referred to by the term 'clocking' and is schematically illustrated in Fig. 2.1. For example, if the readout point is situated in the lower left corner of the CCD, the bottom row of pixels can be clocked horizontally until it is entirely read out, after which the remaining image is clocked vertically by one row to prepare for reading out the next row of pixels. During readout, the numbers of electrons are digitised and stored. Reading out a full-frame 1024×1024 pixel^2 CCD generally takes about ten seconds. This readout time sets the so-called dead time between exposures, the time in which the CCD cannot be used for collecting data.

If shorter exposures are required, it is possible to use a CCD with $2 - 4$ readout points, up to one at each corner, which reduces the readout time by $2 - 4$. In addition, it is sometimes possible to use a faster mode to digitise the data, although this comes with the disadvantage of a higher readout noise level. For CCDs, the readout noise is introduced by the conversions from analogue signals to digital number, and by the electronics themselves, and is therefore present in every pixel separately.

One of the main advantages of CCDs is that they are linear in their output, meaning that they generate the same number of electrons per incoming photon up to several tens of thousands of photons per pixel. CCDs also have high quantum efficiencies, which can be well over 90% at certain wavelength ranges. In addition, they are geometrically stable and can nowadays have large formats of up to $\sim 10^4 \times 10^4$ pixel^2.

Frame-transfer CCDs are similar to conventional CCDs, except that they have twice as many pixels in one direction (say vertically) than in the other. The top half of the CCD is the image area and is exposed as normal, while the bottom half is covered by an opaque layer and is known as the storage area. At the end of each exposure, all the charges are

quickly clocked to the storage area, from where they are read out one-by-one while the image area can be exposed again. By this method, the dead time between exposures is reduced to the time it takes to clock the entire image to the storage area. For example, the frame-transfer CCDs used in ULTRACAM take just under 24 ms to clock the full image to storage (Dhillon et al., 2007).

Electron-Multiplying CCDs (EMCCDs) are another subset of CCDs, which have the option to read out data in avalanche mode. Rather than immediately digitising the electrons in a given potential well when reading out the CCD, the charges are fed through a gain register. In this register the electrons fall through a number of high-voltage potential drops, in which an avalanche of electrons is created. The avalanche gain is typically ~ 1000, leaving any readout noise negligibly small in comparison. For this last reason, the CCD can be read out in its fastest possible mode, thereby decreasing the dead time between exposures.

Although EMCCDs are superior to normal CCDs when it comes to readout time and readout noise, they are limited by the fact that the gain factor is determined in a stochastic way. Effectively the gain factor is drawn from a distribution around a certain mean value, so that there is a high probability of drawing a number that differs slightly from the mean. This uncertainty in the gain factor is statistically equivalent to halving the quantum efficiency of the detector (Tulloch & Dhillon, 2011), so that one effectively loses half of the signal. In addition, EMCCDs are only really useful for a limited range of both astronomical targets and observational weather conditions. In particular, the avalanche mode is useful in situations in which the quality of the data is limited by the readout noise when using normal readout. This restriction limits its usefulness for example during bright time (nights when the moon is close to full), since the EMCCD's avalanche mode amplifies the rather bright sky background as well. The same argument holds for observations with exposure times longer than roughly 1 second, during which photons accumulate in the sky background regions. The highest gain from using avalanche rather than normal readout mode is typically found when observing faint targets (magnitude > 20), at the highest frame rates (> 100 Hz) during dark time (nights when the moon is close to new) (Dhillon et al., 2014).

2.3   Photometric observations

2.3.1   ULTRACAM

ULTRACAM is a high-speed photometric camera commissioned in 2002, with three frame-transfer E2V CCDs that operate simultaneously and a field of view of $5' \times 5'$ (Dhillon et al., 2007). All incoming light travels through four optical elements, after which two dichroics split it into three beams, one for each CCD detector, each Peltier cooled to 233 K. Fig 2.2 illustrates how the light rays travel to the blue, green and red arms of the instrument, which receive light at wavelengths of $\lambda < 3870$ Å, 3870 Å $< \lambda < 5580$ Å, and $\lambda > 5580$ Å respectively, where the cutoffs are determined by the dichroic mirrors. In front of
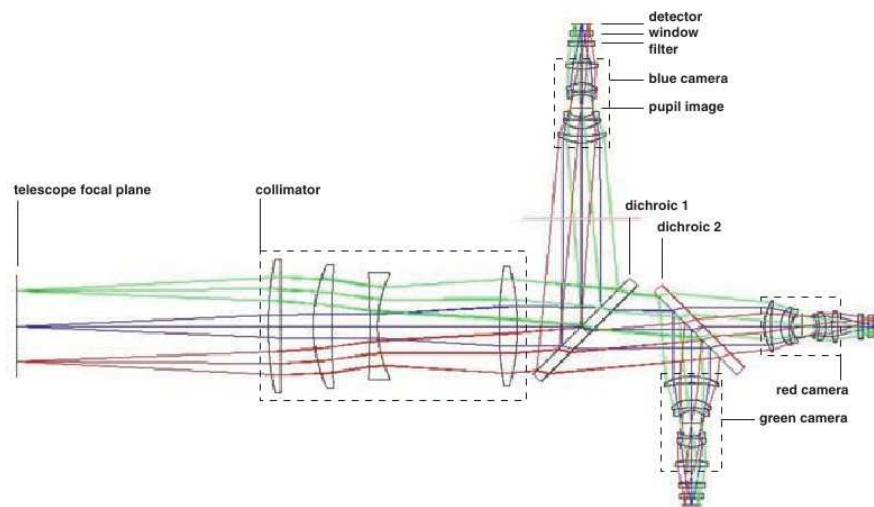
Figure 2.2: Paths of light traced through the ULTRACAM optics (to scale). Figure from Dhillon et al. (2007).

each detector a filter can be placed to further specify the wavelength of the light that is detected on the CCDs.

Each of the three detectors are frame-transfer CCDs, the detailed function of which is illustrated in Fig 2.3. The top half of the CCD is a 1024×1024 pixel^2 imaging area, which is exposed when observing a target. Once the exposure is finished, the data are transferred to the bottom half of the CCD, the storage area. This vertical clocking takes 23.3 μs per row, and therefore it takes 23.8 ms to clock the entire image to the storage area. These 24 ms set the minimum dead time between exposures. Once in the storage area, the data will be read out through two channels, one for each half of the CCD. Once a row is clocked horizontally through the readout channels, the entire image is clocked down vertically by one row, and the next row is read out. The horizontal clocking takes 0.48 μs per pixel. Thanks to GPS time stamping, the ULTRACAM data has absolute timestamps better than 0.001 seconds.

The readout itself can be performed in three modes: slow, fast and turbo, for which the full frame readout time is ~ 6 s, ~ 3 s and ~ 2 s respectively. Longer exposures can be obtained by setting a delay time in addition to these minimum readout times. Although faster readout may seem desirable, one has to remember it suffers from higher readout noise levels. It is also possible to bin the pixels on the CCD, which is particularly useful when weather conditions are not ideal, and which will increase the signal-to-noise ratio in favour of spatial resolution.

If exposure times shorter than the full frame readout time are required, it is possible to set up windows on the CCDs, an example of which is shown in Fig. 2.3. Due to the vertically symmetric readout of the CCD, the window sizes need to be identical on the left and right halves of the CCDs. They can therefore be specified in pairs of two only, with a maximum of six individual windows. Only the pixels inside the specified windows will be read out, which can significantly decrease the readout time and therefore the minimum
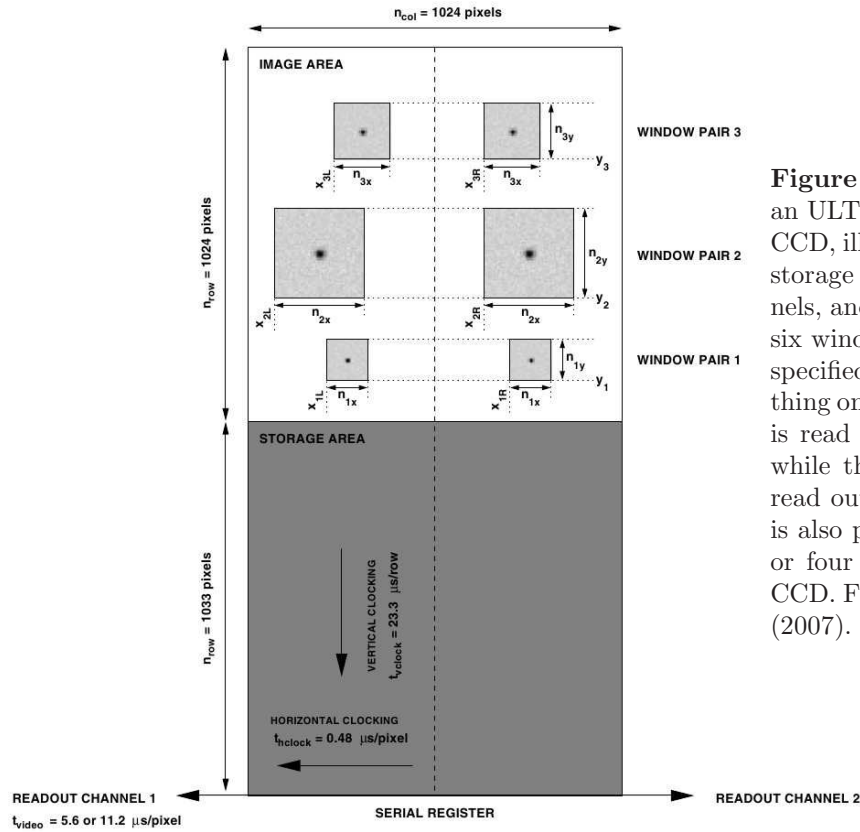
Figure 2.3: Illustration of an ULTRACAM frame-transfer CCD, illustrating the image and storage areas, the readout channels, and the option to read out six windows on the CCD, to be specified by the user. Everything on the left half of the CCD is read out through channel 1, while that on the right half is read out through channel 2. It is also possible to read out two or four windows, or the entire CCD. Figure from Dhillon et al. (2007).

exposure time.

If exposure times shorter than 0.1 s are required, it is possible to use the so-called drift mode, which makes it possible to reach frame rates of 500 Hz. In this mode, only two windows can be used, each with an area of only a few dozen pixels, and the vertical clocking operates slightly differently in order to reach even shorter exposure times (see Dhillon et al., 2007, for details).

Ideally, for any given observation, the exposure time is longer than the time needed to read out the full frame or windowed image from the storage area, so that only ~ 24 ms (or fewer in drift mode) are lost between exposures. By windowing the CCD and carefully choosing the readout mode, one can reach the time-resolution required, while keeping a duty cycle close to 100%. The duty cycle is defined as the exposure time divided by the sum of the exposure and dead times.

The ULTRACAM combination of high-speed photometry with multi-channel observations covering a wide wavelength range is very powerful. It enables observations of astrophysical processes that occur on timescales shorter than a few seconds. Examples include, but are not limited to, eclipsing detached white dwarf binaries (Parsons et al., 2012a; Marsh et al., 2014; Bours et al., 2014a), cataclysmic variables (Littlefair et al., 2006, 2014; Savoury et al., 2011; Bours et al., 2014b), X-ray binaries (Shahbaz et al., 2010; Durant et al., 2011), asteroseismology (Dhillon et al., 2011; Maxted et al., 2013; Pyrzas et al., 2015), planetary transits (Copperwheat et al., 2013; Bento et al., 2014) and occultations of Kuiper Belt Objects (Roques et al., 2006; Doressoundiram et al., 2013).
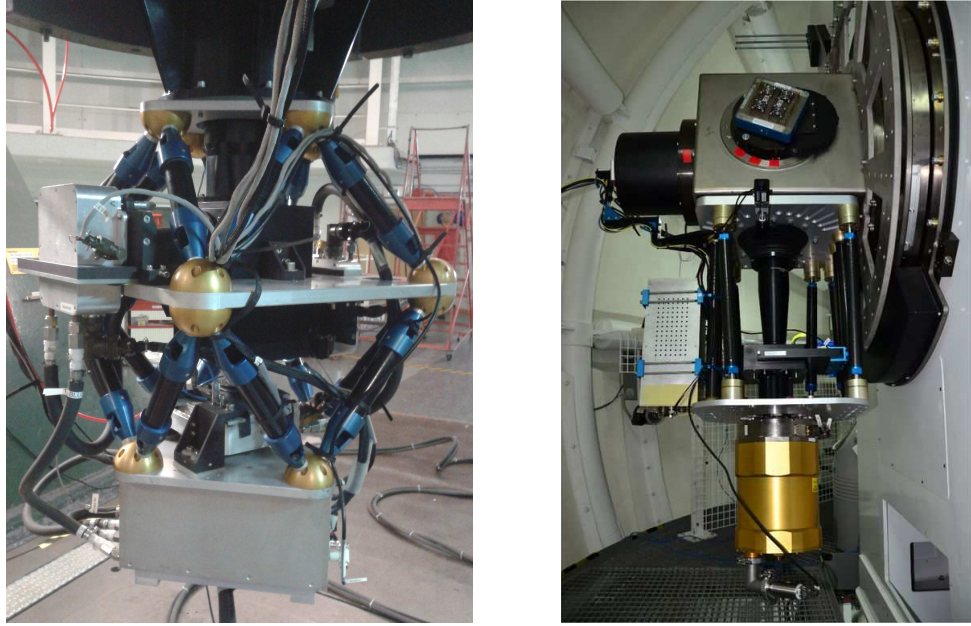
Figure 2.4: *Left:* ULTRACAM on the Cassegrain focus of the William Herschel Telescope. *Right:* ULTRASPEC on the Nasmyth focus of the Thai National Telescope.

For the observations discussed in this thesis, ULTRACAM has been mounted on several telescopes. Most often, it was on the 4.2 m William Herschel Telescope (WHT), which is part of the Isaac Newton Group of Telescopes situated at the Roque de los Muchachos Observatory on La Palma, one of the Canary Islands of Spain. The instrument was also mounted on the 3.5 m New Technology Telescope (NTT) at the La Silla Observatory and on one of the 8.0 m Unit Telescopes of the Very Large Telescope (VLT) at the Paranal Observatory, both part of the European Southern Observatory (ESO) in Chile.

A range of filters is available for observations. The ULTRACAM $u'g'r'i'z'$ filterset is identical to the SDSS $ugriz$ filters. See Dhillon et al. (2007), where also the dichroic cutoffs, the quantum efficiency and the transmission profiles of the ULTRACAM lenses are shown. Clear filters are available to maximise throughput, and in addition, there is a range of narrow-band filters available, see Dhillon et al. (2007) for details. Note that the filters can only be used in certain combinations, as a given filter is only useful in one of the three arms due to the dichroic cutoffs. A picture of the instrument itself is shown in Fig. 2.4.

2.3.2   ULTRASPEC on the Thai National Telescope

ULTRASPEC was originally designed to be the spectroscopic counterpart of the high-speed photometer ULTRACAM described in the previous section (Ives et al., 2008). Due to the inherent nature of a spectrograph, through which the light is spread over many pixels, the design included a frame-transfer EMCCD rather than a standard CCD, to maximise the signal-to-noise ratio (Tulloch & Dhillon, 2011). This detector was set in a cryostat to operate at a temperature of 160 K. The instrument did not include optical elements, as it was possible to mount it on a number of existing spectrographs with external focii. UL-TRASPEC was mounted behind the ESO Faint Object Spectrograph and Camera Version
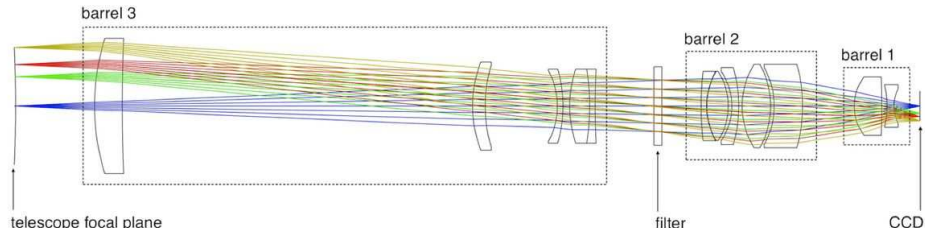
Figure 2.5: A to scale ray trace through the ULTRASPEC optics, with the telescope focal plane on the left and the EMCCD in its cryostat on the right. Figure from Dhillon et al. (2014).

2 on the ESO 3.6 m telescope and the NTT at La Silla, Chile, during one commissioning run and two ~ 20 night science runs which took place in 2006 – 2009. After that, the purpose of the instrument changed with the goal to find a permanent home on a telescope, rather than having to rely on requests and schedules as a visiting instrument.

In November 2013 ULTRASPEC was recommissioned on the 2.4 m Thai National Telescope (TNT) on Doi Inthanon, Thailand, in its new guise as a high-speed photometer (Dhillon et al., 2014, see Fig. 2.4 for a picture of the instrument). The core of ULTRASPEC is still the EMCCD in its cryostat, which is now accompanied by a mechanical chassis and optical elements. The new design is schematically illustrated in Fig. 2.5. In its current form, ULTRASPEC operates as a single-arm version of ULTRACAM. The wheel holding the filters has six positions, and can easily be operated during the night to observe targets at a range of wavelengths. The available filters that are most used include those from the ULTRACAM SDSS filter set $u'g'r'i'z'$ and a Schott KG5 filter ($\lambda_c = 5075$ Å, FWHM $= 3605$ Å). See Fig. 2.6 for transmission profiles of these filters. For details of other available filters, as well as for the quantum efficiency curve and the transmission of the ULTRASPEC lenses, see Dhillon et al. (2014).

2.3.3   RISE on the Liverpool Telescope

RISE (Steele et al., 2008) is a high-speed photometer on the 2.0 m Liverpool Telescope (LT; Steele et al., 2004), with a frame-transfer E2V CCD and a single 'V+R' filter (see Fig. 2.6). The field of view is $9.2' \times 9.2'$, with an $11'$ unvignetted circle. It was designed to be an instrument for exoplanet transit timing, and in terms of time resolution it is equally well suited to observe eclipses of white dwarfs in binary systems (Parsons et al., 2011a; Bours et al., 2014b). A somewhat bluer filter would be better for observing white dwarf + M-dwarf binaries, since the red M-dwarfs start dominating at longer wavelengths. However, this downside is outweighed by the upside of the robotic nature of the telescope, which schedules observations at the start of each night, taking into account a target's visibility, priority, and the required weather conditions. This robotic type of scheduling allows for flexible observations and for eclipse observations on a monthly basis.
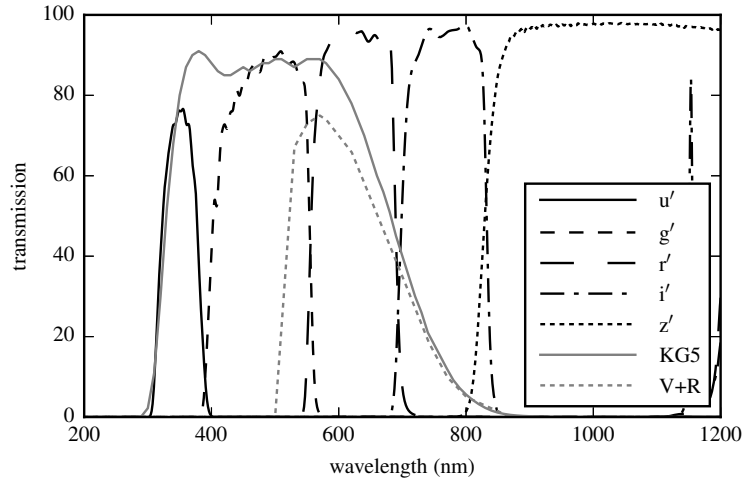
Figure 2.6: Transmission curves of the $u'g'r'i'z'$ filters used in ULTRACAM and ULTRASPEC, the ULTRASPEC Schott KG5 filter and the RISE V+R filter. For details, see Fukugita et al. (1996); Dhillon et al. (2007, 2014); Steele et al. (2008).

2.3.4 The Wide Field Camera on the Isaac Newton Telescope

The Wide Field Camera (WFC) is mounted on the prime focus of the 2.5 m Isaac Newton Telescope (INT) situated on La Palma, Spain, since 1997[1]. The instrument is a mosaic consisting of four thinned EEV 2k×4k CCDs. It is cooled by liquid nitrogen, to operate at 153 K. The field of view of the four CCDs is $34'\times34'$, neglecting the spacing of $\sim 1'$ between the chips. The readout time for the entire mosaic is close to 48 s in slow readout mode, which sets the minimum dead time between exposures if one wants to read out all four CCDs. However, it is possible to read out in fast mode, to read out only CCD 4, or to window CCD 4, all of which significantly decrease the readout time and therefore improve the duty cycle, especially when exposure times below 1 minute are required. A wide range of filters is available, with wavelengths ranging from 4200 Å to 8200 Å, see the website for details.

2.3.5 Photometric data reduction with the ULTRACAM pipeline

The ULTRACAM pipeline was used to reduce the photometric data taken with the instruments described in the previous sections, except for the LT+RISE data which is reduced by the LT's automatic pipeline. The first step in reducing raw data is subtracting a bias frame. Every recorded CCD image includes the so-called bias level, which is equivalent to the number of electrons detected in a given pixel during an exposure of zero seconds. This background level can be easily accounted for by taking some zero-second exposures, and subtracting a mean bias frame from the science data. Because the exposure time is non-existent, the filter used for the observations is not important. However, one should pay careful attention to the readout speed and the binning. These influence the bias levels and should therefore be the same in both the bias and the science data.

---

[1]See *http://www.ing.iac.es/astronomy/ instruments/wfc/* for more information.
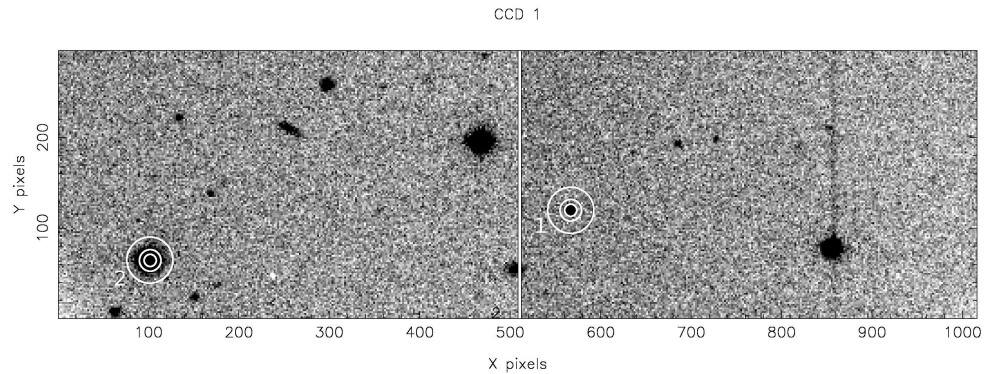
Figure 2.7: ULTRACAM image of the red CCD from an observation of CSS 41177 on 21 Jan 2012. For this particular observation two windows were set on the CCD, using the full x-range, but only 350 pixels in the y-range. This allowed exposure times of 2 seconds, while still keeping the readout noise low by using the slow readout speed. Two apertures for data reduction are set around the target (labelled 1, near pixel position 570,120) and a brighter comparison star (labelled 2, near pixel position 100,70).

The second step involves normalising for the different sensitivity of individual pixels. This is done with flatfield frames, which are uniform, blank images, and can be taken either of the twilight sky or of the lamp-illuminated inside of a telescope dome. Generally, one aims for a large number of photon counts, while ensuring that the signal stays well within the linear range of the CCD. Because the CCD is illuminated uniformly, the number of counts in the pixels of flatfield frames accurately represent the sensitivity of the pixels. Ideally, one combines a large number of mean-normalised flatfield frames by taking the median, thereby rejecting possible cosmic ray hits. Note that a corresponding bias should first be subtracted from the flatfield frames, before creating the final master flatfield. The science data can then be divided by the flatfield to normalise the response of the pixels.

With these two steps of the data reduction process the science data is prepared for extraction of the fluxes of the science targets. Throughout this thesis the photometric data are reduced using relative aperture photometry, in which the target's flux is divided by the flux of a comparison star to remove flux variations caused by variable atmospheric conditions. To further eliminate signal variations due to changing atmospheric conditions I use variable apertures, where the radius of the aperture is scaled according to the full width at half maximum of the stellar profile. Each profile is fit with a Moffat distribution (Moffat, 1969). An example of an ULTRACAM image with specified apertures is shown in Fig. 2.7.

2.4 Spectroscopic observations and data reduction

2.4.1 X-shooter on the Very Large Telescope

X-shooter (Vernet et al., 2011) is the first of the 2nd generation instruments at the Very Large Telescope array of the European Southern Observatory. The instrument covers a wide wavelength range of 3000 to 25000 Å with three echelle spectrographs: the ultraviolet-blue (UVB), visible (VIS) and near-infrared (NIR), see Fig. 2.8. Each has an intermediate
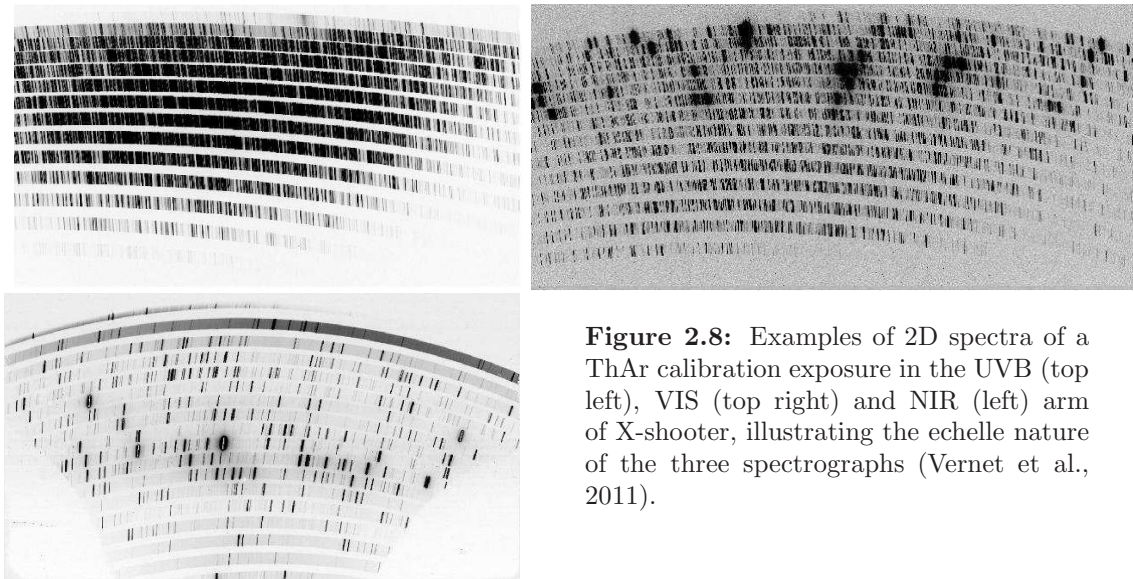
Figure 2.8: Examples of 2D spectra of a ThAr calibration exposure in the UVB (top left), VIS (top right) and NIR (left) arm of X-shooter, illustrating the echelle nature of the three spectrographs (Vernet et al., 2011).

resolution of $R = \lambda/\Delta\lambda = 5000 - 9000$. The detectors are CCDs, cooled with liquid nitrogen to temperatures of 153 K, 135 K and 105 K respectively, to minimise dark current.

The good resolution and the fact that the instrument is mounted on an 8.0 m VLT telescope, make it possible to obtain phase-resolved spectroscopy of short-period white dwarf binaries, because exposure times as short as ~ 5 minutes can be reached while keeping a good signal-to-noise level (Bours et al., 2014a, chapter 3). The wide wavelength coverage in particular makes it an ideal instrument for studying radial velocity variations in white dwarf + M-dwarf binaries, because the two stars dominate the flux in different parts of the spectrum (Copperwheat et al., 2012; Parsons et al., 2012a,b).

X-Shooter data reduction with ESO Reflex

To reduce X-Shooter data I use the X-Shooter pipeline in the ESO Reflex workflow management tool[2]. The reduction includes several steps. In the first step the master calibration files are created, which includes the master bias, the master dark frame and the master flatfield, from individual bias, dark and flatfield frames. Note that in the standard reduction the UVB and VIS arm data are debiased using the overscan regions, rather than the master bias frame, although the user can specify this according to his/her preferences. In the second step an initial guess is made at the wavelength calibration and the position of the echelle orders on the CCD. This is done by using a physical model of the instrument combined with information on the atmospheric pressure and temperature, and the corresponding instrument settings as saved in a data fits file of a calibration arc frame. Then a flat field frame is used to determine the central positions of the individual orders. During the third step a detailed wavelength calibration is performed and spatial distortions are determined to update the rough model made in the previous step. If standard star observations have been taken within $\pm$ 3 days of the science observations, the instrument response curve will be determined in a fourth step. This curve will later be used to flux-calibrate

---

[2]See *ftp://ftp.eso.org/pub/dfs/pipelines/xshooter/xsh-reflex-tutorial-2.2.pdf* for more information.

the science data. In the last step the science data are extracted, the orders are connected and the sky level is subtracted, after which one has obtained the 1D science spectra.

2.4.2   STIS on the Hubble Space Telescope

The Space Telescope Imaging Spectrograph (STIS; Woodgate et al., 1998) is a 2nd generation instrument and a general purpose spectrograph aboard the Hubble Space Telescope (HST) since February 1997. It has an imaging and a spectroscopic mode, both with several options to set the resolution and wavelength range. The total wavelength range covers four bands in the far-ultraviolet (FUV), the near-ultraviolet (NUV), the visible and near-infrared and ranges from 1150 Å to 10000 Å.

The visible / near-infrared detector is a conventional CCD, cooled to 190 K, while the FUV and NUV detectors are multi-anode multichannel array (MAMA) detectors. These are photon-counting photocathodes, which can operate uncooled and reject visible photons to avoid contamination from this regime where sources are often brighter than in the ultraviolet. The MAMAs were preferred over CCDs because the latter's quantum efficiency tends to degrade quickly at ultraviolet wavelengths and because even before degradation the combined quantum efficiency of a CCD and the throughput of available filters[3] is lower than that of the MAMA.

All STIS data are automatically reduced by a pipeline at the Space Telescope Science Institute (STScI) where the HST headquarters are located.

2.4.3   COS on the Hubble Space Telescope

The Cosmic Origins Spectrograph (COS; Green et al., 2012) is a 4th generation instrument that has been on board the HST since May 2009. The instrument was developed to complement STIS and to operate simultaneously with STIS, thereby increasing the wavelength range of observations. COS has a far-ultraviolet (1150 – 2000 Å) and near-ultraviolet (1700 – 3200 Å) optical channel, with a microchannel plate detector in the FUV arm to maximise quantum efficiency (see Vallerga et al., 2001, for details), and a redundant STIS MAMA detector in the NUV arm. Both arms have a minimum of optical elements to decrease losses through inefficient reflectivity, which can be significant at ultraviolet wavelengths. Various gratings with different spectral resolution and central wavelengths can be chosen, to optimise the observation according to the science goal. The instrument also has an imaging mode, which is primarily used for target acquisition.

COS was originally designed to operate for 3 years, but it has spectacularly outperformed these expectations. However, the FUV detector sensitivity has been degrading since the start, and has become significant in the last few years. This complicates the relative flux- and wavelength-calibrations of the detector (private communication J. Debes). This is a general problem of UV-astronomy, and from cycle 21 in 2014 onwards this prompted an HST UV-initiative in which proposals relying on UV observations were favoured in order to make full use of HST's UV capabilities before the relevant instruments become unusable.

---

[3]See *http://www.stsci.edu/hst/stis/design/filters/*.

All COS data are reduced by the automatic pipeline at the STScI.

2.5   Statistical techniques

This section describes some important aspects of two statistical approaches used throughout this thesis. This includes the Monte Carlo method and the numerical Markov chain Monte Carlo method. Both are very powerful in estimating the statistical significance of model fits to data, as well as determining the values and statistical uncertainties of model parameters. Depending on the data and model one wants to fit to the data, as well as on their complexity, one can choose which method provides the best approach to the problem.

2.5.1   Monte Carlo method

The Monte Carlo method is a relatively simple approach useful for evaluating the expectation value of a function or model parameter, by randomly drawing many samples from a distribution that can be used to approximate the expectation value. For example, with this approach it is possible to estimate statistical uncertainties of model parameters by repeatedly fitting the model to the data while slightly perturbing that data based on the uncertainties of the individual data points. Therefore, Monte Carlo analysis is based on repetition in order to explore a certain distribution. Note also that during Monte Carlo analysis, the original data may be altered in order to arrive at useful results for the model.

For purposes of illustration, consider the ingress and egress features of white dwarf eclipses in light curves of cataclysmic variables. In Chapters 5 and 6 a Monte Carlo approach is used to determine the statistical uncertainties of the parameters in a simple model used to fit these features. The best fit of the model to the data can simply be found by χ^2 minimisation. Determining uncertainties on the model parameters can be done by repeating this fit numerous times, say 1000 times. In every fit each individual data point is perturbed by a normal distribution with a mean and standard deviation equal to the value and uncertainty of the data point itself. In addition, another 1000 fits are performed in which the start and end points of the data included in the fit are varied by a few. The resulting (generally Gaussian) distributions for each model parameter not only describe the value of the parameters more accurately then a straight fit to the data, they also describe the uncertainties in these parameters better. This is a particularly good approach for fitting white dwarf eclipses of cataclysmic variables because the inherent flickering present in these systems shows itself as random jitter in the data points.

2.5.2   Markov chain Monte Carlo simulation

The Markov chain Monte Carlo method (MCMC; see for example Gilks et al., 1996; Mackay, 2003; Gelman et al., 2014) is a numerical method that often relies on Bayesian inference. One uses information known to be true and derives logical conclusions from them using Bayes' theorem. The known information D generally consists of observed data, while the information being sought M generally includes a number of model parameters, or some

missing data. Bayes' theorem describes the probability distribution of M given that D is true, denoted as $P(M|D)$, as follows:

$$P(M|D) = \frac{P(D|M)P(M)}{P(D)}. \tag{2.1}$$

Here $P(M|D)$ is the posterior distribution of the model M assuming that the data D is true, $P(M)$ and $P(D)$ are the a priori distributions of the model and data, and $P(D|M)$ is the probability of observing the data given that the model is true. Determining these probability distributions analytically quickly becomes difficult, especially in high dimensions. In such cases, a robust alternative approach is the numerical method MCMC.

The Monte Carlo and Markov chain Monte Carlo techniques share (parts of) their name because both are based on drawing many samples from certain parameter distributions. This is done to evaluate, for example, a statistical distribution or a target distribution such as the posterior probability of a model's parameters given some data (maximising $P(M|D)$ is approximately equivalent to minimising χ^2). A significant difference between the two approaches is that during MCMC the data itself is never altered, while this may be a justified approach in the Monte Carlo method. MCMC is especially useful for problems with many dimensions, even thousands or more, where the random exploration of Monte Carlo techniques could take longer than the age of the Universe.

In contrast to the Monte Carlo approach described before, in MCMC simulations the samples are not drawn randomly, but through the use of a Markov chain. In such chains, each next sample x_{i+1} is drawn based only on the current sample x_i and a proposal density distribution at this position for all parameters. One has to choose an initial sample to start the chain from, but after a warm-up phase, also called the burn-in phase, the new samples do not depend on the original starting position. This is illustrated in Fig. 2.9, which shows the value of three parameters throughout a chain. After the warm-up phase, the chain has converged to a stationary distribution in all dimensions, which is also called the target or posterior distribution. These posterior distributions can be used to estimate means, variances, expectation values, correlation between parameters, etcetera for the relevant individual parameters that were used in the model. Besides removing the warm-up phase, one can choose to discard all but every nth draw, thereby reducing correlations between subsequent samples in the chain and possible effects this may have on the final distributions.

The Markov chain itself can be constructed by the general Metropolis-Hastings algorithm or by a specialised version thereof. In this class of algorithms each proposed step, from draw x_i to draw x_{i+1}, is accepted with a certain probability. If the step is accepted, the newest addition to the chain is x_{i+1}. If the step is not accepted, x_i is added to the chain again. Next a new draw x_{i+2} is made and evaluated for acceptance, and so on.

Where used in this thesis, MCMC has been implemented using the python package `emcee` (Foreman-Mackey et al., 2013), which is based on ensemble Markov chains (Goodman & Weare, 2010). In this case, there is not one sample x that is evolved throughout the chain, but an ensemble of samples, or so-called 'walkers', each starting at a slightly
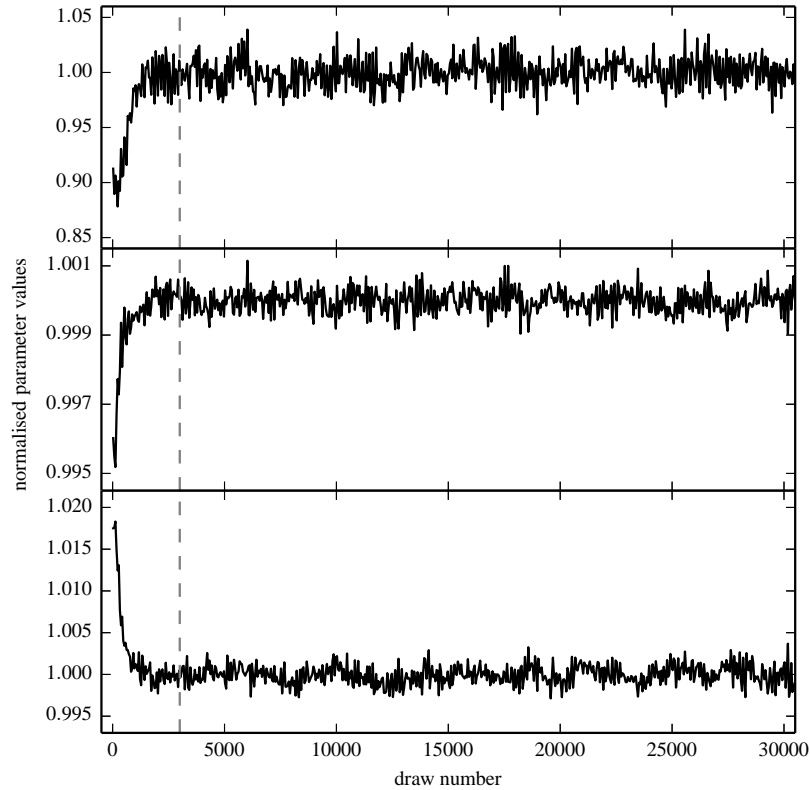
Figure 2.9: Normalised parameter values as a function of the number of draws in a Markov chain Monte Carlo simulation to illustrate convergence of the chain and the warm-up phase (to the left of the vertical dashed line).

different position. The number of walkers in the ensemble should always be at least twice the number of free parameters in the model used to fit the data. Generally, a Markov chain explores the parameter space more effectively with 100 – 200 walkers. One cycle of draws through all walkers constitutes one step for the ensemble and one step in the Markov chain. In the implementation used throughout this thesis, the proposed draw for a given walker is determined by stretching or compressing along the straight line between the walker and the position of a random other walker in the set. The so-called stretch factor is now an additional parameter that has to be set. It should always be larger than unity, to ensure that the walkers move around and fully explore the parameter space, with my default value equal to 2. The acceptance probability for the individual walkers is still determined by the Metropolis-Hastings algorithm. The ensemble of walkers as a whole contains information about the multi-dimensional target distribution, and is especially useful when exploring highly-skewed parameter distributions.

When fitting a model to a set of data using an MCMC approach, it may be the case that the data do not constrain all model parameters equally well. In this case one can choose to constrain a given parameter by adding a prior to the evaluation criteria used to determine whether a step is accepted or not. This prior can be Gaussian, flat, with or without a hard cutoff, etcetera, where the choice is motivated by additional information that is available about this particular parameter. For example, if one is fitting a model

that includes a temperature as a free parameter, one can safely constrain this temperature to be always positive on a Kelvin scale.

One important issue that comes up when using MCMC methods is the so-called acceptance fraction, which is the number of accepted steps divided by the total number of steps in the chain. Remember that if a certain draw is not accepted, the previous draw is repeated in the chain before a new draw is attempted. If the acceptance fraction of a chain is too low, the chain has not been able to explore the full parameter space effectively, as it moved around slowly and may even have been stuck for a long time in a certain place. On the other hand, if the acceptance fraction is too high, practically every proposed step has been accepted and the chain cannot converge to the posterior distribution. Typically, in MCMC simulations that explore five or more dimensions the acceptance fraction should be ~ 0.25 (Gelman et al., 2014). In ensemble MCMC, one can manipulate the acceptance fraction of a chain by varying the stretch factor.

Another essential aspect of running an MCMC simulation lies in deciding when a chain has fully converged and represents the posterior distribution correctly. The choice is somewhat subjective, and may be limited by the available time and computational power. However, there are several ways to check convergence. One can run multiple chains, each with a different initial starting point. After the respective warm-up phases, the chains should all converge on the same distribution. One extremely long chain will also be able to fully explore the available parameter space and converge on the target distribution, but this approach may not be feasible for practical reasons such as those mentioned.

2.6 Conclusions

I have discussed the various techniques used throughout this thesis to obtain, reduce and analyse data. This covered the current-day standard of CCDs as the basis of most astronomical instrumentation, and somewhat more technical details of a number of instruments that were used to obtain photometric or spectroscopic observations presented in this thesis. In later chapters, some data may be used that was obtained with instruments not discussed in this chapter, and, if necessary, these will be briefly discussed in place, accompanied by appropriate references. In this chapter I have also introduced two statistical techniques that are useful in performing fits of models to data sets, as will become clear in the following chapters.

$\star\;\star\;\star$

Chapter 3

CSS 41177: an eclipsing double white dwarf binary

3.1 Introduction

Despite the abundance and importance of white dwarfs, it has proved difficult to measure fundamental parameters such as mass and radius directly, without the use of theoretical mass – radius relations, as we saw in Chapter 1. For single white dwarfs, spectral fitting can be used to obtain the temperature and surface gravity, after which both mass and radius can be inferred, but only when combined with a mass – radius relation (see for example Provencal et al., 2002). White dwarfs in visual binaries, common proper motion pairs, or in open clusters allow one to determine parameters without the use of this relation, therefore providing a direct test of it. These methods rely on accurate parallax measurements, spectral fitting and/or radial velocity measurements (Holberg et al., 2012; Provencal et al., 2002; Casewell et al., 2009). The number of stars to which these methods can be applied is limited, and with the exception of Sirius B (Barstow et al., 2005), they cluster around a mass of $M_{WD} \sim 0.6$ $M_{\odot}$, making it difficult to test the full range of the mass – radius relation.

Observing white dwarfs in eclipsing binaries enables high precision in determining masses and radii and these types of binaries also include white dwarfs across a wide range of masses (Pyrzas et al., 2012; O'Brien et al., 2001; Parsons et al., 2012c; Bours et al., 2014a). For these systems, masses can be determined from orbital velocities and radii from light curve analysis (Parsons et al., 2012b,a). Eclipsing double white dwarf binaries are especially ideal for this kind of analysis, as they allow for precise and independent mass and radius measurements for two white dwarfs through one analysis. Currently, there are five known eclipsing double white dwarf binaries: NLTT 11748 (Steinfadt et al., 2010), CSS 41177 (Parsons et al., 2011a; Bours et al., 2014a, 2015a), GALEX J171708.5+675712 (Vennes et al., 2011), SDSS J065133.33+284423.37 (Brown et al., 2011) and SDSS J075141.18-014120.9 (Kilic et al., 2014b). The double white dwarf binary that is the subject of this chapter, CSS 41177 (SDSS J100559.10+224932.2), is the only one of the five that is also a double-lined spectroscopic binary, allowing direct measurement of the stars' orbital velocities and therefore their masses (Parsons et al., 2011a).

CSS 41177 was initially discovered to be an eclipsing binary by Drake et al. (2010), who constrained it to be a white dwarf with a small M-dwarf companion, although they noted

Table 3.1: Log of the X-shooter observations. On all three nights the conditions were clear, with the seeing between $0.5''$ and $1.0''$.

Date	UT		No. of exposures		
	start	end	UVB	VIS	NIR
25 March 2012	00:13	04:31	44	40	48
26 March 2012	00:09	04:10	39	35	42
27 March 2012	23:51	04:36	46	42	50

that a small faint object could produce a signal similar to what they observed. Parsons et al. (2011a) obtained LT + RISE fast photometry and Gemini + GMOS (Gemini Multi-Object Spectrograph) spectroscopy, which allowed them to determine that there were in fact two white dwarfs and to carry out an initial parameter study. In this chapter I present higher signal-to-noise data in order to determine the system parameters more precisely as well as recently obtained HST spectroscopy to measure accurate temperatures and surface gravities.

3.2   Spectroscopic data

3.2.1   Very Large Telescope + X-shooter

Spectra were acquired with the X-shooter spectrograph on the VLT Unit Telescope 2 (*Kueyen*) on the nights of the 25$^{\text{th}}$, 26$^{\text{th}}$ and 27$^{\text{th}}$ of March 2012, obtaining a total of 117 spectra across 1.5, 1.4 and 1.7 orbital cycles in the three nights. A log of the observations is given in Table 3.1.

The X-shooter spectrograph consists of three independent arms (UVB, VIS and NIR), giving a simultaneous wavelength coverage from 3000 – 25000 Å. A series of spectra 310, 334 and 300 seconds in length were obtained for the UVB, VIS and NIR arms respectively. Spectra were obtained consecutively with occasional short breaks of a few minutes in order to check the position of the target on the slit. The data were binned by a factor of two both spatially and in the dispersion direction for the UVB and VIS arms, and obtained using slit widths of $0.8''$, $0.9''$ and $0.9''$ for the UVB, VIS and NIR arms respectively. The NIR arm slit includes a K-band blocking filter which reduces the thermal background in the J- and H-bands.

The data were reduced using version 1.5.0 of the X-shooter pipeline and the Reflex workflow management tool. The standard recipes were used to optimally extract and wavelength calibrate each spectrum. To remove the instrumental response observations of the spectrophotometric standard star LTT4364 (GJ-440) were used. All data were obtained and reduced in 'stare' mode. For optimum sky subtraction in the infrared arm, 'nod' mode would be preferable, but the priority was to maximise the temporal resolution for the spectral features of interest in the other two arms.
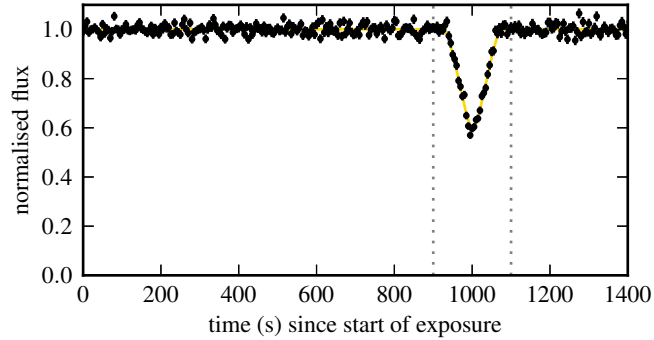
Figure 3.1: HST+COS light curve of CSS 41177, displayed in 5 second bins, showing the eclipse of the hotter white dwarf (primary eclipse) and the model used to determine the mid-eclipse time (see Section 3.2.2). The data between the dotted lines was excluded from the spectroscopic fits described later in this chapter.

3.2.2 Hubble Space Telescope + Cosmic Origins Spectrograph

Far-UV HST+COS (Green et al., 2012) data of CSS 41177 were obtained as part of Cycle 21, program ID 13421. CSS 41177 was observed during two consecutive HST orbits on the 28th of May, 2014. Each orbit was split in two exposures to retain a good signal-to-noise ratio while minimising the effects of fixed pattern noise using all four FP+POS settings. The exposures obtained were 19, 20 and 2x24 minutes long and each used the G140L grating at a central wavelength of 1105 Å. During the third exposure a primary eclipse occurred (cycle 7491, using the ephemeris from Bours et al. 2014a), with a mid-eclipse time $t_{\mathrm{MJD(UTC)}} = 56805.41665(34)$, equivalent to the barycentrically-corrected time $t_{\mathrm{BMJD(TDB)}} = 56805.41628(34)$, see Fig. 3.1.

The part of the exposure in which the eclipse occurred was removed for the following analysis using `calcos` to filter out the data at $900 - 1100$ s. I also removed the geocoronal Lyman-α and O I (1304 Å) emission from the spectra, as well as interstellar absorption lines (see Section 3.5.3). The lower limit for the data is set at 1150 Å, to exclude artificial features near the edge of the observable wavelength range. The upper limit is fixed at 1700 Å, motivated by the decreasing sensitivity of COS and the therefore increasing difficulty of relative flux calibration at longer wavelengths (J. Debes, private communication).

3.3 Photometric data

3.3.1 ULTRACAM

Most of the photometric data on CSS 41177 were taken with ULTRACAM (Dhillon et al., 2007), mounted on the 4.2 m William Herschel Telescope (WHT) on the island of La Palma, Spain and on the 3.5 m New Technology Telescope (NTT) at the La Silla Observatory, Chile. The u′, g′ and r′ filters were used and the CCDs were windowed to allow exposure times as short as 1.5 seconds. Eleven primary eclipses of CSS 41177 and nine secondary

eclipses were observed in January 2012, including one observation spanning a complete orbit (1.1 cycles). In addition, there is one observed primary eclipse from May 2011.

The ULTRACAM pipeline was used to debias and flatfield the data, as described in Section 2.3.5. The source flux was determined with relative aperture photometry, using a nearby star as a comparison. I used a variable aperture, where the radius of the aperture was scaled according to the full width at half maximum of the stellar profile, which was fit with a Moffat distribution (Moffat, 1969).

The ULTRACAM data has absolute timestamps better than 0.001 seconds. All times were converted onto a TDB time scale, and corrected to the Solar System barycentre to obtain times in the BMJD(TDB) frame. A code based on SLALIB was used for these corrections, which has been found to be accurate at a level of 50 microseconds compared to TEMPO2 (a pulsar timing package, see Hobbs et al., 2006). Compared to the statistical uncertainties of the observations, this is insignificant.

3.3.2   Liverpool Telescope + RISE

In order to monitor any long-term orbital period variations, primary eclipses of CSS 41177 have also been regularly observed with the fully-robotic 2.0 m Liverpool Telescope (LT; Steele et al., 2004) and RISE camera. A total of 9 primary eclipses were obtained between February 2011 and December 2014.

The data were flatfielded and debiased in the automatic pipeline, in which a scaled dark-frame is removed as well. The data were analysed using the ULTRACAM pipeline in the same manner as outlined above. Again, the resulting mid-eclipse times were converted to the TDB timescale. LT+RISE has absolute timestamps better than 0.1 second (D. Pollacco, private communication). Although significantly larger than the accuracy reached with ULTRACAM, the observing schedule of LT+RISE is much more flexible and allows observations of the double white dwarf regularly throughout the year.

3.3.3   ULTRASPEC

Since ULTRASPEC became available for science observations after its commissioning in November 2013, I have also regularly observed CSS 41177 with this instrument in order to monitor the eclipse times. In particular, I observed a total of 10 primary eclipses of the double white dwarf during observing runs from November 2013 to February 2015, using either the g′ or Schott KG5 filter. The data were reduced using the ULTRACAM pipeline, as described before.
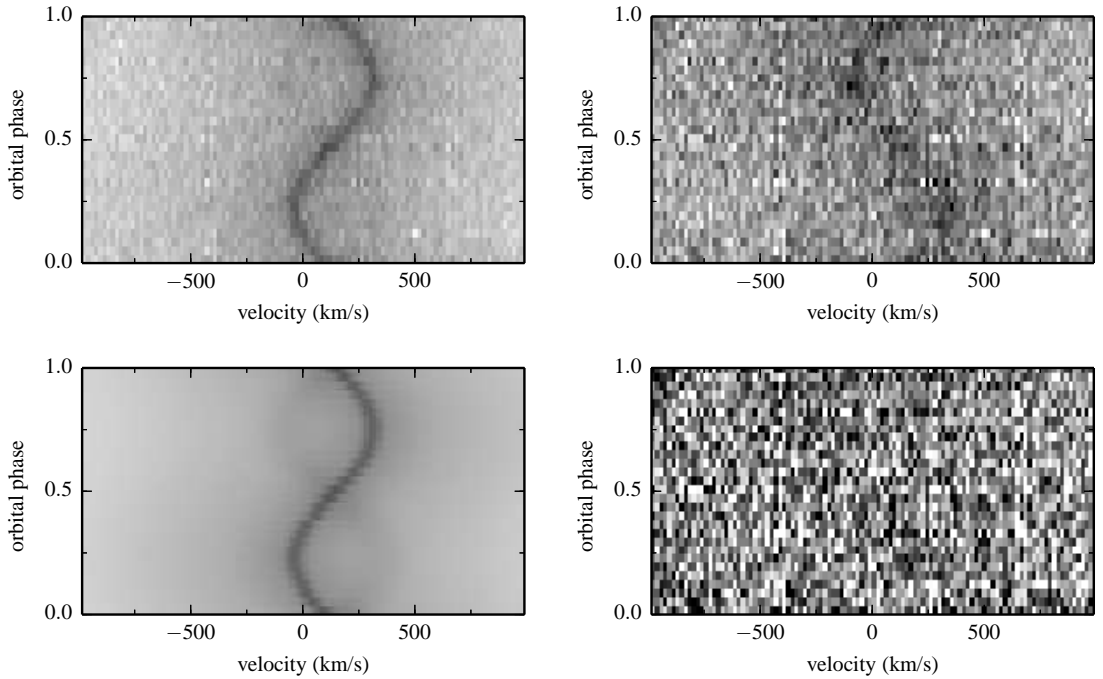
Figure 3.2: X-shooter spectroscopy of CSS 41177. *Top left:* spectra of the Hα absorption line at 6562.76 Å, folded with the orbital period. The scale is such that black equals 20% of the continuum and white 100%. *Top right:* phase-folded spectra after removal of the primary white dwarf's Hα absorption line, showing the contribution of the secondary white dwarf, which is offset from the primary white dwarf by half an orbital phase. Here black equals 80% of the continuum and white 100%. *Bottom left:* model trail of the Hα absorption line. *Bottom right:* residuals after subtracting the model from the data, where black equals 99% of the continuum and white 100%.

3.4 Data analysis & results

3.4.1 Radial velocity amplitudes

I analysed the reduced X-shooter data using the MOLLY software[1], and used observations of the standard star to normalise the continuum and reduce telluric absorption features present in the CSS 41177 science spectra as far as possible.

To measure the radial velocity amplitudes K_1 and K_2 I folded all spectra on the orbital period as calculated from the photometric mid-eclipse times. The phase-folded trail of the Hα absorption line is shown in the top left panel of Fig. 3.2. I then proceeded to fit the Hα line with multiple Gaussian profiles combined with a straight line fit to the local continuum using Marquardt's method of minimisation. The radial velocity v_r for each star was calculated using

$$v_r = \gamma + K_{1,2}\sin(2\pi\phi), \tag{3.1}$$

where γ accounts for a systemic radial velocity, K_1 and K_2 are the radial velocity amplitudes of the two white dwarfs and ϕ is the orbital phase. My best fit gave $K_1 = -176.1 \pm 1.1$

---

[1]MOLLY was written by T. R. Marsh and is available from http://www.warwick.ac.uk/go/trmarsh/software.

km s^{-1} and $K_2 = 210.4 \pm 6.1$ km s^{-1} for the primary and secondary white dwarfs, and $\gamma = 130.5 \pm 0.7$ km s^{-1} for the offset. From this best model I set the Gaussian profiles corresponding to the secondary star's line to zero, leaving a model of only the primary star's line. I then subtracted this model from the original spectra to bring out the secondary's contribution, shown in the top right panel of Fig. 3.2. The systemic radial velocity is clearly visible in both of these figures as the offset from zero. The bottom two panels show the model of both the primary and secondary absorption line on the left, and the residuals after subtraction of the model from the data on the right.

Both radial velocity amplitudes are in agreement with the measurements in Parsons et al. (2011a), but have uncertainties reduced by a factor of 3 and 2 respectively.

3.4.2   Light curve analysis with ULTRACAM and X-shooter data

I initially modelled both white dwarfs using regular grids covering their surfaces. While computing the models I found them to be sensitive to the density of the chosen grid. To avoid the resulting 'edge effects' I had to significantly increase the number of grid points, which became computationally very expensive. Therefore I developed a different model which also allowed incorporation of several important physical processes. In this model, the visible face of each white dwarf is represented as a circle, subdivided into 200 limb-darkened concentric annuli. After obtaining an initial model that represents the shape of the eclipses, I determined the mid-eclipse times for all primary eclipses by varying only the mid-eclipse time t, the temperature of the eclipsing white dwarf T_2 and an overall scaling factor to minimise χ^2. Because the depth of the eclipse is strongly dependent on the white dwarf temperatures, which are strongly correlated in the model, only t and T_2 are needed to accurately model the shape of the light curve and eclipse, and to determine the mid-eclipse times, once the radii are relatively well known. All the primary mid-eclipse times are listed in Table 3.2.

To obtain the binary and white dwarf parameters I then proceeded to fit all light curves simultaneously. Each annulus on the face of the white dwarf contributes an amount to the total stellar flux which depends upon the limb darkening. More details on how limb darkening was included are given below. Doppler beaming from the white dwarfs was accounted for by following Bloemen et al. (2011), and modifying the flux by a factor

$$1 - B\,\frac{v_r}{c}\,, \qquad\qquad (3.2)$$

with B the spectrum-dependent beaming factor and v_r the radial velocity of the star, and with v_r positive when the star is moving away from the observer. To calculate the beaming factors, I used white dwarf model spectra with $\log(g) = 7.25$ for both white dwarfs, and T = 24000K and T = 12000K for the primary and secondary respectively. With these models, and following Bloemen et al. (2011), the bandpass-integrated beaming factors for the (u$'$, g$'$, r$'$) filters are (1.9, 2.2, 1.3) for the primary white dwarf and (3.4, 3.5, 1.8) for the secondary white dwarf. Gravitational lensing is not included in the models. Due to the similarity of the white dwarfs' masses and radii, and their relatively small separation, the

Table 3.2: Mid-eclipse times for the primary eclipses of CSS 41177. All ULTRACAM times shown are the weighted averages of the u′, g′ and r′ mid-eclipse times.

cycle number	mid-eclipse time BMJD(TDB)	t_{exp} (seconds)	telescope+instrument	observing conditions (cloud coverage, seeing)
-2907	55599.087790(13)	13	LT+RISE	clear, seeing 1.8″
-2736	55618.926465(15)	12	LT+RISE	clear, seeing 2.5″
-2434	55653.963110(18)	12	LT+RISE	clear, seeing 3″
-2020	55701.9935029(77)	2 - 8.2	NTT+ULTRACAM	thin clouds, seeing 1 - 2″
-199	55913.257605(22)	10	LT+RISE	clear, seeing 1.5″
66	55944.0016959(49)	3 - 6	WHT+ULTRACAM	thin clouds, seeing 1 - 3″
67	55944.1177028(65)	3 - 6	WHT+ULTRACAM	thin clouds, seeing 1.5 - 3.5″
68	55944.233727(10)	3 - 6	WHT+ULTRACAM	clouds, seeing 3 - 10″
76	55945.1618417(55)	1.5 - 3	WHT+ULTRACAM	clear, seeing 2″
77	55945.2778585(53)	1.5 - 3	WHT+ULTRACAM	some small clouds, seeing 2 - 7″
94	55947.2501251(62)	1.5 - 3	WHT+ULTRACAM	thin clouds, seeing 2 - 4″
102	55948.1782455(38)	2 - 4	WHT+ULTRACAM	clear, seeing 1 - 2″
103	55948.2942481(58)	2 - 4	WHT+ULTRACAM	cloud during egress, seeing 1-5″
109	55948.9903480(47)	2 - 4	WHT+ULTRACAM	clear, seeing 1.2″
110	55949.1063669(37)	2 - 4	WHT+ULTRACAM	clear, seeing 1″
111	55949.2223834(39)	2 - 4	WHT+ULTRACAM	clear, seeing 1″
3187	56306.085857(15)	10	LT+RISE	clear, seeing 2″
3369	56327.200698(16)	10	LT+RISE	clear, seeing 2″
3678	56363.049447(13)	10	LT+RISE	thin clouds, seeing 2″
5737	56601.9252468(69)	5	TNT+ULTRASPEC	clear, seeing 1.5″
6434	56682.7879973(62)	5	TNT+ULTRASPEC	clear, seeing 2″
6452	56684.8762755(54)	3	TNT+ULTRASPEC	clear, seeing 1.5″
6485	56688.7047726(69)	3	TNT+ULTRASPEC	thin haze, seeing 2″
6488	56689.052833(12)	10	LT+RISE	thin haze, seeing 2″
9072	56988.8367219(72)	4	TNT+ULTRASPEC	clear, seeing 1 - 2″
9238	57008.095265(23)	10	LT+RISE	thin clouds, seeing 3″

Table 3.3: Coordinates and magnitudes CSS 41177, taken from SDSS III DR9. The magnitudes are the photometric PSF magnitudes, with the corresponding uncertainties in the parentheses.

R.A.	Dec	m_u	m_g	m_r	m_i	m_z
10:05:59.1	+22:49:32.26	17.32(2)	17.29(2)	17.62(2)	17.89(1)	18.15(3)

lensing amplification factor near both primary and secondary eclipses is ~ 1.00003, making this effect negligible (for the relevant equations, see Marsh, 2001).

I normalised each observed light curve individually to reduce any night-to-night variations and used the SDSS magnitudes for CSS 41177 (see Table 3.3) to determine the binary's overall out-of-eclipse flux level, allowing for a spread due to the uncertainties in the magnitudes. I allowed for an additional shift δ, of the secondary eclipse, on top of the 0.5 phase difference with respect to the primary eclipse, by adjusting the phase ϕ according to

$$\phi' = \phi + \frac{\delta}{2P}\left(\cos(2\pi\phi) - 1\right), \tag{3.3}$$

where P is the orbital period. This shift near the secondary eclipse allows for possible

Rømer delays[2] (Kaplan, 2010) and/or a small eccentricity of the orbit.

The program uses a Markov chain Monte Carlo (MCMC) method to explore the ten-dimensional parameter space, favouring regions with small χ^2 values of the model with respect to the data. The free parameters in the model were the two radii scaled by the binary separation, R_1/a and R_2/a, the white dwarf temperatures, T_1 and T_2, the radial velocity amplitudes, K_1 and K_2, the inclination of the binary i, the time delay δ, the orbital period P and the zero point of the ephemeris, T_0, which was chosen to minimise the correlation between the zero point and the orbital period.

Because I have accurate measurements for the radial velocity amplitudes from the analysis of the X-shooter data I used a Gaussian prior to constrain them while modelling the ULTRACAM data. Given the ten free parameters and combining them with

$$K_1 + K_2 = \frac{2\pi a}{P}\sin(i)\,, \tag{3.4}$$

and Kepler's equation given by

$$\frac{G(M_1 + M_2)}{a^3} = \frac{4\pi^2}{P^2}\,, \tag{3.5}$$

the binary's orbital separation a and the white dwarf masses M_1 and M_2 could also be calculated. Note that $q = K_1/K_2 = M_2/M_1$ and that the surface gravities follow from $g_{1,2} = GM_{1,2}/R_{1,2}^2$.

The best model, using the ULTRACAM light curve data and the priors on the radial velocities from the X-shooter spectra, has a reduced chi-squared of $\chi_\nu^2 = 1.03$ (43351 data points, 10 fit parameters, 43341 degrees of freedom). The MCMC parameters are summarised in Table 3.4 (columns 2 and 3), which lists both the mean and root mean square for each parameter.

With this approach I effectively measured the white dwarf temperatures from the depths of the eclipses in the different bands and the temperature-dependent specific intensities from Gianninas et al. (2013). The temperatures determined are independent of both the SDSS spectrum and model spectra, which formed the basis of the temperatures derived by Parsons et al. (2011a). In contrast to their results, I obtain somewhat higher values for both white dwarf temperatures. This is, at least in part, due to the fact that they did not include the effects of reddening. To assess how this influences the values for the masses and radii I ran an additional MCMC analysis in which the temperature of the hotter white dwarf was fixed to $T_1 = 21100$ K, the value found in Parsons et al. (2011a). The results are shown in the last column of Table 3.4. As expected, the temperature of the cooler white dwarf is also reduced, but the effect on other parameters is well within the uncertainties.

---

[2]Named after the Danish astronomer O. Rømer, who was the first to realise that the speed of light is finite by observing deviations from strict periodicity for eclipses of Io, a satellite of Jupiter (Sterken, 2005).

Table 3.4: Parameters of the binary and both white dwarfs, from MCMC analyses of the ULTRA-CAM light curves with additional constraints from the X-shooter data. Numbers in parentheses indicate the uncertainty in the last digit(s). The second and third column list the results from the analysis of the spectroscopic and photometric data. The last two columns shows the results from two more MCMC analyses, where the limb darkening coefficients (ldc) have been multiplied by 1.05 (fourth column) and where T_1 has been fixed (fifth column).

parameter	spectroscopy	MCMC analysis	MCMC with ldc*1.05	MCMC with fixed T_1
T_0 (BMJD(TDB))	-	55936.3446719(6)	55936.3446719(6)	55936.3446720(6)
P_{orb} (days)	-	0.1160154352(15)	0.1160154352(15)	0.1160154351(15)
a ($R_\odot$)	-	0.886(14)	0.886(14)	0.888(14)
i (deg)	-	88.97(2)	88.96(2)	88.95(2)
δ (seconds)	-	-0.79(24)	-0.80(25)	-0.78(25)
M_1 ($M_\odot$)	-	0.378(23)	0.378(23)	0.381(23)
M_2 ($M_\odot$)	-	0.316(11)	0.316(11)	0.317(11)
R_1 ($R_\odot$)	-	0.02224(41)	0.02227(41)	0.02220(41)
R_2 ($R_\odot$)	-	0.02066(42)	0.02066(42)	0.02087(42)
T_1 (K)	-	24407(654)	24362(652)	21100
T_2 (K)	-	11678(313)	11664(311)	10436(21)
$\log g_1$	-	7.321(15)	7.319(15)	7.325(15)
$\log g_2$	-	7.307(11)	7.307(11)	7.300(11)
K_1 (km s^{-1})	-176.1(1.1)	-	-	-
K_2 (km s^{-1})	210.4(6.1)	-	-	-
γ (km s^{-1})	130.5(0.7)	-	-	-
minimum χ^2	-	44457	44457	44482

Limb darkening

To account for limb darkening of the white dwarfs I used the limb darkening law as first described by Claret (2000), in which the specific intensity across the stellar disc can be calculated using

$$\frac{I(\mu)}{I(1)} = 1 - c_1(1 - \mu^{1/2}) - c_2(1 - \mu) - c_3(1 - \mu^{3/2}) - c_4(1 - \mu^2), \qquad (3.6)$$

where $c_1 - c_4$ are the limb darkening coefficients, and μ is the cosine of the angle between the line of sight and the surface normal of the white dwarf, so that $I(1)$ is the specific intensity at the centre of the white dwarf's disc.

White dwarf limb darkening coefficients were calculated by Gianninas et al. (2013) for a wide range of white dwarf temperatures and surface gravities, for both the Johnson-Kron-Cousins *UBVRI* system and the *ugrizy* filters to be used by the LSST. The filter profiles of the ULTRACAM u′, g′ and r′ filters are similar to those of the LSST and therefore I used the coefficients calculated for these LSST filters. I also obtained the central specific intensities for these three filters (A. Gianninas, private communication).

For a given temperature and surface gravity I used a bilinear interpolation between the closest values to calculate all four coefficients and the central specific intensity. These then allowed determination of the total specific intensity of the white dwarfs, depending on where they are in their orbit and on the fraction of each annulus is visible. The total

specific intensity[3] is related to the binary's flux[4] by a constant, α, which I calculated during the MCMC by minimising the difference between the flux defined by the SDSS magnitudes for CSS 41177 and the product of the total specific intensity with α. The constant is related to the solid angle the binary subtends in the sky as

$$\alpha = a^2/d^2 \, , \tag{3.7}$$

where a is the binary's orbital separation and d is the distance to the binary, allowing me to effectively measure the distance from the light curves. For the three filters the resulting distances are $d_u = 481 \pm 37$ pc, $d_g = 473 \pm 35$ pc, and $d_r = 464 \pm 34$ pc, giving a weighted average value of $d = 472 \pm 35$ pc. These values are significantly higher than the distance quoted in Parsons et al. (2011a), a natural result due to the fact that I also obtained higher temperatures for both white dwarfs.

The calculations for the limb darkening coefficients in Gianninas et al. (2013) are based on 1D white dwarf models. Tremblay et al. (2013a) have shown that the standard 1D mixing-length theory overpredicts surface gravities and, to a lesser extent, temperatures, especially near the values I found for the cooler white dwarf. To assess the effect of using 1D models a comparison was made between a 1D and an averaged 3D intensity profile, using a temperature and surface gravity representative of the cooler white dwarf. Full 3D and averaged 3D spectral synthesis produce very similar results at all wavelengths (Tremblay et al., 2011b), and so the averaged 3D approximation, where the average is performed over constant Rosseland optical depth, is likely to be appropriate for the present study. The difference between the two profiles was found to be a factor of 1.05 in the limb darkening coefficients. Running a separate MCMC analysis in which I multiplied each limb darkening coefficient by 1.05, showed that the effect on the values for the parameters is much less than the statistical uncertainty in the parameters (Table 3.4, column 4).

3.4.3   Addition of HST+COS data to the light curve analysis

One of the largest uncertainties remaining after the analysis described above is the temperature of the primary, hot white dwarf in CSS 41177 (and through their correlation also the temperature of the secondary, cooler white dwarf). The HST+COS spectra taken in May 2014 go a long way to resolve this uncertainty, because they precisely measure the flux at far-ultraviolet wavelengths. At these wavelengths, the primary white dwarf dominates the flux, with the secondary only contributing a small amount.

To determine the white dwarf temperatures, I fit the HST+COS data with model spectra (Koester, 2010), which employ a mixing length of ML2/α = 0.8. However, simply fitting the HST+COS data with a single white dwarf model spectrum over predicts the flux from the hot white dwarf at optical wavelengths. Because the secondary white dwarf starts contributing to the total flux at $\lambda > 1400$ Å, the slope of the HST+COS spectrum is shallower than would be the case if only the primary white dwarf is visible in this regime.

---

[3]In units of erg/s/cm^2/Hz/sr.
[4]In units of erg/s/cm^2/Hz.

Table 3.5: White dwarf parameter results from the MCMC analyses performed on the HST+COS and ULTRACAM data, the HST+COS and SDSS data with two different cut-offs for the HST+COS data and, for comparison, the results based on the ULTRACAM light curves alone (see Section 3.4.2 as well as Bours et al., 2014a, $E(B-V)$ was fixed to the mean value from Schlegel et al. 1998). Numbers in parentheses indicate uncertainties in the last digit(s).

data included restrictions	HST+ULTRACAM $\lambda < 1700$ Å	HST+SDSS $\lambda < 1700$ Å	HST+SDSS $\lambda < 2000$ Å $E(B-V) < 0.0308$	ULTRACAM $E(B-V) = 0.0339$
T_1 (K)	22439(59)	22390(58)	22443(79)	24407(654)
T_2 (K)	10876(32)	11421(88)	9481(600)	11678(313)
$E(B-V)$ (mag)	0.0292(9)	0.0192(19)	0.0296(21)	0.0339 (fixed)
$\log(g_1)$	7.322(15)	7.322(14)	7.335(18)	7.321(15)
$\log(g_2)$	7.305(11)	7.288(10)	7.286(11)	7.307(11)
R_1/a	0.02508(22)	0.02471(21)	0.02467(21)	0.02510(22)
R_2/a	0.02340(28)	0.02385(27)	0.02389(27)	0.02332(28)
minimum χ^2	44465	23215	30603	44457
degrees of freedom	37745	23667	37745	43351

As a result, the temperature I would find for the primary white dwarf is too low. Therefore I used an iterative process which, after the first step, includes the secondary white dwarf's contribution to the far-UV flux in order to find a more accurate temperature for the primary white dwarf.

In the first step I fit the HST+COS spectra with a single white dwarf model spectrum using MCMC. This fit includes as free parameters the primary white dwarf's temperature (T_1) and surface gravity ($\log g_1$), the reddening towards CSS 41177 ($E(B-V)$), and a scale factor to allow for the unknown distance to the binary. In order to include reddening as a free parameter I assume a visual extinction to reddening ratio $R = A_V/E(B-V) = 3.1$ (Schlafly & Finkbeiner, 2011) and interstellar extinction laws at UV wavelengths following Seaton (1979) and at optical wavelengths following Howarth (1983). The surface gravity is constrained by a Gaussian prior at $\log g_1 = 7.32 \pm 0.02$ (based on the results presented in the previous section, see also Bours et al., 2014a) and the reddening by a Gaussian prior at $E(B-V) = 0.0292 \pm 0.0009$ (Schlafly & Finkbeiner, 2011).

I then fitted the ULTRACAM light curve data as presented and discussed before, but now with a prior on the temperature of the primary white dwarf T_1 based on the results from the MCMC analysis of the HST+COS data described above. As before the free parameters are T_1 & T_2, R_1/a & R_2/a, K_1 & K_2, P, T_0, i and δ, but this time I also include the reddening $E(B-V)$ as a free parameter. The tight prior on T_1 given by the HST+COS data leads to a much more precise temperature for the secondary white dwarf T_2 as well.

This, in turn, allowed me to refit of the HST+COS data while accounting for 'contamination' to the UV-flux by the secondary white dwarf by subtracting a reddened model spectrum from the data, with values T_2 and $\log g_2$ fixed at the mean values from the ULTRACAM light curve fit. The new value found for T_1 then becomes a more accurate prior in the light curve fits. By including the contribution of the secondary white dwarf,
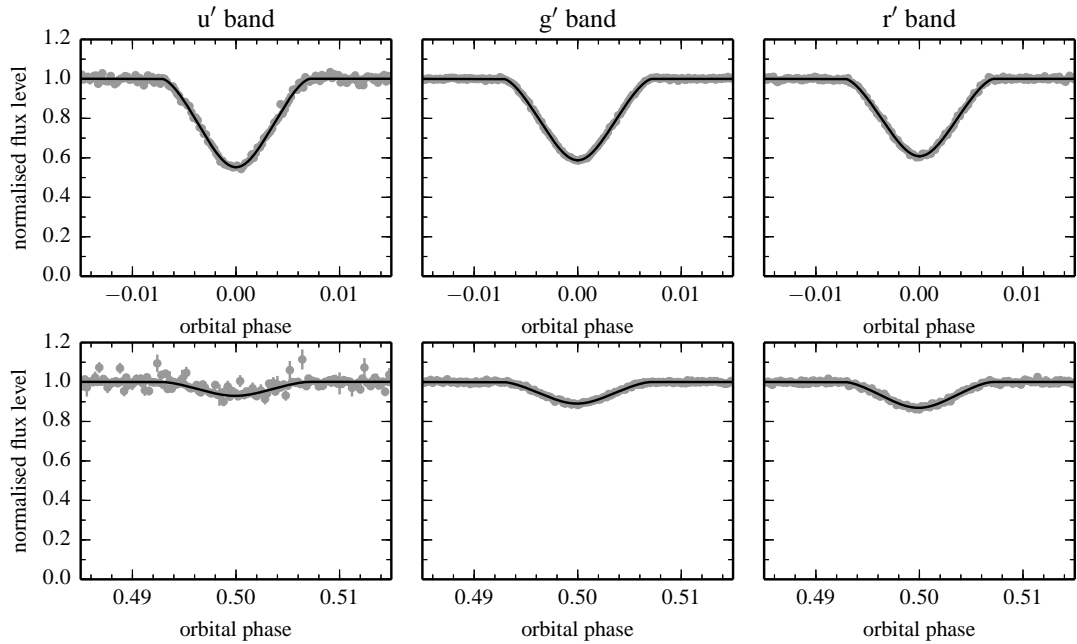
Figure 3.3: ULTRACAM u′ (left), g′ (centre) and r′ (right) data, folded with the binary's orbital period, normalised and binned by a factor of six. The black lines show the best model. The total time span shown here covers 5 minutes. *Top:* a total of twelve observed eclipses of the primary, hot white dwarf. *Bottom:* a total of nine observed eclipses of the secondary, cool white dwarf.

the primary white dwarf's temperature increases by ~ 150 K after the first iteration, and ~ 10 K after the second iteration. The latter is well within the statistical uncertainty and eliminates the need for further iterations.

The converged results are listed in Table 3.5, excluding those parameters that did not change by more than 1σ. I have experimented with placing the long wavelength cut on the HST+COS spectra at 1500 Å, which decreases the primary white dwarf's temperature by ~ 150 K, roughly illustrating the magnitude of the systematic uncertainties. The uncertainties in Table 3.5 should be considered as statistical uncertainties only.

The final best fit to the light curves is shown in Fig. 3.3, which also shows the binned u′g′r′ observations, folded on the orbital period. The difference in eclipse depth, that constrains the relative temperatures of the two white dwarfs, can clearly be seen in this figure. The HST+COS data and the best synthetic model for the double white dwarf are shown in Fig. 3.4. My final best ephemeris for CSS 41177 is given by

$$\text{BMJD(TDB)} = 55936.3446719(6) + 0.1160154352(15)\,E, \tag{3.8}$$

with E the cycle number.

3.4.4   Fitting the HST+COS and SDSS spectral energy distribution

I have also tried to constrain the effective temperatures for both white dwarfs by fitting the HST+COS data together with the *ugriz* flux measurements from SDSS, in the first
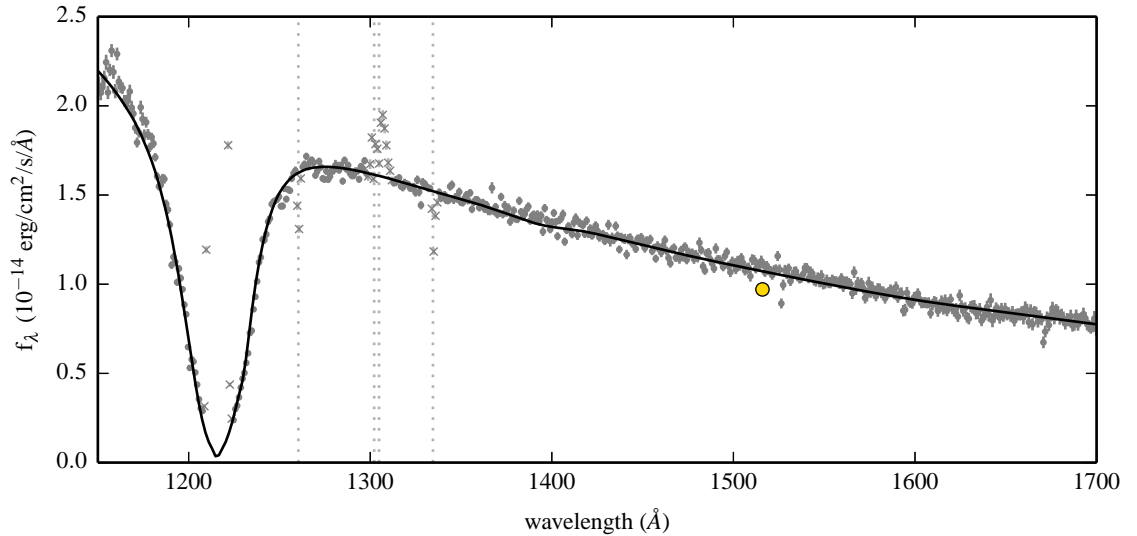
Figure 3.4: HST+COS spectrum of CSS 41177 (grey dots, 1 Å bins; crosses denote data excluded from the fits). The solid black line is the sum of the primary and secondary white dwarf model spectra corresponding to the best fit from the HST+ULTRACAM analysis described in Section 3.4.3. Also shown is the GALEX far-UV flux (filled circle, errorbar too small to be seen) and the position of interstellar absorption lines (vertical grey dotted lines).

instance using COS data out to $\lambda = 2000$ Å. To obtain the SDSS fluxes I start from the photometric PSF magnitudes given in Data Release 9. These I convert to AB magnitudes using offsets of (-0.04, 0, 0, 0, 0.02) for the *ugriz* measurements respectively[5], and then transform these into fluxes with unit erg/cm^2/s/Å. None of the SDSS observations were made during or near a primary or secondary eclipse.

I fit the data using an MCMC analysis that includes eight free parameters: the primary and secondary white dwarf temperatures (T_1, T_2), the reddening in the column towards CSS 41177 ($E(B - V)$), the two surface gravities (log g_1, log g_2), the white dwarf radii scaled to the binary's semi-major axis (R_1/a, R_2/a)) and an overall scale factor to allow for the unknown distance. I placed Gaussian priors on both the surface gravities and radii based on results of fits to the phase-resolved X-shooter spectroscopy and the ULTRACAM multi-colour eclipse observations (Section 3.4.2 in this chapter and Bours et al., 2014a), in which I include the correlations between these four parameters.

I soon realised there is a significant degeneracy between the secondary white dwarf's temperature T_2 and the reddening $E(B - V)$. This is illustrated in the left hand panel in Fig. 3.5, where the landscape of χ^2 is plotted for a range of values of T_2 and $E(B - V)$. Note that for each of the grid points, all other free parameters were optimised, to find the best fit to the HST+SDSS data. The reddening is negatively correlated with the secondary white dwarf's temperature. In the χ^2 landscape this creates a valley, stretching from low reddening and high temperatures, to high reddening and low temperatures (Fig 3.5), with minima at both ends. In this parameter space, all other free parameters only vary mildly, and stay well within their 1σ uncertainties.

[5]https://www.sdss3.org/dr9/algorithms/fluxcal.php#SDSStoAB
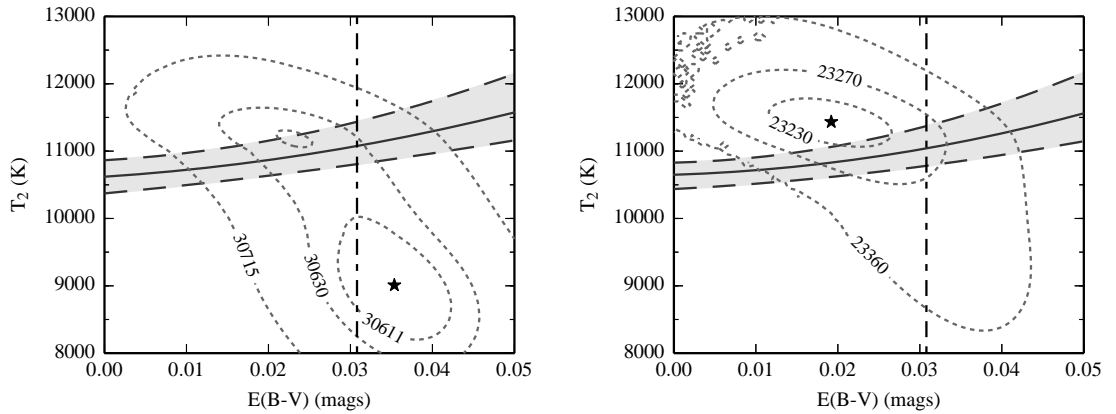
Figure 3.5: χ^2 parameter space from the HST+SDSS analysis, as a function of the secondary white dwarf's temperature T_2 and the reddening $E(B-V)$, with contours for three different χ^2 values. The shaded region where the secondary mid-eclipse depth is $11.3\% \pm 0.5\%$. The vertical dash-dotted line shows the maximum value of the reddening towards CSS 41177 at $E(B-V) = 0.0308$ (Schlafly & Finkbeiner, 2011). *Left:* including HST+COS data at wavelengths up to 2000 Å, with the star indicating minimum $\chi^2 = 30595$ (37745 dof). The results from this MCMC are also listed in column 4 of Table 3.5. *Right:* including HST+COS data at wavelengths up to 1700 Å, with the star indicating minimum $\chi^2 = 23214$ (23667 dof). The results from this MCMC are also listed in column 3 of Table 3.5.

The best fit is found for $E(B-V) = 0.0354$ mags and $T_2 = 9010$ K, with $\chi^2 = 30595$ and 37745 degrees of freedom (black star in left hand panel of Fig. 3.5). However, in the direction of CSS 41177, the reddening $E(B-V)$ does not exceed 0.0308 mags (Schlafly & Finkbeiner, 2011). In addition, a model light curve shows that with such a low temperature, the maximum depth of the g'-band secondary eclipse is only 6.6%. Yet, from the ULTRA-CAM data it is known that this mid-eclipse depth is $\sim 11.3\%$. Given that the eclipse depth at a certain wavelength is almost independent of the reddening $E(B-V)$, the measured ULTRACAM mid-eclipse depth of 11.3% indicates a temperature for the secondary white dwarf that is significantly higher than 9010 K. Given restrictions of $E(B-V) < 0.0308$ mags and secondary mid-eclipse depth $11.3\% \pm 0.5\%$, the best fit is found with $E(B-V) = 0.0232$ mags and $T_2 = 11181$ K, with $\chi^2 = 30610$, only 15 points worse than the best fit.

Using an older generation of white dwarf model spectra I have performed the same analysis. The results also showed the χ^2 valley in the $T_2 - E(B-V)$ parameter space. However, it extended to higher temperatures and the best fit was found at the other end of the valley, near $T_2 \sim 12000$ K. Therefore the difference in χ^2 between the best fit in Fig. 3.5 and the best fit when the cut of $E(B-V) < 0.0308$ mags is applied, which is only 15 points, is likely smaller than any systematic uncertainties present in the white dwarf model atmospheres. The cut in reddening therefore only excludes non-realistic solutions. The results of an MCMC analysis with a maximum on the reddening at $E(B-V) = 0.0308$ mags are listed in Table 3.4. The large uncertainty on T_2 reflects what is also seen on the left hand side in Fig. 3.5: just below the cut-off on $E(B-V)$ there is a wide range of temperatures at fairly constant χ^2. Note that because of the applied cut-off, the mean
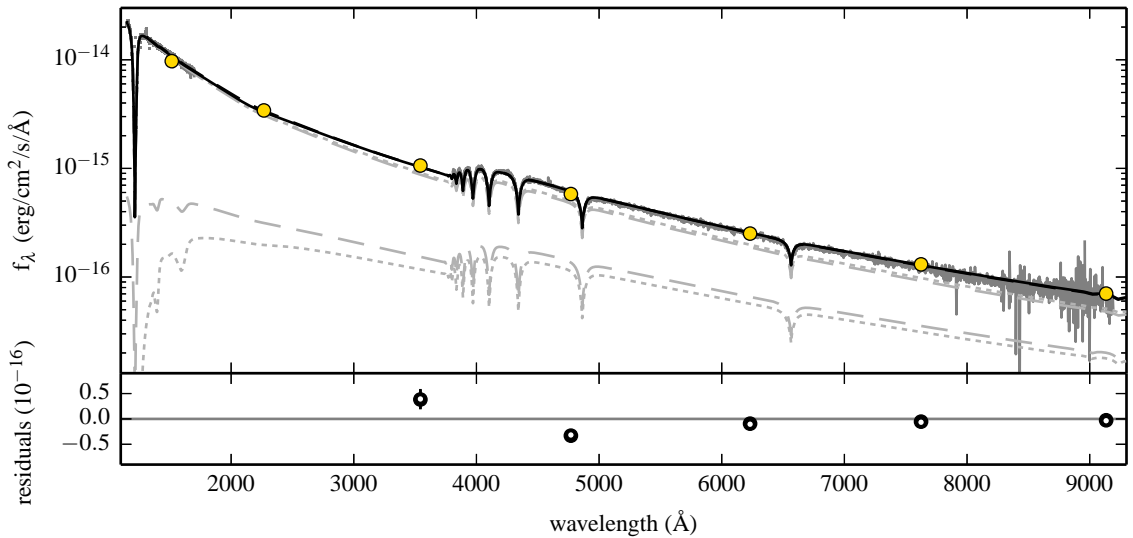
Figure 3.6: *Top panel:* best model spectra from the HST+ULTRACAM and HST+SDSS analyses: for the double white dwarf binary CSS 41177 (solid and dashed black lines respectively) and individual white dwarfs (dotted and dashed grey lines respectively). The HST+COS and SDSS data are shown in dark grey. Filled circles indicate the GALEX far-UV, GALEX near-UV and SDSS *ugriz* fluxes (errorbars too small to be seen). *Bottom panel:* residuals of the model CSS 41177 spectra folded through the SDSS filter curves with respect to the measured SDSS fluxes, for the HST+ULTRACAM (white dots) and HST+SDSS analysis (black circles).

and uncertainty for the parameters in Table 3.4, in particular $E(B - V)$, should not be considered as corresponding to a Gaussian distribution.

Following my analysis of the HST+COS and ULTRACAM data, I also analysed the HST+SDSS data while using only the COS data out to a wavelength of $\lambda = 1700$ Å. The results from this analysis are shown in the right hand panel of Fig. 3.5, and in Table 3.4. The area where the best solution for HST(<2000 Å)+SDSS was found is still favoured somewhat over the neighbouring areas, but the best solution is now found at lower values for the reddening, and higher values for the secondary's temperature. This is more consistent with the expectations from the eclipse depth, and adds to the previous suspicion that the HST+COS data at $\lambda > 1700$ Å may suffer from miscalibration.

Fig. 3.6 shows the best synthetic models for both the double white dwarf binary as well as the individual white dwarfs from the far-UV through to the near-IR. The CSS 41177 models are the sum of two white dwarf model spectra, accounting for the difference in their surface areas, where the parameters (T_{eff}, log g) for the two white dwarfs' model spectra are those from the best fits to the data. Again, I include the results from both the HST+ULTRACAM and HST+SDSS analyses. The parameters (T_{eff}, log g) for the primary white dwarf's model spectrum of the HST+ULTRACAM analysis are those from the best fit in the last iteration to the HST+COS data, and the parameters for the secondary white dwarf are taken from the corresponding model to the ULTRACAM light curves.

Both CSS 41177 model spectra are in good agreement with the HST+COS data and the SDSS data at wavelengths $\lambda > 5000$ Å, while at shorter wavelengths the models slightly

under/over predict the flux. In the u' band the difference is $1 - 2.5\sigma$ or, equivalently, a few %. Because the SDSS uncertainties do not include systematic uncertainties, this difference is likely not significant.

3.5 Discussion

3.5.1 Details of the binary orbit

For an eclipsing binary on a circular orbit it is often assumed that the primary and secondary eclipses occur exactly half an orbital phase apart. However, this is not the case if the two binary components are of unequal mass. The changing distance to the stars at times of eclipses and the finite speed of light cause a shift in the phase of the secondary eclipse. While modelling the light curve I allowed for such a time shift, and found an indication of a small displacement of δ = -0.78 $\pm$ 0.24 seconds. For CSS 41177 the Rømer delay is theoretically expected to be $\delta_R = P(K_2 - K_1)/\pi c = 0.36 \pm 0.08$ seconds (Kaplan, 2010), so that the secondary eclipse should occur slightly after phase 0.5. The fact that I measure a delay with the opposite sign, and that my measurement is 4.6σ away from the theoretical prediction indicates that there may be another process at work.

The measured time delay could be the result of a small eccentricity of the binary's orbit, in which case the measured time delay can be used to constrain the eccentricity. With $\delta_e = 2Pe\cos(\omega)/\pi$ (Kaplan, 2010; Winn, 2010), where ω is the argument of pericenter, I obtain $e\cos(\omega) = (1.24 \pm 0.38) \times 10^{-4}$, which is a lower limit on the eccentricity. Although not extremely significant, it is certainly possible that the binary did not emerge from the last common envelope phase on a completely circular orbit, or that small perturbations are induced into the binary's orbit by a third body.

I tried to confirm the measurement of a small eccentricity by fitting the primary white dwarf's radial velocity curve. This was obtained by subtracting the secondary white dwarf's contribution, fixing all the parameters defining the Gaussians that represent the primary's absorption line, and fitting each individual spectrum with only the parameters of the straight line and a single velocity as free parameters. The result is consistent with an eccentricity of zero, with a 3σ limit at 0.034, so is some way short of testing the photometric result.

The only other precise eccentricity measurement in an eclipsing double white dwarf binary (NLTT 11748) is consistent with a circular orbit, and the measured Rømer delay for this system agrees with the expected value (Kaplan et al., 2014).

If the CSS 41177 binary orbit is indeed eccentric, apsidal precession will occur. Tidal deformation and rotational distortions of both stars and relativistic processes all contribute to the apsidal precession (Sterne, 1939; Valsecchi et al., 2012). The relativistic apsidal precession amounts to 5.6 deg/yr, compared to which the precession rates due to tides and rotation are negligible.
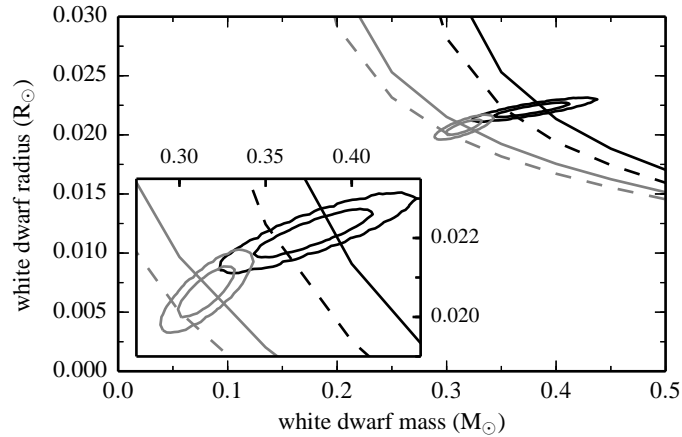
Figure 3.7: The 68 and 95 percentile contours for the masses and radii of the hot white dwarf (black) and cool white dwarf (grey) in CSS 41177 from the HST+ULTRACAM analysis described in Section 3.4.3. The lines indicate mass – radius relations for hydrogen envelopes of $M_H/M_* = 10^{-4}$ (solid) $M_H/M_* = 10^{-8}$ (dashed), for temperatures of $T_{WD} = 22500$ K (black) and $T_{WD} = 11000$ K (grey), and all with a metallicity of $Z = 0.001$ (Benvenuto & Althaus, 1998).

3.5.2   Masses, radii, and hydrogen envelopes

Typical white dwarf surface gravities are high enough to force elements heavier than hydrogen and helium to settle out of the photosphere on time scales much shorter than evolutionary time scales (Paquette et al., 1986). As a result, all heavy elements sink below the white dwarf's photosphere, leaving the light elements to form the outer layers. The two low-mass helium white dwarfs in CSS 41177 have hydrogen envelopes, and are therefore classified as DA white dwarfs.

Fig. 3.7 shows the results from the HST+ULTRACAM MCMC analysis for the masses and radii of both white dwarfs, as 68 and 95 percentile joint confidence regions. Also shown in Fig. 3.7 are mass – radius relations for hydrogen envelope masses of 10^{-4} (solid lines) and 10^{-8} (dashed lines) of the stellar mass, M_*, for both white dwarf temperatures (Benvenuto & Althaus, 1998). My results are in good agreement with both relations. Observational studies of pulsating white dwarfs suggest that the hydrogen content can be several orders of magnitude smaller than the standard prediction of stellar evolution of 10^{-4} M_*, see Bradley (2001, Table 1). However, note that their listed white dwarfs are all of significantly higher mass than the two CSS 41177 white dwarfs. Mass determinations of hydrogen layers on top of extremely low-mass white dwarfs ($M_{WD} < 0.2$ $M_\odot$) have shown that these tend to have more massive atmospheres of up to 10^{-2} M_* (Kaplan et al., 2012).

The current state of affairs is displayed in Fig. 3.8, which shows all highly accurate white dwarf masses and radii, determined independently of mass – radius relations. The two CSS 41177 white dwarfs (numbered 1 and 2) fall in an area of the mass – radius diagram that has been unexplored so far, and supply new tests for the theoretical mass – radius relations at low white dwarf masses. The measurements agree well with the models. Note that the solid and dashed grey mass – radius relations are for temperatures of $T_{eff} =$
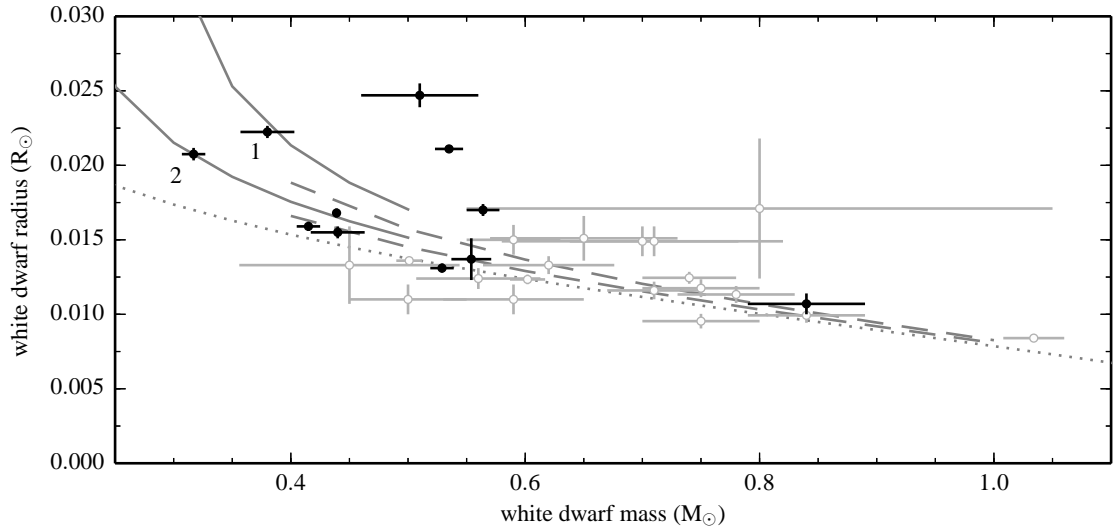
Figure 3.8: Mass – radius diagram showing all white dwarfs with model-independent mass and radius determinations. The hot and cool white dwarf in CSS 41177 are indicated with a 1 and 2 respectively. Other model-independent measurements from eclipsing white dwarf binaries are shown as black symbols (O'Brien et al., 2001; Parsons et al., 2010b, 2012a,c; Pyrzas et al., 2012). The grey symbols are for white dwarfs based on parallax measurements (Provencal et al., 1998, 2002; Casewell et al., 2009). The dotted line shows the zero-temperature mass – radius relations from Verbunt & Rappaport (1988). The solid grey lines are mass – radius relations for helium core white dwarfs with a hydrogen envelope mass of $M_H/M_* = 10^{-4}$, metallicity of $Z = 0.001$, and with $T = 22500$K (upper curve) and $T = 11000$K (lower curve) (Benvenuto & Althaus, 1998). The dashed grey lines are for carbon/oxygen core white dwarfs, again with $M_H/M_* = 10^{-4}$ and $T = 22500$K (upper curve) and $T = 11000$K (lower curve) (Wood, 1995).

22500 K and 11000 K (upper and lower curves), and that the two notable outliers are both white dwarfs that are significantly hotter (CSS 03170: Parsons et al. 2012c and NN Ser: Parsons et al. 2010a).

Using the same models by Benvenuto & Althaus (1998), I determined the cooling age for the hot white dwarf to be ∼ 50 Myr. The cool white dwarf is substantially older with ∼ 330 Myr.

In general, there is good agreement that double white dwarf binaries like CSS 41177 go through two phases of mass transfer during their evolution, the second of which is thought to result in a common envelope phase. The nature of the first is less certain, but was most likely a common envelope or stable Algol-like mass transfer (Iben et al., 1997). Different binary population synthesis codes agree that both of these evolutionary paths could produce the final CSS 41177 parameters (Toonen et al., 2014, Fig. A.22 and A.24). Under conservative mass transfer, Algol evolution may lead to too small a final orbital separation. Therefore stable non-conservative mass transfer (Woods et al., 2012), or a common envelope following the γ-prescription (Nelemans et al., 2000) could be a more accurate description of the first phase of mass transfer.
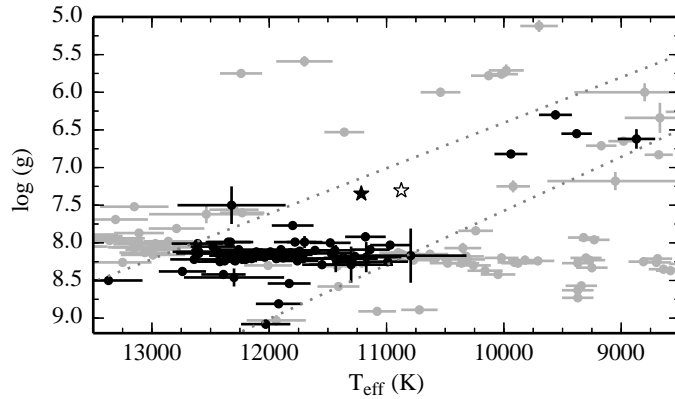
Figure 3.9: ZZ Ceti diagram, with the filled, black star showing the position of the secondary white dwarf in CSS 41177 at the overestimated values that would have been recovered if the parameters were found by fitting the secondary white dwarf's spectra with 1D model atmospheres (Tremblay et al., 2013b). The open star indicates the direct values found from the fit to the HST+COS and ULTRACAM data. The black and grey dots indicate confirmed pulsating and non-pulsating white dwarfs respectively, and the dotted lines are empirical boundaries for the instability strip (Gianninas et al., 2014a).

3.5.3   Metal lines in the HST+COS spectra

The HST+COS spectra reveal a handful of absorption lines. The positions of these lines coincide with known interstellar absorption features: Si II 1260 Å; O I 1302,1304 Å; C II 1334/5 Å. Given that the lines also do not shift position between the four individual exposures I conclude that they are indeed of interstellar origin. The Si II 1265 Å excited state is not detected, further corroborating the interstellar nature of the metal lines.

3.5.4   A pulsating second white dwarf?

Depending on their atmospheric composition, white dwarfs experience non-radial gravity-mode pulsations at different epochs in their cooling curves. Based on extrapolating observations of white dwarfs with lower and higher surface gravities, this instability should occur close to $T_{WD} = 11000$ K for white dwarfs with a mass of $M_{WD} \sim 0.3$ M$_\odot$ and hydrogen-rich atmospheres (DA) (see e.g. Bergeron et al., 1995; Gianninas et al., 2014a). In the log g – T_{eff} plane, this region is called the ZZ Ceti instability strip.

The values of the secondary white dwarf's temperature and surface gravity are shown in Fig. 3.9, where known pulsators (Gianninas et al., 2011; Hermes et al., 2012a, 2013a,c, 2014b; Pyrzas et al., 2015) and non-pulsators at 10 mmag (Gianninas et al., 2011; Steinfadt et al., 2012; Hermes et al., 2012a, 2013c,d) are also indicated. The values used for low-mass white dwarfs are the updated atmospheric parameters from Gianninas et al. (2014a), who used the latest model spectra, with a 1-dimensional mixing length theory to approximate convection, to fit the white dwarf Balmer lines. It has been known for some time that fitting Balmer lines with 1D models overpredicts surface gravities and temperatures in the regime where white dwarf atmospheres become convective ($T_{eff} < 13000$ K; Tremblay

et al., 2010, 2011b).

The method presented in this chapter does not rely on fitting Balmer lines, but rather uses the continuum of the spectral energy distribution and the ULTRACAM light curves to find the temperature and surface gravity of the secondary white dwarf in CSS 41177. These results are likely close to the true atmospheric parameters, and therefore presumably similar to results that would be obtained if it was possible to fit the secondary's Balmer lines directly with the latest 3D model spectra. For this reason, I correct my results in Fig. 3.9 using the 3D to 1D correction given by Tremblay et al. (2013b), to facilitate direct comparison with other data points in this figure. The filled star indicates the position in the ZZ Ceti strip that would have been recovered if fits to the secondary star's Balmer lines were performed with 1D model atmospheres. The open star shows the atmospheric parameters found with my method, also listed in Table 3.4. Note that the average of the 3D models is performed over constant Rosseland optical depth, which produces very similar results to full 3D spectral synthesis at all wavelengths for these temperatures and surface gravities (Tremblay et al., 2011b).

The results place the secondary white dwarf inside the empirical instability strip, just under 350 K from the blue edge, which prompted a search for pulsations in the light curves. I inspected the January 2012 ULTRACAM data, excluding the single primary eclipse observation from May 2011 to avoid artificial low-frequency signals. Looking at the out-of-eclipse data, no pulsations with an amplitude exceeding 3.0, 1.0 and 1.1 mmag in the u', g' and r' band were found. However, the secondary white dwarf's contribution to the flux is strongly diluted by the presence of the primary white dwarf and the flux ratios differ in the three bands. For the u', g' and r' band the primary to secondary flux ratios are 7.7, 4.3 and 3.5 respectively. Correcting for the flux dilution this translates to a non-detection of pulsations with an amplitude exceeding 26.1, 5.3 and 5.0 mmag in the u', g' and r' band.

The contribution of the secondary to the total amount of flux is highest in the r' band, but white dwarf pulsation amplitudes for non-radial modes increase towards bluer wavelengths. For the $l = 1$ and $l = 2$ non-radial modes the amplitude in the g' band is $\sim$ 1.4 times higher than the amplitude in the r' band (Robinson et al., 1995). Therefore my strongest constraint comes from the g' band.

Note that the available data are not ideally suited to search for pulsations, because the observations targeted the eclipses, and mostly covered only brief stretches (5 – 10 minutes) of out-of-eclipse data. Typically, pulsation periods are between $\sim 7 - 70$ minutes (Hermes et al., 2012a, 2013c), and increase with decreasing surface gravity and temperature. Therefore it is likely that the ULTRACAM observations are too short for detecting pulsations. Furthermore, pulsating white dwarfs can have amplitudes $< 0.5\%$ (Mukadam et al., 2006). These combined effects might explain why no pulsations have been detected. New, dedicated observations are required to reveal whether pulsations are indeed present or not.

Note that I have assumed a prior for the reddening at $E(B - V) = 0.0292 \pm 0.0009$ in the final MCMC analyses, which is the total estimated reddening in the direction of
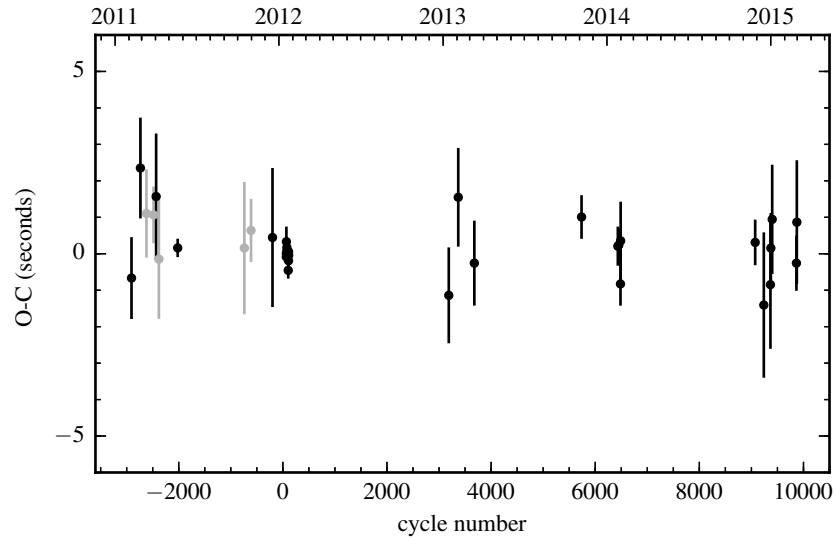
Figure 3.10: Observed minus calculated (O-C) diagram for the primary eclipses of CSS 41177, including the ULTRACAM, ULTRASPEC and LT+RISE data as well as five eclipse observations from Backhaus et al. (2012, plotted in grey). The ULTRACAM eclipses were observed in three filters simultaneously, and the times shown here are the weighted averages of these. The eclipse times are listed in Table 3.2.

CSS 41177. Since the reddening affects the flux at shorter wavelengths more than the flux at longer wavelengths, a smaller $E(B - V)$ results in a shallower slope of the HST+COS spectra. This translates to a lower temperature for the primary white dwarf, and, through the ULTRACAM light curves, also in a lower temperature of the secondary white dwarf. Therefore any decrease in the reddening will push the secondary white dwarf further into the instability strip.

3.5.5 Orbital period variations

Fig. 3.10 shows the mid-eclipse times of the primary eclipses in an observed minus calculated (O-C) diagram, where the calculation is based on the linear ephemeris of Eq. 3.8. All ULTRACAM, ULTRASPEC and LT+RISE data are included. For the ULTRACAM data I show the weighted mean of the u′, g′ and r′ data. All eclipse times are listed in Table 3.2.

There is as yet no indication of any variation in the binary's orbital period. This may be expected as the white dwarfs cannot induce orbital period variations through magnetic cycles (the Applegate mechanism as discussed in Chapter 1, see Applegate, 1992). This mechanism has regularly been called upon to explain observed orbital period variations in white dwarf + M-dwarf binaries, where the M-dwarf can indeed undergo such magnetic cycles and the resulting changing gravitational quadrupole moment can cause orbital period variations. However, a number of these binaries show variations too large to be the result of this mechanism (Brinkworth et al., 2006), and a popular alternative explanation has been the presence of circumbinary planetary-like companions. See for example the proposed planetary systems for NN Serpentis (Beuermann et al., 2010; Marsh et al., 2014)

or UZ Fornacis (Potter et al., 2011), both eclipsing white dwarf + M-dwarf binaries with large orbital period variations. However, it should be noted that several of these invoked planetary systems do not show any long-term ($\sim$ Myr) dynamical stability (Hinse et al., 2012; Wittenmyer et al., 2012), although the case for NN Serpentis becomes more and more convincing (Marsh et al., 2014; Beuermann et al., 2014).

Should any orbital period variations be seen in a double white dwarf, this would be a strong indication that circumbinary planets around evolved binaries indeed do exist. A situation that raises interesting questions regarding the formation and evolution of planetary systems. The possible planets could be first-generation planets that survived the common-envelope phase of the binary, or be second-generation planets that formed from the large amount of mass expelled after the common-envelope phase. Only data spanning several years, or even decades, can shed light on the answers, and so it is key to keep observing binaries like CSS 41177 regularly. So far CSS 41177 shows no deviation from a linear ephemeris and may indeed prove to be useful as an optical timing standard.

3.6 Conclusions

I have presented high signal-to-noise ULTRACAM, X-shooter and HST+COS observations of CSS 41177 and the combined analysis of these data sets. The high spectral and temporal resolution of the X-shooter data and the ULTRACAM observations in three wavelength bands allowed me to accurately model the binary and both white dwarfs, without needing to use theoretical mass – radius relations.

The results place these two white dwarfs in a region of the mass – radius diagram that is as yet unexplored; they are the lowest mass white dwarfs with model-independent parameters. The results agree with white dwarf models for the corresponding temperatures and with standard hydrogen atmospheres.

The HST+COS spectra allowed me to precisely measure the primary white dwarf's temperature: $T_1 = 22439 \pm 59 \pm 150$ K. Combined with the ULTRACAM eclipse data this puts a very tight constraint on the secondary temperature as well: $T_2 = 10876 \pm 32 \pm 150$ K. In this analysis I chose to use the HST+COS data up to $\lambda = 1700$ Å, motivated by the decreasing sensitivity of COS and the therefore increasing difficulties with the relative flux calibration at longer wavelengths.

I also found an indication that the secondary eclipse does not occur exactly half an orbital period after the primary eclipse. Although the Rømer delay predicts such an offset, it also predicts that the secondary eclipse will occur late, whereas I measured it to occur early. Therefore the orbit of the two white dwarfs may be slightly eccentric. To measure this effect with higher accuracy more secondary eclipses observations are needed.

I also performed an analysis of the HST+COS data combined with SDSS *ugriz* fluxes. Because the latter extends into the infrared, the combined data has to be fit with two white dwarf model spectra simultaneously to account for the contribution of both white dwarfs to the total flux. When using the HST+COS data out to $\lambda = 2000$ Å, this caused a degeneracy between the reddening $E(B-V)$ and the secondary white dwarf's temperature

T_2, which I was only able to break using the measured eclipse depth from the ULTRA-CAM data. Performing the same fit with different generations of white dwarf models as well as using a cut-off at $\lambda = 1700$ Å for the far-UV HST+COS data showed that the systematic uncertainties in this method are large. Using the same data and models as used for the HST+ULTRACAM method, I found a solution in which the primary white dwarf's temperature agrees with that found from the HST+ULTRACAM data, but the secondary temperature is significantly higher at $T_2 = 11421 \pm 88$ K. This 6σ difference is compensated for by a 5σ difference in the reddening. This solution fits the spectroscopic data, and agrees with optical eclipse observations, but given the larger uncertainties (both statistical and systematic) I favour the results from the HST+ULTRACAM analysis.

Besides the white dwarf temperatures, I can constrain the surface gravities from the ULTRACAM light curves, combined with constraints from the X-shooter time-series spectroscopy. For the secondary white dwarf I found $\log g_2 = 7.305 \pm 0.011$, which places it inside the pulsational instability strip for white dwarfs with hydrogen-rich atmospheres, and in particular in the gap between the canonical $\log g \simeq 8$ white dwarfs and the extremely low mass white dwarfs at $\log g \simeq 6.5$. The ULTRACAM data include only short stretches of out-of-eclipse data, in which I was unable to detect pulsations. Given the results presented here, dedicated high-speed photometric observations resulting in higher signal-to-noise ratio data may still reveal the presence of pulsations. This white dwarf is particularly interesting because it is positioned in an as-yet-unexplored part of the ZZ Ceti diagram, as well as being close to the edge of the instability strip. Determining if it pulsates or not will help determine where the border of the instability strip is and whether the strip is continuous from high mass to extremely low mass white dwarfs.

★ ★ ★

Chapter 4

The paradox of
SDSS J125733.63+542850.5

4.1 Introduction

As we saw before, double white dwarf binaries are common end products of binary evolution (Marsh et al., 1995; Toonen et al., 2014), and those with separations small enough to have experienced one or two common envelope phases are possible progenitors of supernovae Type Ia (Iben & Tutukov, 1984; Webbink, 1984), Type .Ia (Bildsten et al., 2007), R CrB stars (Webbink, 1984) and AM CVn systems (Breedt et al., 2012; Kilic et al., 2014b). In addition, mergers of Galactic double white dwarfs occur relatively frequently (Badenes & Maoz, 2012), and constitute the main source of the background gravitational wave signal at frequencies detectable from space (Nelemans et al., 2001; Hermes et al., 2012b).

The initial-final mass relation (Weidemann, 2000), predicts that extremely low-mass (ELM) white dwarfs, typically with masses $M_{WD} \lesssim 0.3$ $M_\odot$, cannot yet form as a natural product of stellar evolution because the main-sequence lifetime of their low-mass progenitors is longer than the present age of our Galaxy. However, ELM white dwarfs can be formed in binary systems in which the separation is close enough for the two stars to interact significantly before the ELM white dwarf's progenitor has evolved off the main-sequence (mass transfer via Case A or early Case B Roche-lobe overflow). The binary companion causes the evolution of the ELM white dwarf's progenitor to be truncated before ignition of helium, and after ejection of the envelope the helium core is exposed as the ELM white dwarf. Typically, these white dwarfs have surface gravities $\log g < 7$, as well as relatively massive hydrogen envelopes ($\sim 10^{-3} - 10^{-2}$ $M_\odot$; Istrate et al., 2014b). New dedicated searches such as the ELM Survey have significantly increased the known population in recent years (Brown et al., 2010, 2012, 2013; Kilic et al., 2011, 2012). The majority of ELM white dwarfs are companions to other white dwarfs (Kaplan et al., 2014, this chapter) or millisecond pulsars (see for example van Kerkwijk et al., 1996; Bassa et al., 2006; Antoniadis et al., 2013) and a few have been found in hierarchical triple systems (Ransom et al., 2014; Kilic et al., 2014a, 2015) or orbiting A- or F-type main-sequence stars (Maxted et al., 2014; Breton et al., 2012). The subject of this chapter, SDSS J1257+5428, is a binary that likely belongs to the first of these classes, but, as we shall see, how it evolved into the system we see today is a mystery.

4.1.1   Introduction to SDSS J1257+5428

The double white dwarf binary SDSS J1257+5428 (full name: SDSS J125733.63+542850.5) was first discovered when the available SDSS (Eisenstein et al., 2006; York et al., 2000) subspectra were examined for radial velocity variations as part of the Sloan White dwArf Radial velocity Mining Survey (SWARMS; Badenes et al., 2009). Follow-up spectroscopy revealed radial velocity variations with a semi-amplitude of 323 km s^{-1}, which were interpreted to come from a 0.9 M$_\odot$ white dwarf. Combined with the orbital period of 4.6 h and the absence of additional spectral features, this suggested that the most likely companion would be a neutron star or a black hole (Badenes et al., 2009).

Follow-up B and R band spectroscopy revealed two distinct components in the spectra, although the Balmer absorption lines only showed a single sharp core (Marsh et al., 2011; Kulkarni & van Kerkwijk, 2010). These deep, radial-velocity variable Balmer lines in fact originate in a cool ELM white dwarf, which I hereafter refer to as the primary (because it dominates the flux at visual wavelengths, and following Kulkarni & van Kerkwijk 2010 and Marsh et al. 2011). The secondary is another white dwarf, which is hotter and significantly more massive, causing it to have very broad absorption lines. In addition, it is likely rotating fast, causing its line cores to be smeared out. Due to the shallow nature of these lines, and the absence of sharp cores, it was not possible to detect a radial velocity variation of the massive white dwarf.

The combination of these two white dwarfs in the same binary system is very interesting. The primary component is of much lower mass, and therefore has a much larger surface area than the secondary component. This causes the cooler primary to dominate the flux at wavelengths $\lambda \gtrsim 4000$ Å. At shorter wavelengths the secondary white dwarf starts dominating due to its higher temperature. Note that the fact that the higher mass white dwarf is hotter is contrary to expectation since it presumably formed much earlier than the low-mass white dwarf. At the time of the studies by Kulkarni & van Kerkwijk (2010) and Marsh et al. (2011) there were only a limited number of low-mass white dwarf models available, leaving it unclear whether or not the cool, low-mass white dwarf could have overtaken the secondary white dwarf on the cooling track. To securely measure the secondary's temperature, Hubble Space Telescope far-ultraviolet spectra have been obtained. These new measurements of the hot white dwarf are presented in this chapter (see also Bours et al., 2015b) and combined with recent binary models for ELM helium white dwarfs (Istrate et al., 2014b; Althaus et al., 2013) to study this binary's evolutionary history further.

4.2   Observational data

4.2.1   The Hubble Space Telescope data

SDSS J1257+5428 was observed with the Hubble Space Telescope (HST) in Cycle 18, with program ID 12207. Part of the observations were done with the Cosmic Origins Spectrograph (COS) on 2011 May 9, with the G140L grating and a central wavelength of $\lambda_{\rm cen} =$

1280 Å. The total exposure time of these data is 146 minutes. The double white dwarf was also observed with the Space Telescope Imaging Spectrograph (STIS), on 2011 Oct 22. For these observations, totalling 95 minutes, the G230L grating was used at $\lambda_{cen} = 2376$ Å. The raw data were processed by the standard pipeline at the Space Telescope Science Institute.

In the following analysis I exclude parts of the HST spectra that are contaminated by geocoronal O<small>I</small> (1304 Å) emission. In addition, for the COS and STIS data, I have excluded data at wavelengths $\lambda > 1700$ Å, and $\lambda < 1650$ Å respectively, where the signal-to-noise ratio is very low. The measured flux is consistent with the Swift Ultra-Violet / Optical Telescope data presented in Marsh et al. (2011).

4.2.2   Parallax observations

The 2.4 m Hiltner telescope at the MDM Observatory on Kitt Peak was used for 19 observing runs between January 2010 and June 2014. The astrometric solution includes 128 exposures, all taken in the I-band. Observations, reductions, and analysis followed procedures similar to those described in Thorstensen (2003) and Thorstensen et al. (2008). The parallax of SDSS 1257+5428 relative to the reference stars was 8.3 mas, with a formal fitting error of only 0.8 mas, although the external error is judged to be 1.3 mas from the scatter of the reference stars. The colours and magnitudes of the reference stars yield a 1.6 mas correction due to the finite distance of the stars forming the reference frame, so the absolute parallax estimate is 9.9 ± 1.3 mas, which on face value gives a distance to SDSS J1257+5428 of $\sim 101 \pm 15$ pc. The proper motion relative to the reference frame is modest, $[\mu_X, \mu_Y] = [-45, +9]$ mas yr^{-1}; the PPMXL catalogue (Roeser et al., 2010) gives $[-41.0, +11.8]$ mas yr^{-1}, in very good agreement. Thorstensen (2003) describes a Bayesian procedure for estimating a distance by combining parallax information with proper motion (interpreted using an assumed space-velocity distribution) and with photometric distances. For the present case, only the proper-motion constraint is used to avoid tautology. The small proper motion combines with the Lutz-Kelker correction to give an estimated distance of 112^{+20}_{-15} pc, which is consistent with the inverse of the parallax. Assuming a thick-disk velocity distribution increases this by another ~ 5 pc.

4.2.3   ULTRASPEC photometry

On the nights of March 2 and March 3, 2015, SDSS J1257+5428 was observed with the high-speed photometric camera ULTRASPEC (Dhillon et al., 2014), on the Thai National Telescope located on Doi Inthanon, Thailand. In total, 240 minutes of g' band data were obtained. The data were reduced using the ULTRACAM pipeline (Dhillon et al., 2007), with which I debiased and flatfielded the data and performed relative aperture photometry using a nearby bright star to minimise the effects of atmospheric variations in the light curves.

Table 4.1: White dwarf parameter results from the MCMC analysis performed on the HST+COS, HST+STIS and SDSS data. The reddening is constrained to $0 < E(B-V) < 0.0173$ by a uniform prior. Numbers in parentheses indicate statistical uncertainties in the last digit(s). The distance is calculated from the scale factor s (see Section 4.3 for details). The cooling ages τ_2 in each column are based on carbon/oxygen and oxygen/neon white dwarf models, with an estimated uncertainty of 0.1 Gyr. The last three columns correspond to MCMC runs where the value of $\log g_1$ was fixed. The motivation for this is explained in Sect. 4.4.2.

parameters	MCMC results	best model (see Fig. 4.2)	MCMC (fixed $\log g_1$)	MCMC (fixed $\log g_1$)	MCMC (fixed $\log g_1$)
T_2 (K)	13030(70)	13033	13050(59)	12965(82)	12811(94)
T_1 (K)	6400(37)	6399	6402(38)	6395(29)	6460(24)
$E(B-V)$ (mag)	0.0089(34)	0.0101	0.0109(23)	0.0038(21)	0.0008(8)
$\log(g_2)$	8.73(5)	8.72	8.73(5)	8.70(7)	8.61(9)
$\log(g_1)$	5.26(36)	5.10	5.0	6.0	7.0
R_1/R_2	4.27(9)	4.27	4.29(9)	4.21(10)	3.89(9)
d (pc)	102(9)	103	102(9)	105(8)	109(8)
M_2 ($M_\odot$)	1.06(5)	1.05	1.06(5)	1.04(5)	1.00(5)
τ_2 (Gyr)	1.0 / 1.2	1.0 / 1.2	1.0 / 1.2	1.0 / 1.2	0.9 /1.2
Details of the various fits					
minimum χ^2	5771(4)	5764	5771(4)	5774(4)	5817(4)
degrees of freedom	11071	11071	11072	11072	11072

4.3 Fitting spectra: a Markov-chain Monte Carlo approach

I fit both the HST COS and STIS spectra as well as the SDSS *ugriz* fluxes using a Markov Chain Monte Carlo (MCMC) analysis, through the affine-invariant ensemble sampler in the PYTHON package EMCEE (Foreman-Mackey et al., 2013). To obtain the SDSS fluxes, I use the PSF magnitudes, which are corrected for the offset between the SDSS and AB magnitude systems using (-0.04, 0, 0, 0, 0.02) for the *ugriz* measurements respectively[1].

I fit the data with a sum of two white dwarf model spectra from Koester (2010), which employ a 1D mixing length theory, with $ML2/\alpha = 0.8$, to approximate convection, and which list the Eddington flux density at the surface of the white dwarf. The relative contribution of the two model spectra is determined by the radius ratio of the two white dwarfs. The MCMC method maximises the posterior probability, equivalent to minimising χ^2, to find the best fit. Each data point is weighted by its uncertainty, with no additional weight in favour of either the HST or SDSS data.

The free parameters in the model are the temperatures T_1 and T_2, the surface gravities $\log g_1$, $\log g_2$, the radius ratio R_1/R_2, a scale factor $s = 4\pi R_1^2/d^2$ to account for the distance d to SDSS J1257+5428, and the maximum reddening along the line of sight $E(B-V)$, which is incorporated using the expressions presented in Seaton (1979) and Howarth (1983). I included a uniform prior on the reddening, constraining it to $0 < E(B-V)/\text{mag} < 0.0173$, where the maximum is given by the dust map of Schlafly & Finkbeiner (2011) and I assume a minimum of zero. All other parameters are left unconstrained. I chose not to include a prior on the distance based on the parallax measurements, to allow a self-consistency check afterwards.

---

[1]http://www.sdss.org/dr12/algorithms/fluxcal/#SDSStoAB
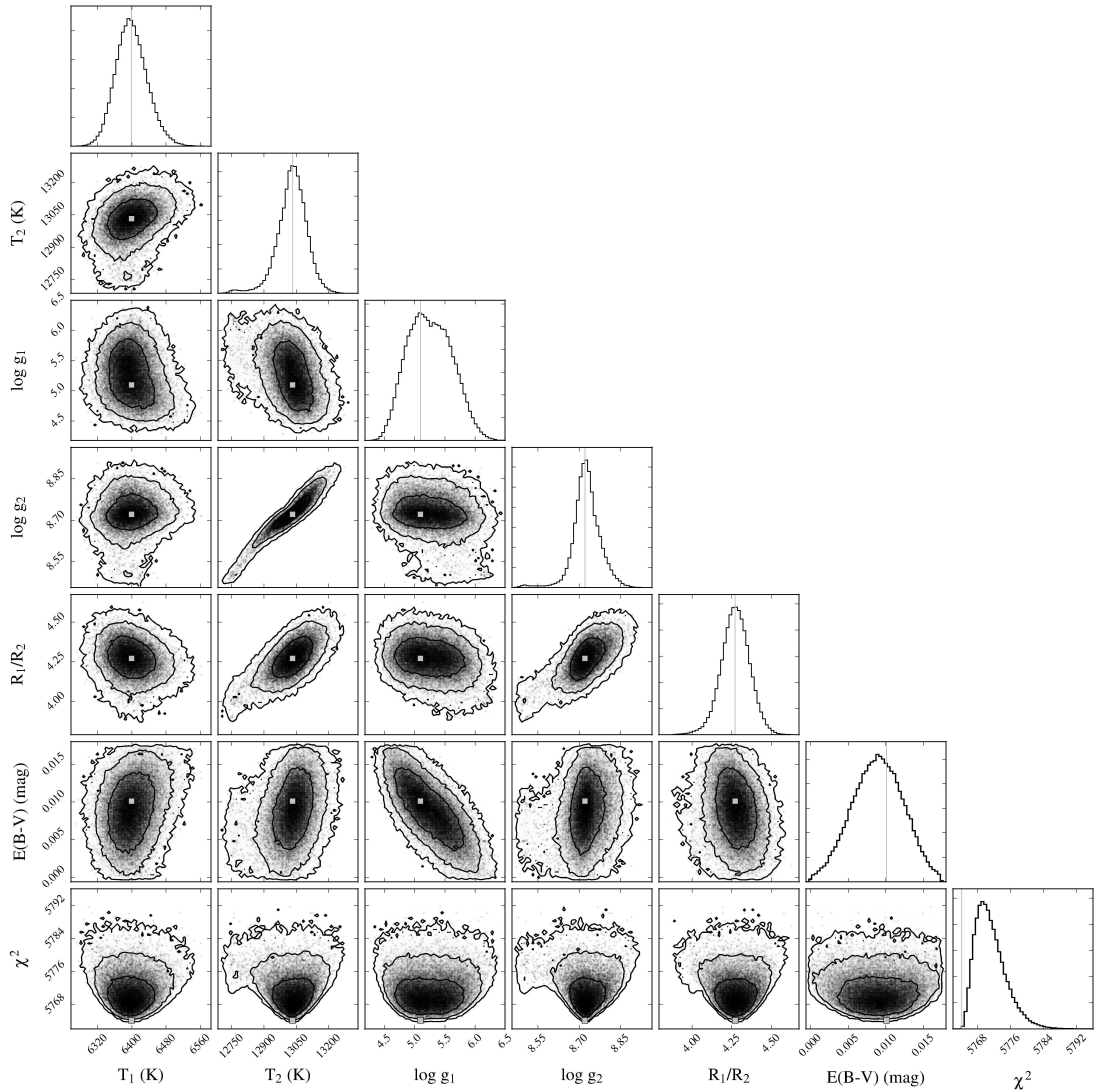
Figure 4.1: Converged MCMC chain projected onto 2-dimensional parameter spaces and showing histograms for the individual free parameters in the fits. The contours are at the 1σ, 2σ and 3σ levels, and include 68%, 95% and 99.7% of the data respectively. The grey squares and vertical lines indicate the best fitting model with $\chi^2 = 5764$, as listed in Table 4.1.

The results presented here are based on converged chains, from which the burn-in phase is removed. I have also thinned the chains, by only storing every 20th model, in order to reduce correlations between successive models in the unthinned chain.

4.4   Results

For each of the free parameters, the mean value and 1σ uncertainty of the converged MCMC chain are listed in Table 4.1, column 2. Note that the quoted uncertainties are purely statistical. They do not include any systematic uncertainties that may be present, and are therefore underestimates of the true uncertainties. For the best model, the reduced $\chi^2 = \chi^2_\nu \simeq 0.5$. However, scaling the errorbars on the data such that $\chi^2_\nu \simeq 1$, a common
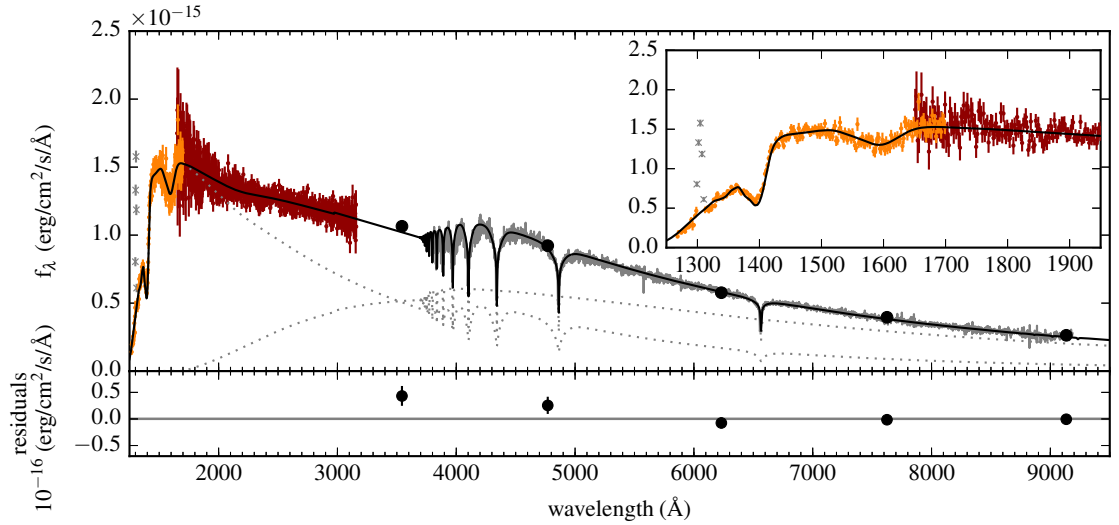
Figure 4.2: *Top panel:* best fit model spectra for the double white dwarf binary SDSS J1257+5428 (solid black line) and the individual white dwarfs (dotted grey lines). The HST+COS and STIS spectra are shown at $1200 < \lambda/\text{Å} < 1700$ and $1650 < \lambda/\text{Å} < 3200$ respectively and are binned to 2 Å. Solid black dots indicate the SDSS *ugriz* fluxes (errorbars too small to be seen). The inset shows a closer view of the far-UV where the flux is almost entirely dominated by the hot white dwarf. The grey crosses indicate geocoronal oxygen emission ($\lambda \sim 1300$ Å), and are excluded from my fits. *Bottom panel:* residuals of the model SDSS J1257+5428 spectrum folded through the SDSS filter curves with respect to the measured SDSS fluxes.

practice, would only decrease the statistical uncertainties further, and I refrain from doing so. The results from the MCMC run are shown in Fig. 4.1, projected on the various 2-dimensional parameter planes, as well as in 1-dimensional histograms. The best model, together with the HST and SDSS data, is shown in Fig. 4.2, and fits the data well at all wavelengths. The underpredictions of the model with respect to the u and g SDSS fluxes (shown in the bottom panel) are less than 3σ of the SDSS flux. Given that SDSS uncertainties do not include systematic uncertainties, this difference is likely not significant.

4.4.1 The hot, massive white dwarf and possible pulsations

With an effective temperature of $T_2 = 13030 \pm 70$ K and a surface gravity of log $g_2 = 8.73 \pm 0.05$, detailed evolutionary models show that the secondary star has a mass of $M_2 = 1.06 \pm 0.05$ M$_\odot$. The corresponding cooling age is $\tau_2 = 1.0$ Gyr or $\tau_2 = 1.2$ Gyr, with an estimated uncertainty of 0.1 Gyr, for carbon/oxygen and oxygen/neon white dwarf models respectively (Tremblay et al., 2011a; Kowalski & Saumon, 2006; Althaus et al., 2007)[2]. The values for the mass and surface gravity translate into a radius of $R_2 = 0.0074 \pm 0.0006$ R$_\odot$. These results are in agreement with those of Kulkarni & van Kerkwijk (2010), and the results of the fits to the phase resolved and ultraviolet-optical spectral energy distribution presented in Marsh et al. (2011).

At different composition-dependent epochs during a white dwarf's cooling process, the

---

[2]See http://www.astro.umontreal.ca/~bergeron/CoolingModels.

star experiences non-radial gravity-mode pulsations. The atmospheric parameters of the secondary white dwarf place it inside the empirical and theoretical instability strip for white dwarfs with hydrogen-rich atmospheres (Gianninas et al., 2014a; Van Grootel et al., 2013). At this high surface gravity, there are only two confirmed white dwarf pulsators (Gianninas et al., 2011; Hermes et al., 2013a). I reiterate here that this empirical instability strip is based on atmospheric parameters determined from Balmer line fits, in which the models used include a 1D mixing-length theory to approximate convective motion. The most recent models are based on 3D simulations instead, and give slightly different results for both white dwarf temperatures and surface gravities (Tremblay et al., 2013b). Because our atmospheric parameters were not obtained through Balmer line fits, these do not suffer from inaccuracies in the 1D models. To be able to make a direct comparison to the empirical instability strip, I therefore followed what I did in Chapter 3 and decided to 'correct' my results using the offsets from 3D to 1D parameters (Tremblay et al., 2013b, $\Delta T \simeq 250$ K; $\Delta \log g \simeq 0.01$), rather than correcting every other source from 1D to 3D.

Although the secondary is placed ~ 600 K from the blue edge inside the instability strip, I did not detect any pulsations in the time-tagged HST COS data down to an amplitude of 1.7%, equivalent to 18 mmag at the 3σ limit. To obtain an even better limit, SDSS J1257+5428 was observed with ULTRASPEC. However, these data also do not show any pulsations with an amplitude exceeding 0.5%. In the g' band light curve the contribution of the secondary white dwarf is diluted by that of the primary, as the latter contributes 1.6 times as much flux at these wavelengths. This puts the 3σ pulsation amplitude limit at 14 mmag. Note that the HST limit is from data at far-ultraviolet wavelengths, where pulsation amplitudes are generally much larger than at optical wavelengths (Robinson et al., 1995), and may therefore still be the stronger limit even though the absolute value is somewhat higher than that from the ULTRASPEC data. Pulsation amplitudes tend to decline for white dwarfs with effective temperatures exceeding 11500 K (Mukadam et al., 2006), and so it is possible that they are still present, but with amplitudes below the limits presented here.

4.4.2   The cool low-mass white dwarf

The secondary white dwarf mass determined above combined with the radial velocity variation of $K_1 = 330$ km s^{-1} measured by Marsh et al. (2011) put an upper limit on the mass of the primary white dwarf at $M_1 \leq 0.24$ M$_\odot$ (see their Fig. 6). This is consistent with the system not being a supernova Type Ia progenitor, as well as with the favoured solution found in Marsh et al. (2011).

One interesting result from the analysis presented here is that the data strongly suggest that the surface gravity of the primary, cooler white dwarf is close to $\log g = 5.3$ (see Fig. 4.1). However, given the radius ratio of $R_1/R_2 = 4.27$ and a maximum possible mass ratio of $M_2/M_1 \simeq 10$, generously assuming a minimum white dwarf mass of 0.1 M$_\odot$ (Istrate et al., 2014a; Althaus et al., 2013), the surface gravities can differ by $\log g_2 - \log g_1 \simeq 2.3$ at most. Given that the surface gravity of the hot white dwarf is well-constrained by the
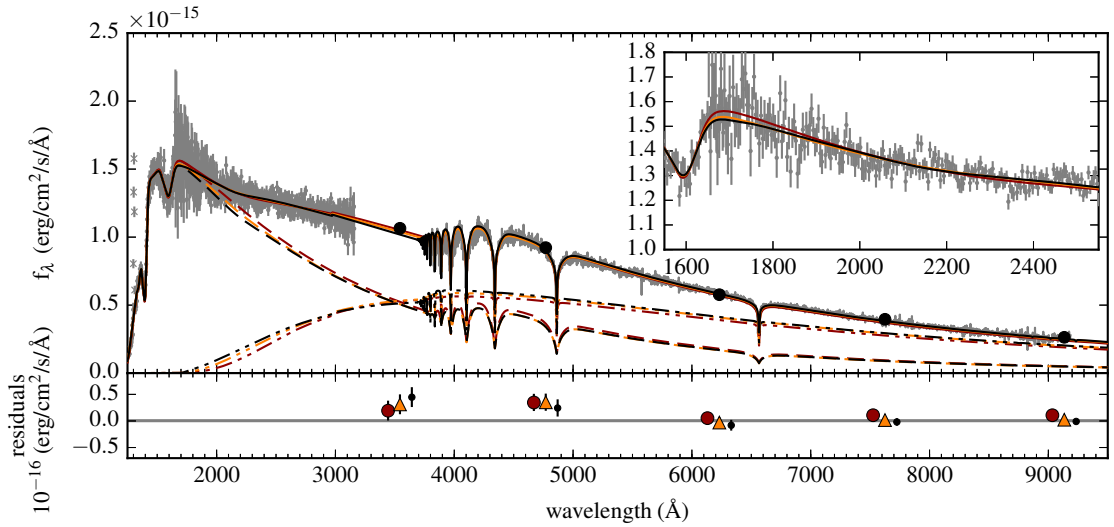
Figure 4.3: *Top panel:* best fit model spectra for the double white dwarf binary SDSS J1257+5428 (solid lines) and the individual white dwarfs (dashed and dot-dashed lines) from MCMC fits with log g_1 fixed at 5.0, 6.0 and 7.0 (black, dark grey and light grey respectively). The HST+COS and STIS spectra (binned to 2 Å in the main panel, and 4 Å in the inset) and the SDSS spectrum are shown as well. Solid black dots indicate the SDSS *ugriz* fluxes (errorbars too small to be seen). The inset highlights the part of the spectrum where the models differ most. *Bottom panel:* residuals of the model SDSS J1257+5428 spectra folded through the SDSS filter curves with respect to the measured SDSS fluxes, offset by -100 Å, 0, +100 Å for log g_1 fixed at 7.0, 6.0 and 5.0, respectively.

features in the HST+COS data it is therefore likely that the surface gravity of the cool white dwarf should be closer to log $g_1 \sim 6.5$. In addition, there is no indication of any absorption lines besides the Balmer lines, even though at the very least the Ca H/K lines are often present in white dwarfs with log $g \lesssim 6$ (Hermes et al., 2014a; Brown et al., 2013; Gianninas et al., 2014b; Kaplan et al., 2013). This therefore also points towards a surface gravity larger than 5.3 for the low-mass white dwarf in SDSS J1257+5428. I do not know why the data imply the low surface gravity as found in an unconstrained fit. Considering the entire range of possible white dwarf surface gravities, a log $g_1 \sim 6.5$ is still at the low end, and the combination with the low effective temperature is unprecedented, making it difficult to draw robust conclusions.

For these reasons, I reanalysed the data while keeping log g_1 fixed, choosing values of 5.0, 6.0 and 7.0. The results are listed in the last three columns of Table 4.1. The large changes in log g_1 have relatively little effect on the χ^2 values of the fits. The main difference between these results and those from the initial MCMC run is in the values of the reddening and the radius ratio. The reddening decreases significantly, becoming consistent with zero when the primary white dwarf's surface gravity is fixed at higher values. This behaviour is likely caused by the near-ultraviolet feature in the interstellar extinction curve, which is adjusted to compensate for the change in the cool white dwarf's spectrum, which starts contributing to the total flux in this same wavelength range. The variation in the other parameters illustrates the extent of the systematic uncertainties, which are ~ 150 K for T_2, ~ 50 K for T_1, and ~ 0.05 for log g_2. Note that these uncertainties are too small to
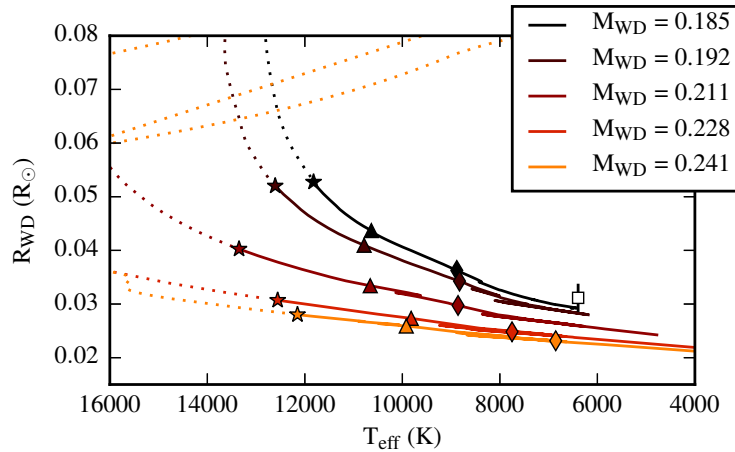
Figure 4.4: Cooling tracks for ELM white dwarfs, together with the radius and effective temperature of the cool low-mass white dwarf (square). The lines are evolutionary models from Istrate et al. (2014b, see text for more details) for white dwarfs of different mass (in $M_\odot$, see legend). The various lines are dotted up to a cooling age of 1.0 Gyr (first set of stars), and solid after. Triangles and diamonds are placed at cooling ages of 2.5 and 5 Gyr for each track. At $T_{eff} = 6400$ K, the white dwarf cooling ages are roughly 13, 13, 10.5, 7.2 and 6.7 Gyr, with increasing mass, respectively.

move the secondary out of the instability strip. The best fits from the three MCMC runs with fixed, different values of $\log g_1$ are shown in Fig. 4.3. Comparison of these models with the Balmer lines in the WHT+ISIS spectra presented in Marsh et al. (2011) shows that the model with $\log g_1 = 6.0$ matches the depths of those lines best, consistent with my reasoning above. From now on I therefore assume that $\log g_1 \simeq 6.0 - 6.5$, which agrees with the results from the unconstrained MCMC analysis at the $\sim 3\sigma$ level (see Fig. 4.1).

Given that the surface gravity of the cool white dwarf is poorly constrained by the spectra I do not rely on it hereafter, and instead use the radius derived for the hot, secondary white dwarf in section 4.4.1, and the radius ratio from the MCMC analysis. The latter is constrained by the relative flux contributions of the two white dwarfs across the spectral energy distribution, and together they provide a radius for the primary of $R_1 = 0.032 \pm 0.003$ $R_\odot$. In Fig. 4.4 I show this value and the effective temperature for the cool white dwarf, together with evolutionary models for white dwarfs of different mass from Istrate et al. (2014b). These models were obtained for ELM white dwarfs in close binaries with neutron stars, but the white dwarf's formation via Roche lobe overflow and detachment likely proceeds similarly independent of the nature of the companion, apart from possible issues of mass-transfer instability. To avoid cluttering the figure, I only selected a few of the many models with various values of the initial mass of the donor star (the progenitor of the helium white dwarf), the index of magnetic braking, and the mass of the neutron star companion (see Istrate et al. 2014a for further discussion). My results indicate that the cool white dwarf has a low mass, close to 0.2 $M_\odot$, consistent with a low surface gravity. However, the models also show that such low-mass white dwarfs take ≥ 5 Gyrs to cool to a temperature of 6400 K, much longer than the cooling age derived for the hot white dwarf, which is close to 1 Gyr. These values suggest, surprisingly, that the
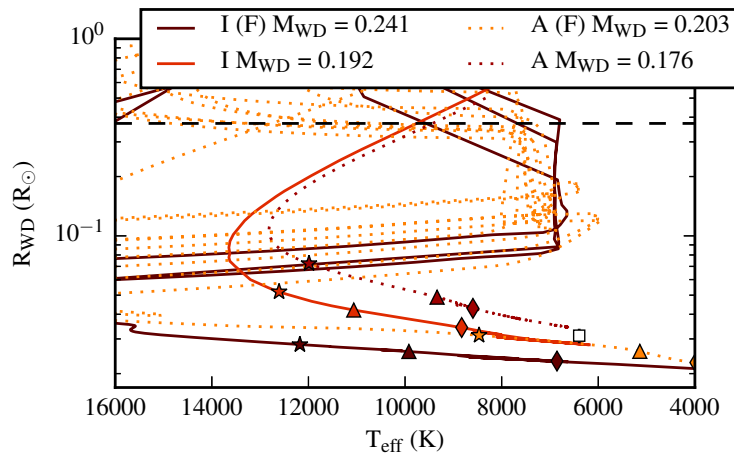
Figure 4.5: Cooling tracks for ELM white dwarfs, together with the radius and effective temperature of the cool low-mass white dwarf (square). The solid and dotted lines are evolutionary models from Istrate et al. (2014b, labelled I in the legend) and Althaus et al. (2013, labelled A) respectively. For each, a model with (labelled F) and without CNO flashes is included. The white dwarf masses are in $M_\odot$ as in the legend. The stars, triangles and diamonds indicate cooling ages of 1, 2.5 and 5 Gyr, respectively. The horizontal dashed line indicates the size of the ELM white dwarf's Roche lobe in the current binary configuration.

low-mass white dwarf formed first.

Fig. 4.5 shows a larger area of the same parameter space as shown in Fig. 4.4, now also including ELM white dwarf cooling models from Althaus et al. (2013). It is clear from this figure that the ELM white dwarf in SDSS J1257+5428 has settled on the cooling track and is not currently in a CNO flash cycle. Only ELM white dwarfs that exceed a certain mass experience CNO flashes, during which the thick hydrogen layer is quickly consumed, thereby speeding up the entire cooling process. The upper limit of 0.24 $M_\odot$ found for the ELM white dwarf in SDSS J1257+5428 is just above the minimum mass of 0.18 $M_\odot$ (Althaus et al., 2013) – 0.20 $M_\odot$ (Istrate et al., 2014b) necessary for cooling with CNO flashes.

As demonstrated in Figs. 4.4 and 4.5, the age of the primary white dwarf estimated from current cooling models is very sensitive to both its mass and the degree of element diffusion. The shortest possible cooling age for the ELM white dwarf is given by a model from Althaus et al. (2013), in which the white dwarf is formed with a mass of 0.203 $M_\odot$, experiences CNO flashes, and takes 1.6 Gyr to reach a temperature of 6400 K. The difference in cooling ages between the Istrate et al. (2014b) and Althaus et al. (2013) models are most likely related to the amount of element diffusion (for example, via gravitational settling and radiative levitation, Althaus et al. 2001). The former models are calculated with gravitational settling, whereas the latter models do not include this effect. In addition, the treatment of convection may play a role. Finally, long-term helium white dwarf cooling (beyond the proto-white dwarf stage) could also be affected by rotation of the white dwarf, which might lead to significant mixing and thus prevention of strong element diffusion. New models investigating these issues are currently in progress (Istrate et al., in prep).

The shorter cooling age of Althaus et al. (2013) is still too long to resolve the paradox of the formation of this binary. The 1.6 Gyr is compounded by the time the ELM white dwarf took to form, since its progenitor most likely had a mass < 1.6 M$_\odot$ (Istrate et al., 2014a), and thus had a main-sequence lifetime of order 1.5 Gyr (Hurley et al., 2000), which needs to be added to the white dwarf cooling age to estimate its total age. Therefore it appears impossible to avoid the conclusion that the ELM white dwarf is older than its massive white dwarf companion.

4.4.3   Distance to SDSS J1257+5428

Using the results for the scale factor, the radius ratio and the secondary radius from my MCMC analysis, the distance can be calculated via $d = R_1\sqrt{4\pi/s}$ and becomes $d = 105 \pm 8$ pc. This is consistent with the distance derived using the parallax measurements, where $d = 112^{+20}_{-15}$ pc, as presented in Sect. 4.2.2, indicating that the analysis presented in this chapter is sensible. At this point I could redo my analysis and include a prior on the distance, based on the parallax observations. However, given that the uncertainty on my current result is smaller than that from the parallax measurements, the prior would have little effect. Given furthermore that the scale factor s does not correlate significantly with any of the other free parameters, the values of these free parameters would change little and so I refrain from reanalysing the data.

4.5   Discussion

The combined results of the HST data and evolutionary models for low-mass white dwarfs present an intriguing puzzle. The secondary white dwarf has a mass just over 1 M$_\odot$, which is near the threshold separating white dwarfs with a chemical core-composition of carbon/oxygen from those with oxygen/neon dominated cores (Lazarus et al., 2014). If it was an isolated star, I could use an initial-final mass relation to obtain an initial zero-age main sequence mass of $5 - 6$ M$_\odot$ (Catalán et al., 2008a), for which main-sequence lifetimes are close to 100 Myr (Hurley et al., 2000). In close binaries the initial masses are often greater than those predicted from initial-final mass relations due to interactions between the stars, and so these numbers have to be considered cautiously. Nonetheless, together with the cooling age of 1.0 Gyr, it allows an estimate to be made for the total age of the hot, massive white dwarf as 1.1 ± 0.1 Gyr. The low temperature of the primary, low-mass white dwarf combined with evolutionary models shows that the age of the primary white dwarf is at least $\sim 1.6 - 5$ Gyr. Given the 1.6 M$_\odot$ maximum progenitor mass, its total age is $\gtrsim 3$ Gyr.

I considered whether the cooling age of the massive white dwarf could have been reset by accretion heating during the formation of the ELM white dwarf companion. However, this would imply that its cooling age would now be the same or longer (if only partially reset) than that of the ELM white dwarf, which does not explain the observations. There should be accretion after the birth of the ELM white dwarf during the CNO flashes as the

white dwarf fills its Roche lobe (see Fig. 4.5). However, these events are very short lived (~ 100 yr) and cannot significantly alter the thermal structure of the massive white dwarf, which takes $\sim 10^6$ yr to change (Bildsten et al., 2006).

A more exotic possibility is that the massive white dwarf formed out of a merger of two white dwarfs roughly 1 Gyr ago, and 4 Gyr after the formation of the ELM white dwarf. The pair had to form well before the ELM white dwarf and therefore survive at least 4 Gyr before merging. Considerations of dynamical stability (Eggleton et al., 1989) show that if the outer period of this hypothetical triple matched today's 4.6 h period the inner period would have had to have been < 1 h. This would result in a merger timescale well short of the 4 Gyr minimum. Therefore the triple scenario also requires shrinkage of the outermost orbit, which implies that the merger was a common-envelope event that shrunk both the inner binary and the outer binary / ELM white dwarf orbit. I cannot say whether this is impossible, but it seems unlikely; simulations of white dwarf mergers seem to show that the merged object does not expand significantly (Shen et al., 2012; Dan et al., 2011). If anything, one might expect that angular momentum from the merged pair would be transferred to the outermost orbit, resulting in a period increase, not the necessary decrease. Even if the proposed scenario is possible, it is hard to see how an initial configuration of a tight inner binary containing at least one carbon/oxygen white dwarf in a close triple with an ELM white dwarf could have formed.

Finally, it is possible that SDSS J1257+5428 is not a close double white dwarf, contrary to my assumption throughout the analysis presented in this chapter. As it has not been ruled out that the broad Balmer lines from the secondary massive white dwarf are stationary (Marsh et al., 2011; Kulkarni & van Kerkwijk, 2010), the system could be a triple or the massive white dwarf could be aligned per chance with the ELM WD binary. Perhaps the low-mass white dwarf is in a close binary with an unseen massive companion such as a neutron star, while the hotter, massive white dwarf is a wide companion. Recently, Ransom et al. (2014) discovered a triple system in the Galactic disk consisting of a neutron star and two white dwarfs, of which one is very low mass, and hence nature is apparently producing such triple compact star systems (Tauris & van den Heuvel, 2014). However, in this scenario the problem with the incompatible cooling ages and masses remains, unless the hot white dwarf was captured as the third component later on and did not form at the same time as the close binary. Such an unusual scenario is only likely within a dense stellar cluster environment. Inspection of the HST+STIS acquisition image reveals that the point-spread function from the source is consistent with being a point source, and so the stars would have to be extremely well aligned if it was a chance alignment. This is also an argument against the system being a wide triple, although a close multiple system with a separation $\lesssim 10$ AU at the time of the observations cannot be ruled out.

Irrespective of the above possibilities, any binary or triple system, in which both of the observed white dwarfs discussed in this chapter were formed, is difficult to reconcile with binary stellar evolution. This is mainly due to the fact that the progenitor star of the low-mass helium white dwarf most likely had a mass of $1 - 2$ M$_\odot$ (Istrate et al., 2014a),

and thus a much longer nuclear burning timescale than that of the $5 - 6$ M$_\odot$ progenitor of the ~ 1 M$_\odot$ secondary massive white dwarf.

Future observations to clarify the nature of SDSS J1257+5428 could include radio observations to search for a neutron star component, as well as phase-resolved spectroscopy to measure (or put an upper limit on) the radial velocity of the massive white dwarf. If such observations confirm the common binary nature of the two white dwarfs investigated here, it might be possible to use their measured masses, radii and temperatures to constrain binary evolution and white dwarf cooling models further.

4.6   Conclusions

I have analysed the spectral energy distribution of the double white dwarf SDSS J1257+5428, consisting of HST COS and STIS data and $ugriz$ flux measurements from SDSS. The effective temperature and surface gravity of the hot white dwarf are found to be $T_2 = 13030 \pm 70 \pm 150$ K and $\log g_2 = 8.73 \pm 0.05 \pm 0.05$. Evolutionary models show that this white dwarf has a mass of $M_2 = 1.06$ M$_\odot$ and a cooling age of $\tau_2 \simeq 1.0$ Gyr. The atmospheric parameters place the star inside the ZZ Ceti instability strip, but no pulsations were found with amplitudes exceeding 18 mmag at far-ultraviolet wavelengths or 14 mmag in the optical g' band.

The temperature for the cool white dwarf is $T_1 = 6400 \pm 37 \pm 50$ K, while its surface gravity is constrained to $\log g_1 \sim 6.0 - 6.5$ by the radius ratio, in turn constrained by the relative flux contributions of the two white dwarfs. This yields a best mass estimate of ≤ 0.24 M$_\odot$, in agreement with Marsh et al. (2011). Using evolutionary models I find that the age must be > 3 Gyrs, significantly longer than the 1.1 Gyr age of the hot white dwarf. The odd combination of both a higher temperature and a higher mass for the secondary white dwarf thus cannot be explained by substantial accretion during the time the primary white dwarf's progenitor evolved. The difference in cooling ages also rules out recent accretion-induced heating as the cause of the significant temperature difference between these two white dwarfs. Therefore the data surprisingly suggest that the low-mass progenitor of the primary white dwarf evolved before the high-mass progenitor of the secondary white dwarf, thus posing an interesting puzzle regarding their formation scenario.

★ ★ ★

Chapter 5

Eclipse timing of white dwarf binaries

5.1 Introduction

It has been known for quite some time now that certain binaries show apparent variations in their orbital periods (Green et al., 1978; Beavers et al., 1986; Horne et al., 1991; O'Donoghue et al., 2003; Schwope et al., 2001). For now, these are called apparent because the observed variations can not only reflect actual changes in the orbital periods, but also a varying distance to these binaries which may otherwise be fixed systems. It is as yet unclear what may cause these variations, although Applegate's mechanism and the presence of circumbinary planets are currently the main contending theories. The former is an example of a mechanism able to change the orbital period of a binary (through redistribution of angular momentum), while the latter causes a reflex motion of the binary around the common centre of mass of the system consisting of both the binary and the circumbinary planets (Irwin, 1959).

In the last few years the first circumbinary planets have been discovered around double main-sequence star binaries through transits in the light curves (Doyle et al., 2011; Welsh et al., 2012; Orosz et al., 2012a,b), leaving no doubt about the existence of planets in so-called P-type orbits (Dvorak, 1986). However, in close white dwarf binaries the primary star has evolved off the main-sequence, and the binary has gone through a common-envelope phase. This may have destroyed any planetary system present (Veras & Tout, 2012; Mustill et al., 2013), leaving it far from certain that planetary systems exist around white dwarf + main-sequence star binaries. On the other hand, circumbinary planets may be able to form again in a second phase of planet formation, triggered in the ejecta of the binary's common-envelope phase (Schleicher & Dreizler, 2014; Bear & Soker, 2014), and so it is not completely unlikely that some indeed exist.

Close monitoring of the eclipse times of individual binaries such as NN Ser (Marsh et al., 2014; Beuermann et al., 2014) and HU Aqr (Goździewski et al., 2012, 2015; Bours et al., 2014b, and see Chapter 6), to name two of the most popular systems, enables detailed studies of their eclipse timing variations. For some binaries it is possible to fit the eclipse times with models based on the assumption that circumbinary planets are present, but for most binaries such models have been refuted again by additional data (Parsons et al., 2010b; Bours et al., 2014b) or by detailed dynamical stability analyses (Hinse et al., 2012; Horner et al., 2012a; Wittenmyer et al., 2013). Applegate's mechanism, on the contrary, is somewhat more difficult to rule out, although arguments on energetic grounds can be

called upon (Brinkworth et al., 2006).

To complement the ongoing discussion, this chapter focuses on measuring eclipse times of a large number of close white dwarf binaries. Through regular observations, I hope to create a picture that shows which binaries display orbital period variations and how prominently these are present in certain categories of binaries. By expanding the empirical knowledge it may be possible to find such trends and clues, which can eventually reveal the underlying cause of the observed behaviour. Large surveys such as the Sloan Digital Sky Survey (SDSS, York et al., 2000) and the Catalina Sky Survey (CSS, Drake et al., 2009) have increased the number of known eclipsing white dwarf binaries significantly in recent years (Parsons et al., 2013b, 2015, see also Fig. 1.12). With this increase in sample size, it is now possible to perform long-term monitoring of an entire population of evolved binaries. Previous studies using smaller samples of binaries have already shown that almost all binaries that have been monitored for more than ~ 5 years show apparent orbital period variations (Zorotovic & Schreiber, 2013). The new, larger sample presented here is the first step towards revealing the extent and amplitude of eclipse timing variations throughout the class of white dwarf binaries. In addition, it will enable the systematic search for correlations between the amount of eclipse timing variability and characteristics of the systems such as orbital period, stellar spectral types and the Roche-lobe filling factor of the companion to the white dwarf.

In this chapter I will first introduce the binaries included in my eclipse timing programme, and then detail how I measure accurate eclipse times. The eclipse times and O-C diagrams for each individual binary are presented in Appendices A and B. The rest of this chapter is dedicated to finding trends in the behaviour of the eclipse timing variability for the group of binaries as a whole.

5.2   Targets & observations

5.2.1   Detached white dwarf binaries

This group consists of 60 targets in total, including 56 white dwarf + main-sequence star binaries, 1 white dwarf + brown dwarf binary and 3 double white dwarf binaries, all detached. The coordinates, best linear ephemerides and secondary star spectral types for these binaries are listed in Table 5.1.

5.2.2   Cataclysmic variables

This group of semi-detached white dwarf binaries includes 11 cataclysmic variable systems, of which 3 are polars in which the white dwarf is strongly magnetic and of which 1 has a brown dwarf donor star. See Table 5.2 for details of these binaries.

Although the erratic features in the light curves caused by the variable accretion rate in these systems complicate the determination of accurate eclipse times, their tendency to experience outbursts also means that some of these cataclysmic variables have first been discovered decades ago. Their eclipse observations therefore tend to span a much longer

baseline than those of the more-recently discovered detached binaries. This may be useful for revealing periodic variability of the eclipse times on decade time scales.

5.2.3   Observations

The eclipse observations presented in this thesis were taken over the last several years, using a number of telescopes and instruments. Mostly they were done with ULTRACAM on the William Herschel Telescope and the New Technology Telescope, ULTRASPEC on the Thai National Telescope and RISE on the Liverpool Telescope. For each binary in the timing programme, the number of new eclipse times are listed in Tables 5.1 and 5.2. The eclipse times themselves are listed in Appendix A for each binary. The tables in the appendix also include eclipse times from the literature, where available, for the purpose of completeness.

In total, the sample includes 605 new, previously unpublished eclipse times, ranging from 1 for some of the newer or very long-period white dwarf binaries up to $20 - 30$ for those binaries that were starting to show O-C variability and therefore justified close monitoring.

5.3   The O-C method

The method of timing a specific feature in the light curve of a star or binary and comparing this observed time to a predicted time based on model calculations is a validated approach that has been in use for decades. The residuals in the form of observed minus calculated (O-C) times can be used to investigate the evolution of the star or binary in which the feature that is being timed originates. This technique is a powerful tool for revealing behaviour that deviates from the assumed model, as such deviations will show up as non-zero residuals, although the accuracy depends on the accuracy with which the feature itself can be timed. This feature is generally a steady periodic phenomenon, such as the pulses emitted by a rapidly-rotating neutron star (Wolszczan & Frail, 1992; Wolszczan, 1994), eclipses in binary stars (Wood & Forbes, 1963; Parsons et al., 2010b; Hermes et al., 2012b; Lohr et al., 2014), or stellar pulsations (Silvotti et al., 2007; Mullally et al., 2008; Hermes et al., 2013b). Modelling these residuals can reveal the underlying process that causes them. Here, one can think of the presence of circumstellar or circumbinary planets, a change in orbital period due to angular momentum loss or redistribution through magnetic braking, gravitational wave emission or Applegate's mechanism, but also long-term evolutionary processes such as white dwarf cooling which affects pulsation periods and amplitudes.

In the rest of this chapter, I will use O-C diagrams of white dwarf eclipse times to search for deviations from a constant orbital period, by assuming a linear ephemeris that takes the form of

$$T = T_0 + P_{\mathrm{orb}}\, E \,, \tag{5.1}$$

for each binary. Here P_{orb} is the orbital period of the white dwarf binary, T_0 is the time at which the cycle number $E = 0$, and T is the time of a given orbital cycle E. The best

Table 5.1: List of all detached eclipsing white dwarf binaries included in the monitoring programme described in this chapter, sorted by RA. The SIMBAD identifier, frequently used alternative name and spectral type of the companion star to the white dwarf are given where available. The numbers in the parentheses of the zero-point and orbital period of the best linear ephemeris indicate the uncertainty in the last digits. Also listed are the number of new eclipse times presented in this chapter and a reference to the corresponding table in Appendix A and the O-C diagram in Appendix B.

White Dwarf binary		SpT$_2$	RA	Dec	best linear ephemeris		eclipse times		O-C
SIMBAD identifier	alternative name		(hours)	(degrees)	T$_0$ (BMJD$_{TDB}$)	P$_{orb}$ (days)	new	Table	diagram
-	SDSS J0024+1745	-	00:24:12.87	+17:45:31.4	53328.1893(10)	0.200038530(61)	2	A.2	-
SDSS J010623.01-001456.2	-	M8	01:06:22.99	−00:14:56.2	55059.0561216(13)	0.08501532934(13)	25	A.3	Fig B.1
SDSS J011009.09+132616.3	-	M4	01:10:09.09	+13:26:16.1	53993.9490871(11)	0.33268675465(23)	9	A.4	Fig B.2
SDSS J013851.49-001621.6	-	M5	01:38:51.54	−00:16:21.6	55867.0074052(68)	0.0727649563(51)	1	A.5	Fig B.3
PTF1 J015256.60+384413.4	-	M3	01:52:56.60	+38:44:13.4	56195.168443(21)	0.386120343(17)	6	A.6	Fig B.4
SDSS J025953.32-004400.2	-	M3	02:59:53.30	−00:44:00.2	51819.4150(10)	0.1441834(1)	1	A.7	-
SDSS J030308.35+005444.1	-	M4.5	03:03:08.35	+00:54:44.1	53991.1173057(16)	0.13443766659(12)	11	A.8	Fig B.5
SDSS J030856.55-005450.6	-	M4.5	03:08:56.55	−00:54:50.7	56181.143559(10)	0.185959421(15)	4	A.9	Fig B.6
WD 0312+019	-	K5-M5	03:14:52.11	+02:06:07.1	56195.20635076(86)	0.3052967628(20)	11	A.10	Fig B.7
NLTT 11748	-	WD	03:45:16.80	+17:48:09.1	55772.0413869(56)	0.2350604821(19)	13	A.11	Fig B.8
V471 Tau	-	K2	03:50:24.97	+17:14:47.4	54027.9530258(13)	0.521183431173(79)	1	A.12	Fig B.9
RR Cae	-	M4	04:21:05.53	−48:39:08.3	51522.54845119(51)	0.303703680025(46)	14	A.13	Fig B.10
SDSS J082145.27+455923.3	-	M2	08:21:45.27	+45:59:23.4	55989.038805(14)	0.509092031(11)	4	A.14	Fig B.11
SDSS J083845.86+191416.5	CSS 40190	M7	08:38:45.86	+19:14:16.5	53469.2201028(71)	0.13011231382(37)	13	A.15	Fig B.12
-	SDSS J0857+3318	-	08:57:13.26	+33:18:43.0	55957.1219144(22)	0.1060272754(20)	6	A.16	Fig B.13
SDSS J085746.18+034255.3	CSS 03170	M8	08:57:46.18	+03:42:55.3	55552.71276437(71)	0.06509653815(13)	14	A.17	Fig B.14
SDSS J090812.03+060421.2	CSS 080502	M4	09:08:12.04	+06:04:21.2	53466.3345100(31)	0.14943803757(20)	25	A.18	Fig B.15
SDSS J092741.73+332959.1	-	M3	09:27:41.73	+33:29:59.1	56074.906120(19)	2.308225594(62)	5	A.19	Fig B.16
-	SDSS J0935+2700	-	09:35:08.00	+27:00:49.2	56602.8394862(74)	0.201033495(12)	2	A.20	Fig B.17
SDSS J093947.95+325807.3	CSS 38094	M5	09:39:47.95	+32:58:07.3	55587.3088195(63)	0.3309896668(27)	5	A.21	Fig B.18
SDSS J094634.49+203003.3	-	M5	09:46:34.49	+20:30:03.4	56032.945627(20)	0.2528614510(81)	7	A.22	Fig B.19
SDSS J095719.24+234240.7	CSS 41631	M2	09:57:19.24	+23:42:40.7	55548.3570616(19)	0.15087078942(25)	11	A.23	Fig B.20
SDSS J095737.59+300136.5	-	M3	09:57:37.59	+30:01:36.5	56014.975114(32)	1.9261248(12)	1	A.24	-
SDSS J100559.10+224932.2	CSS 41177	WD	10:05:59.11	+22:49:32.3	55936.34467175(60)	0.11601543726(33)	12	A.25	Fig B.21

Table 5.1: Continues on next page.

Table 5.1: Continued from previous page.

White Dwarf binary		SpT$_2$	RA	Dec	best linear ephemeris		eclipse times		O-C
SIMBAD identifier	alternative name		(hours)	(degrees)	T$_0$ (BMJD$_{TDB}$)	P$_{orb}$ (days)	new	Table	diagram
-	SDSS J1013+2724	M4	10:13:56.32	+27:24:10.6	53831.125497(15)	0.12904038118(69)	7	A.26	Fig B.22
SDSS J102102.25+174439.9	-	M4	10:21:02.25	+17:44:39.9	56093.904987(48)	0.1403587476(72)	10	A.27	Fig B.23
SDSS J102857.78+093129.8	-	M3	10:28:57.78	+09:31:29.8	56001.0942705(63)	0.2350253014(17)	11	A.28	Fig B.24
SDSS J105756.93+130703.5	-	M5	10:57:56.93	+13:07:03.5	56010.062658(11)	0.1251621296(18)	7	A.29	Fig B.25
SDSS J112308.39-115559.2	-	M5	11:23:08.40	−11:55:59.3	56364.2935(5)	0.7691358(14)	1	A.30	-
SDSS J121010.13+334722.9	-	M5	12:10:10.13	+33:47:22.9	54923.0336021(27)	0.12448978061(22)	15	A.31	Fig B.26
SDSS J121258.25-012310.1	-	M4	12:12:58.25	−01:23:10.2	54104.2094389(67)	0.33587087803(97)	10	A.32	Fig B.27
SDSS J122339.61-005631.2	-	M6	12:23:39.61	−00:56:31.1	55707.0169889(53)	0.09007803092(72)	9	A.33	Fig B.28
SDSS J124432.25+101710.8	CSS 25601	M5	12:44:32.25	+10:17:10.8	53466.360374(99)	0.2278563704(67)	5	A.34	Fig B.29
SDSS J130733.49+215636.7	-	M4	13:07:33.49	+21:56:36.7	56007.221295(11)	0.2163223188(25)	8	A.35	Fig B.30
SDSS J132518.18+233808.0	CSS 21616	-	13:25:18.18	+23:38:07.9	55653.4541786(84)	0.1949589909(18)	3	A.36	Fig B.31
DE CVn	-	M3	13:26:53.26	+45:32:46.7	52784.0542113(16)	0.36413925967(29)	13	A.37	Fig B.32
SDSS J132925.21+123025.4	-	M8	13:29:25.21	+12:30:25.4	55271.05483050(64)	0.080966242504(71)	31	A.38	Fig B.33
WD 1333+005	-	M5	13:36:16.05	+00:17:31.9	55611.4766902(17)	0.12195875935(21)	21	A.39	Fig B.34
SDSS J134841.61+183410.5	CSS 21357	M4	13:48:41.61	+18:34:10.5	56000.1619200(46)	0.2484317827(15)	9	A.40	Fig B.35
QS Vir	-	M3	13:49:51.95	−13:13:37.5	48689.14216568(89)	0.150757467717(23)	19	A.41	Fig B.36
SDSS J140847.13+295045.0	-	M5	14:08:47.14	+29:50:44.9	53506.2885(5)	0.19179048(4)	1	A.42	-
SDSS J141057.73-020236.7	CSS 07125	M4	14:10:57.73	−02:02:36.7	53464.48883(11)	0.363497084(12)	7	A.43	Fig B.37
SDSS J141126.20+200911.1	CSS 21055	L7	14:11:26.20	+20:09:11.1	55991.3887187(16)	0.08453274990(21)	8	A.44	Fig B.38
SDSS J141134.70+102839.7	-	M3	14:11:34.70	+10:28:39.7	56031.172782(48)	0.167509605(33)	1	A.45	-
-	SDSS J1411+2117	M3	14:11:50.74	+21:17:50.0	55659.247710(43)	0.321636597(13)	4	A.46	Fig B.39
GK Vir	-	M4.5	14:15:36.41	+01:17:18.2	42543.3377168(24)	0.344330838779(72)	11	A.47	Fig B.40
SDSS J142355.06+240924.3	CSS 080408	M5	14:23:55.06	+24:09:24.3	55648.2061155(77)	0.3820042958(32)	7	A.48	Fig B.41
-	SDSS J1424+1124	-	14:24:27.69	+11:24:57.9	54264.282469(15)	0.2392935570(16)	5	A.49	Fig B.42
SDSS J143547.87+373338.5	-	M5	14:35:47.87	+37:33:38.5	54148.2051974(28)	0.12563096872(14)	20	A.50	Fig B.43
SDSS J145634.29+161137.7	CSS 09797	M5	14:56:34.30	+16:11:37.7	51665.78883(16)	0.2291202218(70)	2	A.51	-
-	SDSS J1540+3705	M4	15:40:57.27	+37:05:43.4	54913.41389(13)	0.261435560(19)	3	A.52	Fig B.44
SDSS J154846.00+405728.7	-	M6	15:48:46.00	+40:57:28.8	54592.073028(11)	0.1855152817(11)	4	A.53	Fig B.45

Table 5.1: Continues on next page.

Table 5.1: Continued from previous page.

| White Dwarf binary | | SpT$_2$ | RA | Dec | best linear ephemeris | | eclipse times | | O-C |
SIMBAD identifier	alternative name		(hours)	(degrees)	T$_0$ (BMJD$_{TDB}$)	P$_{orb}$ (days)	new	Table	diagram
NN Ser	-	M4	15:52:56.20	+12:54:47.2	47344.02526241(48)	0.1300801255927(85)	9	A.54	Fig B.46
-	SDSS J1642-0634	-	16:42:35.97	−06:34:39.7	54921.4933(5)	0.28688689(8)	1	A.55	-
GALEX J171708.5+675712	-	WD	17:17:08.50	+67:57:12.0	55641.431591(45)	0.246135443(15)	1	A.56	Fig B.47
RX J2130.6+4710	-	M3.5	21:30:18.60	+47:10:08.0	52785.18265363(96)	0.52103620576(19)	12	A.57	Fig B.48
-	SDSS J2205-0622	M2	22:05:04.51	−06:22:48.4	54453.078152(41)	0.1323869056(30)	8	A.58	Fig B.49
SDSS J220823.66-011534.2	CSS 09704	M4	22:08:23.66	−01:15:34.1	56175.8795317(18)	0.1565056979(11)	8	A.59	Fig B.50
SDSS J223530.61+142855.0	-	M4	22:35:30.61	+14:28:55.1	55469.0654236(54)	0.1444567649(11)	6	A.60	Fig B.51
-	SDSS J2306-0555	-	23:06:27.54	−00:55:53.3	55509.1090(7)	0.20008319(6)	1	A.61	-

Table 5.2: List of all semi-detached eclipsing white dwarf binaries (cataclysmic variables) included in the monitoring programme described in this chapter, sorted by RA. The SIMBAD identifier, frequently used alternative name and spectral type of the companion star to the white dwarf are given where available, with a star (*) indicating polars in which the white dwarf is strongly magnetic. The numbers in the parentheses of the zero-point and orbital period of the best linear ephemeris indicate the uncertainty in the last digits. Also listed are the number of new eclipse times presented in this chapter and a reference to the corresponding table in Appendix A and the O-C diagram in Appendix B.

White Dwarf binary		SpT$_2$	RA	Dec	best linear ephemeris		eclipse times		O-C
SIMBAD identifier	alternative name		(hours)	(degrees)	T$_0$ (BMJD$_{TDB}$)	P$_{orb}$ (days)	new	Table	diagram
HT Cas	-	M5.4	01:10:13.13	+60:04:35.4	43727.4406673(64)	0.073647179179(39)	17	A.62	Fig B.52
*FL Cet	-	M5.5	01:55:43.43	+00:28:07.5	52968.8229202(26)	0.060516322636(47)	8	A.63	Fig B.53
GY Cnc	-	M3	09:09:50.55	+18:49:47.5	51581.331857(51)	0.1754424342(20)	17	A.64	Fig B.54
SDSS J103533.02+055158.3	-	BD	10:35:33.03	+05:51:58.4	55353.9524405(17)	0.057006671891(87)	7	A.65	Fig B.55
NZ Boo	-	-	15:02:40.98	+33:34:23.9	53799.1406162(12)	0.058909481462(40)	5	A.66	Fig B.56
SDSS J170213.24+322954.1	-	M0	17:02:13.25	+32:29:54.1	53647.7369887(17)	0.10008221504(10)	13	A.67	Fig B.57
*V2301 Oph	-	M5.5	18:00:35.53	+08:10:13.9	48070.525362(29)	0.07844998073(30)	16	A.68	Fig B.58
EP Dra	-	-	19:07:06.16	+69:08:44.0	47681.22690(13)	0.0726563174(11)	10	A.69	Fig B.59
V713 Cep	-	-	20:46:38.70	+60:38:02.8	54337.8766084(68)	0.08541851134(31)	9	A.70	Fig B.60
*HU Aqr	-	M4.3	21:07:58.19	−05:17:40.5	49102.42059625(52)	0.0868203938170(75)	2	A.71	Fig B.61
SDSS J214140.43+050730.0	-	-	21:41:40.43	+05:07:29.9	56214.9541055(15)	0.054691827(58)	3	A.72	Fig B.62
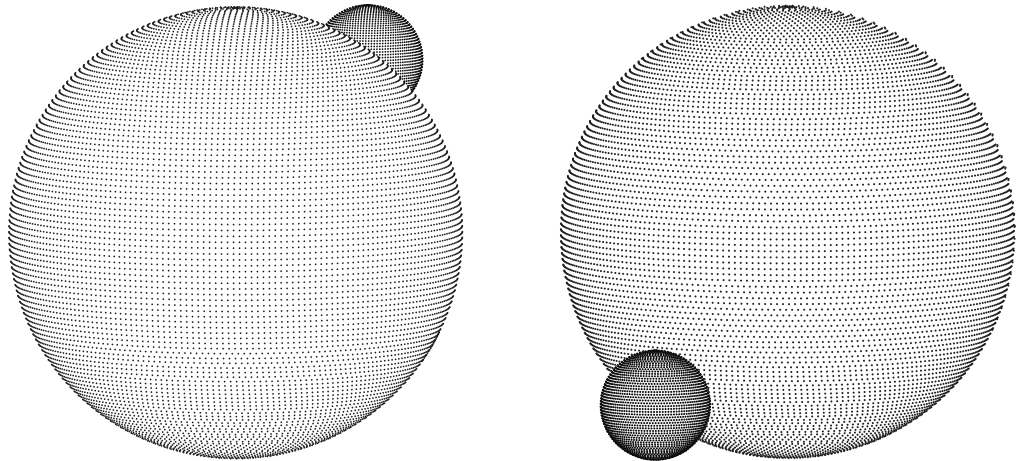
Figure 5.1: Visualisation of the white dwarf and M-dwarf in SDSS J1435+3733 as used in `lcurve`. See Fig. 5.2 for the eclipse light curve. *Left:* at orbital phase $\phi = 0.988$, when the white dwarf is partially eclipsed by the M-dwarf. *Right:* half an orbital phase later, at $\phi = 1.488$, when the M-dwarf is partially eclipsed by the white dwarf.

linear ephemerides for the targets in my timing programme are listed in Tables 5.1 and 5.2, and were calculated using a linear least-squares approach to minimise the residuals.

5.4 Measuring eclipse times

5.4.1 Detached binaries − `lcurve`

For the detached binaries I use the program `lcurve`[1] to measure mid-eclipse times. Here follows a brief description of `lcurve`, and details can also be found in Pyrzas et al. (2009) and Copperwheat et al. (2010). `lcurve` is designed to model short-period white dwarf + main-sequence star binaries, in which the latter can be deformed because it is close to its maximum size, its Roche lobe. The program computes the model light curve by linearly adding the flux from the visible faces of the limb-darkened stars, both of which are subdivided into grid segments, as illustrated in Fig. 5.1. The density of the grid can easily be set by parameters in a model file, and can be larger for certain orbital phases and smaller for the remainder of the orbit. This is particularly useful for modelling eclipses, because one can use a fine grid to calculate the model light curve near an eclipse and a coarser grid at other orbital phases to avoid unnecessarily slow model calculations. The limb-darkening can be specified by the use of a polynomial of up to fourth order, or by the four-parameter law from Claret (2000). Coefficients for the white dwarfs are taken from Gianninas et al. (2013), and those for late main-sequence stars from Claret & Bloemen (2011).

   `lcurve` can account for eclipses and reprocessed light from the white dwarf by the

---

[1] The `lcurve` package was written by T. R. Marsh; for more information see *http://www.warwick.ac.uk/go/trmarsh/software.*
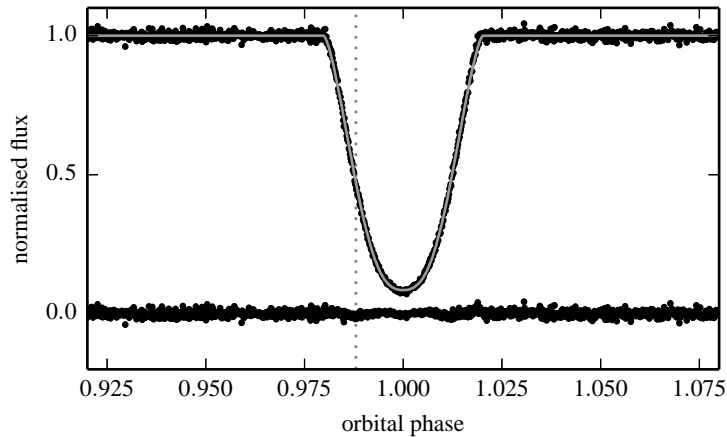
Figure 5.2: ULTRACAM g′-band eclipse and `lcurve` model of SDSS 1435+3733, as well as the residuals. The vertical grey dotted line is drawn at orbital phase 0.988; see the left-hand side of Fig. 5.1 for a visualisation of the binary at this phase.

M-dwarf (reflection effect, see Fig. 1.13). The latter is included using the approximation

$$\sigma T_{\mathrm{MS}}'^{4} = \sigma T_{\mathrm{MS}}^{4} + A\, F_{\mathrm{irr}}\,, \tag{5.2}$$

with σ the Stefan-Boltzmann constant, T_{MS} the effective temperature of the unirradiated main-sequence star and T_{MS}' the modified temperature due to the fraction A of the irradiating flux F_{irr} from the white dwarf, accounting for the distance between the two stars and the angle of incidence.

In addition it is possible to include gravitational lensing (Marsh, 2001) and the effect of gravity darkening for each star. The latter becomes important for significantly Roche-distorted stars and for those stars that are rapidly rotating, and is generally fixed at the representative value of 0.6 for ease of use, although it does vary with stellar temperature, surface gravity and wavelength (Claret & Bloemen, 2011). Doppler beaming can be included as well, for which `lcurve` calculates the observed flux in a given passband F_λ by modifying the emitted flux $F_{\lambda,0}$ by

$$F_\lambda = F_{\lambda,0}\Big(1 - B\,\frac{v_r}{c}\Big)\,, \tag{5.3}$$

with the spectrum-dependent beaming factor $B = 5 + \mathrm{d}(\ln F_\lambda)/\mathrm{d}(\ln \lambda)$ (Loeb & Gaudi, 2003) equivalent to the factor $(3 - \alpha)$ in the standard beaming formula, and v_r the radial velocity of the star, which is defined to be positive when the star moves away from the observer. The bandpass-integrated beaming factors to be included in the `lcurve` model file can be calculated separately with the use of model spectra through

$$\langle B \rangle = \frac{\int S_\lambda \lambda F_\lambda B d\lambda}{\int S_\lambda \lambda F_\lambda d\lambda}\,, \tag{5.4}$$

where S_λ is the response function of the filter, instrument and telescope used to obtain the

observations.

The centre of the primary, white dwarf eclipse is defined as orbital phase $\phi = 0$. A slight offset δ of the secondary eclipse from orbital phase $\phi = 0.5$ can be included as well, to account for an eccentricity or Rømer delay in the binary orbit (Kaplan, 2010), so that

$$\phi' = \phi + \frac{\delta}{2P_{\mathrm{orb}}}\left(\cos(2\pi\phi) - 1\right). \tag{5.5}$$

Finally, an overall linear, quadratic and/or cubic trend can be added, to account for long-term effects caused by, for example, varying airmass during the observations.

When modelling light curves of semi-detached binaries, it is possible to include an accretion disc around the white dwarf and a bright spot on that disc, as well as a hot or cold spot on the surface of either star. These options will not be used for the analyses presented here since I am only considering detached white dwarf binaries at the moment, but I will use a model including a hot spot on the surface of a white dwarf in Chapter 6.

`lcurve` includes two optimisation algorithms, `simplex` and `levmarq`. The simplex method is a robust routine that always moves downhill in χ^2-space, searching for the minimum value. The Levenberg-Marquardt minimisation method is somewhat more complex, but has the advantage of returning reliable uncertainty estimates of the free model parameters once the model has converged. Both methods are susceptible to issues caused by degeneracies in the model and may as a result thereof become stuck in a local χ^2 minimum, rather than find the global minimum. A great help in determining whether a model returned by `simplex` or `levmarq` fits the data well is looking at the resulting light curve model with respect to the data, as shown in Fig. 5.2.

The most important parameters in the `lcurve` models are summarised in Table 5.3. For an example of a detailed study of an eclipsing binary that includes a reflection effect, ellipsoidal modulation, gravitational lensing and Doppler beaming, see Bloemen et al. (2011).

Once a good model is found, subsequent fits of new eclipse data only require as free parameters the mid-eclipse time t_{mid} and the secondary star's temperature T_2 to obtain a good fit. By not optimising every parameter for every individual data set one avoids ending up with highly degenerate models and overly large uncertainty estimates.

5.4.2 Semi-detached binaries

Measuring eclipse times for semi-detached binaries is complicated by the inherent flickering in the light curves of these systems, which is caused by the varying accretion rate. On top of this, there are additional features near a white dwarf eclipse caused by the eclipse of the accretion disc and bright spot in non-magnetic systems and intermediate polars, and of the hot spot on the white dwarf's surface in polars. Therefore I chose a different approach to measure mid-ingress and/or mid-egress times of the white dwarf eclipses in these systems.

The ingress and egress of the white dwarf eclipse are fit by a least-squares approach

Table 5.3: Parameters in `lcurve` models used to model light curves of detached white dwarf binaries. Additionally, four parameters that can be used to model a hot spot on the surface of the white dwarf are included, because I will use this option in Chapter 6.

parameter	details
i	orbital inclination
q	mass ratio: M_2/M_1
$r_{1,2}$	$R_{1,2}/a$, stellar radius relative to the semi-major axis a along the line of centres of the two stars
$T_{1,2}$	unirradiated stellar effective temperature
v_s	sum of the unprojected orbital speeds, so that $v_s \sin i = K_1 + K_2$
$l_{1,2,i}$	up to four coefficients for polynomial or Claret limb-darkening
t_{mid}	mid-eclipse time of primary eclipse
P_{orb}	orbital period
$b_{1,2}$	beaming factors
$g_{1,2}$	gravity-darkening coefficients
A	fraction of the irradiated flux from star 1 by star 2
$n^c_{1,2}$	number of coarse grid points
$n^f_{1,2}$	number of fine grid points, used at orbital phases near eclipse
w	wavelength at which the model light curve has to be computed
$limb_{1,2}$	set to 'Claret' or 'Poly' to set the limb-darkening law used
S_{long}	longitude of a spot on the star's surface
S_{lat}	latitude of a spot on the star's surface
S_{FWHM}	full-width at half-maximum of the spot, as seen from the star's centre
S_T	central temperature of the spot

using a function that is composed of a sigmoid and a straight line,

$$y = \frac{k_1}{1 + e^{-k_2(x-k_3)}} + k_4 + k_5(x - k_3)\,, \tag{5.6}$$

where x and y are the time and flux measurements of the light curve, and k_1 to k_5 are coefficients of the fit.

The straight line part allows fitting the overall trend outside and during ingress and egress. This includes the ingress and egress of the white dwarf itself, which can have a significant contribution, especially when the entire system is in a low state. The sigmoid part of the function fits any sharp features that may be created by the accretion stream or spot. To determine uncertainties, these fits are performed in a Monte Carlo manner in which the values of the data points are perturbed based on their uncertainties and the number of included data points are varied by a few at each edge, thereby reducing any strong effects in the results caused by single data points. An example of good fits to a white dwarf ingress and egress feature used to calculate a mid-eclipse time is shown in Fig. 5.3.
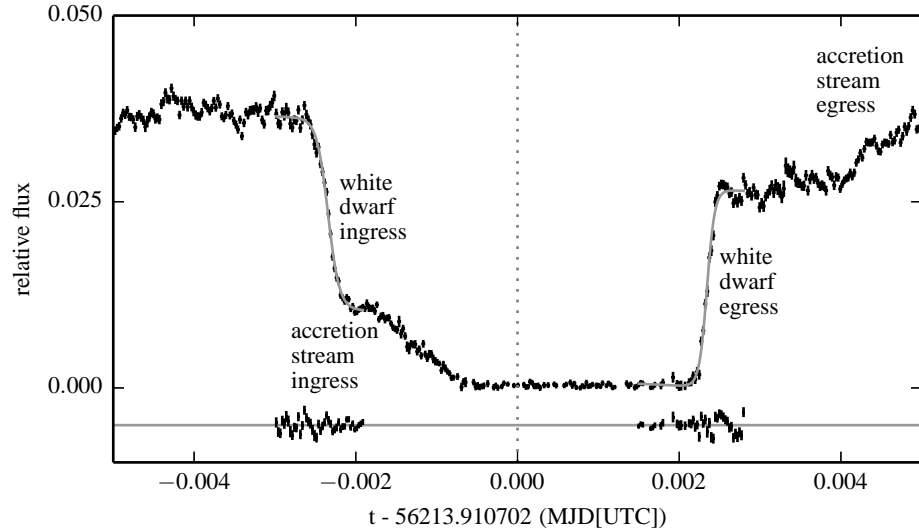
Figure 5.3: ULTRACAM g′-band eclipse light curve of the polar EP Dra, with sigmoid+linear fits to the ingress and egress of the white dwarf (grey lines). Immediately after the white dwarf ingress is the ingress of the accretion stream, and at the far right the start of the egress of the accretion stream can be seen. The vertical dotted line indicates mid-eclipse. The residuals of the fits are shown at the bottom, vertically offset by -0.005.

5.5 Trends in eclipse time variations

While it can be difficult to confidently determine the cause of eclipse time variations in a given binary, I may be able to say something about the principal mechanism at work in these binaries by searching for trends in a large set of binaries. First of all, I explore whether a correlation exists between the amount of observed O-C variations and the baseline of the eclipse observations. Such a correlation would indicate that my data set is still too limited to draw robust conclusions.

If this is not the case, and for those binaries that have longer baselines, I may be able to find a hint of the underlying cause of the eclipse timing variations. A correlation between the amount of O-C variability and either the secondary star's spectral type or the secondary star's Roche lobe filling factor could indicate that a form of Applegate's mechanism is at work. In particular, with increasing spectral type, from M0 to M8 and into the brown dwarf regime, Applegate's mechanism is expected to become less effective. Therefore the O-C variations should become less pronounced, if not completely disappear. For double white dwarf binaries I expect to see no orbital period variations, because white dwarfs are not thought to experience magnetic cyclic behaviour, and therefore cannot drive orbital period variations of the kind in the Applegate and Lanza mechanisms (Applegate, 1992; Lanza et al., 1998; Lanza, 2006).

In the event that the observed behaviour is caused by the presence of circumbinary planets, it is likely that there is no particular correlation present. This is because circumbinary planets can, in principle, form around a wide variety of binaries, and so there is
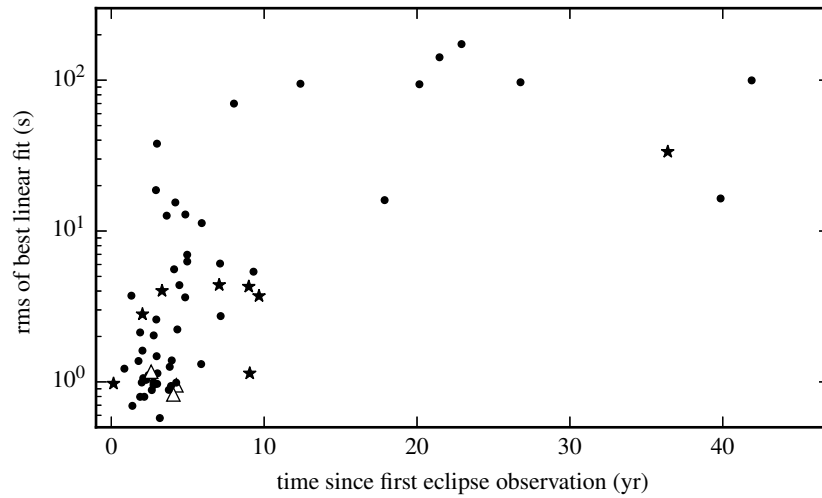
Figure 5.4: Measure of the extent of eclipse timing variations with respect to a linear ephemeris (RMS in seconds) as a function of the baseline of the observations. Binaries with at least three eclipse time measurements have been included. The triangle, circle and star symbols represent detached double white dwarf binaries, other detached binaries and cataclysmic variables respectively.

no reason for them to be present preferentially around certain types of binaries. However, if circumbinary planets are indeed present, one has to be able to fit the O-C residuals with models of circumbinary planetary systems, which, in addition, have to be dynamically stable (Marsh et al., 2014). For a number of close white dwarf binaries it is already known that such a planetary system cannot explain the observed O-C variability (Hinse et al., 2012; Horner et al., 2012a; Wittenmyer et al., 2013).

5.5.1   Baseline of observations

An attempt to quantify the amount of eclipse timing variations as a function of the baseline of the observations for the various binaries is shown in Fig. 5.4. Here, the root mean square (RMS) of the residuals is calculated using the standard formula,

$$\text{RMS} = \frac{1}{N} \sum_i \left(\frac{y_i - y(x_i)}{\sigma_i} \right)^2 , \tag{5.7}$$

in which x_i, y_i and σ_i are the cycle number, eclipse time and uncertainty in the eclipse time and y is the best linear fit to these N data points. Fig. 5.4 shows the RMS values for each binary as a function of the total baseline that the eclipse observations for the given binary span. It appears that the RMS saturates at a value near 100, although the log-scale of the plot enhances this feature beyond what the data show. Nevertheless, the figure indicates that any binary with eclipse observations spanning at least 10 years is extremely likely to show significant residuals in the O-C eclipse times.

This idea is reinforced by Fig. 5.5, which, in addition to the points in Fig. 5.4, also shows the RMS values of intermediate sets of eclipse times in grey. These intermediate RMS
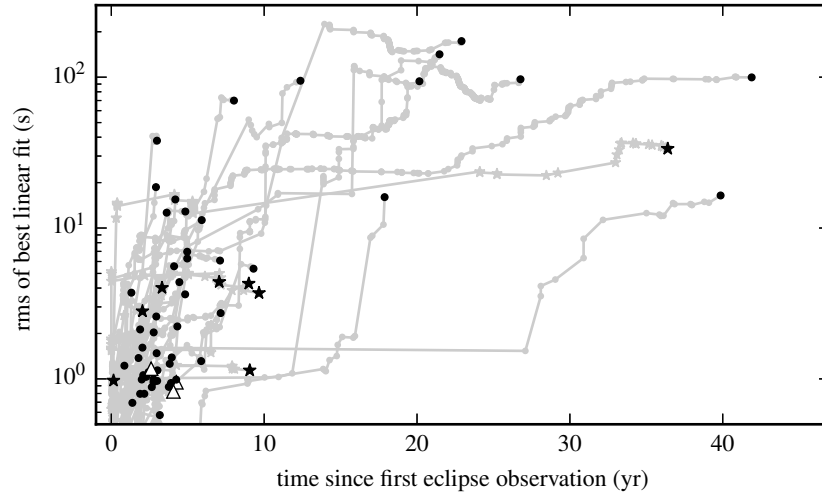
Figure 5.5: Measure of the extent of eclipse timing variations with respect to a linear ephemeris (RMS in seconds) as a function of the baseline of the observations, starting with the first three eclipse times and subsequently increasing the number of data points included by one for the next RMS calculation. See the text for more details. The triangle, circle and star symbols represent detached double white dwarf binaries, other detached binaries and cataclysmic variables respectively.

values are calculated using an integer number of eclipse times, starting with the first three, increasing by one with each step, and calculating the best linear ephemeris and matching RMS for these sets of eclipse times. The one clear exception to the general trend is GK Vir, which continues at an RMS close to 1, until the baseline of the observations reaches ~ 27 years. However, this behaviour is caused by the extremely large gap of nearly the same duration in the eclipse observations, as can also be clearly seen in the corresponding O-C diagram in Fig. B.40, rather than by an actual feature of the data.

It appears that the baseline of the eclipse observations is indeed quite an important factor in determining whether or not O-C variations are present. Although not unexpected, the long minimum baseline of ~ 10 years required means that a lot of data needs to be acquired before robust general conclusions can be drawn. This is particularly important because mixing short and long baselines may work to obscure trends in the data.

5.5.2   Companion's spectral type & Roche lobe filling factor

There are two good indicators that can point towards it being Applegate's mechanism, or a variation thereof, that is causing the orbital period variations observed in many close binary systems. The first is the spectral type of the companion star to the white dwarf. Because Applegate's mechanism is driven by magnetic cycles in this companion, and because magnetic activity decreases towards later spectral types, a correlation between the spectral type and amount of O-C variations is to be expected. In addition, the spectral type of a star strongly correlates with its mass, and because the star's luminosity depends strongly on the mass, as $L \propto M^5$. Therefore we expect a strong correlation between the secondary star's spectral type and the amount of O-C variations.
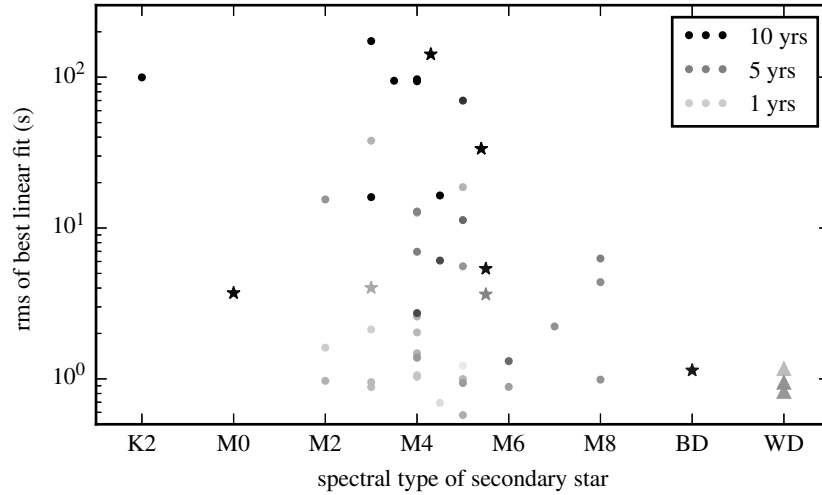
Figure 5.6: Measure of the extent of eclipse timing variations with respect to the best linear ephemeris (RMS in seconds) as a function of the secondary star's spectral type. The grey scale corresponds to the baseline of the eclipse observations, with white for 0 yrs and black for 10 yrs as indicated in the legend. All binaries with a baseline exceeding 10 yrs are plotted in black to avoid excessive stretching of the grey scale. The triangle, circle and star symbols represent detached double white dwarf binaries, other detached binaries and cataclysmic variables respectively.

To search for such a correlation, Fig. 5.6 shows the RMS of the eclipse time residuals with respect to the best linear ephemeris as a function of the secondary star's spectral type. In addition, the grey scale indicates the length of the baseline of the eclipse time observations, which continues to be an important factor.

It appears that there is indeed some correlation present. Binaries with secondaries of spectral type M6 – M8, brown dwarfs or white dwarfs evidently have smaller RMS values, indicating that they show less O-C variability. However, only one of these binaries has a baseline exceeding ~ 5 years. This is SDSS J1035+0551, a cataclysmic variable with a brown dwarf donor, see also Fig. B.55 and Littlefair et al. (2006).

The second indicator for which I expect to see a correlation with the O-C variability if Applegate's mechanism is at work, is the Roche lobe filling factor of the secondary star. This is mainly due to the fact that tidal forces are more effective for stars that are large relative to the binary's orbit, or, equivalently, the star's own Roche lobe. Therefore any change in gravitational quadrupole moment of these stars couples more easily to the binary's orbit in binaries in which the secondary stars have larger Roche lobe filling factors.

The Roche lobe filling factor is defined as the radius of the secondary star divided by the radius of the secondary star's Roche lobe: R_{MS}/R_L. To calculate the latter, I use Eq. 1.8, for which the mass-ratio q is required. Those detached white dwarf binaries that have accurate measurements of the stellar radial velocity amplitudes, and therefore of $q = K_{WD}/K_{MS}$, are listed in Table 5.4. Note that R_L is the radius of a sphere with approximately the same volume as the star's Roche lobe. Therefore, where possible, I used the volume-averaged radius for the secondary star as well to calculate the Roche lobe filling
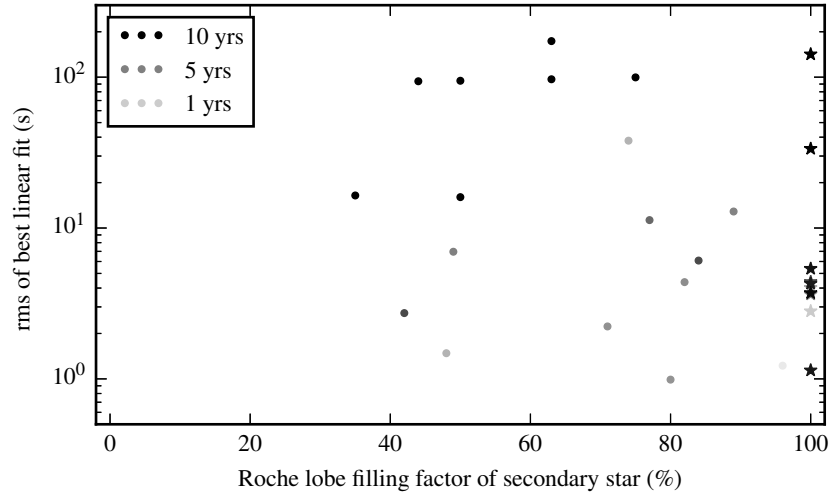
Figure 5.7: Measure of the extent of eclipse timing variations with respect to the best linear ephemeris (RMS in seconds) as a function of the secondary star's Roche lobe filling factor. For cataclysmic variables this value is set to 100%, since the secondaries completely fill their Roche lobes in these binaries. See Table 5.4 for details on the Roche lobe filling factors for the detached binaries. The grey scale corresponds to the baseline of the eclipse observations, with white for 0 yrs and black for ≥ 10 yrs. The triangle, circle and star symbols represent detached double white dwarf binaries, other detached binaries and cataclysmic variables respectively.

factor.

Fig. 5.7 shows the RMS values of the eclipse time residuals with respect to the best linear ephemeris as a function of the Roche lobe filling factor, expressed in %. The figure includes the binaries listed in Table 5.4, as well as all cataclysmic variables, for which I have set $R_{MS}/R_L = 100\%$, since the secondaries in these binaries fill their Roche lobes. As before, the grey scale indicates the length of the baseline of the eclipse observations. Besides the obvious influence of the observational baseline on the RMS values, there is apparently no correlation between the Roche lobe filling factor and those RMS values. Perhaps with an increased sample size and with a baseline closer to ~ 10 yrs for each binary, such a correlation will become discernible.

An alternative way of looking at the effects just described is shown in Figs. 5.8 and 5.9, where small thumbnails of O-C diagrams are ordered by baseline of the eclipse observations and secondary star's spectral type respectively. These figures reinforce what was seen before, namely that I am limited by the baseline of the observations.

Table 5.4: Roche lobe filling factors for those detached white dwarf binaries in the eclipse timing programme that have secure measurements of the radial velocity amplitudes and/or mass ratio, and the secondary star's radius. Note that because $R_{\rm L}$ is the radius of a sphere with the same volume as the star's Roche lobe, we have adopted the volume averaged radius for $R_{\rm ms}$ where possible. References and/or important notes are given in the footnotes. The first column is a simple ID number and the second indicates the eclipse timing coverage in years. See also Fig. 5.7.

ID	yr	white dwarf binary	$K_{\rm wd}$ (km/s)	$K_{\rm ms}$ (km/s)	$q = K_{\rm wd}/K_{\rm ms}$	$R_{\rm L}/a$	$R_{\rm ms}/a$	$R_{\rm ms}/R_{\rm L}$	SpT$_{\rm ms}$
1	4	SDSS J010623.01-001456.2	92 ± 3 [1]	328 ± 3 [1]	0.280 ± 0.009	0.28 ± 0.04	0.23 ± 0.01 [7,a]	0.82 ± 0.12	M6 ± 1 [1]
2	6	SDSS J011009.09+132616.3	73 ± 1 [1]	191 ± 1 [1]	0.382 ± 0.005	0.300 ± 0.009	0.127 ± 0.002 [7,a]	0.42 ± 0.01	M4.5 ± 0.5 [1]
3	1	SDSS J013851.49-001621.6	86.5 ± 1.0 [2]	346.7 ± 2.3 [2]	0.249 ± 0.003	0.27 ± 0.02	0.258 ± 0.002 [2,a]	0.96 ± 0.07	M5 ± 1 [2]
4	7	SDSS J030308.35+005444.1	-	339.9 ± 0.3 [3]	0.23 ± 0.01 [3]	0.26 ± 0.07	0.219 ± 0.003 [3,a]	0.84 ± 0.23	M4.5 - M5 [3]
5	42	V471 Tau	164 ± 4 [4]	148.5 ± 0.6 [5]	1.10 ± 0.03	0.387 ± 0.001	0.29 ± 0.01 [4]	0.75 ± 0.03	K2 [4]
6	20	RR Cae	73.2 ± 0.4 [1]	194.8 ± 0.1 [1]	0.376 ± 0.002	0.298 ± 0.004	0.1298 ± 0.0009 [7,a]	0.44 ± 0.01	M4 ± 1 [1]
7	4	CSS 40190	81 ± 5 [1]	275.9 ± 0.9 [1]	0.29 ± 0.02	0.28 ± 0.07	0.198 ± 0.003 [7,a]	0.71 ± 0.18	M5.0 ± 0.5 [1]
8	4	SDSS J085746.18+034255.3	64 ± 6 [6]	364 - 398 [6]	0.17 ± 0.02	0.24 ± 0.33	0.191 ± 0.009 [6]	0.80 ± 1.09	M8 ± 1 [6]
9	5	CSS 080502	154 ± 1 [1]	215.3 ± 0.4 [1]	0.715 ± 0.004	0.350 ± 0.001	0.311 ± 0.004 [7,a]	0.89 ± 0.01	M3.5 ± 0.5 [1]
10	3	SDSS J102857.78+093129.8	167 ± 1 [1]	164.7 ± 0.5 [1]	1.014 ± 0.007	0.3801 ± 0.0004	0.282 ± 0.004 [7,a]	0.74 ± 0.01	M2.5 ± 0.5 [1]
11	0	SDSS J112308.39-115559.2	72 ± 1 [1]	151.2 ± 0.2 [1]	0.476 ± 0.007	0.317 ± 0.006	0.093 ± 0.003 [7,a]	0.29 ± 0.01	M3.5 ± 0.5 [1]
12	6	SDSS J121010.13+334722.9	95.3 ± 2.1 [7]	251.7 ± 2.0 [7]	0.379 ± 0.009	0.30 ± 0.02	0.230 ± 0.004 [1,a]	0.77 ± 0.05	M5 [7]
13	5	SDSS J121258.25-012310.1	104.4 ± 0.5 [8]	168.3 ± 0.3 [8]	0.620 ± 0.003	0.338 ± 0.001	0.167 ± 0.004 [5,a]	0.49 ± 0.01	M4 [8]
14	9	DE CVn	-	166 ± 4 [9]	0.8 ± 0.1 [9]	0.36 ± 0.01	0.18 ± 0.03 [9]	0.50 ± 0.08	M3 [9]
15	3	CSS 21357	101 ± 3 [1]	230.3 ± 0.5 [1]	0.44 ± 0.01	0.31 ± 0.01	0.179 ± 0.006 [7,a]	0.48 ± 0.03	M3.0 ± 0.5 [1]
16	23	QS Vir [b]	133 ± 10 [10]	258 ± 6 [10]	0.52 ± 0.04	0.32 ± 0.03	0.330 [10]	∼ 0.96 [1]	M3.5 - M4 [10]
17	40	GK Vir	38.6 ± 0.8 [8]	221.6 ± 2.0 [8]	0.174 ± 0.004	0.24 ± 0.06	0.085 ± 0.002 [5,a]	0.35 ± 0.09	M4.5 ± 0.5 [8]
18	26	NN Ser	62.3 ± 1.9 [11]	301 ± 3 [11]	0.207 ± 0.007	0.25 ± 0.07	0.160 ± 0.003 [6,a]	0.64 ± 0.18	M4 ± 0.5 [11]
19	12	RX J2130.6+4710	137 ± 4 [12]	136.4 ± 0.8 [12]	1.00 ± 0.03	0.379 ± 0.002	0.19 ± 0.02 [12]	0.50 ± 0.05	M3.5 [12]

References: [1] Parsons et al. (in prep) – [2] Parsons et al. (2012b) – [3] Parsons et al. (2013a) – [4] O'Brien et al. (2001) – [5] Bois et al. (1988) – [6] Parsons et al. (2012c) – [7] Pyrzas et al. (2012) – [12] Maxted et al. (2004) – [9] van den Besselaar et al. (2007) – [8] Parsons et al. (2012a) – [10] O'Donoghue et al. (2006) – [11] Parsons et al. (2010a)

Notes: [a] Using the volume averaged secondary star radius. – [b] Radial velocity amplitudes and the secondary star's relative radius are for an orbital inclination of $i = 75.5°$, see O'Donoghue et al. (2006).
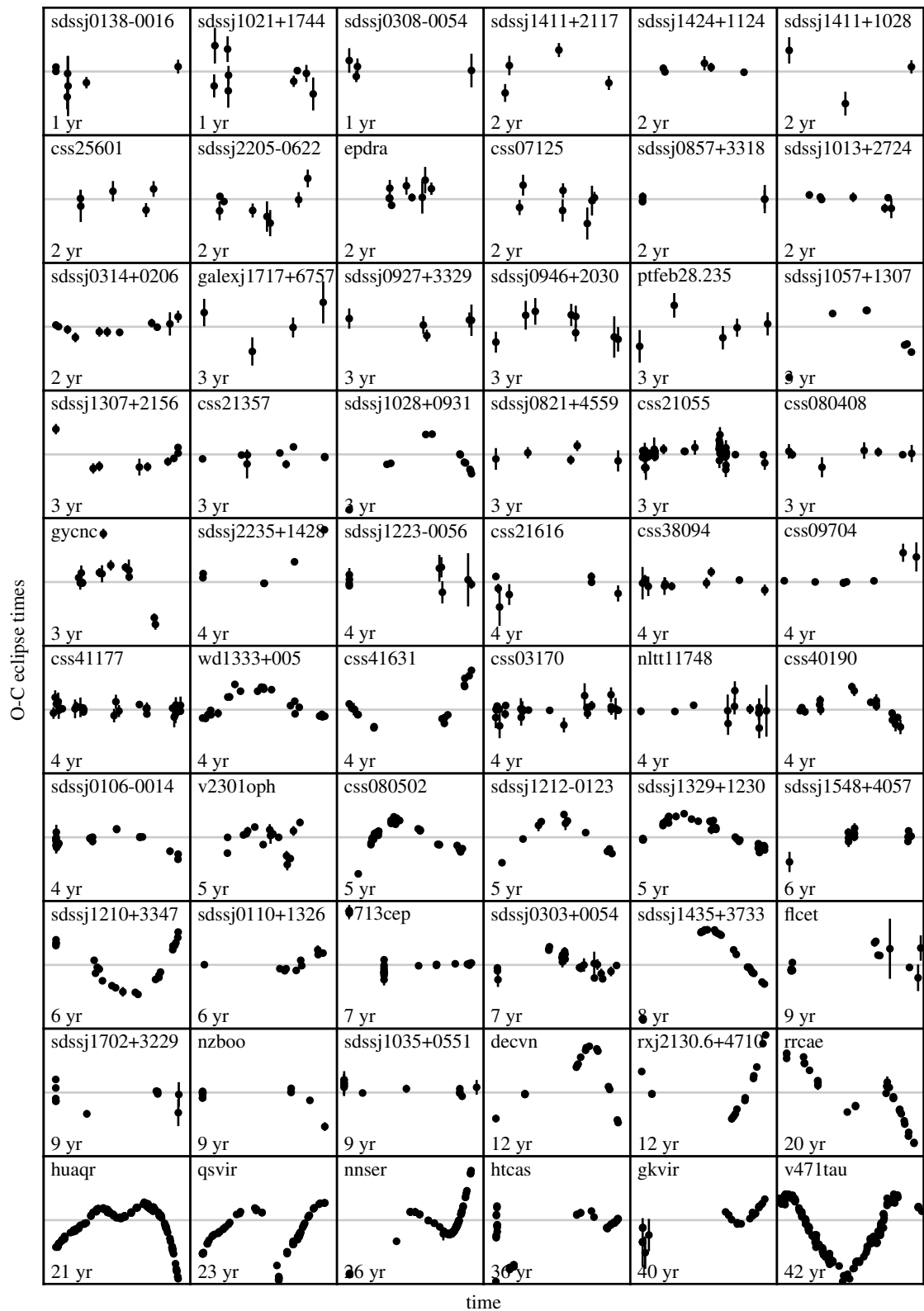
Figure 5.8: Thumbnails of O-C diagram of binaries in the timing programme, ordered by the baseline of observations with the shortest at the top left and the longest at the bottom right. Each O-C diagram includes the name of the binary in the top left corner and the baseline of observations in the bottom left corner. Detailed individual O-C diagrams can be found in Appendix B.

nltt11748	css41177	galexj1717+6757	sdssj1035+0551	css21055	sdssj0106-0014
WD - 4 yr	WD - 4 yr	WD - 3 yr	BD - 9 yr	L7 - 3 yr	M8 - 4 yr
css03170	sdssj1329+1230	css40190	sdssj1223-0056	sdssj1548+4057	flcet
M8 - 4 yr	M8 - 5 yr	M7 - 4 yr	M6 - 4 yr	M6 - 6 yr	M5.5 - 8 yr
v2301oph	htcas	sdssj0138-0016	css38094	sdssj0946+2030	sdssj1057+1307
M5.5 - 5 yr	M5.4 - 36 yr	M5 - 1 yr	M5 - 4 yr	M5 - 3 yr	M5 - 3 yr
sdssj1210+3347	css25601	wd1333+005	css080408	sdssj1435+3733	sdssj0303+0054
M5 - 6 yr	M5 - 2 yr	M5 - 4 yr	M5 - 3 yr	M5 - 8 yr	M4.5 - 7 yr
sdssj0308-0054	gkvir	huaqr	sdssj0110+1326	rrcae	css080502
M4.5 - 1 yr	M4.5 - 40 yr	M4.3 - 21 yr	M4 - 6 yr	M4 - 20 yr	M4 - 5 yr
sdssj1013+2724	sdssj1021+1744	sdssj1212-0123	sdssj1307+2156	css21357	css07125
M4 - 2 yr	M4 - 1 yr	M4 - 5 yr	M4 - 3 yr	M4 - 3 yr	M4 - 2 yr
nnser	css09704	sdssj2235+1428	rxj2130.6+4710	ptfeb28.235	sdssj0927+3329
M4 - 26 yr	M4 - 4 yr	M4 - 4 yr	M3.5 - 12 yr	M3 - 3 yr	M3 - 3 yr
sdssj1028+0931	decvn	qsvir	sdssj1411+1028	sdssj1411+2117	gycnc
M3 - 3 yr	M3 - 12 yr	M3 - 23 yr	M3 - 2 yr	M3 - 2 yr	M3 - 3 yr
sdssj0821+4559	css41631	sdssj2205-0622	sdssj1702+3229	v471tau	
M2 - 3 yr	M2 - 4 yr	M2 - 2 yr	M0 - 9 yr	K2 - 42	

O-C eclipse times

time

Figure 5.9: Thumbnails of O-C diagram of binaries in the timing programme, ordered by the spectral type of the companion star to the white dwarf. Double white dwarfs are located at the top left, and brown dwarf, M-dwarf and K-dwarf companions with increasingly early spectral subtypes are located towards the bottom right. Each O-C diagram includes the name of the binary in the top left corner and the spectral type and baseline of the observations in the bottom left corner. Detailed individual O-C diagrams can be found in Appendix B.
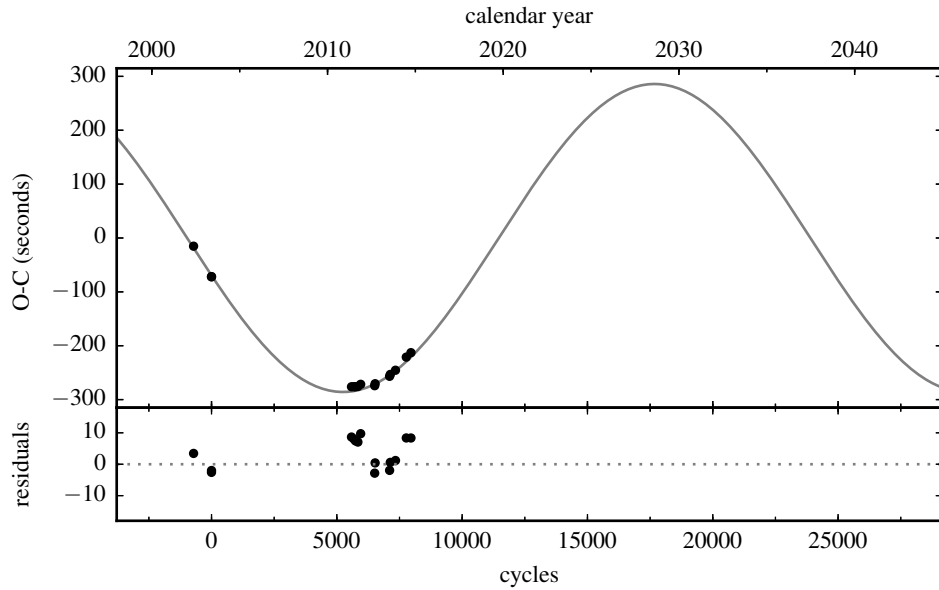
Figure 5.10: O-C diagram of RX J2130+4710. The best-fit sinusoidal ephemeris (grey line) corresponds to a single brown dwarf orbiting RX J2130.6+4710. The brown dwarf in this model has a mass of $M_{BD} = 0.06 \, M_\odot$ and is on an orbit with a period of almost 35.5 years.

5.6 A look at a few selected binaries

This section includes a more detailed look at a few selected binaries, which are either interesting in their own right, or show behaviour representative of a group of targets in the timing programme.

5.6.1 RX J2130.6+4710

RX J2130.6+4710 is a detached white dwarf + M-dwarf binary, on an orbital period of 12.5 hours. A study of the system parameters based on phase-resolved spectroscopy and ULTRACAM photometry of this binary was published by Maxted et al. (2004), who also published the first mid-eclipse times. Unluckily, RX J2130.6+4710 lies only 12″ away from a bright G0 star (HD 204906), which complicates the extraction of the light curve, especially if the data was taken under variable observing conditions. In addition, the M3.5 – M4 main-sequence star (Maxted et al., 2004) frequently experiences flares.

Table A.57 lists the mid-eclipse times from Maxted et al. (2004), as well as the subsequent times obtained with ULTRACAM, ULTRASPEC and RISE. These additional times immediately revealed a large shift in the mid-eclipse times with respect to a linear ephemeris, see also Fig. B.48. The overall shape of the O-C times appears to be parabolic-like, and could correspond to a part of a sinusoidal variation. Such a sinusoidal variability could indeed be the result of the reflex motion of the binary caused by a third companion. Fig. 5.10 shows the O-C times together with the best sinusoidal fit, corresponding to a single brown dwarf of $M_{BD} = 0.06 \, M_\odot$ orbiting RX J2130.6+4710 every 35.5 years. Note that these numbers are only very loosely constrained, given that the data only covers a
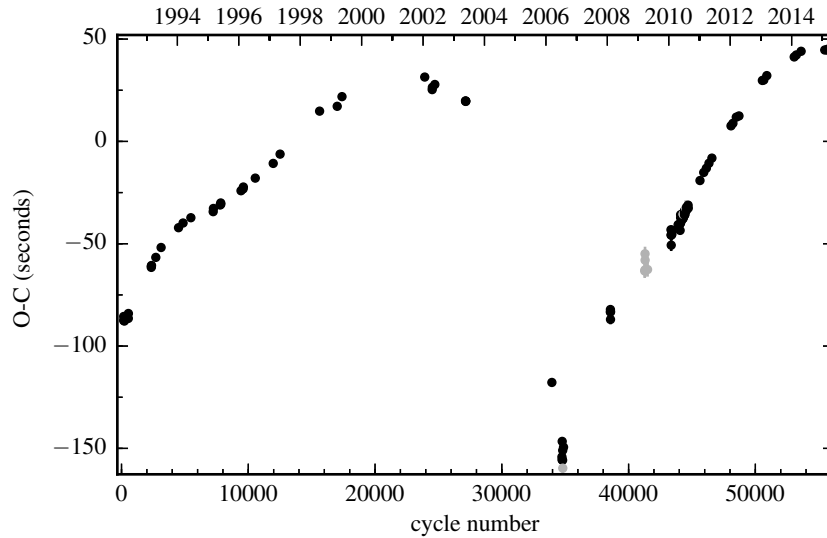
Figure 5.11: O-C diagram of QS Vir, with respect to the linear ephemeris in Table 5.1. Times with uncertainties larger than 3 seconds are shown in grey. This figure is a duplicate of Fig. B.36.

small part of the proposed orbit. With only the one companion, such a system would automatically be dynamically stable. To verify the presence of the brown dwarf, it may be possible to observe it directly, as was tried for V471 Tau (Hardy et al., 2015). In addition, regular eclipse observations over the next years will also be able to prove or disprove the presence of the proposed circumbinary brown dwarf.

5.6.2   QS Vir

QS Vir is a white dwarf + M-dwarf binary, also known as EC 13471-1258, discovered in the Edinburgh-Cape blue object survey (Stobie et al., 1997). The red dwarf has a spectral type of M3, and almost completely fills its Roche lobe (O'Donoghue et al., 2003), and the binary is has therefore been classified as a hibernating cataclysmic variable by those authors. However, analysis of the white dwarf rotation showed that the system could also be pre-cataclysmic variable (Parsons et al., 2011b), although the hibernation theory is not fully excluded (Drake et al., 2014b). Besides the white dwarf eclipse, the binary's light curve shows a small reflection effect at blue wavelengths, and ellipsoidal modulation at redder wavelengths (Parsons et al., 2010b).

There are 86 published mid-eclipse times as well as 19 unpublished as part of the eclipse timing programme presented here. For a complete list of these times and for the appropriate references, see Table A.41. As can be seen in Fig. 5.11, QS Vir shows eclipse time variations with large amplitudes and with occasional extreme changes. The new eclipse observations indicate that the O-C times have reached a second maximum, and perhaps the binary will experience a second abrupt shift such as the one seen near cycle number 30000 in the upcoming years.

There have been several attempts to explain the cause of these large and erratic O-C
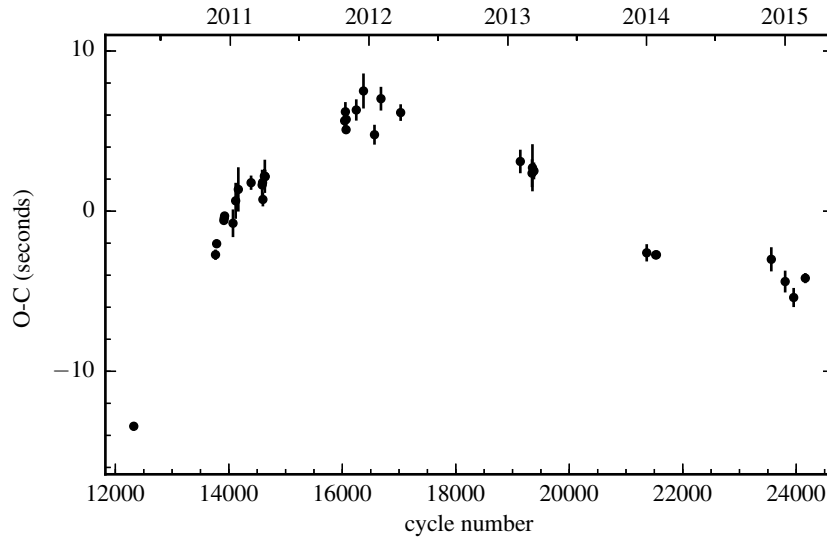
Figure 5.12: O-C diagram of CSS 080502, also known as SDSS J090812.03+060421.2, with respect to the linear ephemeris in Table 5.1. Times with uncertainties larger than 3 seconds are shown in grey. This figure is a duplicate of Fig. B.15.

variations. Qian et al. (2010), following Brinkworth et al. (2006), calculated the energy available in the secondary star, and showed that this was insufficient to cause the observed large-amplitude O-C variations through Applegate's mechanism. Instead, they proposed a combination of a large continuous decrease in the binary's orbital period and the presence of a circumbinary planet of $\sim 7\,M_{\mathrm{Jup}}$. New eclipse data quickly showed that this hypothesis was wrong (Parsons et al., 2010b). Almeida & Jablonski (2011) then presented a new fit to the data, which included two circumbinary planets. However, the extreme shift near cycle number 30000 forces at least one planet into a highly eccentric orbit, causing the entire planetary system to dynamically unstable (Horner et al., 2013).

Clearly, the eclipse time variations in this binary are complex, and what causes them remains to be discovered. As can be seen in Appendix B, there are a few other binaries in the timing programme that show similarly large O-C variations, such as V471 Tau and HU Aqr (see also Chapter 6). Close monitoring of the white dwarf eclipses in these binaries is necessary in order to reveal the origin of these variations.

5.6.3   CSS 080502

The binaries mentioned above have eclipse observations spanning over at least a decade. CSS 080502 is a detached white dwarf + M-dwarf binary that has a baseline of only about five years, but has already started to show some O-C variations, see Fig 5.12. It was discovered as an eclipsing white dwarf binary in CSS data (Drake et al., 2009), and has also been observed as part of SDSS as SDSS J090812.03+060421.2. Pyrzas et al. (2009) determined approximate parameters for the white dwarf and M-dwarf through decomposing and fitting the available SDSS spectra. The M-dwarf has a spectral type of M4, as determined
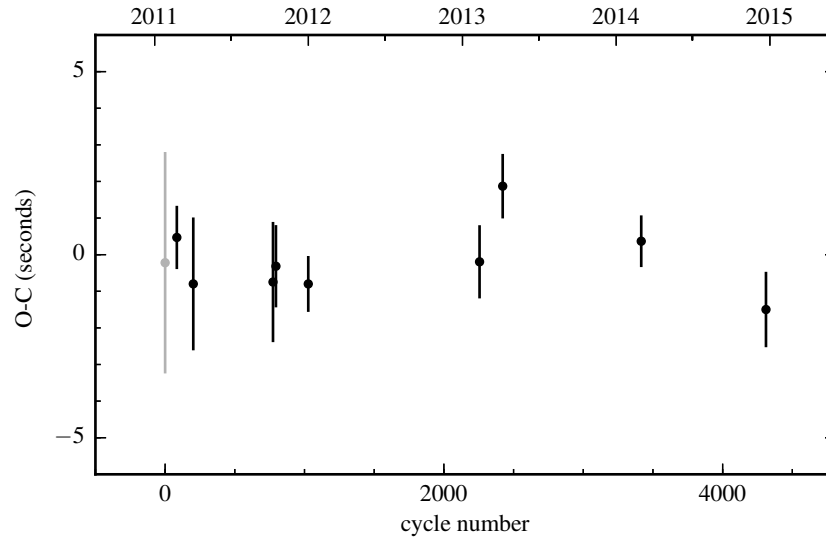
Figure 5.13: O-C diagram of CSS 38094, also known as SDSS J093947.95+325807.3, with respect to the linear ephemeris in Table 5.1. Times with uncertainties larger than 3 seconds are shown in grey. This figure is a duplicate of Fig. B.18.

by Rebassa-Mansergas et al. (2012), in good agreement with the previous determinations of Drake et al. (2010) and Silvestri et al. (2006).

CSS 080502 is a representative example of a number of targets in the timing programme, all of which have eclipse observations covering a few years and have started to show small-scale O-C variations on the order of $\pm\ 5 - 10$ seconds. See for example the O-C diagrams of SDSS J1210+3347, SDSS J1212-0123 and others in Appendix B. More data is needed before conclusions can be drawn about the extent of the O-C variations in these binaries.

5.6.4   CSS 38094

Finally, there are a few binaries which have so far shown no variability in their eclipse arrival times. One example of this class is CSS 38094, also known as SDSS J093947.95+325807.3. CSS 38094 was discovered in CSS data as a white dwarf + red dwarf binary, with the latter having a spectral type of M5. The more recent determination of spectral type from SDSS data agrees with this (Rebassa-Mansergas et al., 2012). The first white dwarf eclipse times were published by Backhaus et al. (2012), and we obtained five more as part of the timing programme, see Table A.21.

The O-C diagram is shown in Fig. 5.13, and is so far consistent with a linear ephemeris. Binaries with similarly flat O-C diagrams are SDSS J0314+0206, CSS 080408 and CSS 03170, see Appendix B. However, for all of these binaries the eclipse observations span only a few years, and it is therefore too early to say whether these binaries indeed show no variations in the eclipse arrival times.

5.7 Complementary and alternative observations

Clearly, it is quite difficult to determine the cause of the O-C variations observed in so many white dwarf binaries. Although I focused here on the timing of eclipses, there are several other observational features that can be used for O-C timing. For example, if the white dwarf in a close, eclipsing binary is also pulsating, these pulsations can be monitored and timed as well (Mullally et al., 2008). Several people are keenly searching for such a binary, to independently confirm the presence or absence of O-C residuals measured through eclipse timing.

Besides confirming the measured O-C variability, it may be possible to directly confirm or rule out the theory proposed to explain the variability. For example, to confirm the presence of a suspected circumbinary companion, one can try to directly detect this companion through high-contrast adaptive-optics assisted imaging. This approach was taken by Hardy et al. (2015) for the suspected brown dwarf around the close detached white dwarf + main-sequence star binary V471 Tau, which shows large and approximately sinusoidal O-C variations (see Fig. B.9). These O-C residuals can be modelled by the presence of a 0.04 $M_\odot$ brown dwarf. In this particular case, the relatively wide orbit places the brown dwarf at a projected separation of up to 0.3″ on the sky at certain times. In addition, because V471 Tau is part of the Hyades cluster, the cooling time since the brown dwarf's formation is less than 625 Myr (O'Brien et al., 2001), so that the suspected brown dwarf is still relatively bright (Burrows et al., 1997). Best contrast is reached at red wavelengths, in the H- and K-bands, but even here the presence of the circumbinary brown dwarf around V471 Tau was ruled out. Although the O-C residuals have large peak-to-peak amplitudes of ~ 400 s, the main-sequence star in this binary has quite an early spectral type of K2, and therefore may still be able to drive such large orbital period variations through a form of Applegate's mechanism. The periodicity would then be an indicator of the K-dwarf's magnetic cycles.

Besides direct imaging, a circumbinary companion may also be revealed through direct detection of the reflex motion of the host binary, either through precision astrometry or through very accurate measurements of the binaries systemic velocity with respect to Earth. For example, calculations assuming a planetary system around HU Aqr reveals that the reflex motion would only be as large as 0.17 mas on the sky (Goździewski et al., 2015). Such observations would have to be obtained over time scales comparable to the orbital period of the most massive circumbinary object present, as the binary needs to complete a decent chunk of an orbit around the system's barycentre. The required accuracy may be obtained with Gaia (de Bruijne et al., 2015), although the projected lifetime of this mission is only 5 years.

To confirm suspicions that Applegate's mechanism, or a variation thereof, is at work instead, the M-dwarfs in close, eclipsing binaries that show O-C variability could be monitored at X-ray wavelengths. The M-dwarf's magnetic activity visible at these wavelengths should then correlate with the amplitude of the O-C residuals. For example, it may be possible to obtain a measure of the number of starspots on the M-dwarf, which is expected

to vary over the same magnetic cycle that drives the orbital period variations through Applegate's mechanism.

5.8   Conclusions

In this chapter, and in Appendices A and B, I have presented my extensive set of 605 eclipse observations of 71 close white dwarf binaries. I have analysed the amount of O-C variability as a function of the baseline of the eclipse observations, the secondary star's spectral type and the secondary star's Roche lobe filling factor. All close binaries with baselines exceeding ~ 10 years show large O-C residuals, while those with shorter baselines show varying degrees of O-C variability. Although there is some indication that the spectral type of the secondary star is correlated with the RMS of the O-C residuals with respect to the best linear ephemeris, the effect of the different observational baselines is strong and prevents definitive conclusions from being drawn. Currently, there is no correlation between the O-C RMS and the Roche lobe filling factor of the secondary star, but a larger sample of binaries, as well as more homogeneous baselines across the sample may be required for revealing such a correlation.

This leaves me with the conclusion that the data of the timing programme as presented in this thesis are as yet insufficient to reveal the underlying cause of the apparent orbital period variations observed in so many eclipsing close white dwarf binaries. However, I am hopeful that with more data the effect of the baseline of the eclipse observations will become less prominent, so that correlations with real characteristics will become visible.

$\star\,\star\,\star$

Chapter 6

Testing the planetary models of HU Aqr

6.1 Introduction

HU Aqr was discovered independently by Schwope et al. (1993) and Hakala et al. (1993) as an eclipsing binary of the AM Her type, also known as polars. Systems from this class of CVs contain Roche-lobe filling M-dwarf secondary stars and strongly magnetic (~ 10 MG) white dwarf primary stars. From its discovery onwards, HU Aqr has been studied extensively and over a wide range of wavelengths (e.g. Glenn et al., 1994; Schwope et al., 1997, 2001; Heerlein et al., 1999; Howell et al., 2002; Harrop-Allin et al., 2001, 1999; Vrielmann & Schwope, 2001; Bridge et al., 2002; Watson et al., 2003; Schwarz et al., 2009). The general picture is as follows: the M-dwarf loses matter at the inner Lagrange point, which then follows a ballistic trajectory until the ram pressure equals the white dwarf's magnetic pressure and the stream couples to the magnetic field lines. At that point the stream leaves the orbital plane and is guided along the field lines until it accretes onto the white dwarf's magnetic pole, creating a luminous accretion spot.

The accretion rate in this system is highly variable, and the binary has changed from a high to a low state and back several times over the last decades. The variability causes both flickering typical of CVs on time scales of minutes, and significant changes in the overall shape of the observed light curves on time scales as short as one orbital cycle (Harrop-Allin et al., 2001).

One constant in the light curves is the eclipse of the white dwarf by the secondary star, the ingress and egress of which last for ~ 30 seconds. In a high state the eclipse is dominated by contributions from the accretion spot and stream, while the ingress and egress of the white dwarf itself are hardly visible. Due to the geometry of the system the accretion spot and accretion stream are well separated during egress, giving this part of the light curve a fairly constant shape. During ingress the distinction between the accretion spot and stream features is less clear. From X-ray data there is also evidence of enhanced absorption by an accretion curtain along the ballistic stream at this phase (Schwope et al., 2001). To accurately determine the eclipse times the timing has therefore been based on the egress of the accretion spot. Comparison of observed mid-egress times to expected mid-egress times, which are calculated assuming a constant orbital period, have revealed considerable variations (Schwope & Thinius, 2014; Goździewski et al., 2012; Schwarz et al., 2009; Schwope et al., 2001).

Several explanations for these eclipse time variations have been offered in the literature,

including Applegate's mechanism (Applegate, 1992). However, for HU Aqr, the energy available in the M-dwarf is insufficient to explain the large variations observed (Schwarz et al., 2009). A second explanation for the eclipse time variations is that they are caused by the presence of planet-like or brown dwarf-like bodies in wide orbits around the binary, and models with 1, 2 and even 3 planets have been proposed for HU Aqr (Goździewski et al., 2012; Qian et al., 2011). All have since been disproved on grounds of dynamical instability (Wittenmyer et al., 2012; Horner et al., 2011) or by new data (this chapter, Schwope & Thinius, 2014; Goździewski et al., 2012, 2015).

In this chapter, which is based on Bours et al. (2014b), I present 24 new eclipse times from data taken between June 2010 and October 2014.

6.2 Observations

In this section the technical details of the observations are described. The light curves themselves are discussed in Sect. 6.3. All mid-egress times are listed in Table 6.1, which also summarises the technical details and contains notes on the observing conditions. Mid-egress times are described as discussed in Sect. 5.4.2 and some additional details can be found in Sect. 6.4.

6.2.1 RISE on the Liverpool Telescope

A total of 14 eclipse observations were obtained of HU Aqr between 2 Aug 2011 and 14 Oct 2014 with the Liverpool Telescope (LT; Steele et al., 2004) and the RISE camera (Steele et al., 2008) which was used with the 2x2 binned mode. The data were flatfielded and debiased in the automatic pipeline, in which a scaled dark-frame was removed as well. Aperture photometry was then performed using the ULTRACAM pipeline (Dhillon et al., 2007), and care was taken to use the same comparison star for all data reductions. This comparison is a non-variable star located 93" South and 88" West of HU Aqr. I chose this star rather than comparison 'C' as in Schwope et al. (1993, their Fig. 1) because of their relative brightnesses in RISE's V+R filter. I did use comparison 'C' to calculate magnitudes for HU Aqr, as will be explained in Sect. 6.3. All stellar profiles were fitted with a Moffat profile (Moffat, 1969), the target aperture diameters scaled with the seeing and the comparison star was used to account for variations in the transmission. The light curves are shown in Fig. 6.1.

6.2.2 ULTRACAM observations

Between June 2010 and October 2012 I obtained six eclipses of HU Aqr with ULTRACAM (Dhillon et al., 2007). ULTRACAM was mounted on the New Technology Telescope (NTT) in Chile during the first three observations and on the William Herschel Telescope (WHT) on La Palma, Spain, for the last three observations. The light curves are shown in Fig. 6.2.

For the data reduction and the relative aperture photometry I used the ULTRACAM pipeline. Due to different fields of view and windowed setups during the observations I
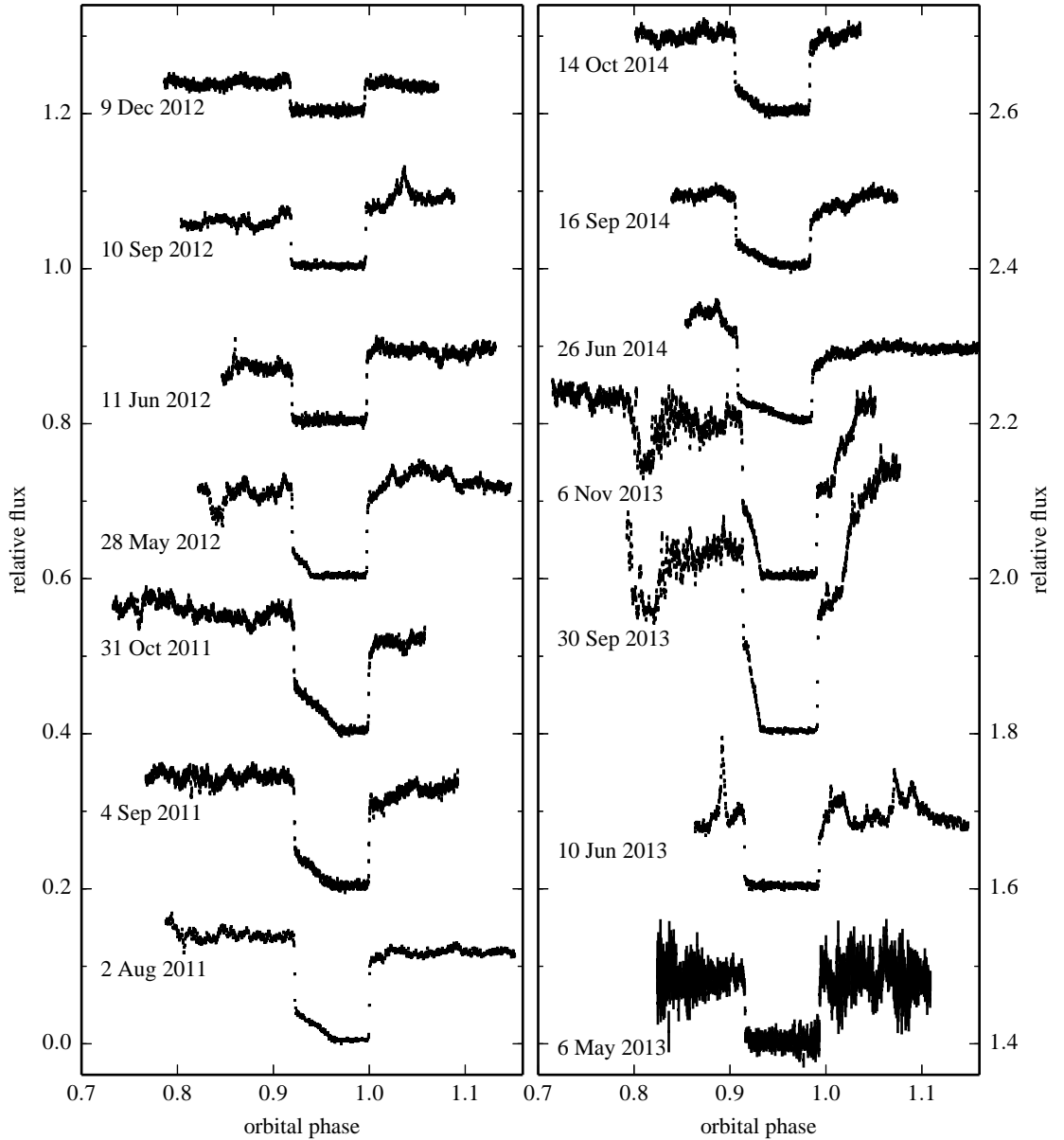
Figure 6.1: LT+RISE light curves of HU Aqr, taken between 2 Aug 2011 (bottom left) and 14 Oct 2014 (top right), with each eclipse vertically offset from the previous one by 0.2. The vertical axis shows the flux relative to the comparison star, which is the same star for all LT+RISE and TNT+ULTRASPEC data. To calculate the orbital phase I used the ephemeris in equation 6.2.

could not use the same comparison star as for the LT+RISE and TNT+ULTRASPEC data.

6.2.3   ULTRASPEC on the Thai National Telescope

In November 2013 I observed two HU Aqr eclipses with the Thai National Telescope (TNT), located on Doi Inthanon in northern Thailand. I used the ULTRASPEC camera (Dhillon et al., 2014), and an SDSS g′ filter on November 10, and a Schott KG5 filter on November
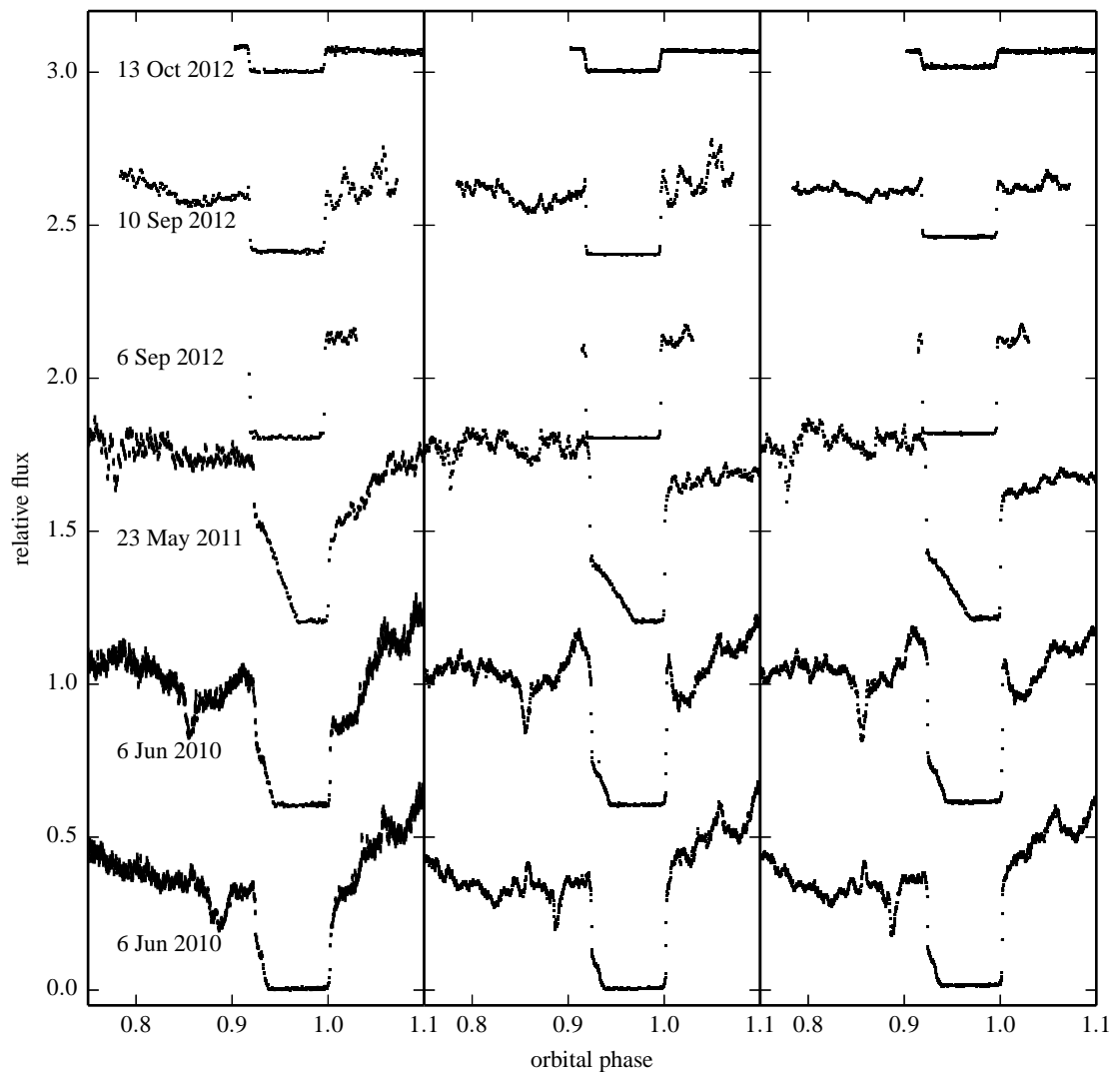
Figure 6.2: ULTRACAM+NTT (bottom three) and ULTRACAM+WHT (upper three) light curves of HU Aqr, taken between 6 Jun 2010 and 13 Oct 2012. From left to right are shown the blue (u′), green (g′), and red (r′ or i′) data. The blue and red light curves are scaled to the green light curves to facilitate easy comparison. Each light curve is vertically offset from the previous one by 0.6. To calculate the orbital phase I used the ephemeris from equation 6.2.

13. The Schott KG5 filter is a broad filter with its central wavelength at 5075 Å and a FWHM of 3605 Å, see Fig 2.6.

The data were reduced using the ULTRACAM pipeline, with which I debiased and flatfielded the data and performed aperture photometry. I used the same comparison star as for the reduction of the LT+RISE data. Both ULTRASPEC light curves are shown in Fig. 6.3. During the observations on November 10, the telescope briefly stopped tracking, causing the gap seen during ingress in the light curve in Fig. 6.3.
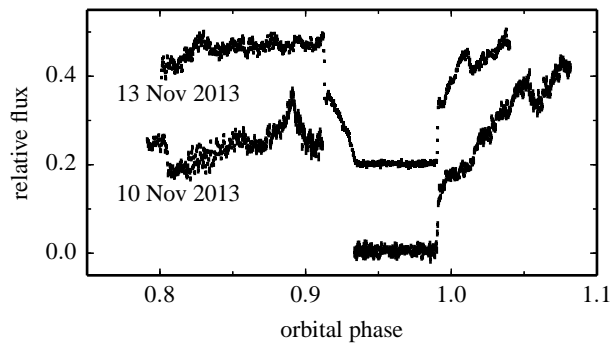
Figure 6.3: TNT+ULTRASPEC light curves of HU Aqr, taken in November 2013, displayed with a vertical offset of 0.2. To calculate the orbital phase I used the ephemeris from equation 6.2.
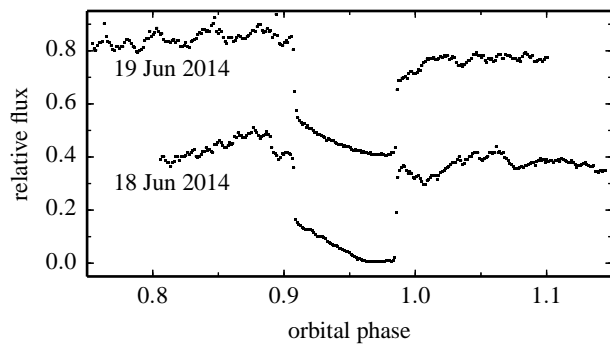
Figure 6.4: INT+WFC light curves of HU Aqr, taken in June 2014, displayed with a vertical offset of 0.4. To calculate the orbital phase I used the ephemeris from equation 6.2.

6.2.4   Wide Field Camera on the Isaac Newton Telescope

In June 2014 two more eclipses were obtained of HU Aqr using the Wide Field Camera (WFC) mounted on the Isaac Newton Telescope (INT) on La Palma, Spain. The read-out time of the WFC is ~ 2 seconds, and a Sloan-Gunn g filter was used, which is very similar to the ULTRACAM g′ filter.

The data were reduced using the ULTRACAM pipeline, with which I debiased and flatfielded the data and performed aperture photometry. As a comparison star I used star 'C' as in Schwope et al. (1993). Both light curves are shown in Fig 6.4.

Table 6.1: Mid-egress times for the observed eclipses of HU Aqr. For the ULTRACAM data the exposure times are listed for each of the arms separately and the mid-egress times are the weighted averages of the three times from the individual arms. The magnitudes are calculated as detailed in Section 6.3 and correspond to the given filter of each observation and the g'-filter for the ULTRACAM data. The dead-time between exposures is 8 ms (LT+RISE), 25 ms (ULTRACAM), 15 ms (ULTRASPEC) and 2 s (INT+WFC).

date	cycle number	mid-egress time BMJD(TDB)	t_{exp} (sec)	telescope + instrument	filter(s)	approximate magnitude	observing conditions
06 Jun 2010	72009	55354.2706040(4)	4, 2, 2	NTT+UCAM	u'g'r'	15.8	clear, seeing 1.5″
06 Jun 2010	72010	55354.3574451(5)	4, 2, 2	NTT+UCAM	u'g'r'	15.7	clear, seeing 1-2″
23 May 2011	76053	55705.3721585(9)	8, 4, 4	NTT+UCAM	u'g'r'	15.5	clear, seeing 1.5″
02 Aug 2011	76868	55776.1307426(20)	3	LT+RISE	V+R	15.9	clear, seeing 2″
04 Sep 2011	77247	55809.0356564(25)	2	LT+RISE	V+R	15.8	clear, seeing 2.5″
31 Oct 2011	77902	55865.9029864(22)	2	LT+RISE	V+R	15.7	clear, seeing 1.6-2.5″
28 May 2012	80324	56076.1818394(22)	2	LT+RISE	V+R	15.9	clear, seeing 1.8-2.4″
11 Jun 2012	80485	56090.1598976(19)	2	LT+RISE	V+R	17.3	thin clouds, seeing 2-4″
06 Sep 2012	81486	56177.0670248(8)	7, 4, 4	WHT+UCAM	u'g'r'	16.1	clear, seeing 1-2″
10 Sep 2012	81531	56180.9739470(22)	2	LT+RISE	V+R	16.4	thin clouds, seeing 2.2″
10 Sep 2012	81532	56191.0607721(6)	7, 4, 4	WHT+UCAM	u'g'i'	16.6	thin clouds, seeing 2″
13 Oct 2012	81910	56213.8788462(2)	6, 2, 2	WHT+UCAM	u'g'r'	17.8	thin clouds, seeing 2-4″
09 Dec 2012	82566	56270.8329602(53)	2	LT+RISE	V+R	17.2	clear, seeing 2″
06 May 2013	84275	56419.208883(11)	2	LT+RISE	V+R	17.3	thick clouds, seeing 2-3″
10 Jun 2013	84678	56454.1974374(17)	2	LT+RISE	V+R	16.2	clear, seeing 2″
30 Sep 2013	85965	56565.9351702(10)	2	LT+RISE	V+R	14.8	clear, seeing 1.8″
06 Nov 2013	86391	56602.9205819(16)	2	LT+RISE	V+R	15.3	thin clouds, seeing 1.8-2.5″
10 Nov 2013	86433	56606.5670216(45)	3	TNT+USPEC	g'	15.1	cloudy, seeing 1.5-2″
13 Nov 2013	86467	56609.5189097(21)	2	TNT+USPEC	Schott KG5	15.2	thin clouds, seeing 1.5″
18 Jun 2014	88973	56827.0904134(16)	5	INT+WFC	g	15.7	clear, seeing 1.5″
19 Jun 2014	88985	56828.1322517(37)	5	INT+WFC	g	15.7	clear, seeing 2-3″
26 Jun 2014	89066	56835.1647131(24)	2	LT+RISE	V+R	16.1	clear, seeing 2″
16 Sep 2014	90009	56917.0361809(34)	2	LT+RISE	V+R	16.2	clear, seeing 2-2.5″
14 Oct 2014	90330	56944.9054808(23)	2	LT+RISE	V+R	16.1	thin clouds, seeing 2″

6.3 Ever-changing light curves

HU Aqr is known for its variable accretion rate, which significantly influences the brightness of the system and the morphology of its light curves, as is immediately clear from Figs. 6.1, 6.2, 6.3 and 6.4. HU Aqr was in a high state until mid 2012, then went into a low state, and returned to a high state in the second half of 2013, after which it dropped to a lower state again. I calculated the magnitude of HU Aqr for each data set, using the out-of-eclipse data, and excluding obvious flares from the M-dwarf and dips due to the accretion stream. Using simultaneous g′ and r′ ULTRACAM data, I determined a magnitude offset for comparison 'C' (Schwope et al., 1993, their Fig. 1) for each filter type with respect to its V-band magnitude of $m_V = 14.65$ (mean of various measurements). I then calculated magnitudes for HU Aqr as normal, using the relative flux and corrected magnitude for comparison 'C'. These approximate magnitudes are listed in Table 6.1. Typical magnitudes were $m_{g'} \simeq$ 15.1 - 15.5 during the high states, and $m_{g'} \simeq 17.8$ during the low state.

The out-of-eclipse data shows the characteristic flickering of a CV, caused by the irregular, blobby nature of the accretion. In the high state light curves the eclipse is dominated by both the accretion spot on the white dwarf and the accretion stream. The eclipse of the spot is characterised by the abrupt ingress when the spot goes behind the M-dwarf, and the egress when it re-emerges, each typically lasting ~ 8 seconds.

Due to the small physical size of the accretion region on the white dwarf, this spot can reach very high temperatures and contributes significantly to the total light from the system when accretion rates are high. The data shows no signs of a varying width or height of the ingress or egress feature, over time nor with changing accretion rate. Assuming for the masses $M_{WD} = 0.81$ M$_\odot$ and $M_2 = 0.18$ M$_\odot$, an inclination $i = 87°$ (see Sect. 6.3.2 and Schwope et al., 2011) and the orbital period from equation 6.2, I arrive at an orbital velocity of the M-dwarf of 479 km s^{-1} and a maximum spot diameter of $D_{spot} \simeq 3829$ km. Using the mass-radius relation of Verbunt & Rappaport (1988) for the white dwarf, this corresponds to a fractional area on the white dwarf of 0.018 and an opening angle of the accretion spot of $\sim 30°$. This is significantly larger than the value of 3° found by Schwope et al. (2001) using ROSAT-PSPC soft X-ray data although some difference is to be expected, as only the hottest parts of the spot will radiate at X-ray wavelengths.

In the high state the ingress of the accretion stream, caused by irradiation of the stream by the hot accretion spot, is visible as an additional, shallower slope after the sharp ingress of the accretion spot. Depending on the exact geometry of the stream and its relative position to the spot, the duration and height of the stream ingress vary considerably.

Some of the light curves taken during a high state also show a narrow dip near orbital phase $0.8 − 0.9$. This has been seen in many of the other studies on HU Aqr, and is also observed in other polars (Watson, 1995). It is caused by the obscuration of the accretion spot by part of the stream if the inclination of the system is such that the hemisphere with both the spot and stream is towards the observer (Bridge et al., 2002). The depth and width of this dip carry information about the temperature difference between the white dwarf and the spot and about the physical extent of the magnetically coupled stream respectively.
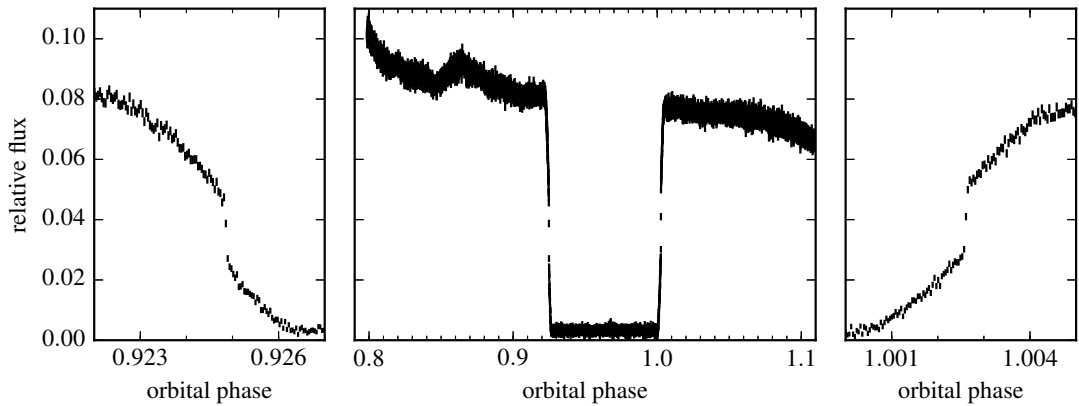
Figure 6.5: Archival g′-band ULTRACAM+VLT light curve of HU Aqr, taken on the night of 21 Jun 2007 when HU Aqr was in a low state. Exposure times for this observation were 0.3 seconds. The subplots to the left and right of the full eclipse span 0.005 orbital phases around the ingress and egress, equivalent to 38 seconds. To calculate the orbital phase I used the ephemeris from equation 6.2.

The dip moves further away from the spot ingress during high accretion states, which agrees with the expectation that the ballistic stream penetrates further before coupling to the magnetic field lines in the high state. I also notice some interesting colour differences in the dip as well as in some of the other variable features in the high state ULTRACAM light curves (Fig. 6.2). At blue wavelengths the dip is wider than observed in the other two bands, and it possibly consists of two components. This indicates a fluffy and blobby nature of the stream, and a strongly wavelength-dependent opacity within the stream.

During a low state, the stream ingress disappears completely, flickering is less pronounced and the system is noticeably fainter.

6.3.1   Archival ULTRACAM observations of HU Aqr in a low state

HU Aqr has been observed with ULTRACAM before (Schwarz et al., 2009), in May 2002 and May 2003 when the instrument was mounted on the WHT, and in May 2005 and June 2007 when mounted on the Very Large Telescope (VLT). During the last two of these runs HU Aqr was in a deep low state. The 2005 data was briefly discussed in Schwarz et al. (2009), as it was taken simultaneously with some of their X-ray data.

Fig. 6.5 shows the white dwarf in one of the light curves from June 2007. The variability present in the out-of-eclipse data reveals that some accretion is still ongoing. The eclipse ingress and egress are now dominated by the eclipse of the white dwarf, lasting ∼ 25 seconds. However, it appears that there is still a small area, hotter than the white dwarf itself, that is also being eclipsed. This is evident from the steep 0.5 – 1 second features visible near the middle of white dwarfs ingress and egress. These parts of the light curve are shown in more detail in the two side panels in Fig. 6.5. The sharp, brief features are visible in all eclipses observed with ULTRACAM in May 2005 and June 2007, demonstrating it is not a short-lived transient phenomenon. When looking up close, a short, faster ingress/egress

Table 6.2: Masses for the white dwarf and Roche lobe filling companion star in HU Aqr for a given inclination i. The last column lists the χ^2 values for the fits corresponding to the parameters as in the other columns.

i (degrees)	M_{WD} ($M_\odot$)	M_2 ($M_\odot$)	χ^2
90	0.802	0.161	1.15
89	0.800	0.162	0.99
88	0.794	0.166	0.87
87	0.805	0.177	0.86
86	0.811	0.189	0.89
85	0.824	0.207	0.92

part also seems visible in the WHT+ULTRACAM observation of 13 Oct 2012 (presented in Fig. 6.2), although the time resolution of that light curve is rather long (2 seconds) compared to the duration of the feature. The LT+RISE observations taken when HU Aqr was in a low state have similar time resolution and lower signal-to-noise, making it even more difficult to judge whether this feature is present or not.

It is likely that these features are caused by the eclipse of the remaining base of the accretion column near where the main accretion spot used to be.

6.3.2 Characterising the white dwarf

Since the eclipses in the ULTRACAM data taken when HU Aqr was in a deep low state are dominated by the eclipse of the white dwarf, they allow determination of the system's inclination and the white dwarf's radius. The variation in eclipse arrival times and the remaining flickering still present in the data complicate normalisation and folding of the light curves on the orbital period. I therefore focus on a single light curve, and have chosen the g′-band eclipse observed on 21 Jun 2007, as shown in Fig. 6.5. The width of the eclipse determines the mass ratio (q) for a given inclination (i), while the duration of the ingress and egress features fix the radii of the stars relative to the orbital separation (R_{WD}/a and R_2/a). Using a mass – radius relation for the white dwarf (Wood, 1995), I can then find the masses of both stars.

To model the white dwarf eclipse I used the code `lcurve`, as described in Chapter 5. For the white dwarf I assume a temperature of $T_{WD} = 15000$ K, and quadratic limb darkening with coefficients $l_{WD,1} = 0.115$ and $l_{WD,2} = 0.348$ (Gianninas et al., 2013, for log $g = 8.25$). I now included a hot spot on the white dwarf, with a longitude, latitude, full-width at half-maximum and central temperature as its parameters, as already detailed in Table 5.3. This allows me to model the fast and sharp features seen during ingress and egress of the white dwarf. I force the M-dwarf companion to fill its Roche lobe, and assume quadratic limb darkening with coefficients $l_{dM,1} = 0.996$ and $l_{dM,2} = 0.015$ (Claret et al., 2012, for reasonable values of $T_2 = 3000$ K and log $g = 5.0$). The orbital period was fixed to the value in equation 6.2. For a range of inclinations the resulting stellar masses are given in Table 6.2.

The model that best fits the light curve (shown in Fig. 6.6) assumes an inclination
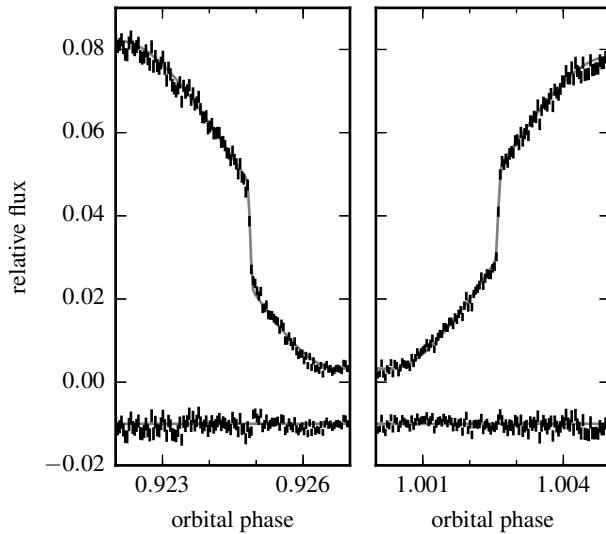
Figure 6.6: Data as in Fig. 6.5, with my best `lcurve` model over-plotted (light grey lines), corresponding to an inclination $i = 87°$. The residuals are shown as well (vertically offset by -0.01).

$i = 87°$, and results in a mass ratio $q = 0.22$. These values agree well with the latest published values (Schwope et al., 2011), as do the corresponding masses. The duration of the spot ingress and egress is only ~ 0.6 s in this low-state light curve. Using the same procedure as before, the spot size during these observations had an opening angle of $\sim 2.5°$, which is very comparable to the $3°$ size of the X-ray spot (Schwope et al., 2001).

The ingress and egress of the remaining spot are much shorter in these extreme low-state light curves (Fig. 6.5) than observed in my other data (Figs. 6.1, 6.2, 6.3 and 6.4). It is probable that in this low accretion state only the very core of the accretion spot remains hot enough to contribute a significant amount of light, while the surrounding area has cooled to a temperature more closely resembling that of the white dwarf itself. Such a correlation between spot size and accretion state has not been observed in, for example, the polar AM Her, which has been studied extensively during high as well as low states (Gänsicke et al., 2006).

6.4 Egress times

As has been done for previously published times of HU Aqr, I measured mid-egress times as opposed to mid-eclipse times. This because the egress feature is relatively stable, even with the variable accretion rate, whereas the shape of the ingress feature varies significantly with the changing accretion rate and even differs from cycle to cycle. For all my new data I determined the time of mid-egress by a least-squares fit of a function composed of a sigmoid and a straight line,

$$y = \frac{k_1}{1 + e^{-k_2(x-k_3)}} + k_4 + k_5(x - k_3) \, , \tag{6.1}$$

where x and y are the time and flux measurements of the light curve, and k_1 to k_5 are coefficients of the fit. An example of one of the fits is shown in Fig. 6.7.
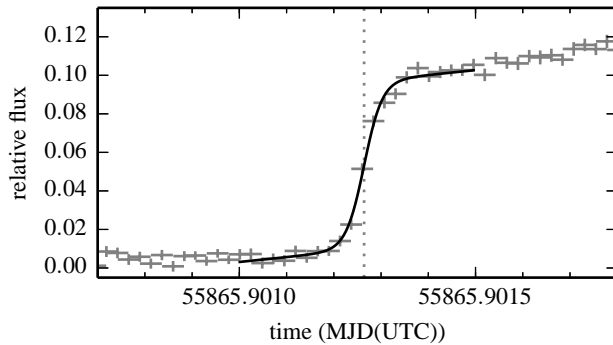
Figure 6.7: Egress of the LT+RISE eclipse light curve of HU Aqr, taken on 31 Oct 2011, with 2 second exposures. The solid black line shows the sigmoid+linear function that is fitted to the data. The vertical dotted line indicates the mid-egress time at MJD(UTC) = 55865.9012656(22).

The straight line part allows me to fit the overall trend outside and during egress. This includes the egress of the white dwarf itself, which can have a significant contribution, especially when the system is in a lower state. The sigmoid part of the function fits the sharp egress feature created by the egress of the accretion spot. To determine uncertainties, I have performed these fits in a Monte Carlo manner in which I perturb the value of the data points based on their uncertainties and vary the number of included data points by a few at each edge, reducing any strong effects in the results caused by single data points.

I converted all mid-egress times to barycentric dynamical time (TDB) in the form of modified Julian days and corrected to the barycentre of the Solar System, giving BMJD(TDB). The times are listed in Table 6.1 and I used the ephemeris of Schwarz et al. (2009) to calculate the corresponding cycle number E. Including the new times the best linear ephemeris is given by:

$$\text{BMJD(TDB)} = 49102.42039316(1) + 0.0868203980(4)E \,, \tag{6.2}$$

with E the orbital cycle number.

For the ULTRACAM data I find that the times from the three individual arms agree well with each other, see Fig. 6.8, although the times from the blue arm are comparatively poor due to its lower time resolution (necessary to compensate for the lower flux in this band). The ULTRACAM times listed in Table 6.1 are the error-weighted averages of the three individual times.

The agreement of the individual times and the absence of a particular ordering of the u′, g′, and r′ or i′ times around the weighted mean indicate that there is no significant correlation between the observed egress time and the wavelength at which the data were taken.

6.5   Orbital period variations

The O-C diagram in Fig. 6.9 shows the observed eclipse times minus times calculated assuming a constant orbital period. A mechanism that could explain observed O-C variations in white dwarf + M-dwarf binaries was proposed by Applegate (1992). He suggested that magnetic cycles in the secondary star cause quasi-periodic variations in its gravitational
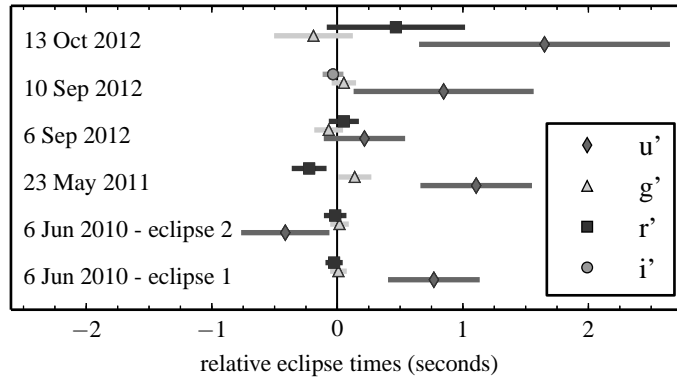
Figure 6.8: Eclipse times relative to the weighted mean, with 1σ errorbars, determined for data from the three ULTRACAM arms.

quadrupole moment, which couple to the binary's orbit and cause semi-periodic variations in the orbital period. However, as orbital period variations were monitored more extensively and over longer periods of time, it became clear that, in HU Aqr and other binaries, the variations can be larger than energetically possible with Applegate's mechanism. For the pre-CV NN Ser, Brinkworth et al. (2006) showed that the energy required for the observed variations was at least an order of magnitude larger than the energy available from the M-dwarf. Given that HU Aqr has a similarly low-mass M-dwarf star, and the O-C variations are even more extreme, a similar discrepancy exists for this system (Schwarz et al., 2009).

6.5.1 Planetary companions to HU Aqr

For eclipsing white dwarf binaries that show O-C variations too large to be explained by Applegate's mechanism a number of models invoking circumbinary planets around close binaries have been suggested. These planets are generally in orbits with periods of years to decades, and would introduce periodic variations in the O-C eclipse times much like the ones observed. A comprehensive overview of the relevant binaries and models can be found in Zorotovic & Schreiber (2013). Due to the long periods of the suspected circumbinary planets, and the often relatively short coverage of eclipse times, published models for planetary systems are only weakly constrained and are often proved incorrect when new eclipse times become available (Fig 6.9; Bours et al., 2014b; Goździewski et al., 2012; Beuermann et al., 2012; Parsons et al., 2010b). Besides creating a model that fits the data, analysing the dynamical stability of the resulting system is a crucial step in determining the probability that circumbinary planets are present. Several published systems for which multiple planetary companions were proposed have turned out to be unstable on time scales as short as a few centuries (Horner et al., 2013; Wittenmyer et al., 2013; Hinse et al., 2012), which makes their existence unlikely. Systems for which models invoke a single planetary companion are of course dynamically stable, but not necessarily more likely to exist. Only
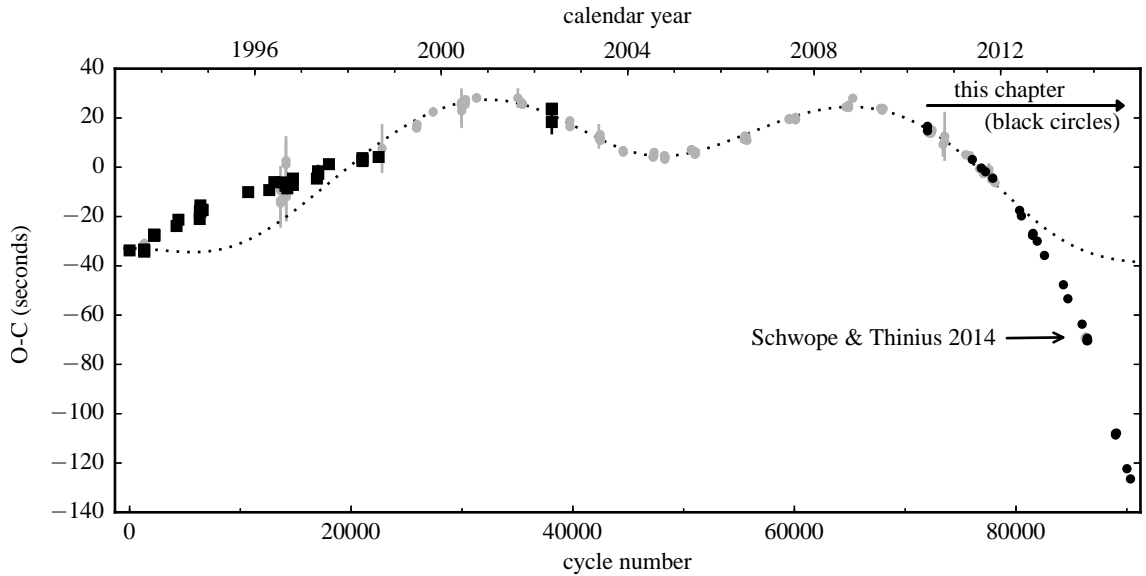
Figure 6.9: O-C diagram for the mid-egress times of HU Aqr with respect to the ephemeris in equation 6.2, including the new times presented in this chapter (black dots) and literature times from optical (grey dots, excluding those from Qian et al. (2011)) and non-optical data (black squares). The dotted line is the 1-planet model by Goździewski et al. (2012).

for the post-common envelope binary NN Ser have planetary models (which include two planets) correctly predicted future eclipse times and shown long-term dynamical stability (Marsh et al., 2014; Beuermann et al., 2013a; Horner et al., 2012b), while at the same time both Applegate's mechanism (Brinkworth et al., 2006) and apsidal motion (Parsons et al., 2014) have been ruled out as the main cause of the eclipse timing variations. Despite the difficulties encountered, determining parameters of current-day planetary systems around evolved binary stars could provide a unique way to constrain uncertainties in close binary evolution, such as the common envelope phase (Portegies Zwart, 2013), as well as answer questions related to planet formation and evolution.

HU Aqr has been the topic of much discussion and speculation concerning possible planetary companions. A few years after the first egress times were published by Schwope et al. (2001) and Schwarz et al. (2009), Qian et al. (2011) published a model with two circumbinary planets, and a possible third planet on a much larger orbit. This model was proven to be dynamically unstable on very short time scales (10^3 - 10^4 years) by Horner et al. (2011), after which both Wittenmyer et al. (2012) and Hinse et al. (2012) reanalysed the data and found models with different parameters, which were nonetheless still dynamically unstable. Goździewski et al. (2012) then suggested that there may be a significant correlation between eclipse times and the wavelength at which the relevant data is obtained, and proposed a single-planet model to explain the observed O-C variations seen in data taken in white light or V-band only, thereby excluding data that was taken at X-rays (ROSAT, XMM) and UV wavelengths (EUVE, XMM OM-UVM2, HST/FOS) and all polarimetric data. They also excluded the outliers from Qian et al. (2011), which do not agree well with other data taken at similar times.

The O-C diagram as shown in Fig. 6.9 includes all previously published eclipse egress times, except those from Qian et al. (2011) which I exclude for the same reason as Goździewski et al. (2012). Also plotted is the 1-planet model that was proposed by Goździewski et al. (2012). My new times and the recent time from Schwope & Thinius (2014) depart dramatically from this model, and I therefore conclude that the proposed orbit is incorrect. The deviation of the new data also suggests that the times derived from satellite data (which Goździewski et al. (2012) argued were unreliable) should be considered alongside optical data. This is also supported by the agreement between the optical and satellite times when taken at similar epochs. As mentioned before, from the separate u', g' and r'/i' data there was no evidence that mid-egress times are wavelength dependent.

For completeness I fitted the O-C times with three different planetary models, containing one, two and three eccentric planets respectively. I did not include a quadratic term, since such long-term behaviour can be mimicked by a distant planet, and chose to investigate a possible secular change of the orbital period separately in Sect. 6.5.2. Unsurprisingly, all planets in these models are forced into highly eccentric orbits in order to fit the recent steep decline in the O-C times, leading to the belief that these system would be dynamically unstable. In addition, the models leave significant residuals. I conclude that the observed variability in eclipse egress times is not caused purely by the presence of a reasonable number of circumbinary planets. However, see the recent paper by Goździewski et al. (2015) for a comprehensive analysis of the eclipse timing variations and the possibility that they are caused by circumbinary planets.

6.5.2 A secular change of the orbital period?

It seems that the current set of O-C times cannot be explained simply by a model that introduces one or multiple planets, but given the recent steep decline in the O-C times, I now consider whether it is the long-term evolution of the binary's orbital period that is visible. Using a quadratic model, shown in Fig. 6.10, I measure the rate of orbital period change as -5.2×10^{-12} s/s (= -4.5×10^{-13} days/cycle).

With an orbital period of only 125 minutes, HU Aqr is located just below the CV period gap (Knigge, 2006), so that gravitational wave emission is expected to be the main cause of angular momentum loss. Using $M_{WD} = 0.81$ $M_\odot$, $M_2 = 0.18$ $M_\odot$ for the masses of the two stars (Table 6.2), and the orbital period from equation 6.2, I calculated the period change due to gravitational wave emission to be $\dot{P}_{GW} = -1.9 \times 10^{-13}$ s s^{-1}, 27 times smaller than the result from my best fit to the O-C times. If the measured quadratic term in the O-C times represents an actual change in the binary's orbital period, this is not caused by gravitational wave emission alone. For binaries that lie below the period gap it is likely that some magnetic braking is still ongoing (Knigge et al., 2011). If this occurs in short bursts of strong magnetic braking, rather than long-term steady magnetic braking, it might be possible to create large changes in the binary's orbital period on short time scales.
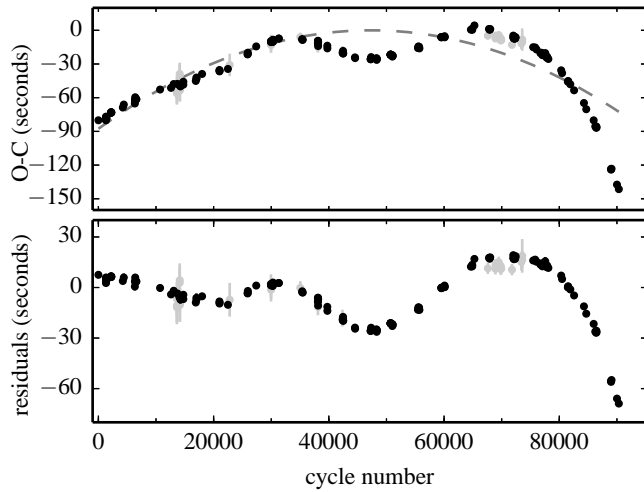
Figure 6.10: O-C diagram of the mid-egress times of HU Aqr including the best quadratic fit as the dashed grey line (top panel), and the residuals relative to that fit (bottom panel). O-C times with uncertainties exceeding 3 seconds have been greyed out for clarity, but all data were used to obtain the fit.

6.5.3   Magnetic alignment of the accretion spot

A last possibility I consider is that the accretion spot, the egress of which is the feature being timed, moves with respect to the line of centres between the two stars. This could happen either because of asynchronous rotation of the white dwarf (Cropper, 1988), or because the spot itself migrates on the surface of the white dwarf (Cropper et al., 1989).

From Fig. 6.5 it is clear that the ingress and egress of the white dwarf last for ~ 30 seconds. Therefore the maximum libration of the spot on the surface of the white dwarf can generate O-C deviations with an amplitude of 15 seconds. For geometrical reasons, this would have to be accompanied by shifts in the time of maximum light from the accretion spot of ~ 0.25 orbital phases, an effect that has not been observed. Additionally, even with a large quadratic term removed from the original O-C times, an amplitude of 15 seconds is not large enough to explain the residuals, which still fluctuate by more than 20 seconds (Fig. 6.10). Furthermore, I find no correlation between the accretion state of the binary and the magnitude of the O-C deviations, in the original O-C diagram, nor in the residuals after removal of the best quadratic fit.

6.6   Conclusions

I have presented new eclipse observations across the optical spectrum of the eclipsing polar HU Aqr while in high as well as low accretion states. Using archival VLT+ULTRACAM observations of HU Aqr in an extreme low state, I measured the inclination of the binary to be $i = 87°$, giving a mass ratio of $q = 0.22$ and the stellar masses of $M_{WD} = 0.81$ M$_\odot$ and $M_2 = 0.18$ M$_\odot$.

From the egress feature of the accretion spot on the white dwarf I have determined the

mid-egress times. The ULTRACAM data shows that times from data taken using different SDSS filters agree well with each other. The new O-C times indicate that the eclipses are still occurring increasingly earlier than expected when using a linear ephemeris and a constant orbital period. They also confirm the result found by Schwope & Thinius (2014) that the circumbinary planet proposed by Goździewski et al. (2012) does not exist, nor can the entire set of egress times be well fitted by a model introducing one or multiple planets.

Given the large amplitude of the observed O-C times, Applegate's mechanism can likely be excluded, and also asynchronous rotation of the white dwarf or movement of the accretion spot seem unlikely. Also a long-term orbital period change induced by gravitational wave emission or constant magnetic braking is not large enough to explain the observed O-C variations. Currently, my best guess is that more than one of these mechanisms act at the same time, working together to produce the dramatic eclipse time variations observed in this binary.

$\star \star \star$

Chapter 7

Concluding summary

In this thesis I have presented a detailed study of the eclipsing double white dwarf binary CSS 41177. The data consisted of high-speed ULTRACAM photometry of the primary and secondary eclipses, phase-resolved X-shooter spectroscopy and far-ultraviolet spectra obtained with COS on the Hubble Space Telescope. Using Markov chain Monte Carlo analyses I have determined the white dwarf masses and radii, thereby exploring a new part of the mass – radius parameter space, and providing empirical data at the low-mass end to test theoretical relations against. I have also measured the white dwarf effective temperatures and surface gravities, and showed that the cooler of the two white dwarfs is a prime candidate for showing non-radial g-mode pulsations. Although none have been found so far, further searches may reveal low-amplitude pulsations, and will in either case further constrain the boundaries of the empirical ZZ Ceti instability strip, as well as shed light on whether the strip is pure or not.

I also presented an analysis of the (non-eclipsing) double white dwarf binary SDSS J1257 +5428, for which far-ultraviolet HST spectra and SDSS magnitude measurements at optical wavelengths showed that the massive ~ 1 $M_\odot$ white dwarf is much younger than its extremely low-mass ~ 0.2 $M_\odot$ white dwarf companion. This is in direct contradiction to the general expectation that more massive stars evolve faster, and their remnants should therefore be older than remnants of lower mass stars. Despite several suggestion to explain this apparent paradox, including the possibility that SDSS J1257+5428 is actually a triple system or consist of a chance alignment, I was unable to solve the puzzle presented by this system. Future observations to further determine the system parameters could include radio observations to search for a possible neutron star component, as well as high signal-to-noise phase-resolved spectroscopy to ascertain whether lines originating in the massive white dwarf show radial velocity variations consistent with the star being indeed part of the binary. More detailed determination of the mass and cooling age of the extremely low-mass white dwarf could also help clarify which physical processes need to be included in detailed white dwarf evolutionary models.

Next, I introduced a large eclipse timing programme, that currently includes 71 binaries with regular monitoring of their eclipses to search for apparent and/or real orbital period variations. Currently, there are two contending theories to explain these ubiquitous variations. The first explains them as a results of redistribution of angular momentum in the low-mass main sequence star companions to the white dwarfs, caused by Solar-like

magnetic cycles in these stars, and which couple to the binary's orbital period. The second suggests that planet-like or brown dwarf-like bodies of mass are present on wide orbits around the close binary. These cause a reflex motion of the binary around the system's barycentre, which results in the observed variations in the eclipse arrival times. The results from my programme show that all binaries with long observational baseline show substantial O-C variations, and that for many of the more extreme examples neither theoretical explanation is satisfactory. Besides regular eclipse observations of all the binaries in the programme, there are several approaches that can be taken to clarify the underlying cause of the O-C variations. These include searches for second, independant clocks to confirm the O-C variations, such as white dwarf pulsations, direct adaptive-optics assisted imaging to search for suspected brown dwarf circumbinary companions, direct high-precision astrometric observations, and X-ray observations to measure starspots and pin down the magnetic variability in the M-dwarfs, to name a few.

Finally, I included a detailed look at the cataclysmic variable and polar HU Aqr. This binary is part of the timing pogramme, and shows some of the largest O-C variations. All planetary companions previously proposed to accompany this binary have been disproved by new data and by dynamical stability analyses. However, the apparent variability seems also too large to be caused by Applegate's mechanism, although perhaps a variation of that mechanism may still be able to explain the observations. Model fits to archival ULTRA-CAM light curves taken when HU Aqr was in a low-state revealed a small remnant spot on the surface of the white dwarf, and allowed me to determine the system's inclination and stellar masses. With it's extreme variability caused by the semi-detached nature of the binary, and with the seemingly inexplicable eclipse timing variability, this system is likely to be a favourite target for observers around the world in years to come.

$$\star\,\star\,\star$$

Appendix A

Eclipse times of white dwarf binaries in the timing program

This appendix lists all eclipse times obtained for the white dwarf binaries in the timing program as described in Chapter 5 and Tables 5.1 and 5.2. A few details of the telescopes and instruments used for these observations, and a reminder of their abbreviations, can be found in Table A.1. The rest of this appendix consists of tables, one for each individual binary, with for each eclipse observation the relevant cycle number, eclipse time, and the reference if this time is published and the telescope and instrument used to obtain the observations if not published. The eclipse times are either mid-eclipse or mid-egress times, as specified in the table captions. O-C diagrams for each binary that include both the eclipse times listed in this appendix as well as any that may be available in the literature can be found in Appendix B.

Table A.1: Telescopes and instruments used for eclipse observations, listed in aphabetical order.

telescope or instrument	details and/or explanation of acronym
ACAM	Imager mounted on the WHT.
DFOSC	Danish Faint Object Spectrograph and Camera, mounted on the DT.
DT	1.5 m Danish Telescope situated at La Silla, Chile.
HAWK-I	High-Acuity Wide-field K-band Imager on the VLT.
INT	2.5 m Isaac Newton Telescope, situated on La Palma, Spain.
LT	2.0 m robotic Liverpool Telescope, situated on La Palma, Spain.
NTT	3.6 m New Technology Telescope situated at La Silla, Chile.
pt5m	0.5 m Sheffield telescope, situated on La Palma, Spain.
RISE	High-speed photometer on the LT, see Sect. 2.3.3.
SOAR	4.1 m Southern Astrophysical Research telescope, situated at Cerro Pachón, Chile.
SOI	SOAR Optical Imager.
SOFI	Son of Isaac, infrared spectrograph and imaging camera on the NTT.
TNT	2.4 m Thai National Telescope, situated on Doi Inthanon, Thailand.
TRAPPIST	0.6 m robotic telescope at La Silla, Chile, equiped with TRAPPISTCAM photometer.
ULTRACAM	Three-channel high-speed photometer, see Sect. 2.3.1.
ULTRASPEC	High-speed photometer, see Sect. 2.3.2.
VLT	8.0 m Unit Telescope of the Very Large Telescope, situated on Paranal, Chile.
WFC	Wide-Field Camera on the INT, see Sect. 2.3.4.
WHT	4.2 m William Herschel Telescope, situated on La Palma, Spain.

Table A.2: 0 published and 2 unpublished mid-eclipse times for SDSS J0024+1745, a detached white dwarf + M-dwarf of unknown spectral type. Numbers in parenthesis indicate the uncertainty in the last digit(s).

cycle	MJD(UTC)	BMJD(TDB)	pub?	source
15767	56482.195608(89)	56482.196806(89)	no	LT+RISE
17976	56924.075625(102)	56924.081918(102)	no	LT+RISE

Table A.3: 0 published and 25 unpublished mid-eclipse times for SDSS J0106-0014, a detached white dwarf + M-dwarf of spectral type M8. Numbers in parenthesis indicate the uncertainty in the last digit(s). See Fig. B.1 for the O-C diagram of all eclipse times with respect to the best linear ephemeris.

cycle	MJD(UTC)	BMJD(TDB)	pub?	source
0	55059.051789(16)	55059.056118(16)	no	LT+RISE
12	55060.071890(15)	55060.076296(15)	no	LT+RISE
24	55061.092000(17)	55061.096482(17)	no	LT+RISE
36	55062.112095(13)	55062.116652(13)	no	LT+RISE
37	55062.197102(21)	55062.201665(21)	no	LT+RISE
47	55063.047217(21)	55063.051841(21)	no	LT+RISE
61	55064.237361(20)	55064.242071(20)	no	LT+RISE
107	55068.147757(13)	55068.152733(13)	no	LT+RISE
319	55086.170040(8)	55086.175990(8)	no	WHT+ACAM
471	55099.091971(4)	55099.098325(4)	no	WHT+ACAM
5317	55511.077129(2)	55511.082625(2)	no	NTT+ULTRACAM
5458	55523.065056(5)	55523.069785(5)	no	NTT+ULTRACAM
5493	55526.040814(1)	55526.045324(1)	no	NTT+ULTRACAM
5495	55526.210854(5)	55526.215351(5)	no	NTT+ULTRACAM
5505	55527.061073(1)	55527.065506(1)	no	NTT+ULTRACAM
5740	55547.041403(5)	55547.044112(5)	no	NTT+ULTRACAM
5741	55547.126414(11)	55547.129116(11)	no	NTT+ULTRACAM
9502	55866.865847(2)	55866.871804(2)	no	WHT+ULTRACAM
9514	55867.886073(3)	55867.891987(3)	no	WHT+ULTRACAM
13150	56177.001963(2)	56177.007702(2)	no	WHT+ULTRACAM
13151	56177.086976(2)	56177.092719(2)	no	WHT+ULTRACAM
13549	56210.922336(1)	56210.928820(1)	no	WHT+ULTRACAM
17856	56577.083313(10)	56577.089804(10)	no	LT+RISE
19108	56683.530225(5)	56683.528974(5)	no	TNT+ULTRASPEC
19132	56685.570797(7)	56685.569356(7)	no	TNT+ULTRASPEC

Table A.4: 5 published and 9 unpublished mid-eclipse times for SDSS J0110+1326, a detached white dwarf + M-dwarf of spectral type M4. Numbers in parenthesis indicate the uncertainty in the last digit(s). See Fig. B.2 for the O-C diagram of all eclipse times with respect to the best linear ephemeris.

cycle	MJD(UTC)	BMJD(TDB)	pub?	source
0	-	53993.948697(200)	yes	Pyrzas et al. 2009

Table A.4: Continues on next page.

Table A.4: Times for SDSS J0110+1326; continued from previous page.

cycle	MJD(UTC)	BMJD(TDB)	pub?	source
3	-	53994.946534(200)	yes	Pyrzas et al. 2009
6	-	53995.944916(200)	yes	Pyrzas et al. 2009
1170	-	54383.192816(200)	yes	Pyrzas et al. 2009
1203	-	54394.171253(1)	yes	Parsons et al. 2010b
5435	55802.096813(5)	55802.101590(5)	no	LT+RISE
5711	55893.918364(4)	55893.923129(4)	no	LT+RISE
5786	55918.871981(5)	55918.874640(5)	no	LT+RISE
6352	56107.175967(8)	56107.175339(8)	no	LT+RISE
6604	56191.006352(4)	56191.012426(4)	no	LT+RISE
6661	56209.969071(1)	56209.975558(1)	no	WHT+ULTRACAM
7561	-	56509.393675(11)	no	VLT+HAWK-I
7581	56516.043888(5)	56516.047398(5)	no	LT+RISE
7853	56606.532343(6)	56606.538199(6)	no	TNT+ULTRASPEC

Table A.5: 6 published and 1 unpublished mid-eclipse times for SDSS J0138-0016, a detached white dwarf + M-dwarf of spectral type M5. Numbers in parenthesis indicate the uncertainty in the last digit(s). See Fig. B.3 for the O-C diagram of all eclipse times with respect to the best linear ephemeris.

cycle	MJD(UTC)	BMJD(TDB)	pub?	source
0	55867.001238(10)	55867.007406(10)	yes	Parsons et al. 2012b
1	55867.074018(10)	55867.080184(10)	yes	Parsons et al. 2012b
397	55895.890328(37)	55895.895017(37)	yes	Parsons et al. 2012b
411	55896.909180(52)	55896.913796(52)	yes	Parsons et al. 2012b
426	55898.000697(91)	55898.005233(91)	yes	Parsons et al. 2012b
1070	55944.865636(17)	55944.865875(17)	yes	Parsons et al. 2012b
4290	56179.163688(21)	56179.169083(21)	no	WHT+ULTRACAM

Table A.6: 0 published and 6 unpublished mid-eclipse times for PTFEB28.235, a detached white dwarf + M-dwarf of spectral type M3. Numbers in parenthesis indicate the uncertainty in the last digit(s). See Fig. B.4 for the O-C diagram of all eclipse times with respect to the best linear ephemeris.

cycle	MJD(UTC)	BMJD(TDB)	pub?	source
-705	55922.949864(45)	55922.953548(45)	no	LT+RISE
0	56195.163625(34)	56195.168502(34)	no	LT+RISE
243	56288.992035(95)	56288.995675(95)	no	LT+RISE
992	56578.194149(32)	56578.199794(32)	no	LT+RISE
1283	56690.560327(25)	56690.560841(25)	no	TNT+ULTRASPEC
1906	56931.108651(32)	56931.113825(32)	no	LT+RISE

Table A.7: 0 published and 1 unpublished mid-eclipse times for SDSS J0259-0044, a detached white dwarf + M-dwarf of spectral type M3. Numbers in parenthesis indicate the uncertainty in the last digit(s).

cycle	MJD(UTC)	BMJD(TDB)	pub?	source
30459	56211.096093(11)	56211.101880(11)	no	WHT+ULTRACAM

Table A.8: 13 published and 11 unpublished mid-eclipse times for SDSS J0303+0054, a detached white dwarf + M-dwarf of spectral type M4.5. Numbers in parenthesis indicate the uncertainty in the last digit(s). See Fig. B.5 for the O-C diagram of all eclipse times with respect to the best linear ephemeris.

cycle	MJD(UTC)	BMJD(TDB)	pub?	source
2968	54390.122320(2)	54390.128292(2)	yes	Parsons et al. 2010b
2976	54391.197780(2)	54391.203787(2)	yes	Parsons et al. 2010b
3058	54402.221411(18)	54402.227653(18)	yes	Parsons et al. 2010b
11300	55510.256732(2)	55510.262978(2)	no	NTT+ULTRACAM
11307	55511.197801(3)	55511.204039(3)	no	NTT+ULTRACAM
11411	55525.179624(4)	55525.185565(4)	no	NTT+ULTRACAM
13443	-	55798.362876(13)	yes	Backhaus et al. 2012
13510	-	55807.370189(14)	yes	Backhaus et al. 2012
13533	-	55810.462273(12)	yes	Backhaus et al. 2012
13874	-	55856.305526(11)	yes	Backhaus et al. 2012
13897	-	55859.397585(11)	yes	Backhaus et al. 2012
13926	-	55863.296278(10)	yes	Backhaus et al. 2012
13948	-	55866.253894(13)	yes	Backhaus et al. 2012
16283	56180.161925(2)	56180.165824(2)	yes	Parsons et al. 2013a
16505	56210.005261(2)	56210.010984(2)	yes	Parsons et al. 2013a
16535	56214.038239(2)	56214.044118(2)	yes	Parsons et al. 2013a
17011	56278.031604(17)	56278.036452(17)	no	LT+RISE
18671	56501.203048(30)	56501.202982(30)	no	LT+RISE
18701	56505.235763(5)	56505.236075(5)	no	WHT+ULTRACAM
19191	56571.105019(13)	56571.110566(13)	no	LT+RISE
19800	56652.978910(13)	56652.983082(13)	no	LT+RISE
20035	56684.574551(5)	56684.575920(5)	no	TNT+ULTRASPEC
21386	56866.201304(12)	56866.201227(12)	no	LT+RISE
22296	56988.533625(9)	56988.539519(9)	no	TNT+ULTRASPEC

Table A.9: 0 published and 4 unpublished mid-eclipse times for SDSS J0308-0054, a detached white dwarf + M-dwarf of spectral type M4.5. Numbers in parenthesis indicate the uncertainty in the last digit(s). See Fig. B.6 for the O-C diagram of all eclipse times with respect to the best linear ephemeris.

cycle	MJD(UTC)	BMJD(TDB)	pub?	source
0	56181.139717(27)	56181.143583(27)	no	WHT+ULTRACAM
156	56210.147584(12)	56210.153218(12)	no	WHT+ULTRACAM
182	56214.982363(18)	56214.988184(18)	no	WHT+ULTRACAM

Table A.9: Times for SDSS J0308-0054; continued from previous page.

cycle	MJD(UTC)	BMJD(TDB)	pub?	source
2707	56684.534261(37)	56684.535713(37)	no	TNT+ULTRASPEC

Table A.10: 0 published and 11 unpublished mid-eclipse times for SDSS J0314+0206, a detached white dwarf + K-dwarf of spectral type K5-M5. Numbers in parenthesis indicate the uncertainty in the last digit(s). See Fig. B.7 for the O-C diagram of all eclipse times with respect to the best linear ephemeris.

cycle	MJD(UTC)	BMJD(TDB)	pub?	source
0	56195.201610(7)	56195.206355(7)	no	LT+RISE
62	56214.128990(1)	56214.134750(1)	no	WHT+ULTRACAM
278	56280.073917(10)	56280.078845(10)	no	LT+RISE
464	56336.864053(11)	56336.864026(11)	no	LT+RISE
1035	56511.187938(11)	56511.188489(11)	no	LT+RISE
1225	56569.189593(10)	56569.194874(10)	no	LT+RISE
1519	56658.948160(8)	56658.952121(8)	no	LT+RISE
2283	56892.196827(9)	56892.198868(9)	no	LT+RISE
2414	56932.187569(8)	56932.192735(8)	no	LT+RISE
2717	57024.693727(25)	57024.697662(25)	no	TNT+ULTRASPEC
2913	57084.537436(13)	57084.535843(13)	no	TNT+ULTRASPEC

Table A.11: 14 published and 13 unpublished mid-eclipse times for NLTT 11748, a detached double white dwarf binary. Numbers in parenthesis indicate the uncertainty in the last digit(s). See Fig. B.8 for the O-C diagram of all eclipse times with respect to the best linear ephemeris.

cycle	MJD(UTC)	BMJD(TDB)	pub?	source
-1093	-	55515.120443(21)	yes	Kaplan et al. 2014
-1050	-	55525.228090(18)	yes	Kaplan et al. 2014
-1046	-	55526.168300(13)	yes	Kaplan et al. 2014
-1042	-	55527.108548(12)	yes	Kaplan et al. 2014
-1042	55527.101943(10)	55527.108361(10)	no	NTT+ULTRACAM
-965	-	55545.208237(16)	yes	Kaplan et al. 2014
-961	-	55546.148475(18)	yes	Kaplan et al. 2014
-957	-	55547.088715(23)	yes	Kaplan et al. 2014
731	-	55943.870809(9)	yes	Kaplan et al. 2014
736	-	55945.046118(28)	yes	Kaplan et al. 2014
748	-	55947.866825(9)	yes	Kaplan et al. 2014
748	55947.863289(8)	55947.866623(8)	no	WHT+ULTRACAM
753	-	55949.042137(10)	yes	Kaplan et al. 2014
1698	-	56171.174286(11)	yes	Kaplan et al. 2014
1711	-	56174.230072(11)	yes	Kaplan et al. 2014
1736	-	56180.106572(12)	yes	Kaplan et al. 2014
1736	56180.103694(9)	56180.106395(9)	no	WHT+ULTRACAM
3530	56601.798585(42)	56601.804886(42)	no	TNT+ULTRASPEC
3551	56606.734723(29)	56606.741123(29)	no	TNT+ULTRASPEC

Table A.11: Continues on next page.

Table A.11: Times for NLTT 11748; continued from previous page.

cycle	MJD(UTC)	BMJD(TDB)	pub?	source
3891	56686.659143(21)	56686.661731(21)	no	TNT+ULTRASPEC
3908	56690.655596(24)	56690.657800(24)	no	TNT+ULTRASPEC
4710	-	56879.176259(13)	no	WHT+ULTRACAM
5176	56988.708002(19)	56988.714435(19)	no	TNT+ULTRASPEC
5180	56989.648255(19)	56989.654675(19)	no	TNT+ULTRASPEC
5189	56991.763850(24)	56991.770234(24)	no	TNT+ULTRASPEC
5193	56992.704057(26)	56992.710423(26)	no	TNT+ULTRASPEC
5571	57081.563667(67)	57081.563330(67)	no	TNT+ULTRASPEC

Table A.12: 209 published and 1 unpublished mid-eclipse times for V471 Tau, a detached white dwarf + K-dwarf of spectral type K2. Numbers in parenthesis indicate the uncertainty in the last digit(s). See Fig. B.9 for the O-C diagram of all eclipse times with respect to the best linear ephemeris.

cycle	MHJD(TT)	HMJD(TDB)	BMJD(TDB)	pub?	source
-25741	40612.171250(12)	-	-	yes	İbanoğlu et al. 2005
-25739	40613.213590(12)	-	-	yes	İbanoğlu et al. 2005
-25716	40625.200840(12)	-	-	yes	İbanoğlu et al. 2005
-25695	40636.145780(12)	-	-	yes	İbanoğlu et al. 2005
-25213	40887.356070(12)	-	-	yes	İbanoğlu et al. 2005
-25196	40896.216160(12)	-	-	yes	İbanoğlu et al. 2005
-25192	40898.300840(12)	-	-	yes	İbanoğlu et al. 2005
-25192	40898.300870(12)	-	-	yes	İbanoğlu et al. 2005
-25192	40898.300900(93)	-	-	yes	İbanoğlu et al. 2005
-25190	40899.343150(12)	-	-	yes	İbanoğlu et al. 2005
-25190	40899.343320(12)	-	-	yes	İbanoğlu et al. 2005
-25175	40907.161020(12)	-	-	yes	İbanoğlu et al. 2005
-25167	40911.330420(12)	-	-	yes	İbanoğlu et al. 2005
-25052	40971.266660(12)	-	-	yes	İbanoğlu et al. 2005
-24968	41015.046020(12)	-	-	yes	İbanoğlu et al. 2005
-24943	41028.075710(12)	-	-	yes	İbanoğlu et al. 2005
-24597	41208.405310(12)	-	-	yes	İbanoğlu et al. 2005
-24578	41218.307720(12)	-	-	yes	İbanoğlu et al. 2005
-24551	41232.379670(12)	-	-	yes	İbanoğlu et al. 2005
-24507	41255.311690(12)	-	-	yes	İbanoğlu et al. 2005
-24486	41266.256650(12)	-	-	yes	İbanoğlu et al. 2005
-24469	41275.116730(12)	-	-	yes	İbanoğlu et al. 2005
-24457	41281.370990(12)	-	-	yes	İbanoğlu et al. 2005
-24455	41282.413310(12)	-	-	yes	İbanoğlu et al. 2005
-24444	41288.145960(12)	-	-	yes	İbanoğlu et al. 2005
-24427	41297.006280(12)	-	-	yes	İbanoğlu et al. 2005
-24423	41299.091240(12)	-	-	yes	İbanoğlu et al. 2005
-24379	41322.023290(12)	-	-	yes	İbanoğlu et al. 2005
-24373	41325.150390(12)	-	-	yes	İbanoğlu et al. 2005

Table A.12: Continues on next page.

Table A.12: Times for V471 Tau; continued from previous page.

cycle	MHJD(TT)	HMJD(TDB)	BMJD(TDB)	pub?	source
-24371	41326.192840(12)	-	-	yes	İbanoğlu et al. 2005
-24308	41359.027340(12)	-	-	yes	İbanoğlu et al. 2005
-24302	41362.154500(93)	-	-	yes	İbanoğlu et al. 2005
-24279	41374.141650(12)	-	-	yes	İbanoğlu et al. 2005
-23725	41662.877330(12)	-	-	yes	İbanoğlu et al. 2005
-23721	41664.962020(12)	-	-	yes	İbanoğlu et al. 2005
-23636	41709.262600(93)	-	-	yes	İbanoğlu et al. 2005
-23631	41711.868490(12)	-	-	yes	İbanoğlu et al. 2005
-23114	41981.320200(93)	-	-	yes	İbanoğlu et al. 2005
-23112	41982.362670(12)	-	-	yes	İbanoğlu et al. 2005
-23108	41984.447430(12)	-	-	yes	İbanoğlu et al. 2005
-23067	42005.815910(12)	-	-	yes	İbanoğlu et al. 2005
-23065	42006.858290(12)	-	-	yes	İbanoğlu et al. 2005
-23063	42007.900680(12)	-	-	yes	İbanoğlu et al. 2005
-23049	42015.197210(12)	-	-	yes	İbanoğlu et al. 2005
-23047	42016.239570(12)	-	-	yes	İbanoğlu et al. 2005
-23047	42016.239580(12)	-	-	yes	İbanoğlu et al. 2005
-23045	42017.281950(12)	-	-	yes	İbanoğlu et al. 2005
-23030	42025.099710(12)	-	-	yes	İbanoğlu et al. 2005
-23017	42031.875140(12)	-	-	yes	İbanoğlu et al. 2005
-22990	42045.946940(12)	-	-	yes	İbanoğlu et al. 2005
-22959	42062.103690(12)	-	-	yes	İbanoğlu et al. 2005
-22946	42068.879020(12)	-	-	yes	İbanoğlu et al. 2005
-22904	42090.768880(12)	-	-	yes	İbanoğlu et al. 2005
-22423	42341.457870(12)	-	-	yes	İbanoğlu et al. 2005
-22421	42342.500320(12)	-	-	yes	İbanoğlu et al. 2005
-22414	42346.148460(12)	-	-	yes	İbanoğlu et al. 2005
-22385	42361.262850(12)	-	-	yes	İbanoğlu et al. 2005
-22383	42362.305180(12)	-	-	yes	İbanoğlu et al. 2005
-22336	42386.800820(12)	-	-	yes	İbanoğlu et al. 2005
-21604	42768.306750(12)	-	-	yes	İbanoğlu et al. 2005
-21566	42788.111660(12)	-	-	yes	İbanoğlu et al. 2005
-21495	42825.115630(12)	-	-	yes	İbanoğlu et al. 2005
-21449	42849.090030(12)	-	-	yes	İbanoğlu et al. 2005
-21011	43077.368340(12)	-	-	yes	İbanoğlu et al. 2005
-21009	43078.410540(12)	-	-	yes	İbanoğlu et al. 2005
-21007	43079.452840(12)	-	-	yes	İbanoğlu et al. 2005
-21005	43080.495340(12)	-	-	yes	İbanoğlu et al. 2005
-20277	43459.916550(12)	-	-	yes	İbanoğlu et al. 2005
-20273	43462.001350(12)	-	-	yes	İbanoğlu et al. 2005
-20271	43463.043750(12)	-	-	yes	İbanoğlu et al. 2005
-20238	43480.242580(12)	-	-	yes	İbanoğlu et al. 2005
-20236	43481.284940(12)	-	-	yes	İbanoğlu et al. 2005

Table A.12: Continues on next page.

Table A.12: Times for V471 Tau; continued from previous page.

cycle	MHJD(TT)	HMJD(TDB)	BMJD(TDB)	pub?	source
-20177	43512.034750(12)	-	-	yes	İbanoğlu et al. 2005
-20173	43514.119520(12)	-	-	yes	İbanoğlu et al. 2005
-20164	43518.810310(12)	-	-	yes	İbanoğlu et al. 2005
-19645	43789.304160(12)	-	-	yes	İbanoğlu et al. 2005
-19643	43790.346460(12)	-	-	yes	İbanoğlu et al. 2005
-19603	43811.193840(12)	-	-	yes	İbanoğlu et al. 2005
-19599	43813.278540(12)	-	-	yes	İbanoğlu et al. 2005
-19594	43815.884580(12)	-	-	yes	İbanoğlu et al. 2005
-19592	43816.926740(12)	-	-	yes	İbanoğlu et al. 2005
-19588	43819.011620(12)	-	-	yes	İbanoğlu et al. 2005
-19563	43832.041070(12)	-	-	yes	İbanoğlu et al. 2005
-19508	43860.706310(12)	-	-	yes	İbanoğlu et al. 2005
-19502	43863.833390(12)	-	-	yes	İbanoğlu et al. 2005
-18884	44185.924380(12)	-	-	yes	İbanoğlu et al. 2005
-18880	44188.009100(93)	-	-	yes	İbanoğlu et al. 2005
-18824	44217.195400(93)	-	-	yes	İbanoğlu et al. 2005
-18709	44277.131460(12)	-	-	yes	İbanoğlu et al. 2005
-18702	44280.779790(12)	-	-	yes	İbanoğlu et al. 2005
-18285	44498.112950(12)	-	-	yes	İbanoğlu et al. 2005
-18250	44516.354500(93)	-	-	yes	İbanoğlu et al. 2005
-18248	44517.397090(12)	-	-	yes	İbanoğlu et al. 2005
-18247	44517.918020(12)	-	-	yes	İbanoğlu et al. 2005
-18227	44528.341700(93)	-	-	yes	İbanoğlu et al. 2005
-18221	44531.468700(93)	-	-	yes	İbanoğlu et al. 2005
-18198	44543.456010(12)	-	-	yes	İbanoğlu et al. 2005
-18187	44549.189080(12)	-	-	yes	İbanoğlu et al. 2005
-18137	44575.248430(12)	-	-	yes	İbanoğlu et al. 2005
-18133	44577.332970(12)	-	-	yes	İbanoğlu et al. 2005
-18120	44584.108360(12)	-	-	yes	İbanoğlu et al. 2005
-18112	44588.277460(12)	-	-	yes	İbanoğlu et al. 2005
-18111	44588.799090(12)	-	-	yes	İbanoğlu et al. 2005
-18017	44637.790460(12)	-	-	yes	İbanoğlu et al. 2005
-17560	44875.970780(12)	-	-	yes	İbanoğlu et al. 2005
-17493	44910.890140(12)	-	-	yes	İbanoğlu et al. 2005
-16777	45284.057160(12)	-	-	yes	İbanoğlu et al. 2005
-16759	45293.438610(12)	-	-	yes	İbanoğlu et al. 2005
-16700	45324.188210(12)	-	-	yes	İbanoğlu et al. 2005
-16677	45336.175570(12)	-	-	yes	İbanoğlu et al. 2005
-16539	45408.098640(12)	-	-	yes	İbanoğlu et al. 2005
-16537	45409.141010(12)	-	-	yes	İbanoğlu et al. 2005
-16148	45611.881260(12)	-	-	yes	İbanoğlu et al. 2005
-16144	45613.966070(12)	-	-	yes	İbanoğlu et al. 2005
-15989	45694.749500(93)	-	-	yes	İbanoğlu et al. 2005

Table A.12: Continues on next page.

Table A.12: Times for V471 Tau; continued from previous page.

cycle	MHJD(TT)	HMJD(TDB)	BMJD(TDB)	pub?	source
-15528	45935.014790(12)	-	-	yes	İbanoğlu et al. 2005
-15526	45936.057380(12)	-	-	yes	İbanoğlu et al. 2005
-15367	46018.925410(12)	-	-	yes	İbanoğlu et al. 2005
-15353	46026.222120(12)	-	-	yes	İbanoğlu et al. 2005
-15346	46029.870200(93)	-	-	yes	İbanoğlu et al. 2005
-15330	46038.209470(12)	-	-	yes	İbanoğlu et al. 2005
-15292	46058.013940(12)	-	-	yes	İbanoğlu et al. 2005
-15288	46060.098960(12)	-	-	yes	İbanoğlu et al. 2005
-15280	46064.268250(12)	-	-	yes	İbanoğlu et al. 2005
-15261	46074.170850(12)	-	-	yes	İbanoğlu et al. 2005
-14730	46350.919110(12)	-	-	yes	İbanoğlu et al. 2005
-14728	46351.961560(12)	-	-	yes	İbanoğlu et al. 2005
-14656	46389.486730(12)	-	-	yes	İbanoğlu et al. 2005
-14654	46390.529120(12)	-	-	yes	İbanoğlu et al. 2005
-13362	47063.897800(93)	-	-	yes	İbanoğlu et al. 2005
-13360	47064.940250(12)	-	-	yes	İbanoğlu et al. 2005
-13358	47065.982400(93)	-	-	yes	İbanoğlu et al. 2005
-12625	47448.009350(12)	-	-	yes	İbanoğlu et al. 2005
-12424	47552.767490(12)	-	-	yes	İbanoğlu et al. 2005
-12422	47553.809800(93)	-	-	yes	İbanoğlu et al. 2005
-12420	47554.852300(93)	-	-	yes	İbanoğlu et al. 2005
-11879	47836.812300(93)	-	-	yes	İbanoğlu et al. 2005
-11712	47923.850020(12)	-	-	yes	İbanoğlu et al. 2005
-11645	47958.769200(93)	-	-	yes	İbanoğlu et al. 2005
-11622	47970.756670(12)	-	-	yes	İbanoğlu et al. 2005
-11215	48182.878200(93)	-	-	yes	İbanoğlu et al. 2005
-11213	48183.920480(12)	-	-	yes	İbanoğlu et al. 2005
-10480	48565.948410(12)	-	-	yes	İbanoğlu et al. 2005
-10294	48662.888540(12)	-	-	yes	İbanoğlu et al. 2005
-9887	48875.010460(12)	-	-	yes	İbanoğlu et al. 2005
-9864	48886.997720(12)	-	-	yes	İbanoğlu et al. 2005
-9860	48889.082430(12)	-	-	yes	İbanoğlu et al. 2005
-9726	48958.921060(12)	-	-	yes	İbanoğlu et al. 2005
-9686	48979.768370(12)	-	-	yes	İbanoğlu et al. 2005
-9181	49242.966040(8)	-	-	yes	İbanoğlu et al. 2005
-9179	49244.008350(8)	-	-	yes	İbanoğlu et al. 2005
-8298	49703.171210(12)	-	-	yes	Guinan & Ribas 2001
-7809	49958.030100(15)	-	-	yes	İbanoğlu et al. 2005
-7611	50061.224580(12)	-	-	yes	Guinan & Ribas 2001
-7596	50069.042460(14)	-	-	yes	İbanoğlu et al. 2005
-6969	50395.824590(16)	-	-	yes	İbanoğlu et al. 2005
-6967	50396.867200(12)	-	-	yes	İbanoğlu et al. 2005
-6965	50397.909330(12)	-	-	yes	İbanoğlu et al. 2005

Table A.12: Continues on next page.

Table A.12: Times for V471 Tau; continued from previous page.

cycle	MHJD(TT)	HMJD(TDB)	BMJD(TDB)	pub?	source
-6963	50398.951870(14)	-	-	yes	İbanoğlu et al. 2005
-6391	50697.068730(16)	-	-	yes	İbanoğlu et al. 2005
-6330	50728.860850(15)	-	-	yes	İbanoğlu et al. 2005
-6328	50729.903280(16)	-	-	yes	İbanoğlu et al. 2005
-6326	50730.945880(16)	-	-	yes	İbanoğlu et al. 2005
-6324	50731.988120(15)	-	-	yes	İbanoğlu et al. 2005
-5643	51086.914160(16)	-	-	yes	İbanoğlu et al. 2005
-5641	51087.956210(15)	-	-	yes	İbanoğlu et al. 2005
-5547	51136.947500(12)	-	-	yes	İbanoğlu et al. 2005
-5370	51229.197480(12)	-	-	yes	Guinan & Ribas 2001
-4931	51457.996860(19)	-	-	yes	İbanoğlu et al. 2005
-4908	51469.984040(17)	-	-	yes	İbanoğlu et al. 2005
-4862	51493.958600(14)	-	-	yes	İbanoğlu et al. 2005
-4796	51528.356930(12)	-	-	yes	Guinan & Ribas 2001
-4796	51528.356990(12)	-	-	yes	Guinan & Ribas 2001
-4777	51538.259560(12)	-	-	yes	Guinan & Ribas 2001
-4777	51538.259610(12)	-	-	yes	Guinan & Ribas 2001
-4689	51584.123790(12)	-	-	yes	Guinan & Ribas 2001
-4271	51801.978880(14)	-	-	yes	İbanoğlu et al. 2005
-4269	51803.020600(17)	-	-	yes	İbanoğlu et al. 2005
-4251	51812.402560(12)	-	-	yes	Guinan & Ribas 2001
-4244	51816.050520(15)	-	-	yes	İbanoğlu et al. 2005
-4230	51823.347390(12)	-	-	yes	Guinan & Ribas 2001
-4137	51871.817260(16)	-	-	yes	İbanoğlu et al. 2005
-4135	51872.859770(16)	-	-	yes	İbanoğlu et al. 2005
-3519	52193.909220(15)	-	-	yes	İbanoğlu et al. 2005
-3511	52198.078770(10)	-	-	yes	İbanoğlu et al. 2005
-3511	52198.079020(16)	-	-	yes	İbanoğlu et al. 2005
-3308	52303.879050(16)	-	-	yes	İbanoğlu et al. 2005
-3291	52312.739330(7)	-	-	yes	İbanoğlu et al. 2005
-2832	52551.962380(7)	-	-	yes	İbanoğlu et al. 2005
-2809	52563.949630(7)	-	-	yes	İbanoğlu et al. 2005
-2805	52566.034460(7)	-	-	yes	İbanoğlu et al. 2005
-2788	52574.894440(8)	-	-	yes	İbanoğlu et al. 2005
-2786	52575.936900(8)	-	-	yes	İbanoğlu et al. 2005
-2147	52908.973410(9)	-	-	yes	İbanoğlu et al. 2005
-1946	53013.730870(10)	-	-	yes	İbanoğlu et al. 2005
-1395	53300.903260(10)	-	-	yes	İbanoğlu et al. 2005
-1395	53300.903310(7)	-	-	yes	İbanoğlu et al. 2005
-1307	53346.767340(6)	-	-	yes	İbanoğlu et al. 2005
0	54027.954130(170)	-	-	yes	Kundra & Hric 2011
52	54055.055550(210)	-	-	yes	Kundra & Hric 2011
1500	54809.728950(190)	-	-	yes	Kundra & Hric 2011

Table A.12: Continues on next page.

Table A.12: Times for V471 Tau; continued from previous page.

cycle	MHJD(TT)	HMJD(TDB)	BMJD(TDB)	pub?	source
1642	54883.736990(180)	-	-	yes	Kundra & Hric 2011
1988	55064.066360(200)	-	-	yes	Kundra & Hric 2011
2009	55075.011400(230)	-	-	yes	Kundra & Hric 2011
2011	55076.053640(180)	-	-	yes	Kundra & Hric 2011
2848	-	55512.284058(2)	-	yes	Hardy et al. 2015
2886	-	55532.088988(18)	-	yes	Hardy et al. 2015
2911	-	55545.118594(19)	-	yes	Hardy et al. 2015
2915	-	55547.203361(27)	-	yes	Hardy et al. 2015
3617	-	-	55913.073912(43)	no	pt5m

Table A.13: 21 published and 14 unpublished mid-eclipse times for RR Cae, a detached white dwarf + M-dwarf of spectral type M4. Numbers in parenthesis indicate the uncertainty in the last digit(s). See Fig. B.10 for the O-C diagram of all eclipse times with respect to the best linear ephemeris.

cycle	MJD(UTC)	BMJD(TDB)	pub?	source
-5932	-	49720.978524(3)	yes	Maxted et al. 2007
-5929	-	49721.889675(3)	yes	Maxted et al. 2007
-5916	-	49725.837828(4)	yes	Maxted et al. 2007
-2708	-	50700.119201(4)	yes	Maxted et al. 2007
-2544	-	50749.926547(2)	yes	Maxted et al. 2007
-2534	-	50752.963587(2)	yes	Maxted et al. 2007
-2524	-	50756.000622(2)	yes	Maxted et al. 2007
-1572	-	51045.126463(2)	yes	Maxted et al. 2007
1	-	51522.852260(30)	yes	Maxted et al. 2007
5	-	51524.067070(30)	yes	Maxted et al. 2007
18	-	51528.015180(40)	yes	Maxted et al. 2007
31	-	51531.963350(30)	yes	Maxted et al. 2007
5616	-	53228.148145(2)	yes	Maxted et al. 2007
7173	-	53701.014824(1)	yes	Parsons et al. 2010b
7174	-	53701.318536(0)	yes	Parsons et al. 2010b
12999	-	55470.392581(24)	no	NTT+SOFI
13147	-	55515.340786(0)	no	NTT+ULTRACAM
13170	-	55522.325975(0)	no	NTT+ULTRACAM
13186	-	55527.185233(0)	no	NTT+ULTRACAM
13206	-	55533.259310(50)	yes	Qian et al. 2012
13219	-	55537.207490(50)	yes	Qian et al. 2012
13607	-	55655.044470(20)	yes	Qian et al. 2012
14378	-	55889.199910(20)	yes	Qian et al. 2012
14385	-	55891.325850(20)	yes	Qian et al. 2012
14388	-	55892.236950(20)	yes	Qian et al. 2012
15527	56238.152426(9)	56238.155336(9)	no	SOAR+SOI
15600	56260.323007(9)	56260.325711(9)	no	VLT+HAWKI
15603	56261.234117(7)	56261.236806(7)	no	VLT+HAWKI

Table A.13: Continues on next page.

Table A.13: Times for RR Cae; continued from previous page.

cycle	MJD(UTC)	BMJD(TDB)	pub?	source
15889	56348.096135(14)	56348.096035(14)	no	TRAPPIST
16443	56516.346760(17)	56516.347811(17)	no	TRAPPIST
16545	56547.323470(17)	56547.325558(17)	no	TRAPPIST
17242	56759.008165(18)	56759.006916(18)	no	TRAPPIST
17298	56776.015747(20)	56776.014355(20)	no	TRAPPIST
18306	-	57082.147575(3)	no	DT+DFOSC
18309	-	57083.058679(3)	no	DT+DFOSC

Table A.14: 1 published and 4 unpublished mid-eclipse times for SDSS J0821+4559, a detached white dwarf + M-dwarf of spectral type M2. Numbers in parenthesis indicate the uncertainty in the last digit(s). See Fig. B.11 for the O-C diagram of all eclipse times with respect to the best linear ephemeris.

cycle	MJD(UTC)	BMJD(TDB)	pub?	source
0	55989.034455(23)	55989.038796(23)	yes	Parsons et al. 2013b
562	56275.143526(12)	56275.148530(12)	no	LT+RISE
1318	56660.016368(10)	56660.022091(10)	no	LT+RISE
1432	56718.054178(11)	56718.058612(11)	no	LT+RISE
2152	57084.600487(22)	57084.604843(22)	no	TNT+ULTRASPEC

Table A.15: 5 published and 13 unpublished mid-eclipse times for CSS 40190, a detached white dwarf + M-dwarf of spectral type M7. Numbers in parenthesis indicate the uncertainty in the last digit(s). See Fig. B.12 for the O-C diagram of all eclipse times with respect to the best linear ephemeris.

cycle	MJD(UTC)	BMJD(TDB)	pub?	source
15941	55543.335763(2)	55543.340495(2)	no	NTT+ULTRACAM
16141	-	55569.362966(9)	yes	Backhaus et al. 2012
16516	-	55618.155072(11)	yes	Backhaus et al. 2012
18294	-	55849.494786(16)	yes	Backhaus et al. 2012
18355	-	55857.431650(13)	yes	Backhaus et al. 2012
18417	-	55865.498586(15)	yes	Backhaus et al. 2012
22196	56357.187831(12)	56357.193085(12)	no	VLT+HAWKI
22479	56394.012591(15)	56394.014858(15)	no	VLT+HAWKI
24470	56653.062854(10)	56653.068443(10)	no	LT+RISE
24976	56718.899818(16)	56718.905274(16)	no	LT+RISE
25135	56739.589110(7)	56739.593127(7)	no	TNT+ULTRASPEC
25150	56741.540965(18)	56741.544821(18)	no	TNT+ULTRASPEC
25158	56742.581934(13)	56742.585704(13)	no	TNT+ULTRASPEC
27059	56989.925640(6)	56989.929193(6)	no	TNT+ULTRASPEC
27092	56994.218961(11)	56994.222880(11)	no	LT+RISE
27475	57044.049463(20)	57044.055884(20)	no	LT+RISE
27725	57076.578141(9)	57076.583981(9)	no	TNT+ULTRASPEC
28067	57121.079776(20)	57121.082366(20)	no	VLT+HAWK-I

Table A.16: 0 published and 6 unpublished mid-eclipse times for SDSS J0857+3318, a detached white dwarf + M-dwarf of unknown spectral type. Numbers in parenthesis indicate the uncertainty in the last digit(s). See Fig. B.13 for the O-C diagram of all eclipse times with respect to the best linear ephemeris.

cycle	MJD(UTC)	BMJD(TDB)	pub?	source
0	55957.115665(4)	55957.121911(4)	no	WHT+ULTRACAM
1	55957.221691(4)	55957.227937(4)	no	WHT+ULTRACAM
10	55958.175952(4)	55958.182192(4)	no	WHT+ULTRACAM
11	55958.281979(8)	55958.288219(8)	no	WHT+ULTRACAM
7427	56744.582975(17)	56744.586488(17)	no	TNT+ULTRASPEC
7437	56745.643336(27)	56745.646762(27)	no	TNT+ULTRASPEC

Table A.17: 16 published and 14 unpublished mid-eclipse times for CSS 03170, a detached white dwarf + M-dwarf of spectral type M8. Numbers in parenthesis indicate the uncertainty in the last digit(s). See Fig. B.14 for the O-C diagram of all eclipse times with respect to the best linear ephemeris.

cycle	MJD(UTC)	BMJD(TDB)	pub?	source
-374	-	55528.366640(26)	yes	Backhaus et al. 2012
381	-	55577.514506(30)	yes	Backhaus et al. 2012
1467	-	55648.209375(11)	yes	Backhaus et al. 2012
1558	-	55654.133181(9)	yes	Backhaus et al. 2012
4513	-	55846.493443(26)	yes	Backhaus et al. 2012
4574	-	55850.464311(20)	yes	Backhaus et al. 2012
4804	-	55865.436535(19)	yes	Backhaus et al. 2012
-298	55533.310860(2)	55533.313997(2)	yes	Parsons et al. 2012c
-237	55537.281401(2)	55537.284884(2)	yes	Parsons et al. 2012c
-206	55539.299227(2)	55539.302881(2)	yes	Parsons et al. 2012c
-191	55540.275590(2)	55540.279325(2)	yes	Parsons et al. 2012c
-100	55546.198910(6)	55546.203119(6)	yes	Parsons et al. 2012c
-99	55546.263994(2)	55546.268208(2)	yes	Parsons et al. 2012c
240	55568.330320(2)	55568.335933(2)	yes	Parsons et al. 2012c
269	55570.218033(2)	55570.223734(2)	yes	Parsons et al. 2012c
299	55572.170844(2)	55572.176631(2)	yes	Parsons et al. 2012c
4832	55867.259088(2)	55867.259233(2)	no	WHT+ULTRACAM
5997	55943.090713(2)	55943.096703(2)	no	WHT+ULTRACAM
10116	56211.231176(3)	56211.229343(3)	no	WHT+ULTRACAM
12877	56390.957543(18)	56390.960849(18)	no	LT+RISE
16903	56653.034613(30)	56653.039583(30)	no	LT+RISE
17375	56683.758884(4)	56683.765118(4)	no	TNT+ULTRASPEC
17388	56684.605127(6)	56684.611375(6)	no	TNT+ULTRASPEC
17457	56689.096723(13)	56689.103021(13)	no	LT+RISE
18279	56742.608011(11)	56742.612395(11)	no	TNT+ULTRASPEC
22036	56987.177653(18)	56987.180115(18)	no	LT+RISE
22061	56988.804886(7)	56988.807499(7)	no	TNT+ULTRASPEC
22091	56990.757597(13)	56990.760389(13)	no	TNT+ULTRASPEC

<div align="center">Table A.17: Continues on next page.</div>

Table A.17: Times for CSS 03170; continued from previous page.

cycle	MJD(UTC)	BMJD(TDB)	pub?	source
22927	57045.174939(26)	57045.181097(26)	no	LT+RISE
23441	57078.634737(8)	57078.640713(8)	no	TNT+ULTRASPEC

Table A.18: 11 published and 25 unpublished mid-eclipse times for CSS 080502, a detached white dwarf + M-dwarf of spectral type M4. Numbers in parenthesis indicate the uncertainty in the last digit(s). See Fig. B.15 for the O-C diagram of all eclipse times with respect to the best linear ephemeris.

cycle	MJD(UTC)	BMJD(TDB)	pub?	source
12324	55308.006361(3)	55308.008730(3)	no	NTT+ULTRACAM
13765	55523.347004(4)	55523.349066(4)	no	NTT+ULTRACAM
13785	55526.335496(3)	55526.337834(3)	no	NTT+ULTRACAM
13912	55545.312450(1)	55545.316482(1)	no	NTT+ULTRACAM
13919	55546.358434(2)	55546.362550(2)	no	NTT+ULTRACAM
13925	55547.254993(2)	55547.259180(2)	no	NTT+ULTRACAM
14073	-	55569.376004(10)	yes	Backhaus et al. 2012
14120	-	55576.399608(13)	yes	Backhaus et al. 2012
14167	-	55583.423204(16)	yes	Backhaus et al. 2012
14392	55617.040636(5)	55617.046767(5)	no	LT+RISE
14587	-	55646.187183(11)	yes	Backhaus et al. 2012
14594	-	55647.233251(5)	yes	Backhaus et al. 2012
14600	-	55648.129867(5)	yes	Backhaus et al. 2012
14626	55652.011079(5)	55652.015273(5)	no	LT+RISE
14634	-	55653.210777(12)	yes	Backhaus et al. 2012
14640	-	55654.107405(5)	yes	Backhaus et al. 2012
16041	-	55863.470136(6)	yes	Backhaus et al. 2012
16054	-	55865.412837(7)	yes	Backhaus et al. 2012
16066	55867.206127(1)	55867.206081(1)	no	WHT+ULTRACAM
16068	-	55867.504964(5)	yes	Backhaus et al. 2012
16246	55894.102366(8)	55894.104942(8)	no	LT+RISE
16373	55913.079367(13)	55913.083586(13)	no	LT+RISE
16567	55942.068589(7)	55942.074534(7)	no	LT+RISE
16681	55959.104139(9)	55959.110496(9)	no	LT+RISE
17028	56010.960837(6)	56010.965485(6)	no	LT+RISE
19137	56326.123900(9)	56326.130271(9)	no	LT+RISE
19344	-	56357.063936(10)	no	VLT+HAWK-I
19351	-	56358.110006(17)	no	VLT+HAWK-I
19377	56361.989868(6)	56361.995393(6)	no	LT+RISE
21365	56659.072877(6)	56659.078153(6)	no	LT+RISE
21523	56682.683122(3)	56682.689361(3)	no	TNT+ULTRASPEC
21536	56684.625778(3)	56684.632056(3)	no	TNT+ULTRASPEC
23561	56987.241764(9)	56987.244078(9)	no	LT+RISE
23805	57023.701708(8)	57023.706944(8)	no	TNT+ULTRASPEC
23955	57046.116443(7)	57046.122638(7)	no	LT+RISE

Table A.18: Continues on next page.

Table A.18: Times for CSS 080502; continued from previous page.

cycle	MJD(UTC)	BMJD(TDB)	pub?	source
24160	57076.751302(4)	57076.757449(4)	no	TNT+ULTRASPEC

Table A.19: 0 published and 5 unpublished mid-eclipse times for SDSS J0927+3329, a detached white dwarf + M-dwarf of spectral type M3. Numbers in parenthesis indicate the uncertainty in the last digit(s). See Fig. B.16 for the O-C diagram of all eclipse times with respect to the best linear ephemeris.

cycle	MJD(UTC)	BMJD(TDB)	pub?	source
0	56074.907576(21)	56074.906137(21)	no	LT+RISE
254	56661.189969(18)	56661.195424(18)	no	LT+RISE
266	56688.887922(13)	56688.894109(13)	no	TNT+ULTRASPEC
412	57025.889653(16)	57025.895078(16)	no	TNT+ULTRASPEC
419	57042.046639(33)	57042.052657(33)	no	LT+RISE

Table A.20: 1 published and 2 unpublished mid-eclipse times for SDSS J0935+2700, a detached white dwarf + M-dwarf of unknown spectral type. Numbers in parenthesis indicate the uncertainty in the last digit(s). See Fig. B.17 for the O-C diagram of all eclipse times with respect to the best linear ephemeris.

cycle	MJD(UTC)	BMJD(TDB)	pub?	source
0	-	56602.839467(8)	yes	Parsons et al. 2015
675	56738.532354(11)	56738.537145(11)	no	TNT+ULTRASPEC
2387	57082.700405(33)	57082.706310(33)	no	TNT+ULTRASPEC

Table A.21: 5 published and 5 unpublished mid-eclipse times for CSS 38094, a detached white dwarf + M-dwarf of spectral type M5. Numbers in parenthesis indicate the uncertainty in the last digit(s). See Fig. B.18 for the O-C diagram of all eclipse times with respect to the best linear ephemeris.

cycle	MJD(UTC)	BMJD(TDB)	pub?	source
0	-	55587.308817(35)	yes	Backhaus et al. 2012
84	-	55615.111957(10)	yes	Backhaus et al. 2012
202	-	55654.168723(21)	yes	Backhaus et al. 2012
774	-	55843.494813(19)	yes	Backhaus et al. 2012
795	-	55850.445601(13)	yes	Backhaus et al. 2012
1027	55927.230062(9)	55927.235198(9)	no	LT+RISE
2256	56334.015339(12)	56334.021506(12)	no	LT+RISE
2422	56388.962369(10)	56388.965814(10)	no	LT+RISE
3416	56717.963821(8)	56717.969526(8)	no	LT+RISE
4311	57014.200680(12)	57014.205256(12)	no	LT+RISE

Table A.22: 1 published and 7 unpublished mid-eclipse times for SDSS J0946+2030, a detached white dwarf + M-dwarf of spectral type M5. Numbers in parenthesis indicate the uncertainty in the last digit(s). See Fig. B.19 for the O-C diagram of all eclipse times with respect to the best linear ephemeris.

cycle	MJD(UTC)	BMJD(TDB)	pub?	source
0	56032.942313(25)	56032.945590(25)	yes	Parsons et al. 2013b
970	56278.217369(34)	56278.221262(34)	no	LT+RISE
1282	-	56357.114044(32)	no	VLT+HAWK-I
2453	56653.210151(27)	56653.214795(27)	no	LT+RISE
2597	56689.620462(21)	56689.626801(21)	no	TNT+ULTRASPEC
2601	56690.631930(26)	56690.638286(26)	no	TNT+ULTRASPEC
3853	57007.217022(49)	57007.220773(49)	no	LT+RISE
3979	57039.075458(29)	57039.081311(29)	no	LT+RISE

Table A.23: 6 published and 11 unpublished mid-eclipse times for CSS 41631, a detached white dwarf + M-dwarf of spectral type M2. Numbers in parenthesis indicate the uncertainty in the last digit(s). See Fig. B.20 for the O-C diagram of all eclipse times with respect to the best linear ephemeris.

cycle	MJD(UTC)	BMJD(TDB)	pub?	source
0	55548.353265(2)	55548.357089(2)	no	NTT+ULTRACAM
212	55580.335805(7)	55580.341676(7)	no	NTT+ULTRACAM
371	-	55604.330127(29)	yes	Backhaus et al. 2012
443	-	55615.192822(8)	yes	Backhaus et al. 2012
696	-	55653.363107(9)	yes	Backhaus et al. 2012
741	-	55660.152293(15)	yes	Backhaus et al. 2012
2049	-	55857.491223(9)	yes	Backhaus et al. 2012
2062	-	55859.452549(10)	yes	Backhaus et al. 2012
7700	56710.055800(11)	56710.062097(11)	no	LT+RISE
7889	56738.571458(17)	56738.576655(17)	no	TNT+ULTRASPEC
7922	56743.550535(8)	56743.555418(8)	no	TNT+ULTRASPEC
8176	-	56781.876611(1)	no	WHT+ULTRACAM
9548	56988.869539(4)	56988.871475(4)	no	TNT+ULTRASPEC
9574	56992.791798(8)	56992.794109(8)	no	TNT+ULTRASPEC
9590	56995.205541(14)	56995.208080(14)	no	LT+RISE
9947	57049.062846(15)	57049.068964(15)	no	LT+RISE
10137	57077.728188(4)	57077.734439(4)	no	TNT+ULTRASPEC

Table A.24: 1 published and 0 unpublished mid-eclipse times for SDSS J0957+3001, a detached white dwarf + M-dwarf of spectral type M3. Numbers in parenthesis indicate the uncertainty in the last digit(s).

cycle	MJD(UTC)	BMJD(TDB)	pub?	source
0	56014.970605(32)	56014.975114(32)	yes	Parsons et al. 2013b

Table A.25: 24 published and 12 unpublished mid-eclipse times for CSS 41177, a detached double white dwarf binary. Numbers in parenthesis indicate the uncertainty in the last digit(s). See Fig. B.21 for the O-C diagram of all eclipse times with respect to the best linear ephemeris.

cycle	MJD(UTC)	BMJD(TDB)	pub?	source
-2907	55599.081449(13)	55599.087788(13)	yes	Bours et al. 2014a
-2736	55618.920182(16)	55618.926463(16)	yes	Bours et al. 2014a
-2620	-	55632.384239(14)	yes	Backhaus et al. 2012
-2484	-	55648.162338(9)	yes	Backhaus et al. 2012
-2434	55653.958476(20)	55653.963116(20)	yes	Bours et al. 2014a
-2381	-	55660.111914(19)	yes	Backhaus et al. 2012
-2020	-	55701.993490(3)	yes	Bours et al. 2014a
-740	-	55850.493250(21)	yes	Backhaus et al. 2012
-611	-	55865.459247(10)	yes	Backhaus et al. 2012
-199	55913.254004(22)	55913.257605(22)	yes	Bours et al. 2014a
66	-	55944.001690(2)	yes	Bours et al. 2014a
67	-	55944.117706(2)	yes	Bours et al. 2014a
68	-	55944.233725(5)	yes	Bours et al. 2014a
76	-	55945.161846(2)	yes	Bours et al. 2014a
77	-	55945.277862(2)	yes	Bours et al. 2014a
94	-	55947.250123(3)	yes	Bours et al. 2014a
102	-	55948.178246(2)	yes	Bours et al. 2014a
103	-	55948.294256(3)	yes	Bours et al. 2014a
109	-	55948.990352(2)	yes	Bours et al. 2014a
110	-	55949.106370(2)	yes	Bours et al. 2014a
111	-	55949.222385(2)	yes	Bours et al. 2014a
3187	56306.080321(15)	56306.085857(15)	yes	Bours et al. 2014a
3369	56327.194410(16)	56327.200698(16)	yes	Bours et al. 2014a
3678	56363.043600(13)	56363.049447(13)	yes	Bours et al. 2014a
5737	56601.925648(7)	56601.925247(7)	no	TNT+ULTRASPEC
6434	56682.781974(6)	56682.787997(6)	no	TNT+ULTRASPEC
6452	56684.870184(5)	56684.876275(5)	no	TNT+ULTRASPEC
6485	56688.698575(7)	56688.704773(7)	no	TNT+ULTRASPEC
6488	56689.046626(12)	56689.052833(12)	no	LT+RISE
9072	56988.835002(7)	56988.836722(7)	no	TNT+ULTRASPEC
9238	57008.091759(23)	57008.095265(23)	no	LT+RISE
9365	57022.824562(20)	57022.829232(20)	no	TNT+ULTRASPEC
9373	57023.752632(11)	57023.757367(11)	no	TNT+ULTRASPEC
9399	57026.768838(17)	57026.773777(17)	no	TNT+ULTRASPEC
9864	57080.714702(9)	57080.720942(9)	no	TNT+ULTRASPEC
9872	57081.642859(20)	57081.649078(20)	no	TNT+ULTRASPEC

Table A.26: 0 published and 7 unpublished mid-eclipse times for SDSS J1013+2724, a detached white dwarf + M-dwarf of spectral type M4. Numbers in parenthesis indicate the uncertainty in the last digit(s). See Fig. B.22 for the O-C diagram of all eclipse times with respect to the best linear ephemeris.

cycle	MJD(UTC)	BMJD(TDB)	pub?	source
18979	56280.179218(8)	56280.182901(8)	no	LT+RISE
19838	56391.024506(8)	56391.028583(8)	no	LT+RISE
19946	-	56404.964940(2)	no	WHT+ULTRACAM
22426	56724.979222(10)	56724.985090(10)	no	LT+RISE
24914	57046.031689(10)	57046.037535(10)	no	LT+RISE
25176	57079.839985(3)	57079.846137(3)	no	TNT+ULTRASPEC
25423	57111.714326(21)	57111.719088(21)	no	TNT+ULTRASPEC

Table A.27: 0 published and 10 unpublished mid-eclipse times for SDSS J1021+1744, a detached white dwarf + M-dwarf of spectral type M4. Numbers in parenthesis indicate the uncertainty in the last digit(s). See Fig. B.23 for the O-C diagram of all eclipse times with respect to the best linear ephemeris.

cycle	MJD(UTC)	BMJD(TDB)	pub?	source
0	56093.907207(121)	56093.905576(121)	no	LT+RISE
4216	56685.651390(35)	56685.657384(35)	no	TNT+ULTRASPEC
4238	56688.739295(54)	56688.745400(54)	no	TNT+ULTRASPEC
4622	56742.637709(39)	56742.643154(39)	no	TNT+ULTRASPEC
4643	56745.585285(51)	56745.590561(51)	no	TNT+ULTRASPEC
4650	56746.567903(29)	56746.573120(29)	no	TNT+ULTRASPEC
6626	57023.917609(17)	57023.922019(17)	no	TNT+ULTRASPEC
6734	-	57039.080798(5)	no	WHT+ULTRACAM
7009	57077.673036(26)	57077.679449(26)	no	TNT+ULTRASPEC
7215	57106.587779(50)	57106.593292(50)	no	TNT+ULTRASPEC

Table A.28: 1 published and 11 unpublished mid-eclipse times for SDSS J1028+0931, a detached white dwarf + M-dwarf of spectral type M3. Numbers in parenthesis indicate the uncertainty in the last digit(s). See Fig. B.24 for the O-C diagram of all eclipse times with respect to the best linear ephemeris.

cycle	MJD(UTC)	BMJD(TDB)	pub?	source
0	56001.087312(9)	56001.093511(9)	yes	Parsons et al. 2013b
1434	56338.114004(13)	56338.120416(13)	no	LT+RISE
1578	56371.958079(13)	56371.964074(13)	no	LT+RISE
2909	56684.777351(3)	56684.783145(3)	no	TNT+ULTRASPEC
3148	56740.948375(13)	56740.954197(13)	no	LT+RISE
4203	56988.904863(4)	56988.905617(4)	no	TNT+ULTRASPEC
4220	56992.899880(4)	56992.901036(4)	no	TNT+ULTRASPEC
4373	57028.855353(9)	57028.859806(9)	no	TNT+ULTRASPEC
4417	57039.195727(11)	57039.200909(11)	no	LT+RISE
4585	57078.678595(4)	57078.685072(4)	no	TNT+ULTRASPEC

Table A.28: Continues on next page.

Table A.28: Times for SDSS J1028+0931; continued from previous page.

cycle	MJD(UTC)	BMJD(TDB)	pub?	source
4611	57084.789270(17)	57084.795710(17)	no	TNT+ULTRASPEC
4642	57092.075140(12)	57092.081454(12)	no	LT+RISE

Table A.29: 0 published and 7 unpublished mid-eclipse times for SDSS J1057+1307, a detached white dwarf + M-dwarf of spectral type M5. Numbers in parenthesis indicate the uncertainty in the last digit(s). See Fig. B.25 for the O-C diagram of all eclipse times with respect to the best linear ephemeris.

cycle	MJD(UTC)	BMJD(TDB)	pub?	source
0	56010.056163(14)	56010.062214(14)	no	LT+RISE
3027	56388.923137(14)	56388.928540(14)	no	LT+RISE
5375	56682.803856(8)	56682.809249(8)	no	TNT+ULTRASPEC
5430	56689.687407(8)	56689.693165(8)	no	TNT+ULTRASPEC
8047	57017.239142(23)	57017.242155(23)	no	LT+RISE
8215	57038.264652(17)	57038.269402(17)	no	LT+RISE
8522	57076.687694(9)	57076.694105(9)	no	TNT+ULTRASPEC

Table A.30: 0 published and 1 unpublished mid-eclipse times for SDSS J1123-1155, a detached white dwarf + M-dwarf of spectral type M5. Numbers in parenthesis indicate the uncertainty in the last digit(s).

cycle	MJD(UTC)	BMJD(TDB)	pub?	source
418	56685.785129(9)	56685.789599(9)	no	TNT+ULTRASPEC

Table A.31: 9 published and 15 unpublished mid-eclipse times for SDSS J1210+3347, a detached white dwarf + M-dwarf of spectral type M5. Numbers in parenthesis indicate the uncertainty in the last digit(s). See Fig. B.26 for the O-C diagram of all eclipse times with respect to the best linear ephemeris.

cycle	MJD(UTC)	BMJD(TDB)	pub?	source
0	-	54923.033674(6)	yes	Pyrzas et al. 2012
16	-	54925.025532(8)	yes	Pyrzas et al. 2012
25	-	54926.145928(7)	yes	Pyrzas et al. 2012
33	-	54927.141846(9)	yes	Pyrzas et al. 2012
5431	55599.132609(5)	55599.137618(5)	yes	Pyrzas et al. 2012
5623	55623.033970(5)	55623.039607(5)	yes	Pyrzas et al. 2012
5872	55654.032363(8)	55654.037585(8)	yes	Pyrzas et al. 2012
6161	55690.011905(7)	55690.015125(7)	yes	Pyrzas et al. 2012
6610	55745.912256(7)	55745.910993(7)	yes	Pyrzas et al. 2012
7954	55913.223746(8)	55913.225239(8)	no	LT+RISE
8476	55978.203434(7)	55978.208897(7)	no	LT+RISE
9510	56106.932261(18)	56106.931315(18)	no	LT+RISE
11279	56327.148844(7)	56327.153735(7)	no	LT+RISE
11656	56374.080867(9)	56374.086375(9)	no	LT+RISE

Table A.31: Continues on next page.

Table A.31: Times for SDSS J1210+3347; continued from previous page.

cycle	MJD(UTC)	BMJD(TDB)	pub?	source
14153	56684.932912(3)	56684.937413(3)	no	TNT+ULTRASPEC
14625	56743.691210(5)	56743.696604(5)	no	TNT+ULTRASPEC
14632	56744.562655(8)	56744.568025(8)	no	TNT+ULTRASPEC
14853	56772.076167(9)	56772.080287(9)	no	LT+RISE
16595	56988.941804(5)	56988.941568(5)	no	TNT+ULTRASPEC
16627	56992.925154(5)	56992.925255(5)	no	TNT+ULTRASPEC
16875	57023.796028(9)	57023.798723(9)	no	TNT+ULTRASPEC
17039	57044.210912(6)	57044.215057(6)	no	LT+RISE
17302	57076.950377(5)	57076.955888(5)	no	TNT+ULTRASPEC
17356	57083.672748(11)	57083.678357(11)	no	TNT+ULTRASPEC

Table A.32: 1 published and 10 unpublished mid-eclipse times for SDSS J1212-0123, a detached white dwarf + M-dwarf of spectral type M4. Numbers in parenthesis indicate the uncertainty in the last digit(s). See Fig. B.27 for the O-C diagram of all eclipse times with respect to the best linear ephemeris.

cycle	MJD(UTC)	BMJD(TDB)	pub?	source
3593	55310.987659(6)	55310.993427(6)	yes	Parsons et al. 2012a
4623	55656.934063(4)	55656.940503(4)	no	LT+RISE
5383	55912.202496(18)	55912.202411(18)	no	LT+RISE
5523	55959.219974(5)	55959.224345(5)	no	LT+RISE
6636	56333.043651(10)	56333.048654(10)	no	LT+RISE
6708	-	56357.231330(20)	no	VLT+HAWK-I
6803	56389.132673(7)	56389.139072(7)	no	LT+RISE
7698	56689.739114(3)	56689.743472(3)	no	TNT+ULTRASPEC
8765	57048.113861(11)	57048.117642(11)	no	LT+RISE
8871	57083.713893(6)	57083.719963(6)	no	TNT+ULTRASPEC
8991	57124.018191(5)	57124.024454(5)	no	LT+RISE

Table A.33: 0 published and 9 unpublished mid-eclipse times for SDSS J1223-0056, a detached white dwarf + M-dwarf of spectral type M6. Numbers in parenthesis indicate the uncertainty in the last digit(s). See Fig. B.28 for the O-C diagram of all eclipse times with respect to the best linear ephemeris.

cycle	MJD(UTC)	BMJD(TDB)	pub?	source
-10	55706.112284(12)	55706.116204(12)	no	NTT+ULTRACAM
0	55707.013134(9)	55707.016980(9)	no	NTT+ULTRACAM
2	55707.193331(16)	55707.197162(16)	no	NTT+ULTRACAM
12	55708.094175(9)	55708.097931(9)	no	NTT+ULTRACAM
11236	56719.127759(32)	56719.133777(32)	no	LT+RISE
11488	56741.826915(24)	56741.833443(24)	no	TNT+ULTRASPEC
11613	56753.086682(26)	56753.093138(26)	no	LT+RISE
14822	57042.150521(63)	57042.153568(63)	no	LT+RISE
15241	57079.890447(11)	57079.896253(11)	no	TNT+ULTRASPEC

Table A.34: 0 published and 5 unpublished mid-eclipse times for CSS 25601, a detached white dwarf + M-dwarf of spectral type M5. Numbers in parenthesis indicate the uncertainty in the last digit(s). See Fig. B.29 for the O-C diagram of all eclipse times with respect to the best linear ephemeris.

cycle	MJD(UTC)	BMJD(TDB)	pub?	source
12849	-	56394.086879(19)	no	VLT+HAWK-I
12862	-	56397.048995(35)	no	VLT+HAWK-I
14267	56717.181455(22)	56717.187228(22)	no	LT+RISE
15711	57046.208471(15)	57046.211786(15)	no	LT+RISE
16040	57121.170340(17)	57121.176578(17)	no	VLT+HAWK-I

Table A.35: 1 published and 8 unpublished mid-eclipse times for SDSS J1307+2156, a detached white dwarf + M-dwarf of spectral type M4. Numbers in parenthesis indicate the uncertainty in the last digit(s). See Fig. B.30 for the O-C diagram of all eclipse times with respect to the best linear ephemeris.

cycle	MJD(UTC)	BMJD(TDB)	pub?	source
0	56007.215475(16)	56007.221371(16)	yes	Parsons et al. 2013b
1516	56335.161376(15)	56335.165889(15)	no	LT+RISE
1765	56389.024299(15)	56389.030153(15)	no	LT+RISE
3393	56741.196974(25)	56741.202885(25)	no	LT+RISE
3725	56813.019146(14)	56813.021896(14)	no	LT+RISE
4552	56991.922087(13)	56991.920469(13)	no	TNT+ULTRASPEC
4794	57044.267543(11)	57044.270480(11)	no	LT+RISE
4963	57080.823698(7)	57080.828984(7)	no	TNT+ULTRASPEC
4968	57081.905247(7)	57081.910579(7)	no	TNT+ULTRASPEC

Table A.36: 4 published and 3 unpublished mid-eclipse times for CSS 21616, a detached white dwarf + M-dwarf of unknown spectral type. Numbers in parenthesis indicate the uncertainty in the last digit(s). See Fig. B.31 for the O-C diagram of all eclipse times with respect to the best linear ephemeris.

cycle	MJD(UTC)	BMJD(TDB)	pub?	source
0	-	55653.454195(11)	yes	Backhaus et al. 2012
138	-	55680.358500(14)	yes	Backhaus et al. 2012
215	-	55695.370287(56)	yes	Backhaus et al. 2012
783	-	55806.107031(31)	yes	Backhaus et al. 2012
5592	56743.659117(13)	56743.664872(13)	no	TNT+ULTRASPEC
5603	56745.803639(6)	56745.809404(6)	no	TNT+ULTRASPEC
7159	57049.162565(24)	57049.165560(24)	no	LT+RISE

Table A.37: 26 published and 13 unpublished mid-eclipse times for DE CVn, a detached white dwarf + M-dwarf of spectral type M3. Numbers in parenthesis indicate the uncertainty in the last digit(s). See Fig. B.32 for the O-C diagram of all eclipse times with respect to the best linear ephemeris.

cycle	MJD(UTC)	BMJD(TDB)	pub?	source
-6134	50550.418000(1600)	50550.422100(1600)	yes	van den Besselaar et al. 2007
-6109	50559.521200(1600)	50559.525000(1600)	yes	van den Besselaar et al. 2007
-6107	50560.250000(2000)	50560.253800(2000)	yes	van den Besselaar et al. 2007
-6101	50562.434400(2200)	50562.438100(2200)	yes	van den Besselaar et al. 2007
-6079	50570.447100(1400)	50570.450400(1400)	yes	van den Besselaar et al. 2007
-6063	50576.272500(1400)	50576.275600(1400)	yes	van den Besselaar et al. 2007
-6057	50578.458400(600)	50578.461300(600)	yes	van den Besselaar et al. 2007
-4912	50995.401200(1800)	50995.401100(1800)	yes	van den Besselaar et al. 2007
-3196	51620.259100(1500)	51620.263600(1500)	yes	van den Besselaar et al. 2007
-2015	52050.310800(1600)	52050.313300(1600)	yes	van den Besselaar et al. 2007
-2001	52055.408900(700)	52055.411100(700)	yes	van den Besselaar et al. 2007
-1982	52062.328000(700)	52062.329700(700)	yes	van den Besselaar et al. 2007
-1342	52295.376100(400)	52295.378900(400)	yes	van den Besselaar et al. 2007
-1334	52298.289100(100)	52298.292100(100)	yes	van den Besselaar et al. 2007
-1019	52412.994000(400)	52412.996500(400)	yes	van den Besselaar et al. 2007
-988	52424.282800(600)	52424.284600(600)	yes	van den Besselaar et al. 2007
-900	52456.328800(400)	52456.328600(400)	yes	van den Besselaar et al. 2007
-304	52673.352120(140)	52673.355620(140)	yes	van den Besselaar et al. 2007
-217	52705.032200(300)	52705.036600(300)	yes	van den Besselaar et al. 2007
-157	52726.880000(400)	52726.884400(400)	yes	van den Besselaar et al. 2007
0	52784.051844(25)	52784.054040(25)	yes	van den Besselaar et al. 2007
69	52809.178900(100)	52809.179500(100)	yes	van den Besselaar et al. 2007
2801	53804.003809(2)	53804.008265(2)	yes	Parsons et al. 2010b
2807	53806.188634(2)	53806.193106(2)	yes	Parsons et al. 2010b
2809	53806.916904(3)	53806.921380(3)	yes	Parsons et al. 2010b
2873	53830.222000(400)	53830.226300(400)	yes	van den Besselaar et al. 2007
7769	55613.048083(14)	55613.052287(14)	no	LT+RISE
7865	55648.005196(8)	55648.009670(8)	no	LT+RISE
7942	55676.044648(8)	55676.048399(8)	no	LT+RISE
8186	55764.899763(7)	55764.898424(7)	no	LT+RISE
8659	55937.134044(16)	55937.136339(16)	no	LT+RISE
8722	55960.073615(10)	55960.077130(10)	no	LT+RISE
9021	56068.952400(8)	56068.954778(8)	no	LT+RISE
9744	56332.223638(15)	56332.227445(15)	no	LT+RISE
9851	56371.185807(10)	56371.190331(10)	no	LT+RISE
10869	56741.879381(4)	56741.883863(4)	no	TNT+ULTRASPEC
10990	56785.941589(11)	56785.944695(11)	no	LT+RISE
11724	57053.219327(10)	57053.222710(10)	no	LT+RISE
11800	57080.892947(3)	57080.897277(3)	no	TNT+ULTRASPEC

Table A.38: 6 published and 31 unpublished mid-eclipse times for SDSS J1329+1230, a detached white dwarf + M-dwarf of spectral type M8. Numbers in parenthesis indicate the uncertainty in the last digit(s). See Fig. B.33 for the O-C diagram of all eclipse times with respect to the best linear ephemeris.

cycle	MJD(UTC)	BMJD(TDB)	pub?	source
447	55307.240695(1)	55307.246734(1)	no	NTT+ULTRACAM
470	55309.102967(2)	55309.108961(2)	no	NTT+ULTRACAM
471	55309.183934(1)	55309.189926(1)	no	NTT+ULTRACAM
472	55309.264900(1)	55309.270890(1)	no	NTT+ULTRACAM
496	55311.208145(3)	55311.214082(3)	no	NTT+ULTRACAM
532	55314.123018(9)	55314.128864(9)	no	NTT+ULTRACAM
4168	-	55608.522163(5)	yes	Backhaus et al. 2012
4205	-	55611.517920(9)	yes	Backhaus et al. 2012
4263	55616.209110(5)	55616.213963(5)	no	LT+RISE
4655	55647.946608(5)	55647.952735(5)	no	LT+RISE
5125	55686.001281(5)	55686.006880(5)	no	LT+RISE
5202	-	55692.241265(6)	yes	Backhaus et al. 2012
5227	-	55694.265440(7)	yes	Backhaus et al. 2012
5228	-	55694.346403(12)	yes	Backhaus et al. 2012
6559	-	55802.112475(10)	yes	Backhaus et al. 2012
8055	55923.238102(6)	55923.237982(6)	no	LT+RISE
9423	56033.993672(6)	56033.999786(6)	no	LT+RISE
10657	56133.912978(7)	56133.912123(7)	no	LT+RISE
12810	56308.230700(5)	56308.232443(5)	no	LT+RISE
13056	56328.146610(13)	56328.150114(13)	no	LT+RISE
13119	56333.247099(6)	56333.251009(6)	no	LT+RISE
13427	-	56358.188617(5)	no	VLT+HAWK-I
13586	56371.056261(8)	56371.062225(8)	no	LT+RISE
13871	-	56394.137607(4)	no	VLT+HAWK-I
13872	-	56394.218575(5)	no	VLT+HAWK-I
13910	-	56397.295287(6)	no	VLT+HAWK-I
17462	56684.884591(4)	56684.887358(4)	no	TNT+ULTRASPEC
17775	56710.225057(7)	56710.229786(7)	no	LT+RISE
18166	56741.881499(5)	56741.887580(5)	no	TNT+ULTRASPEC
18304	56753.054732(5)	56753.060925(5)	no	LT+RISE
21686	57026.888134(7)	57026.888734(7)	no	TNT+ULTRASPEC
21711	57028.912111(6)	57028.912903(6)	no	TNT+ULTRASPEC
21913	57045.265740(9)	57045.268059(9)	no	LT+RISE
22329	57078.945101(2)	57078.950035(2)	no	TNT+ULTRASPEC
22733	57111.654258(6)	57111.660397(6)	no	TNT+ULTRASPEC
22850	57121.127256(9)	57121.133435(9)	no	VLT+HAWK-I
22851	57121.208232(5)	57121.214410(5)	no	VLT+HAWK-I

Table A.39: 3 published and 21 unpublished mid-eclipse times for WD 1333+005, a detached white dwarf + M-dwarf of spectral type M5. Numbers in parenthesis indicate the uncertainty in the last digit(s). See Fig. B.34 for the O-C diagram of all eclipse times with respect to the best linear ephemeris.

cycle	MJD(UTC)	BMJD(TDB)	pub?	source
0	-	55611.476665(10)	yes	Backhaus et al. 2012
300	55648.058023(5)	55648.064291(5)	no	LT+RISE
529	55675.986471(5)	55675.992859(5)	no	LT+RISE
679	-	55694.286674(10)	yes	Backhaus et al. 2012
816	55710.990234(5)	55710.995036(5)	no	LT+RISE
842	55714.161372(2)	55714.165950(2)	no	NTT+ULTRACAM
1563	-	55802.098220(13)	yes	Backhaus et al. 2012
2540	55921.252943(7)	55921.251977(7)	no	LT+RISE
2720	55943.203365(12)	55943.204554(12)	no	LT+RISE
3252	56008.080551(10)	56008.086651(10)	no	LT+RISE
3817	56076.988583(7)	56076.993330(7)	no	LT+RISE
5541	56287.251123(11)	56287.250231(11)	no	LT+RISE
5918	56333.225158(9)	56333.228696(9)	no	LT+RISE
6124	-	56358.352199(6)	no	VLT+HAWK-I
6163	56363.102931(7)	56363.108586(7)	no	LT+RISE
6941	56457.988972(6)	56457.992499(6)	no	LT+RISE
8850	56690.808889(3)	56690.811723(3)	no	TNT+ULTRASPEC
9279	56743.125808(9)	56743.132044(9)	no	LT+RISE
9310	56746.906395(9)	56746.912727(9)	no	TNT+ULTRASPEC
9729	56798.008124(5)	56798.013467(5)	no	LT+RISE
11781	57048.270734(11)	57048.272815(11)	no	LT+RISE
12015	57076.806602(3)	57076.811170(3)	no	TNT+ULTRASPEC
12065	57082.904105(3)	57082.909100(3)	no	TNT+ULTRASPEC
12301	57111.685061(7)	57111.691369(7)	no	TNT+ULTRASPEC

Table A.40: 0 published and 9 unpublished mid-eclipse times for CSS 21357, a detached white dwarf + M-dwarf of spectral type M4. Numbers in parenthesis indicate the uncertainty in the last digit(s). See Fig. B.35 for the O-C diagram of all eclipse times with respect to the best linear ephemeris.

cycle	MJD(UTC)	BMJD(TDB)	pub?	source
0	56000.156481(7)	56000.161910(7)	no	LT+RISE
1389	56345.229252(7)	56345.233665(7)	no	LT+RISE
1586	-	56394.174707(31)	no	VLT+HAWK-I
1598	56397.150033(7)	56397.155908(7)	no	LT+RISE
2756	56684.837432(2)	56684.839916(2)	no	TNT+ULTRASPEC
2979	56740.234469(9)	56740.240179(9)	no	LT+RISE
3240	56805.076720(6)	56805.080912(6)	no	LT+RISE
4354	57081.829146(5)	57081.833897(5)	no	TNT+ULTRASPEC
4358	57082.822817(5)	57082.827623(5)	no	TNT+ULTRASPEC

Table A.41: 86 published and 19 unpublished mid-eclipse times for QS Vir, a detached white dwarf + M-dwarf of spectral type M3. Numbers in parenthesis indicate the uncertainty in the last digit(s). See Fig. B.36 for the O-C diagram of all eclipse times with respect to the best linear ephemeris.

cycle	MJD(UTC)	BMJD(TDB)	pub?	source
171	48714.914500(10)	48714.920680(10)	yes	O'Donoghue et al. 2003
172	48715.065270(10)	48715.071460(10)	yes	O'Donoghue et al. 2003
212	48721.095410(10)	48721.101740(10)	yes	O'Donoghue et al. 2003
225	48723.055200(10)	48723.061580(10)	yes	O'Donoghue et al. 2003
535	48769.791060(10)	48769.796410(10)	yes	O'Donoghue et al. 2003
542	48770.846460(10)	48770.851740(10)	yes	O'Donoghue et al. 2003
2347	49042.965190(10)	49042.969230(10)	yes	O'Donoghue et al. 2003
2354	49044.020420(10)	49044.024540(10)	yes	O'Donoghue et al. 2003
2367	49045.980110(10)	49045.984390(10)	yes	O'Donoghue et al. 2003
2705	49096.934000(10)	49096.940460(10)	yes	O'Donoghue et al. 2003
3122	49159.802810(10)	49159.806380(10)	yes	O'Donoghue et al. 2003
4497	49367.097880(10)	49367.098010(10)	yes	O'Donoghue et al. 2003
4855	49421.064200(10)	49421.069210(10)	yes	O'Donoghue et al. 2003
5471	49513.931370(10)	49513.935840(10)	yes	O'Donoghue et al. 2003
7230	49779.113740(10)	49779.118260(10)	yes	O'Donoghue et al. 2003
7249	49781.977940(10)	49781.982670(10)	yes	O'Donoghue et al. 2003
7778	49861.727780(10)	49861.733390(10)	yes	O'Donoghue et al. 2003
7826	49868.964570(10)	49868.969760(10)	yes	O'Donoghue et al. 2003
7831	49869.718400(10)	49869.723540(10)	yes	O'Donoghue et al. 2003
9425	50110.029590(10)	50110.031020(10)	yes	O'Donoghue et al. 2003
9591	50135.052980(10)	50135.056770(10)	yes	O'Donoghue et al. 2003
9611	50138.067880(10)	50138.071930(10)	yes	O'Donoghue et al. 2003
10551	50279.782590(10)	50279.784000(10)	yes	O'Donoghue et al. 2003
11966	50493.102730(10)	50493.105900(10)	yes	O'Donoghue et al. 2003
12508	50574.810160(10)	50574.816500(10)	yes	O'Donoghue et al. 2003
15625	51044.729600(10)	51044.727770(10)	yes	O'Donoghue et al. 2003
17014	51254.124380(10)	51254.129920(10)	yes	O'Donoghue et al. 2003
17391	51310.959330(10)	51310.965540(10)	yes	O'Donoghue et al. 2003
23919	52295.109580(10)	52295.110400(10)	yes	O'Donoghue et al. 2003
24507	52383.749160(10)	52383.755720(10)	yes	O'Donoghue et al. 2003
24520	52385.709020(10)	52385.715580(10)	yes	O'Donoghue et al. 2003
24715	52415.107464(1)	52415.113302(1)	yes	Parsons et al. 2010b
27135	52779.940440(1)	52779.946281(1)	yes	Parsons et al. 2010b
27149	52782.051144(2)	52782.056883(2)	yes	Parsons et al. 2010b
27162	52784.011094(1)	52784.016732(1)	yes	Parsons et al. 2010b
33948	53807.050065(1)	53807.055317(1)	yes	Parsons et al. 2010b
34742	53926.754380(17)	53926.756325(17)	yes	Parsons et al. 2010b
34749	53927.809767(17)	53927.811611(17)	yes	Parsons et al. 2010b
34762	53929.769906(17)	53929.771562(17)	yes	Parsons et al. 2010b
34795	53934.745279(29)	53934.746452(29)	yes	Parsons et al. 2010b

Table A.41: Continues on next page.

Table A.41: Times for QS Vir; continued from previous page.

cycle	MJD(UTC)	BMJD(TDB)	pub?	source
34802	53935.800740(34)	53935.801810(34)	yes	Parsons et al. 2010b
34808	53936.705273(94)	53936.706254(94)	yes	Parsons et al. 2010b
34868	53945.751723(20)	53945.751821(20)	yes	Parsons et al. 2010b
38560	54502.346790(8)	54502.349156(8)	yes	Parsons et al. 2010b
38566	54503.251262(24)	54503.253715(24)	yes	Parsons et al. 2010b
38573	54504.306406(27)	54504.308961(27)	yes	Parsons et al. 2010b
38580	54505.361651(11)	54505.364307(11)	yes	Parsons et al. 2010b
41270	54910.896377(40)	54910.902126(40)	yes	Qian et al. 2010
41296	54914.815887(40)	54914.821826(40)	yes	Qian et al. 2010
41296	54914.815978(40)	54914.821917(40)	yes	Qian et al. 2010
41302	54915.720447(40)	54915.726426(40)	yes	Qian et al. 2010
41495	54944.816001(40)	54944.822564(40)	yes	Qian et al. 2010
43342	55223.270376(22)	55223.271832(22)	yes	Parsons et al. 2010b
43349	55224.325543(25)	55224.327104(25)	yes	Parsons et al. 2010b
43362	55226.285138(33)	55226.286894(33)	yes	Parsons et al. 2010b
43369	55227.340393(28)	55227.342254(28)	yes	Parsons et al. 2010b
43415	55234.274562(30)	55234.277101(30)	yes	Parsons et al. 2010b
43422	55235.329786(14)	55235.332426(14)	yes	Parsons et al. 2010b
44063	-	55331.968000(15)	yes	Almeida & Jablonski 2011
44064	-	55332.118720(15)	yes	Almeida & Jablonski 2011
44096	-	55336.943000(15)	yes	Almeida & Jablonski 2011
44103	-	55337.998350(15)	yes	Almeida & Jablonski 2011
44104	-	55338.149090(15)	yes	Almeida & Jablonski 2011
44177	-	55349.154370(29)	yes	Almeida & Jablonski 2011
44189	-	55350.963470(23)	yes	Almeida & Jablonski 2011
44275	-	55363.928630(23)	yes	Almeida & Jablonski 2011
44276	-	55364.079370(23)	yes	Almeida & Jablonski 2011
44282	-	55364.983940(23)	yes	Almeida & Jablonski 2011
44283	-	55365.134700(23)	yes	Almeida & Jablonski 2011
44289	-	55366.039220(29)	yes	Almeida & Jablonski 2011
44295	-	55366.943770(23)	yes	Almeida & Jablonski 2011
44296	-	55367.094520(23)	yes	Almeida & Jablonski 2011
44302	-	55367.999090(35)	yes	Almeida & Jablonski 2011
44309	-	55369.054390(39)	yes	Almeida & Jablonski 2011
44408	-	55383.979400(23)	yes	Almeida & Jablonski 2011
44415	-	55385.034690(23)	yes	Almeida & Jablonski 2011
44421	-	55385.939240(23)	yes	Almeida & Jablonski 2011
44422	-	55386.089980(23)	yes	Almeida & Jablonski 2011
44434	-	55387.899080(23)	yes	Almeida & Jablonski 2011
44435	-	55388.049830(23)	yes	Almeida & Jablonski 2011
44441	-	55388.954390(23)	yes	Almeida & Jablonski 2011
44508	-	55399.055160(46)	yes	Almeida & Jablonski 2011
44567	-	55407.949840(23)	yes	Almeida & Jablonski 2011

Table A.41: Continues on next page.

Table A.41: Times for QS Vir; continued from previous page.

cycle	MJD(UTC)	BMJD(TDB)	pub?	source
44574	-	55409.005160(23)	yes	Almeida & Jablonski 2011
44693	-	55426.945310(23)	yes	Almeida & Jablonski 2011
44706	-	55428.905140(23)	yes	Almeida & Jablonski 2011
43906	55308.292493(1)	55308.299072(1)	no	NTT+ULTRACAM
45631	55568.356512(1)	55568.355954(1)	no	NTT+ULTRACAM
46572	55710.213408(2)	55710.218858(2)	no	NTT+ULTRACAM
45927	55612.976453(6)	55612.980210(6)	no	LT+RISE
46134	55644.181125(3)	55644.187030(3)	no	LT+RISE
46339	55675.085757(3)	55675.092339(3)	no	LT+RISE
48078	55937.259983(3)	55937.259787(3)	no	LT+RISE
48230	55960.172837(3)	55960.174936(3)	no	LT+RISE
48495	56000.120298(3)	56000.125700(3)	no	LT+RISE
48707	56032.079734(3)	56032.086290(3)	no	LT+RISE
50552	56310.233436(3)	56310.234018(3)	no	LT+RISE
50665	56327.267332(3)	56327.269615(3)	no	LT+RISE
50903	56363.144649(3)	56363.149917(3)	no	LT+RISE
53064	56688.934992(1)	56688.936910(1)	no	TNT+ULTRASPEC
53232	56714.259947(3)	56714.264176(3)	no	LT+RISE
53609	56771.093192(3)	56771.099762(3)	no	LT+RISE
55474	57052.260733(4)	57052.262447(4)	no	LT+RISE
55673	-	57082.263182(3)	no	DT+DFOSC
55677	57082.861736(1)	57082.866217(1)	no	TNT+ULTRASPEC

Table A.42: 1 published and 0 unpublished mid-eclipse times for SDSS J1408+2950, a detached white dwarf + M-dwarf of spectral type M5. Numbers in parenthesis indicate the uncertainty in the last digit(s).

cycle	MJD(UTC)	BMJD(TDB)	pub?	source
13591	56112.911809(184)	56112.912914(184)	yes	Parsons et al. 2013b

Table A.43: 0 published and 7 unpublished mid-eclipse times for CSS 07125, a detached white dwarf + M-dwarf of spectral type M4. Numbers in parenthesis indicate the uncertainty in the last digit(s). See Fig. B.37 for the O-C diagram of all eclipse times with respect to the best linear ephemeris.

cycle	MJD(UTC)	BMJD(TDB)	pub?	source
7961	-	56358.289088(22)	no	VLT+HAWK-I
8060	-	56394.275364(31)	no	VLT+HAWK-I
9168	56797.024187(33)	56797.030058(33)	no	LT+RISE
9179	56801.022899(21)	56801.028585(21)	no	LT+RISE
9859	57048.205306(47)	57048.206505(47)	no	LT+RISE
9991	57096.182925(44)	57096.188187(44)	no	LT+RISE
10060	57121.263177(17)	57121.269494(17)	no	VLT+HAWK-I

Table A.44: 44 published and 8 unpublished mid-eclipse times for CSS 21055, a detached white dwarf + M-dwarf of spectral type M4. Numbers in parenthesis indicate the uncertainty in the last digit(s). See Fig. B.38 for the O-C diagram of all eclipse times with respect to the best linear ephemeris.

cycle	MJD(UTC)	BMJD(TDB)	pub?	source
0	-	55991.388711(6)	yes	Beuermann et al. 2013b
25	-	55993.502047(10)	yes	Beuermann et al. 2013b
119	-	56001.448114(18)	yes	Beuermann et al. 2013b
236	-	56011.338413(15)	yes	Beuermann et al. 2013b
237	-	56011.422991(20)	yes	Beuermann et al. 2013b
261	-	56013.451773(5)	yes	Beuermann et al. 2013b
273	-	56014.466150(8)	yes	Beuermann et al. 2013b
295	-	56016.325886(7)	yes	Beuermann et al. 2013b
296	-	56016.410403(5)	yes	Beuermann et al. 2013b
297	-	56016.494943(6)	yes	Beuermann et al. 2013b
307	-	56017.340267(7)	yes	Beuermann et al. 2013b
308	-	56017.424812(5)	yes	Beuermann et al. 2013b
344	-	56020.467987(11)	yes	Beuermann et al. 2013b
355	-	56021.397810(32)	yes	Beuermann et al. 2013b
356	-	56021.482376(10)	yes	Beuermann et al. 2013b
521	-	56035.430274(8)	yes	Beuermann et al. 2013b
650	-	56046.335001(6)	yes	Beuermann et al. 2013b
651	-	56046.419542(7)	yes	Beuermann et al. 2013b
1240	-	56096.209342(31)	yes	Beuermann et al. 2013b
1324	-	56103.310081(9)	yes	Beuermann et al. 2013b
1335	-	56104.239948(5)	yes	Beuermann et al. 2013b
1336	-	56104.324466(11)	yes	Beuermann et al. 2013b
2244	-	56181.080223(13)	yes	Beuermann et al. 2013b
4461	-	56368.489324(9)	yes	Beuermann et al. 2013b
4532	-	56374.491149(8)	yes	Beuermann et al. 2013b
5589	-	56463.842276(19)	yes	Beuermann et al. 2013b
8180	-	56682.866650(20)	yes	Littlefair et al. 2014
8181	-	56682.951160(10)	yes	Littlefair et al. 2014
8192	-	56683.881020(10)	yes	Littlefair et al. 2014
8203	-	56684.810850(20)	yes	Littlefair et al. 2014
8215	-	56685.825280(20)	yes	Littlefair et al. 2014
8228	-	56686.924210(20)	yes	Littlefair et al. 2014
8252	-	56688.953000(20)	yes	Littlefair et al. 2014
8262	-	56689.798350(20)	yes	Littlefair et al. 2014
8608	-	56719.046632(6)	yes	Littlefair et al. 2014
8776	-	56733.248125(7)	yes	Littlefair et al. 2014
8888	-	56742.715760(20)	yes	Littlefair et al. 2014
8900	-	56743.730210(20)	yes	Littlefair et al. 2014
8901	-	56743.814720(20)	yes	Littlefair et al. 2014
8902	-	56743.899230(20)	yes	Littlefair et al. 2014

Table A.44: Continues on next page.

Table A.44: Times for CSS 21055; continued from previous page.

cycle	MJD(UTC)	BMJD(TDB)	pub?	source
8913	-	56744.829120(10)	yes	Littlefair et al. 2014
8914	-	56744.913650(20)	yes	Littlefair et al. 2014
8937	-	56746.857910(10)	yes	Littlefair et al. 2014
8938	-	56746.942440(20)	yes	Littlefair et al. 2014
8263	56689.880392(3)	56689.882833(3)	no	TNT+ULTRASPEC
8609	-	56719.131161(1)	no	WHT+ULTRACAM
8749	-	56730.965744(4)	no	WHT+ULTRACAM
8750	-	56731.050291(6)	no	WHT+ULTRACAM
8865	56740.766121(4)	56740.771554(4)	no	TNT+ULTRASPEC
9908	56828.936438(9)	56828.939204(9)	no	LT+RISE
12900	57081.856850(5)	57081.861191(5)	no	TNT+ULTRASPEC
13046	57094.197966(18)	57094.202951(18)	no	LT+RISE

Table A.45: 1 published and 1 unpublished mid-eclipse times for SDSS J1411+1028, a detached white dwarf + M-dwarf of spectral type M3. Numbers in parenthesis indicate the uncertainty in the last digit(s).

cycle	MJD(UTC)	BMJD(TDB)	pub?	source
0	56031.166642(48)	56031.172782(48)	yes	Parsons et al. 2013b
1947	-	56357.313983(43)	no	VLT+HAWK-I

Table A.46: 0 published and 4 unpublished mid-eclipse times for SDSS J1411+2117, a detached white dwarf + M-dwarf of spectral type M3. Numbers in parenthesis indicate the uncertainty in the last digit(s). See Fig. B.39 for the O-C diagram of all eclipse times with respect to the best linear ephemeris.

cycle	MJD(UTC)	BMJD(TDB)	pub?	source
2291	56396.111418(24)	56396.117096(24)	no	LT+RISE
2378	56424.094461(27)	56424.099555(27)	no	LT+RISE
3401	56753.128208(19)	56753.133836(19)	no	LT+RISE
4432	57084.736592(19)	57084.741079(19)	no	TNT+ULTRASPEC

Table A.47: 17 published and 11 unpublished mid-eclipse times for GK Vir, a detached white dwarf + M-dwarf of spectral type M4.5. Numbers in parenthesis indicate the uncertainty in the last digit(s). See Fig. B.40 for the O-C diagram of all eclipse times with respect to the best linear ephemeris.

cycle	MJD(UTC)	BMJD(TDB)	pub?	source
-67	42520.261300(10)	42520.267470(10)	yes	Green et al. 1978
-32	42532.312920(20)	42532.319050(20)	yes	Green et al. 1978
-29	42533.345920(90)	42533.352040(90)	yes	Green et al. 1978
0	42543.331790(10)	42543.337690(10)	yes	Green et al. 1978
3	42544.364820(10)	42544.370680(10)	yes	Green et al. 1978
851	42836.359160(60)	42836.363140(60)	yes	Green et al. 1978

Table A.47: Continues on next page.

Table A.47: Times for GK Vir; continued from previous page.

cycle	MJD(UTC)	BMJD(TDB)	pub?	source
1966	43220.286790(120)	43220.292020(120)	yes	Green et al. 1978
2132	43277.445220(60)	43277.451010(60)	yes	Green et al. 1978
2896	43540.518060(120)	43540.519720(120)	yes	Green et al. 1978
28666	52413.919783(1)	52413.925572(1)	yes	Parsons et al. 2010b
29735	52782.009582(1)	52782.015227(1)	yes	Parsons et al. 2010b
29738	52783.042623(1)	52783.048219(1)	yes	Parsons et al. 2010b
30746	53130.127467(3)	53130.133688(3)	yes	Parsons et al. 2010b
32706	53805.017186(2)	53805.022115(2)	yes	Parsons et al. 2010b
32709	53806.050117(1)	53806.055113(1)	yes	Parsons et al. 2010b
34054	54269.176110(0)	54269.180087(0)	yes	Parsons et al. 2010b
37069	55307.331176(1)	55307.337585(1)	yes	Parsons et al. 2012a
38913	55942.283445(1)	55942.283670(1)	no	WHT+ULTRACAM
37963	55615.165589(9)	55615.169378(9)	no	LT+RISE
38076	55654.072650(7)	55654.078751(7)	no	LT+RISE
38250	55713.987170(4)	55713.992323(4)	no	LT+RISE
39023	55980.156295(5)	55980.160063(5)	no	LT+RISE
40121	-	56358.235346(4)	no	VLT+HAWK-I
40211	56389.218891(7)	56389.225126(7)	no	LT+RISE
40234	-	56397.144731(4)	no	VLT+HAWK-I
41084	56689.824079(3)	56689.825955(3)	no	TNT+ULTRASPEC
41404	56800.006161(9)	56800.011828(9)	no	LT+RISE
42214	57078.915832(2)	57078.919823(2)	no	TNT+ULTRASPEC

Table A.48: 0 published and 7 unpublished mid-eclipse times for CSS 080408, a detached white dwarf + M-dwarf of spectral type M5. Numbers in parenthesis indicate the uncertainty in the last digit(s). See Fig. B.41 for the O-C diagram of all eclipse times with respect to the best linear ephemeris.

cycle	MJD(UTC)	BMJD(TDB)	pub?	source
-84	55616.113950(16)	55616.117762(16)	no	LT+RISE
0	55648.200876(9)	55648.206115(9)	no	LT+RISE
733	55928.215485(23)	55928.215235(23)	no	LT+RISE
1775	56326.261360(19)	56326.263749(19)	no	LT+RISE
2125	56459.962220(10)	56459.965249(10)	no	LT+RISE
2727	56689.929573(4)	56689.931829(4)	no	TNT+ULTRASPEC
2950	56775.113446(19)	56775.118790(19)	no	LT+RISE

Table A.49: 0 published and 5 unpublished mid-eclipse times for SDSS J1424+1124, a detached white dwarf + M-dwarf of unknown spectral type. Numbers in parenthesis indicate the uncertainty in the last digit(s). See Fig. B.42 for the O-C diagram of all eclipse times with respect to the best linear ephemeris.

cycle	MJD(UTC)	BMJD(TDB)	pub?	source
8888	56391.117637(8)	56391.123610(8)	no	LT+RISE

Table A.49: Continues on next page.

Table A.49: Times for SDSS J1424+1124; continued from previous page.

cycle	MJD(UTC)	BMJD(TDB)	pub?	source
8946	-	56405.002628(2)	no	WHT+ULTRACAM
10355	56742.161713(15)	56742.167268(15)	no	LT+RISE
10593	56799.113788(9)	56799.119126(9)	no	LT+RISE
11766	57079.806486(4)	57079.810458(4)	no	TNT+ULTRASPEC

Table A.50: 10 published and 20 unpublished mid-eclipse times for SDSS J1435+3733, a detached white dwarf + M-dwarf of spectral type M5. Numbers in parenthesis indicate the uncertainty in the last digit(s). See Fig. B.43 for the O-C diagram of all eclipse times with respect to the best linear ephemeris.

cycle	MJD(UTC)	BMJD(TDB)	pub?	source
0	54148.201120(200)	54148.204200(200)	yes	Pyrzas et al. 2009
8	54149.206260(200)	54149.209390(200)	yes	Pyrzas et al. 2009
15	54150.085590(200)	54150.088760(200)	yes	Pyrzas et al. 2009
16	54150.211530(200)	54150.214710(200)	yes	Pyrzas et al. 2009
722	54238.906160(200)	54238.909900(200)	yes	Pyrzas et al. 2009
730	54239.911190(200)	54239.914890(200)	yes	Pyrzas et al. 2009
732	54240.162580(200)	54240.166270(200)	yes	Pyrzas et al. 2009
804	54249.208480(16)	54249.211771(16)	yes	Pyrzas et al. 2009
820	54251.218682(4)	54251.221877(4)	yes	Pyrzas et al. 2009
829	54252.349395(5)	54252.352535(5)	yes	Pyrzas et al. 2009
11557	55600.120117(7)	55600.122736(7)	no	LT+RISE
11676	55615.069427(17)	55615.072833(17)	no	LT+RISE
11955	55650.119391(9)	55650.123876(9)	no	LT+RISE
12281	55691.075506(8)	55691.079592(8)	no	LT+RISE
12742	55748.994370(8)	55748.995471(8)	no	LT+RISE
14097	55919.225756(11)	55919.225430(11)	no	LT+RISE
14280	55942.214696(2)	55942.215869(2)	no	WHT+ULTRACAM
14661	55990.077430(11)	55990.081253(11)	no	LT+RISE
15003	56033.042499(6)	56033.047033(6)	no	LT+RISE
15305	56070.984039(12)	56070.987571(12)	no	LT+RISE
17623	56362.195888(9)	56362.199960(9)	no	LT+RISE
18115	56424.006325(10)	56424.010336(10)	no	LT+RISE
20200	56685.948718(3)	56685.950735(3)	no	TNT+ULTRASPEC
20457	56718.234168(8)	56718.237894(8)	no	LT+RISE
20645	56741.852082(7)	56741.856500(7)	no	TNT+ULTRASPEC
20926	-	56777.158766(1)	no	WHT+ULTRACAM
21100	56799.014901(8)	56799.018534(8)	no	LT+RISE
21370	56832.937052(8)	56832.938885(8)	no	LT+RISE
22890	57023.897607(4)	57023.897842(4)	no	TNT+ULTRASPEC
23327	57078.795033(5)	57078.798549(5)	no	TNT+ULTRASPEC

Table A.51: 0 published and 2 unpublished mid-eclipse times for CSS 09797, a detached white dwarf + M-dwarf of spectral type M5. Numbers in parenthesis indicate the uncertainty in the last digit(s).

cycle	MJD(UTC)	BMJD(TDB)	pub?	source
22308	-	56777.002737(1)	no	WHT+ULTRACAM
23769	57111.742217(10)	57111.747382(10)	no	TNT+ULTRASPEC

Table A.52: 0 published and 3 unpublished mid-eclipse times for SDSS J1540+3705, a detached white dwarf + M-dwarf of spectral type M4. Numbers in parenthesis indicate the uncertainty in the last digit(s). See Fig. B.44 for the O-C diagram of all eclipse times with respect to the best linear ephemeris.

cycle	MJD(UTC)	BMJD(TDB)	pub?	source
5817	56434.180652(28)	56434.184571(28)	no	LT+RISE
6999	56743.197733(19)	56743.201342(19)	no	LT+RISE
8302	57083.849370(40)	57083.851964(40)	no	TNT+ULTRASPEC

Table A.53: 7 published and 4 unpublished mid-eclipse times for SDSS J1548+4057, a detached white dwarf + M-dwarf of spectral type M6. Numbers in parenthesis indicate the uncertainty in the last digit(s). See Fig. B.45 for the O-C diagram of all eclipse times with respect to the best linear ephemeris.

cycle	MJD(UTC)	BMJD(TDB)	pub?	source
328	54652.919974(30)	54652.921968(30)	yes	Pyrzas et al. 2009
5920	-	55690.323510(12)	yes	Backhaus et al. 2012
5942	-	55694.404830(10)	yes	Backhaus et al. 2012
5947	-	55695.332395(16)	yes	Backhaus et al. 2012
6507	-	55799.220977(23)	yes	Backhaus et al. 2012
6512	-	55800.148543(11)	yes	Backhaus et al. 2012
6523	-	55802.189237(15)	yes	Backhaus et al. 2012
11660	56755.177628(11)	56755.181231(11)	no	LT+RISE
11599	56743.861426(6)	56743.864768(6)	no	TNT+ULTRASPEC
11610	56745.902053(5)	56745.905450(5)	no	TNT+ULTRASPEC
11902	56800.072346(12)	56800.075914(12)	no	LT+RISE

Table A.54: 146 published and 9 unpublished mid-eclipse times for NN Ser, a detached white dwarf + M-dwarf of spectral type M4. Numbers in parenthesis indicate the uncertainty in the last digit(s). See Fig. B.46 for the O-C diagram of all eclipse times with respect to the best linear ephemeris.

cycle	MJD(UTC)	BMJD(TDB)	pub?	source
0	-	47344.025000(5000)	yes	Haefner et al. 2004
2760	-	47703.045744(2)	yes	Haefner et al. 2004
2761	-	47703.175833(6)	yes	Haefner et al. 2004
2769	-	47704.216460(3)	yes	Haefner et al. 2004
2776	-	47705.127023(3)	yes	Wood & Marsh 1991

Table A.54: Continues on next page.

Table A.54: Times for NN Ser; continued from previous page.

cycle	MJD(UTC)	BMJD(TDB)	pub?	source
2777	-	47705.257115(7)	yes	Wood & Marsh 1991
2831	-	47712.281580(150)	yes	Haefner et al. 2004
2839	-	47713.322230(150)	yes	Haefner et al. 2004
7360	-	48301.414200(150)	yes	Haefner et al. 2004
28152	-	51006.040500(200)	yes	Haefner et al. 2004
30721	-	51340.216540(2)	yes	Beuermann et al. 2010
33233	-	51666.978006(96)	yes	Beuermann et al. 2010
38960	-	52411.947057(1)	yes	Parsons et al. 2010a
38961	-	52412.077138(0)	yes	Parsons et al. 2010a
38968	-	52412.987698(1)	yes	Parsons et al. 2010a
38976	-	52414.028339(1)	yes	Parsons et al. 2010a
38984	-	52415.068980(1)	yes	Parsons et al. 2010a
41782	-	52779.033169(1)	yes	Parsons et al. 2010a
41798	-	52781.114452(1)	yes	Parsons et al. 2010a
41806	-	52782.155092(1)	yes	Parsons et al. 2010a
41820	-	52783.976215(1)	yes	Parsons et al. 2010a
44472	-	53128.948679(3)	yes	Parsons et al. 2010a
44473	-	53129.078759(2)	yes	Parsons et al. 2010a
44474	-	53129.208838(1)	yes	Parsons et al. 2010a
44480	-	53129.989321(2)	yes	Parsons et al. 2010a
49662	-	53804.064455(2)	yes	Parsons et al. 2010a
49663	-	53804.194535(1)	yes	Parsons et al. 2010a
49671	-	53805.235178(0)	yes	Parsons et al. 2010a
53230	-	54268.190311(1)	yes	Parsons et al. 2010a
53237	-	54269.100871(0)	yes	Parsons et al. 2010a
56442	-	54686.007628(1)	yes	Parsons et al. 2010a
58638	-	54971.663497(80)	yes	Beuermann et al. 2010
58645	-	54972.574055(100)	yes	Beuermann et al. 2010
58684	-	54977.647179(120)	yes	Beuermann et al. 2010
58745	-	54985.582079(120)	yes	Beuermann et al. 2010
58753	-	54986.622836(130)	yes	Beuermann et al. 2010
58796	-	54992.216192(2)	yes	Beuermann et al. 2010
60489	-	55212.441819(7)	yes	Beuermann et al. 2010
60505	-	55214.523097(7)	yes	Beuermann et al. 2010
60528	-	55217.514938(4)	yes	Beuermann et al. 2010
60735	-	55244.441526(3)	yes	Beuermann et al. 2010
60743	-	55245.482166(3)	yes	Beuermann et al. 2010
60751	-	55246.522807(3)	yes	Beuermann et al. 2010
60774	-	55249.514647(3)	yes	Beuermann et al. 2010
60927	-	55269.416905(1)	yes	Beuermann et al. 2010
60950	-	55272.408749(1)	yes	Beuermann et al. 2010
61426	-	55334.326883(2)	yes	Beuermann et al. 2010
61440	-	55336.148006(2)	yes	Beuermann et al. 2010

Table A.54: Continues on next page.

Table A.54: Times for NN Ser; continued from previous page.

cycle	MJD(UTC)	BMJD(TDB)	pub?	source
61441	-	55336.278089(2)	yes	Beuermann et al. 2010
61564	-	55352.277944(1)	yes	Beuermann et al. 2010
61219	-	55307.400302(1)	yes	Marsh et al. 2014
61579	55354.223835(1)	55354.229144(1)	yes	Marsh et al. 2014
62316	55450.099534(5)	55450.098191(5)	yes	Beuermann et al. 2013a
62339	55453.091601(7)	55453.090037(7)	yes	Beuermann et al. 2013a
62347	55454.132312(7)	55454.130673(7)	yes	Beuermann et al. 2013a
62462	55469.092530(5)	55469.089904(5)	yes	Beuermann et al. 2013a
62531	55478.068543(5)	55478.065427(5)	yes	Beuermann et al. 2013a
63403	55591.495568(3)	55591.495301(3)	yes	Beuermann et al. 2013a
63449	55597.478749(3)	55597.478985(3)	yes	Beuermann et al. 2013a
63457	55598.519309(3)	55598.519633(3)	yes	Beuermann et al. 2013a
63472	55600.470336(7)	55600.470825(7)	yes	Beuermann et al. 2013a
63601	55617.249272(4)	55617.251177(4)	yes	Marsh et al. 2014
63671	55626.354137(4)	55626.356779(4)	yes	Beuermann et al. 2013a
63672	55626.484207(4)	55626.486859(4)	yes	Beuermann et al. 2013a
63679	55627.394690(4)	55627.397413(4)	yes	Beuermann et al. 2013a
63740	55635.328983(4)	55635.332304(4)	yes	Beuermann et al. 2013a
63741	55635.459054(5)	55635.462385(5)	yes	Beuermann et al. 2013a
63756	55637.410112(4)	55637.413583(4)	yes	Beuermann et al. 2013a
63816	55645.214409(6)	55645.218408(6)	yes	Marsh et al. 2014
63833	55647.425618(3)	55647.429756(3)	yes	Beuermann et al. 2013a
63864	55651.457868(5)	55651.462247(5)	yes	Beuermann et al. 2013a
63879	55653.408954(3)	55653.413444(3)	yes	Beuermann et al. 2013a
63886	55654.319462(4)	55654.324002(4)	yes	Beuermann et al. 2013a
63925	55659.392328(4)	55659.397131(4)	yes	Beuermann et al. 2013a
63933	55660.432916(5)	55660.437769(5)	yes	Beuermann et al. 2013a
64032	-	55673.315710(2)	yes	Marsh et al. 2014
64054	55676.172032(5)	55676.177475(5)	yes	Marsh et al. 2014
64079	55679.423950(4)	55679.429475(4)	yes	Beuermann et al. 2013a
64086	55680.334490(4)	55680.340035(4)	yes	Beuermann et al. 2013a
64116	55684.236823(5)	55684.242442(5)	yes	Beuermann et al. 2013a
64132	55686.318070(4)	55686.323719(4)	yes	Beuermann et al. 2013a
64322	55711.033400(5)	55711.038946(5)	yes	Marsh et al. 2014
64330	55712.074070(1)	55712.079593(1)	yes	Marsh et al. 2014
64575	55743.945064(4)	55743.949229(4)	yes	Marsh et al. 2014
64784	55771.133740(4)	55771.135975(4)	yes	Beuermann et al. 2013a
64836	55777.898460(4)	55777.900151(4)	yes	Marsh et al. 2014
64869	55782.191448(7)	55782.192787(7)	yes	Beuermann et al. 2013a
64938	55791.167719(4)	55791.168316(4)	yes	Beuermann et al. 2013a
64961	55794.159820(4)	55794.160169(4)	yes	Beuermann et al. 2013a
64976	55796.111177(4)	55796.111366(4)	yes	Beuermann et al. 2013a
64992	55798.192628(4)	55798.192646(4)	yes	Beuermann et al. 2013a

Table A.54: Continues on next page.

Table A.54: Times for NN Ser; continued from previous page.

cycle	MJD(UTC)	BMJD(TDB)	pub?	source
65053	55806.128161(5)	55806.127538(5)	yes	Beuermann et al. 2013a
65081	55809.770697(4)	55809.769788(4)	yes	Beuermann et al. 2013a
65084	55810.160972(10)	55810.160032(10)	yes	Beuermann et al. 2013a
65099	55812.112315(3)	55812.111224(3)	yes	Beuermann et al. 2013a
65099	55812.112317(5)	55812.111227(5)	yes	Beuermann et al. 2013a
65360	55846.065389(4)	55846.062149(4)	yes	Beuermann et al. 2013a
65460	55859.073898(9)	55859.070161(9)	yes	Beuermann et al. 2013a
65963	55924.503127(8)	55924.500492(8)	yes	Beuermann et al. 2013a
65992	55928.275212(13)	55928.272811(13)	yes	Marsh et al. 2014
65994	55928.535349(5)	55928.532965(5)	yes	Beuermann et al. 2013a
66069	-	55938.288987(3)	yes	Marsh et al. 2014
66092	55941.282322(1)	55941.280829(1)	yes	Marsh et al. 2014
66209	55956.500492(4)	55956.500209(4)	yes	Beuermann et al. 2013a
66324	55971.458447(4)	55971.459427(4)	yes	Beuermann et al. 2013a
66332	55972.499005(6)	55972.500074(6)	yes	Beuermann et al. 2013a
66362	55976.401079(8)	55976.402478(8)	yes	Beuermann et al. 2013a
66370	55977.441625(4)	55977.443111(4)	yes	Beuermann et al. 2013a
66409	55982.514323(5)	55982.516234(5)	yes	Beuermann et al. 2013a
66416	55983.424814(4)	55983.426800(4)	yes	Beuermann et al. 2013a
66545	56000.203857(5)	56000.207154(5)	yes	Marsh et al. 2014
66615	56009.308828(4)	56009.312755(4)	yes	Beuermann et al. 2013a
66631	56011.389971(3)	56011.394032(3)	yes	Beuermann et al. 2013a
66669	56016.332724(3)	56016.337084(3)	yes	Beuermann et al. 2013a
66670	56016.462798(3)	56016.467166(3)	yes	Beuermann et al. 2013a
66677	56017.373310(3)	56017.377730(3)	yes	Beuermann et al. 2013a
66685	56018.413890(3)	56018.418369(3)	yes	Beuermann et al. 2013a
66815	56035.323535(6)	56035.328791(6)	yes	Beuermann et al. 2013a
66868	56042.217573(0)	56042.223041(0)	yes	Marsh et al. 2014
66893	56045.469491(6)	56045.475036(6)	yes	Beuermann et al. 2013a
66900	56046.380035(4)	56046.385599(4)	yes	Beuermann et al. 2013a
66905	56047.030435(1)	56047.036012(1)	yes	Marsh et al. 2014
66908	56047.420657(3)	56047.426242(3)	yes	Beuermann et al. 2013a
67284	56096.331533(3)	56096.336391(3)	yes	Beuermann et al. 2013a
67330	56102.315514(4)	56102.320073(4)	yes	Beuermann et al. 2013a
67337	56103.226126(3)	56103.230636(3)	yes	Beuermann et al. 2013a
67352	56105.177439(4)	56105.181840(4)	yes	Beuermann et al. 2013a
67581	56134.967853(5)	56134.970213(5)	yes	Marsh et al. 2014
67675	56147.196369(6)	56147.197742(6)	yes	Beuermann et al. 2013a
67698	56150.188452(4)	56150.189579(4)	yes	Beuermann et al. 2013a
67775	56160.205466(5)	56160.205763(5)	yes	Beuermann et al. 2013a
67903	56176.857064(0)	56176.856026(0)	yes	Marsh et al. 2014
67928	56180.109313(3)	56180.108027(3)	yes	Beuermann et al. 2013a
67934	56180.889854(1)	56180.888510(1)	yes	Marsh et al. 2014

Table A.54: Continues on next page.

Table A.54: Times for NN Ser; continued from previous page.

cycle	MJD(UTC)	BMJD(TDB)	pub?	source
67936	56181.150036(4)	56181.148673(4)	yes	Beuermann et al. 2013a
68028	56193.118240(5)	56193.116037(5)	yes	Beuermann et al. 2013a
69067	56328.269094(6)	56328.269367(6)	yes	Marsh et al. 2014
69168	56341.406072(3)	56341.407460(3)	yes	Beuermann et al. 2013a
69291	-	56357.407337(8)	yes	Marsh et al. 2014
69298	-	56358.317885(3)	yes	Marsh et al. 2014
69336	56363.257786(6)	56363.260930(6)	yes	Marsh et al. 2014
69575	56394.345081(2)	56394.350099(2)	yes	Beuermann et al. 2013a
69597	-	56397.211872(6)	yes	Marsh et al. 2014
69598	-	56397.341952(5)	yes	Marsh et al. 2014
70287	-	56486.967206(0)	yes	Marsh et al. 2014
70387	-	56499.975225(0)	yes	Marsh et al. 2014
70457	-	56509.080845(6)	no	VLT+HAWK-I
71801	56683.909180(2)	56683.908642(2)	no	TNT+ULTRASPEC
71809	56684.949735(1)	56684.949282(1)	no	TNT+ULTRASPEC
72247	56741.920362(2)	56741.924423(2)	no	TNT+ULTRASPEC
72671	56797.072742(4)	56797.078431(4)	no	LT+RISE
74838	57078.960322(4)	57078.962277(4)	no	TNT+ULTRASPEC
74864	-	57082.344356(6)	no	DT+DFOSC
74884	57084.943529(2)	57084.945970(2)	no	TNT+ULTRASPEC
75164	57121.363594(3)	57121.368433(3)	no	VLT+HAWK-I

Table A.55: 1 published and 0 unpublished mid-eclipse times for SDSS J1642-0634, a detached white dwarf + M-dwarf of unknown spectral type. Numbers in parenthesis indicate the uncertainty in the last digit(s).

cycle	MJD(UTC)	BMJD(TDB)	pub?	source
6444	56770.187193(36)	56770.192429(36)	yes	Parsons et al. 2015

Table A.56: 3 published and 1 unpublished mid-eclipse times for GALEX J1717+6757, a detached double white dwarf binary. Numbers in parenthesis indicate the uncertainty in the last digit(s). See Fig. B.47 for the O-C diagram of all eclipse times with respect to the best linear ephemeris.

cycle	MJD(UTC)	BMJD(TDB)	pub?	source
620	55794.035279(41)	55794.035608(41)	yes	Hermes et al. 2014a
2184	56178.990983(42)	56178.991325(42)	yes	Hermes et al. 2014a
3508	56504.874339(29)	56504.874722(29)	yes	Hermes et al. 2014a
4487	56745.840248(62)	56745.841395(62)	no	TNT+ULTRASPEC

Table A.57: 2 published and 12 unpublished mid-eclipse times for RX J2130.6+4710, a detached white dwarf + M-dwarf of spectral type M3.5. Numbers in parenthesis indicate the uncertainty in the last digit(s). See Fig. B.48 for the O-C diagram of all eclipse times with respect to the best linear ephemeris.

cycle	MJD(UTC)	BMJD(TDB)	pub?	source
-716	-	52412.121116(3)	yes	Maxted et al. 2004
-2	-	52784.140552(3)	yes	Maxted et al. 2004
5585	55695.170119(8)	55695.169378(8)	no	LT+RISE
5681	55745.187036(8)	55745.188888(8)	no	LT+RISE
5744	55778.010933(11)	55778.014189(11)	no	LT+RISE
5840	55828.029825(7)	55828.033705(7)	no	LT+RISE
5951	55885.866842(8)	55885.868808(8)	no	LT+RISE
6510	56177.124270(1)	56177.128207(1)	no	WHT+ULTRACAM
6527	56185.981925(5)	56185.985871(5)	no	LT+RISE
7105	56487.142728(6)	56487.145155(6)	no	LT+RISE
7132	56501.210162(2)	56501.213181(2)	no	WHT+ULTRACAM
7340	56609.586547(3)	56609.588874(3)	no	TNT+ULTRASPEC
7771	56834.154375(6)	56834.155907(6)	no	LT+RISE
7957	56931.064987(9)	56931.068801(9)	no	LT+RISE

Table A.58: 0 published and 8 unpublished mid-eclipse times for SDSS J2205-0622, a detached white dwarf + M-dwarf of spectral type M2. Numbers in parenthesis indicate the uncertainty in the last digit(s). See Fig. B.49 for the O-C diagram of all eclipse times with respect to the best linear ephemeris.

cycle	MJD(UTC)	BMJD(TDB)	pub?	source
13030	56178.073117(28)	56178.079499(28)	no	LT+RISE
13052	56180.985753(4)	56180.992053(4)	no	WHT+ULTRACAM
13308	56214.878678(4)	56214.883086(4)	no	WHT+ULTRACAM
15138	56457.148120(20)	56457.151097(20)	no	LT+RISE
16051	56578.015743(44)	56578.020324(44)	no	LT+RISE
16254	56604.892625(38)	56604.894847(38)	no	LT+RISE
18069	56845.172310(22)	56845.177148(22)	no	LT+RISE
18650	56922.088099(26)	56922.094003(26)	no	LT+RISE

Table A.59: 0 published and 8 unpublished mid-eclipse times for CSS 09704, a detached white dwarf + M-dwarf of spectral type M4. Numbers in parenthesis indicate the uncertainty in the last digit(s). See Fig. B.50 for the O-C diagram of all eclipse times with respect to the best linear ephemeris.

cycle	MJD(UTC)	BMJD(TDB)	pub?	source
-4133	55529.041029(5)	55529.041486(5)	no	NTT+ULTRACAM
-1974	55866.934176(4)	55866.937284(4)	no	WHT+ULTRACAM
0	56175.873099(4)	56175.879528(4)	no	WHT+ULTRACAM
7	56176.968661(3)	56176.975070(3)	no	WHT+ULTRACAM
217	56209.836343(3)	56209.841269(3)	no	WHT+ULTRACAM

Table A.59: Continues on next page.

Table A.59: Times for CSS 09704; continued from previous page.

cycle	MJD(UTC)	BMJD(TDB)	pub?	source
2130	-	56509.236672(12)	no	VLT+HAWK-I
4168	56828.192144(30)	56828.195379(30)	no	LT+RISE
5093	56972.960943(49)	56972.963135(49)	no	LT+RISE

Table A.60: 0 published and 6 unpublished mid-eclipse times for SDSS J2235+1428, a detached white dwarf + M-dwarf of spectral type M4. Numbers in parenthesis indicate the uncertainty in the last digit(s). See Fig. B.51 for the O-C diagram of all eclipse times with respect to the best linear ephemeris.

cycle	MJD(UTC)	BMJD(TDB)	pub?	source
298	-	55512.113583(5)	no	NTT+ULTRACAM
318	-	55515.002759(24)	no	NTT+ULTRACAM
4901	56177.041836(3)	56177.048015(3)	no	WHT+ULTRACAM
4928	56180.942176(3)	56180.948348(3)	no	WHT+ULTRACAM
7200	56509.149014(21)	56509.154334(21)	no	VLT+HAWK-I
9457	56835.191007(19)	56835.193575(19)	no	LT+RISE

Table A.61: 0 published and 1 unpublished mid-eclipse times for SDSS J2306-0555, a detached white dwarf + M-dwarf of unknown spectral type. Numbers in parenthesis indicate the uncertainty in the last digit(s).

cycle	MJD(UTC)	BMJD(TDB)	pub?	source
7574	57024.540637(21)	57024.539104(21)	no	TNT+ULTRASPEC

Table A.62: 34 published and 17 unpublished mid-eclipse times for HT Cas, a cataclysmic variable with an M-dwarf donor of spectral type M5.4. Numbers in parenthesis indicate the uncertainty in the last digit(s). See Fig. B.52 for the O-C diagram of all eclipse times with respect to the best linear ephemeris.

cycle	MJD(UTC)	BMJD(TDB)	pub?	source
0	-	43727.437783(50)	yes	Patterson 1981
448	-	43760.433778(50)	yes	Patterson 1981
461	-	43761.391293(50)	yes	Patterson 1981
462	-	43761.464917(50)	yes	Patterson 1981
732	-	43781.350620(50)	yes	Patterson 1981
746	-	43782.381721(50)	yes	Patterson 1981
1599	-	43845.203167(50)	yes	Patterson 1981
1600	-	43845.276745(50)	yes	Patterson 1981
1897	-	43867.149100(50)	yes	Patterson 1981
1898	-	43867.222796(50)	yes	Patterson 1981
1993	-	43874.218953(50)	yes	Patterson 1981
1926	-	43869.284880(50)	yes	Patterson 1981
1938	-	43870.168673(50)	yes	Patterson 1981
1939	-	43870.242209(50)	yes	Patterson 1981

Table A.62: Continues on next page.

Table A.62: Times for HT Cas; continued from previous page.

cycle	MJD(UTC)	BMJD(TDB)	pub?	source
20473	-	45235.217088(50)	yes	Horne et al. 1991
20475	-	45235.364438(50)	yes	Horne et al. 1991
20476	-	45235.438058(50)	yes	Horne et al. 1991
20477	-	45235.511638(50)	yes	Horne et al. 1991
26338	-	45667.157925(50)	yes	Horne et al. 1991
26339	-	45667.231595(50)	yes	Horne et al. 1991
26351	-	45668.115345(50)	yes	Horne et al. 1991
26352	-	45668.189015(50)	yes	Horne et al. 1991
26394	-	45671.282174(50)	yes	Horne et al. 1991
26421	-	45673.270674(50)	yes	Horne et al. 1991
26447	-	45675.185474(50)	yes	Horne et al. 1991
26473	-	45677.100344(50)	yes	Horne et al. 1991
26475	-	45677.247624(50)	yes	Horne et al. 1991
26501	-	45679.162404(50)	yes	Horne et al. 1991
26502	-	45679.236014(50)	yes	Horne et al. 1991
119537	-	52531.003765(5)	yes	Feline et al. 2005
119550	-	52531.961207(5)	yes	Feline et al. 2005
125129	-	52942.838901(5)	yes	Feline et al. 2005
125130	-	52942.912534(5)	yes	Feline et al. 2005
141152	-	54122.887730(30)	yes	Borges et al. 2008
144918	-	54400.242723(10)	no	WHT+ULTRACAM
163613	-	55777.076233(12)	no	LT+RISE
164035	-	55808.155347(10)	no	LT+RISE
164820	-	55865.968341(10)	no	LT+RISE
165199	-	55893.880677(6)	no	LT+RISE
165540	-	55918.994386(10)	no	LT+RISE
169261	56193.032097(12)	56193.035631(12)	no	LT+RISE
170102	56254.968449(20)	56254.972921(20)	no	LT+RISE
170250	56265.868550(8)	56265.872738(8)	no	LT+RISE
174298	56563.992811(12)	56563.996604(12)	no	LT+RISE
175452	56648.981946(13)	56648.985410(13)	no	LT+RISE
178483	-	56872.210113(3)	no	WHT+ULTRACAM
178508	-	56874.051317(2)	no	WHT+ULTRACAM
179093	56917.131717(10)	56917.134949(10)	no	LT+RISE
180367	57010.957870(13)	57010.961499(13)	no	LT+RISE
180062	56988.494693(7)	56988.499115(7)	no	TNT+ULTRASPEC
180539	57023.625821(12)	57023.628798(12)	no	TNT+ULTRASPEC

Table A.63: 7 published and 8 unpublished mid-eclipse times for FL Cet, a cataclysmic variable with an M-dwarf donor of spectral type M5.5. Numbers in parenthesis indicate the uncertainty in the last digit(s). See Fig. B.53 for the O-C diagram of all eclipse times with respect to the best linear ephemeris.

cycle	MJD(UTC)	BMJD(TDB)	pub?	source
10250	-	53589.115210(6)	yes	O'Donoghue et al. 2006
10251	-	53589.175729(6)	yes	O'Donoghue et al. 2006
10317	-	53593.169806(6)	yes	O'Donoghue et al. 2006
10332	-	53594.077554(6)	yes	O'Donoghue et al. 2006
10761	-	53620.039053(6)	yes	O'Donoghue et al. 2006
10762	-	53620.099568(6)	yes	O'Donoghue et al. 2006
10777	-	53621.007336(6)	yes	O'Donoghue et al. 2006
46390	55776.173120(11)	55776.175191(11)	no	LT+RISE
46917	55808.062576(7)	55808.067297(7)	no	LT+RISE
47875	55866.035618(4)	55866.041894(4)	no	LT+RISE
48650	55912.938371(2)	55912.942043(2)	no	LT+RISE
53033	56178.180048(86)	56178.185105(86)	no	LT+RISE
65243	56917.083757(38)	56917.089321(38)	no	LT+RISE
66397	56986.919938(36)	56986.925243(36)	no	LT+RISE
61499	56690.517033(1)	56690.516239(1)	no	TNT+ULTRASPEC

Table A.64: 0 published and 17 unpublished mid-egress times for GY Cnc, a cataclysmic variable with an M-dwarf donor of spectral type M3. Numbers in parenthesis indicate the uncertainty in the last digit(s). See Fig. B.54 for the O-C diagram of all eclipse times with respect to the best linear ephemeris.

cycle	MJD(UTC)	BMJD(TDB)	pub?	source
24537	55886.160739(25)	55886.162898(25)	no	LT+RISE
24685	55912.123886(50)	55912.128339(50)	no	LT+RISE
24776	55928.088162(55)	55928.093675(55)	no	LT+RISE
24834	55938.263267(29)	55938.269265(29)	no	WHT+ULTRACAM
24851	55941.245674(7)	55941.251783(7)	no	WHT+ULTRACAM
24861	55943.000041(10)	55943.006207(10)	no	WHT+ULTRACAM
24862	55943.175481(4)	55943.181653(4)	no	WHT+ULTRACAM
24885	55947.210540(8)	55947.216826(8)	no	WHT+ULTRACAM
26407	56214.241775(33)	56214.240287(33)	no	LT+RISE
26640	56255.115852(64)	56255.118366(64)	no	LT+RISE
26760	56276.167396(37)	56276.171755(37)	no	LT+RISE
27426	56393.013137(39)	56393.016182(39)	no	LT+RISE
28749	56625.123556(31)	56625.126507(31)	no	LT+RISE
29057	56679.156446(80)	56679.162756(80)	no	LT+RISE
29083	56683.717816(10)	56683.724210(10)	no	TNT+ULTRASPEC
31345	57080.568716(32)	57080.574693(32)	no	TNT+ULTRASPEC
31444	57097.938384(39)	57097.943445(39)	no	LT+RISE

Table A.65: 8 published and 7 unpublished mid-eclipse times for SDSS J1035+0551, a cataclysmic variable with a brown dwarf donor. Numbers in parenthesis indicate the uncertainty in the last digit(s). See Fig. B.55 for the O-C diagram of all eclipse times with respect to the best linear ephemeris.

cycle	MJD(UTC)	BMJD(TDB)	pub?	source
-27277	-	53798.981480(10)	yes	Littlefair et al. 2008
-27276	-	53799.038480(20)	yes	Littlefair et al. 2008
-27275	-	53799.095480(20)	yes	Littlefair et al. 2008
-27258	-	53800.064590(20)	yes	Littlefair et al. 2008
-27226	-	53801.888810(20)	yes	Littlefair et al. 2008
-27225	-	53801.945820(20)	yes	Littlefair et al. 2008
-27224	-	53802.002820(20)	yes	Littlefair et al. 2008
-27205	-	53803.085960(20)	yes	Littlefair et al. 2008
-19154	-	54262.046646(1)	no	VLT+ULTRACAM
0	-	55353.952449(9)	no	NTT+ULTRACAM
23311	56682.829422(10)	56682.834967(10)	no	TNT+ULTRASPEC
23383	56686.933699(8)	56686.939458(8)	no	TNT+ULTRASPEC
23435	56689.897902(6)	56689.903798(6)	no	TNT+ULTRASPEC
24379	56743.712260(8)	56743.718086(8)	no	TNT+ULTRASPEC
30744	57106.559646(17)	57106.565573(17)	no	TNT+ULTRASPEC

Table A.66: 9 published and 5 unpublished mid-eclipse times for NZ Boo, a cataclysmic variable with an M-dwarf donor of unknown spectral type. Numbers in parenthesis indicate the uncertainty in the last digit(s). See Fig. B.56 for the O-C diagram of all eclipse times with respect to the best linear ephemeris.

cycle	MJD(UTC)	BMJD(TDB)	pub?	source
0	-	53799.140618(4)	yes	Littlefair et al. 2008
2	-	53799.258414(7)	yes	Littlefair et al. 2008
17	-	53800.142070(6)	yes	Littlefair et al. 2008
18	-	53800.200966(6)	yes	Littlefair et al. 2008
19	-	53800.259901(6)	yes	Littlefair et al. 2008
52	-	53802.203911(2)	yes	Littlefair et al. 2008
68	-	53803.146461(3)	yes	Littlefair et al. 2008
69	-	53803.205371(6)	yes	Littlefair et al. 2008
70	-	53803.264277(3)	yes	Littlefair et al. 2008
40345	56175.845569(4)	56175.843649(4)	no	WHT+ULTRACAM
40396	56178.850086(2)	56178.848030(2)	no	WHT+ULTRACAM
40430	56180.853111(2)	56180.850968(2)	no	WHT+ULTRACAM
48970	56683.936627(3)	56683.937893(3)	no	TNT+ULTRASPEC
55757	57083.753101(17)	57083.756442(17)	no	TNT+ULTRASPEC

Table A.67: 0 published and 13 unpublished mid-eclipse times for SDSS J1702+3229, a cataclysmic variable with an M-dwarf donor of spectral type M0. Numbers in parenthesis indicate the uncertainty in the last digit(s). See Fig. B.57 for the O-C diagram of all eclipse times with respect to the best linear ephemeris.

cycle	MJD(UTC)	BMJD(TDB)	pub?	source
-538	53593.890944(5)	53593.892793(5)	no	WHT+ULTRACAM
-537	53593.990979(4)	53593.992823(4)	no	WHT+ULTRACAM
-528	53594.891796(3)	53594.893592(3)	no	WHT+ULTRACAM
-508	53596.893512(5)	53596.895200(5)	no	WHT+ULTRACAM
-498	53597.894390(6)	53597.896023(6)	no	WHT+ULTRACAM
7445	54392.850720(10)	54392.849022(10)	no	WHT+ULTRACAM
25291	56178.915967(3)	56178.916293(3)	no	WHT+ULTRACAM
25610	56210.843825(4)	56210.842515(4)	no	WHT+ULTRACAM
25640	56213.846424(7)	56213.844985(7)	no	WHT+ULTRACAM
25650	56214.847281(5)	56214.845801(5)	no	WHT+ULTRACAM
31059	56756.187557(34)	56756.190500(34)	no	LT+RISE
30935	56743.777904(37)	56743.780256(37)	no	TNT+ULTRASPEC
34726	57123.188986(137)	57123.191998(137)	no	LT+RISE

Table A.68: 0 published and 16 unpublished mid-egress times for V2301 Oph, a cataclysmic variable with an M-dwarf donor of spectral type M5.5. Numbers in parenthesis indicate the uncertainty in the last digit(s). See Fig. B.58 for the O-C diagram of all eclipse times with respect to the best linear ephemeris.

cycle	MJD(UTC)	BMJD(TDB)	pub?	source
92350	-	55315.381033(6)	no	NTT+ULTRACAM
92413	-	55320.323431(3)	no	NTT+ULTRACAM
97320	-	55705.277495(2)	no	NTT+ULTRACAM
98234	55776.976242(9)	55776.980781(9)	no	LT+RISE
98629	55807.966128(13)	55807.968532(13)	no	LT+RISE
100838	55981.265858(9)	55981.264552(9)	no	LT+RISE
103447	56185.939127(10)	56185.940496(10)	no	LT+RISE
105478	56345.273839(18)	56345.272454(18)	no	LT+RISE
105720	56364.257181(26)	56364.257331(26)	no	LT+RISE
106446	56421.207520(13)	56421.212022(13)	no	LT+RISE
108239	56561.872344(11)	56561.872827(11)	no	LT+RISE
110691	56754.229898(15)	56754.232121(15)	no	LT+RISE
110907	56771.173768(18)	56771.177289(18)	no	LT+RISE
111848	56844.993112(10)	56844.998740(10)	no	LT+RISE
112829	56921.957346(15)	56921.958259(15)	no	LT+RISE
114843	57079.957619(12)	57079.956547(12)	no	TNT+ULTRASPEC

Table A.69: 0 published and 10 unpublished mid-eclipse times for EP Dra, a cataclysmic variable with an M-dwarf donor of unknown spectral type. Numbers in parenthesis indicate the uncertainty in the last digit(s). See Fig. B.59 for the O-C diagram of all eclipse times with respect to the best linear ephemeris.

cycle	MJD(UTC)	BMJD(TDB)	pub?	source
116874	56172.860125(2)	56172.861351(2)	no	WHT+ULTRACAM
116958	56178.963204(1)	56178.964481(1)	no	WHT+ULTRACAM
116972	56179.980385(1)	56179.981670(1)	no	WHT+ULTRACAM
116999	56181.942116(22)	56181.943416(22)	no	LT+RISE
117439	56213.910702(2)	56213.912152(2)	no	WHT+ULTRACAM
121035	56475.183776(23)	56475.184319(23)	no	LT+RISE
122394	56573.922785(10)	56573.924225(10)	no	LT+RISE
124903	56756.218821(42)	56756.218925(42)	no	LT+RISE
125602	56807.005501(34)	56807.005736(34)	no	LT+RISE
127115	56916.933388(16)	56916.934722(16)	no	LT+RISE

Table A.70: 15 published and 9 unpublished mid-eclipse times for V713 Cep, a cataclysmic variable with an M-dwarf donor of unknown spectral type. Numbers in parenthesis indicate the uncertainty in the last digit(s). See Fig. B.60 for the O-C diagram of all eclipse times with respect to the best linear ephemeris.

cycle	MJD(UTC)	BMJD(TDB)	pub?	source
0	-	54337.877266(70)	yes	Boyd et al. 2011
13	-	54338.987676(40)	yes	Boyd et al. 2011
47	-	54341.891686(130)	yes	Boyd et al. 2011
106	-	54346.931796(210)	yes	Boyd et al. 2011
8596	-	55072.134040(70)	yes	Boyd et al. 2011
8597	-	55072.219370(70)	yes	Boyd et al. 2011
8598	-	55072.304930(30)	yes	Boyd et al. 2011
8599	-	55072.390290(40)	yes	Boyd et al. 2011
8600	-	55072.475800(60)	yes	Boyd et al. 2011
8605	-	55072.902800(20)	yes	Boyd et al. 2011
8605	-	55072.902830(20)	yes	Boyd et al. 2011
8605	-	55072.902960(30)	yes	Boyd et al. 2011
8606	-	55072.988180(100)	yes	Boyd et al. 2011
8606	-	55072.988190(30)	yes	Boyd et al. 2011
8607	-	55073.073580(130)	yes	Boyd et al. 2011
17131	55801.178668(3)	55801.181116(3)	no	WHT+ULTRACAM
21530	56176.934565(3)	56176.937151(3)	no	WHT+ULTRACAM
21541	56177.874169(2)	56177.876763(2)	no	WHT+ULTRACAM
21566	56180.009618(2)	56180.012230(2)	no	WHT+ULTRACAM
26177	56573.874387(31)	56573.876993(31)	no	LT+RISE
29189	56831.156778(34)	56831.157545(34)	no	LT+RISE
29668	-	56872.073000(3)	no	WHT+ULTRACAM
29763	-	56880.187780(9)	no	WHT+ULTRACAM
30181	56915.890070(48)	56915.892722(48)	no	LT+RISE

Table A.71: 215 published and 2 unpublished mid-egress times for HU Aqr, a cataclysmic variable with an M-dwarf donor of spectral type M4.3. Numbers in parenthesis indicate the uncertainty in the last digit(s). See Fig. B.61 for the O-C diagram of all eclipse times with respect to the best linear ephemeris.

cycle	MJD(UTC)	BMJD(TDB)	pub?	source
0	-	49102.420003(3)	yes	Schwope et al. 2001
1319	-	49216.936112(12)	yes	Schwarz et al. 2009
1320	-	49217.022922(12)	yes	Schwarz et al. 2009
1321	-	49217.109749(12)	yes	Schwarz et al. 2009
1322	-	49217.196601(23)	yes	Schwarz et al. 2009
1333	-	49218.151610(23)	yes	Schwarz et al. 2009
1334	-	49218.238439(23)	yes	Schwarz et al. 2009
1367	-	49221.103501(23)	yes	Schwarz et al. 2009
1368	-	49221.190319(23)	yes	Schwarz et al. 2009
1369	-	49221.277148(23)	yes	Schwarz et al. 2009
2212	-	49294.466794(1)	yes	Schwope et al. 2001
2213	-	49294.553612(3)	yes	Schwope et al. 2001
2216	-	49294.814078(2)	yes	Schwope et al. 2001
2222	-	49295.334997(2)	yes	Schwope et al. 2001
2225	-	49295.595459(1)	yes	Schwope et al. 2001
2226	-	49295.682282(2)	yes	Schwope et al. 2001
4241	-	49470.625425(11)	yes	Schwope et al. 2001
4409	-	49485.211281(28)	yes	Schwope et al. 2001
6328	-	49651.819628(27)	yes	Schwope et al. 2001
6341	-	49652.948328(7)	yes	Schwope et al. 2001
6390	-	49657.202533(7)	yes	Schwope et al. 2001
6391	-	49657.289378(20)	yes	Schwope et al. 2001
6403	-	49658.331195(12)	yes	Schwope et al. 2001
6576	-	49673.351129(13)	yes	Schwope et al. 2001
6579	-	49673.611592(7)	yes	Schwope et al. 2001
10707	-	50032.006278(25)	yes	Schwope et al. 2001
12607	-	50196.965043(14)	yes	Schwope et al. 2001
13064	-	50236.642003(10)	yes	Schwope et al. 2001
13620	-	50284.914104(116)	yes	Schwarz et al. 2009
13621	-	50285.000878(116)	yes	Schwarz et al. 2009
13632	-	50285.955890(116)	yes	Schwarz et al. 2009
13707	-	50292.467518(18)	yes	Schwope et al. 2001
14087	-	50325.459254(28)	yes	Schwarz et al. 2009
14088	-	50325.546074(28)	yes	Schwarz et al. 2009
14115	-	50327.890324(116)	yes	Schwarz et al. 2009
14116	-	50327.977162(116)	yes	Schwarz et al. 2009
14138	-	50329.887041(116)	yes	Schwarz et al. 2009
14139	-	50329.973866(116)	yes	Schwarz et al. 2009
14236	-	50338.395480(28)	yes	Schwarz et al. 2009
14250	-	50339.610986(11)	yes	Schwope et al. 2001

Table A.71: Continues on next page.

Table A.71: Times for HU Aqr; continued from previous page.

cycle	MJD(UTC)	BMJD(TDB)	pub?	source
14740	-	50382.152977(13)	yes	Schwope et al. 2001
14746	-	50382.673929(19)	yes	Schwope et al. 2001
16906	-	50570.205988(7)	yes	Schwope et al. 2001
17010	-	50579.235344(31)	yes	Schwope et al. 2001
17030	-	50580.971740(10)	yes	Schwope et al. 2001
17994	-	50664.666649(20)	yes	Schwope et al. 2001
21014	-	50926.864280(13)	yes	Schwope et al. 2001
21023	-	50927.645649(7)	yes	Schwope et al. 2001
21026	-	50927.906116(7)	yes	Schwope et al. 2001
22478	-	51053.969347(9)	yes	Schwope et al. 2001
22788	-	51080.883711(116)	yes	Schwarz et al. 2009
25892	-	51350.374322(12)	yes	Schwarz et al. 2009
25926	-	51353.326219(12)	yes	Schwarz et al. 2009
25938	-	51354.368078(12)	yes	Schwarz et al. 2009
27394	-	51480.778636(23)	yes	Schwarz et al. 2009
29946	-	51702.344335(4)	yes	Goździewski et al. 2012
29955	-	51703.125705(81)	yes	Schwarz et al. 2009
29955	-	51703.125705(92)	yes	Schwarz et al. 2009
29957	-	51703.299354(4)	yes	Goździewski et al. 2012
29958	-	51703.386171(3)	yes	Goździewski et al. 2012
29966	-	51704.080704(81)	yes	Schwarz et al. 2009
30265	-	51730.040032(4)	yes	Goździewski et al. 2012
30276	-	51730.995065(2)	yes	Schwarz et al. 2009
30277	-	51731.081897(2)	yes	Schwarz et al. 2009
30287	-	51731.950090(2)	yes	Goździewski et al. 2012
30299	-	51732.991936(3)	yes	Goździewski et al. 2012
30300	-	51733.078755(5)	yes	Goździewski et al. 2012
30310	-	51733.946974(3)	yes	Goździewski et al. 2012
30311	-	51734.033786(2)	yes	Goździewski et al. 2012
31312	-	51820.941021(12)	yes	Bridge et al. 2002
31313	-	51821.027841(12)	yes	Bridge et al. 2002
35043	-	52144.867925(46)	yes	Schwarz et al. 2009
35376	-	52173.779097(2)	yes	Schwarz et al. 2009
35377	-	52173.865910(2)	yes	Schwarz et al. 2009
35469	-	52181.853385(3)	yes	Goździewski et al. 2012
38098	-	52410.104163(8)	yes	Goździewski et al. 2012
38105	-	52410.711871(58)	yes	Schwarz et al. 2009
38107	-	52410.885575(23)	yes	Schwarz et al. 2009
38107	-	52410.885578(23)	yes	Schwarz et al. 2009
38108	-	52410.972392(23)	yes	Schwarz et al. 2009
38109	-	52411.059193(3)	yes	Schwarz et al. 2009
38133	-	52413.142851(12)	yes	Schwarz et al. 2009
38145	-	52414.184740(12)	yes	Schwarz et al. 2009

Table A.71: Continues on next page.

Table A.71: Times for HU Aqr; continued from previous page.

cycle	MJD(UTC)	BMJD(TDB)	pub?	source
39731	-	52551.881844(12)	yes	Schwarz et al. 2009
39742	-	52552.836841(12)	yes	Schwarz et al. 2009
42352	-	52779.438034(58)	yes	Schwarz et al. 2009
42395	-	52783.171299(12)	yes	Schwarz et al. 2009
42441	-	52787.165040(2)	yes	Schwarz et al. 2009
42463	-	52789.075093(1)	yes	Schwarz et al. 2009
42464	-	52789.161927(2)	yes	Schwarz et al. 2009
42486	-	52791.071948(2)	yes	Goździewski et al. 2012
42487	-	52791.158771(2)	yes	Goździewski et al. 2012
44534	-	52968.880076(3)	yes	Goździewski et al. 2012
44557	-	52970.876938(8)	yes	Goździewski et al. 2012
47253	-	53204.944708(3)	yes	Schwarz et al. 2009
47254	-	53205.031529(4)	yes	Schwarz et al. 2009
47300	-	53209.025273(4)	yes	Schwarz et al. 2009
47335	-	53212.064002(4)	yes	Schwarz et al. 2009
48265	-	53292.806957(10)	yes	Schwarz et al. 2009
48288	-	53294.803823(4)	yes	Schwarz et al. 2009
48299	-	53295.758834(7)	yes	Schwarz et al. 2009
48334	-	53298.797557(2)	yes	Schwarz et al. 2009
50702	-	53504.388294(6)	yes	Schwarz et al. 2009
50713	-	53505.343317(6)	yes	Schwarz et al. 2009
50714	-	53505.430139(6)	yes	Schwarz et al. 2009
50724	-	53506.298342(6)	yes	Schwarz et al. 2009
50725	-	53506.385162(6)	yes	Schwarz et al. 2009
50737	-	53507.427008(6)	yes	Schwarz et al. 2009
51020	-	53531.997160(10)	yes	Goździewski et al. 2012
51032	-	53533.039017(5)	yes	Schwarz et al. 2009
51066	-	53535.990903(6)	yes	Goździewski et al. 2012
51067	-	53536.077728(3)	yes	Goździewski et al. 2012
55466	-	53918.000719(5)	yes	Schwarz et al. 2009
55535	-	53923.991343(10)	yes	Goździewski et al. 2012
55546	-	53924.946356(8)	yes	Schwarz et al. 2009
55627	-	53931.978816(6)	yes	Goździewski et al. 2012
55661	-	53934.930707(6)	yes	Goździewski et al. 2012
55719	-	53939.966275(16)	yes	Goździewski et al. 2012
59524	-	54270.317989(16)	yes	Schwarz et al. 2009
59525	-	54270.404812(16)	yes	Schwarz et al. 2009
59558	-	54273.269884(16)	yes	Schwarz et al. 2009
59559	-	54273.356704(16)	yes	Schwarz et al. 2009
60085	-	54319.024241(7)	yes	Goździewski et al. 2012
60096	-	54319.979254(4)	yes	Schwarz et al. 2009
60097	-	54320.066077(6)	yes	Schwarz et al. 2009
64657	-	54715.967150(5)	yes	Goździewski et al. 2012

Table A.71: Continues on next page.

Table A.71: Times for HU Aqr; continued from previous page.

cycle	MJD(UTC)	BMJD(TDB)	pub?	source
64885	-	54735.762208(4)	yes	Goździewski et al. 2012
64886	-	54735.849018(2)	yes	Goździewski et al. 2012
65265	-	54768.753993(2)	yes	Goździewski et al. 2012
67604	-	54971.826789(39)	yes	Qian et al. 2011
67791	-	54988.062271(3)	yes	Goździewski et al. 2012
67917	-	54999.001639(2)	yes	Goździewski et al. 2012
67918	-	54999.088453(5)	yes	Goździewski et al. 2012
68009	-	55006.989116(2)	yes	Goździewski et al. 2012
68914	-	55085.561477(39)	yes	Qian et al. 2011
68926	-	55086.603349(39)	yes	Qian et al. 2011
69328	-	55121.505145(39)	yes	Qian et al. 2011
69490	-	55135.570057(39)	yes	Qian et al. 2011
69800	-	55162.484342(39)	yes	Qian et al. 2011
69812	-	55163.526193(39)	yes	Qian et al. 2011
69823	-	55164.481195(39)	yes	Qian et al. 2011
69915	-	55172.468672(39)	yes	Qian et al. 2011
71785	-	55334.822762(39)	yes	Qian et al. 2011
72009	-	55354.270604(0)	yes	Bours et al. 2014b
72010	-	55354.357445(1)	yes	Bours et al. 2014b
72099	-	55362.084437(3)	yes	Goździewski et al. 2012
72110	-	55363.039455(2)	yes	Goździewski et al. 2012
72121	-	55363.994489(3)	yes	Goździewski et al. 2012
72133	-	55365.036344(2)	yes	Goździewski et al. 2012
72225	-	55373.023804(5)	yes	Goździewski et al. 2012
72237	-	55374.065646(4)	yes	Goździewski et al. 2012
72248	-	55375.020672(4)	yes	Goździewski et al. 2012
72305	-	55379.969429(3)	yes	Goździewski et al. 2012
72351	-	55383.963175(2)	yes	Goździewski et al. 2012
72352	-	55384.049994(2)	yes	Goździewski et al. 2012
72421	-	55390.040611(1)	yes	Goździewski et al. 2012
73409	-	55475.819097(58)	yes	Goździewski et al. 2012
73559	-	55488.842170(58)	yes	Goździewski et al. 2012
73560	-	55488.929015(116)	yes	Goździewski et al. 2012
75467	-	55654.495428(4)	yes	Goździewski et al. 2012
75812	-	55684.448461(2)	yes	Goździewski et al. 2012
76053	-	55705.372159(1)	yes	Bours et al. 2014b
76348	-	55730.984142(5)	yes	Goździewski et al. 2015
76394	-	55734.977882(2)	yes	Goździewski et al. 2015
76395	-	55735.064695(2)	yes	Goździewski et al. 2015
76406	-	55736.019723(2)	yes	Goździewski et al. 2015
76464	-	55741.055278(9)	yes	Goździewski et al. 2015
76532	-	55746.959088(3)	yes	Goździewski et al. 2015
76555	-	55748.955959(2)	yes	Goździewski et al. 2015

Table A.71: Continues on next page.

Table A.71: Times for HU Aqr; continued from previous page.

cycle	MJD(UTC)	BMJD(TDB)	pub?	source
76556	-	55749.042775(2)	yes	Goździewski et al. 2015
76567	-	55749.997804(2)	yes	Goździewski et al. 2015
76648	-	55757.030248(7)	yes	Goździewski et al. 2015
76721	-	55763.368141(4)	yes	Goździewski et al. 2012
76868	55776.124280(2)	55776.130743(2)	yes	Bours et al. 2014b
77031	-	55790.282457(4)	yes	Goździewski et al. 2012
77066	-	55793.321156(8)	yes	Goździewski et al. 2012
77067	-	55793.407984(6)	yes	Goździewski et al. 2012
77078	-	55794.363018(6)	yes	Goździewski et al. 2012
77247	55809.029681(3)	55809.035656(3)	yes	Bours et al. 2014b
77546	-	55834.994949(6)	yes	Goździewski et al. 2012
77557	-	55835.949990(30)	yes	Goździewski et al. 2012
77789	-	55856.092285(4)	yes	Goździewski et al. 2012
77802	-	55857.220940(9)	yes	Goździewski et al. 2012
77823	-	55859.044179(7)	yes	Goździewski et al. 2012
77902	55865.901266(2)	55865.902986(2)	yes	Bours et al. 2014b
78100	-	55883.093404(2)	yes	Goździewski et al. 2012
80324	56076.179088(2)	56076.181839(2)	yes	Bours et al. 2014b
80485	56090.155945(2)	56090.159898(2)	yes	Bours et al. 2014b
81001	-	56134.959164(7)	yes	Goździewski et al. 2015
81013	-	56136.001030(6)	yes	Goździewski et al. 2015
81162	-	56148.937269(6)	yes	Goździewski et al. 2015
81186	-	56151.020949(2)	yes	Goździewski et al. 2015
81231	-	56154.927850(3)	yes	Goździewski et al. 2015
81486	-	56177.067025(1)	yes	Bours et al. 2014b
81531	56180.968253(2)	56180.973947(2)	yes	Bours et al. 2014b
81532	-	56181.060772(1)	yes	Bours et al. 2014b
81910	-	56213.878846(2)	yes	Bours et al. 2014b
82566	56270.834988(5)	56270.832960(5)	yes	Bours et al. 2014b
84275	56419.208217(11)	56419.208883(11)	yes	Bours et al. 2014b
84678	56454.193561(2)	56454.197437(2)	yes	Bours et al. 2014b
85746	-	56546.921478(7)	yes	Goździewski et al. 2015
85965	56565.930722(1)	56565.935170(1)	yes	Bours et al. 2014b
86032	-	56571.752079(3)	yes	Goździewski et al. 2015
86241	-	56589.897536(26)	yes	Schwope & Thinius 2014
86391	56602.919464(2)	56602.920582(2)	yes	Bours et al. 2014b
86412	-	56604.743777(3)	yes	Goździewski et al. 2015
86433	56606.566292(5)	56606.567051(5)	yes	Bours et al. 2014b
86467	56609.518465(2)	56609.518933(2)	yes	Bours et al. 2014b
86976	-	56653.710428(36)	yes	Goździewski et al. 2015
88383	-	56775.866504(2)	yes	Goździewski et al. 2015
88973	56827.085936(2)	56827.090413(2)	yes	Bours et al. 2014b
88985	56828.127697(4)	56828.132252(4)	yes	Bours et al. 2014b

Table A.71: Continues on next page.

Table A.71: Times for HU Aqr; continued from previous page.

cycle	MJD(UTC)	BMJD(TDB)	pub?	source
89066	56835.159672(2)	56835.164713(2)	yes	Bours et al. 2014b
89339	-	56858.866633(6)	yes	Goździewski et al. 2015
89340	-	56858.953452(10)	yes	Goździewski et al. 2015
90009	56917.030775(3)	56917.036181(3)	no	LT+RISE
90330	56944.902157(2)	56944.905481(2)	no	LT+RISE

Table A.72: 0 published and 3 unpublished mid-eclipse times for SDSS J2141+0507, a cataclysmic variable with an M-dwarf donor of unknown spectral type. Numbers in parenthesis indicate the uncertainty in the last digit(s). See Fig. B.62 for the O-C diagram of all eclipse times with respect to the best linear ephemeris.

cycle	MJD(UTC)	BMJD(TDB)	pub?	source
-1	56214.895281(2)	56214.899412(2)	no	WHT+ULTRACAM
0	56214.949982(2)	56214.954108(2)	no	WHT+ULTRACAM
967	56267.841765(56)	56267.841100(56)	no	LT+RISE

★ ★ ★

Appendix B

Observed - Calculated diagrams

This appendix includes all the observed minus calculated eclipse time diagrams, also known as O-C diagrams, for the white dwarf binaries in the timing program as described in Chapter 5. All diagrams include previously published times from the literature as well as the yet unpublished times, as presented in Appendix A. The O-C diagrams are plotted with respect to the best linear ephemerides, listed in Tables 5.1 for the detached binaries and in Table 5.2 for the cataclysmic variables in the program. Times with uncertainties larger than 3 seconds have been greyed out for clarity.

★ ★ ★
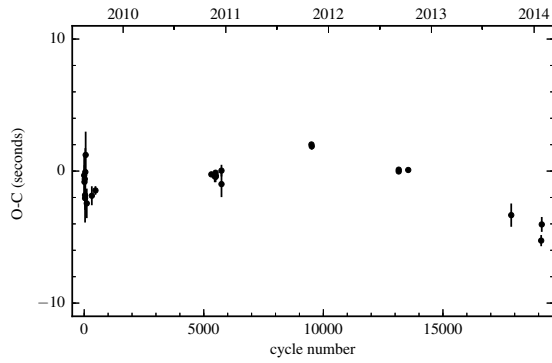
Figure B.1: O-C diagram of SDSS J0106-0014.
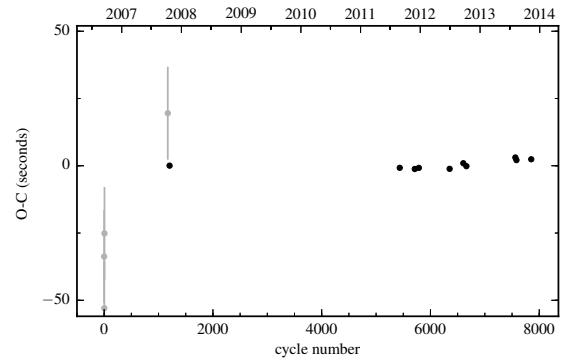
Figure B.2: O-C diagram of SDSS J0110+1326.
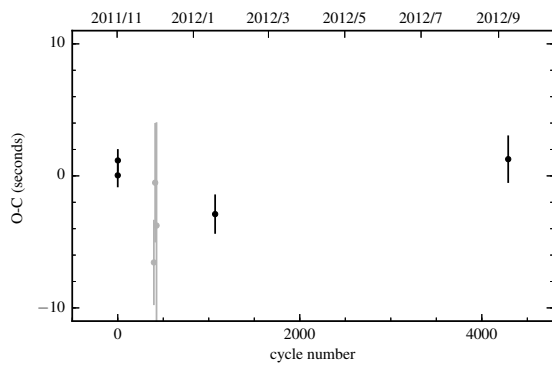
Figure B.3: O-C diagram of SDSS J0138-0016.
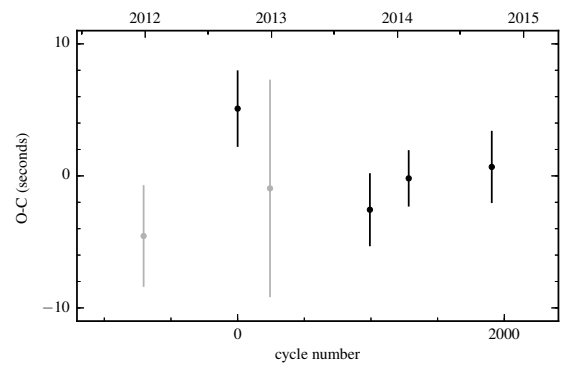
Figure B.4: O-C diagram of PTFEB28.235.
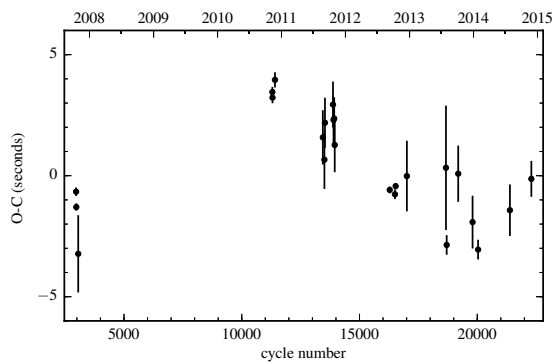
Figure B.5: O-C diagram of SDSS J0303+0054.
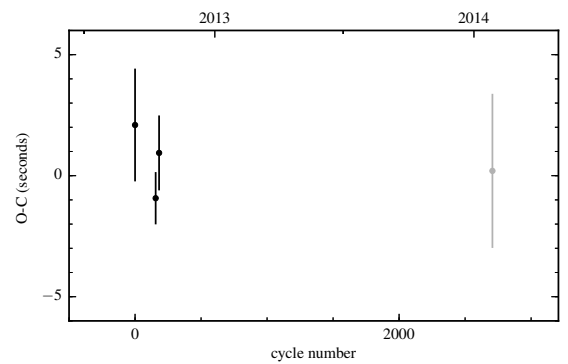
Figure B.6: O-C diagram of SDSS J0308-0054.
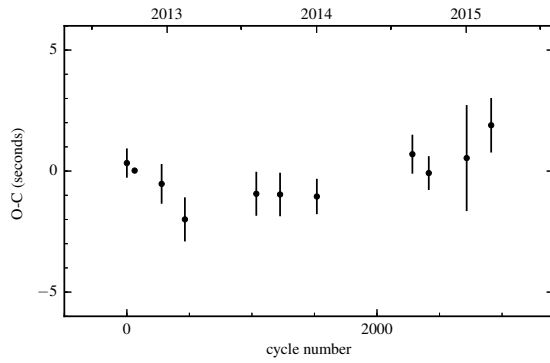
Figure B.7: O-C diagram of SDSS J0314+0206.
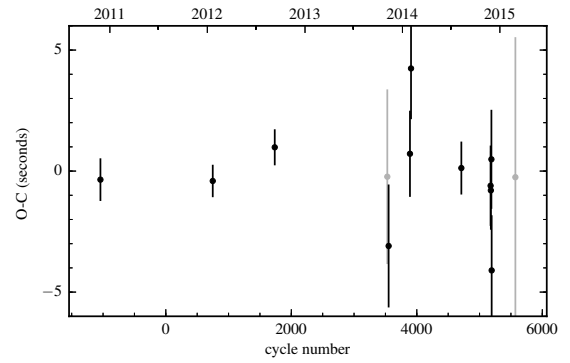
Figure B.8: O-C diagram of NLTT 11748.
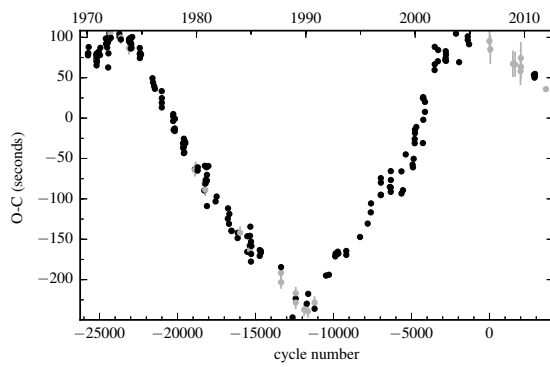
Figure B.9: O-C diagram of V471 Tau.
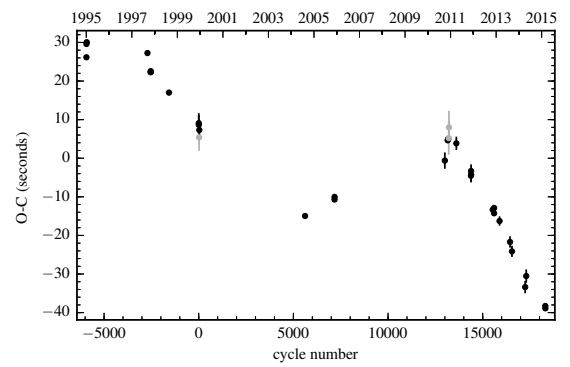
Figure B.10: O-C diagram of RR Cae.
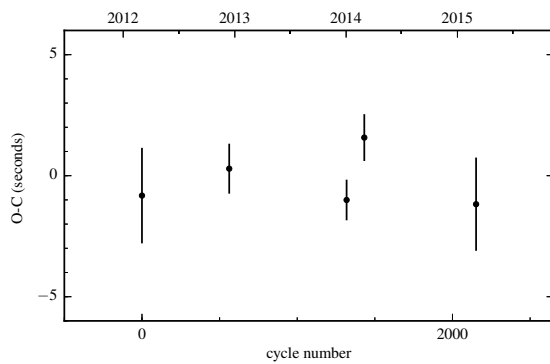
Figure B.11: O-C diagram of SDSS J0821+4559.
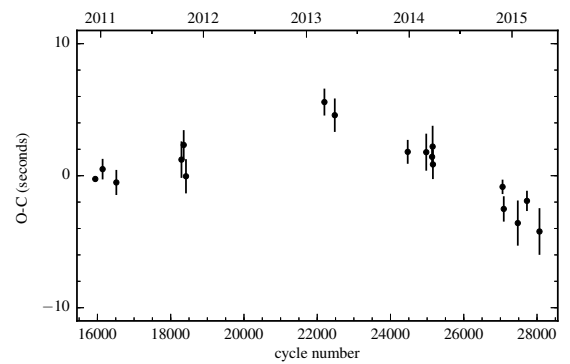
Figure B.12: O-C diagram of CSS 40190.
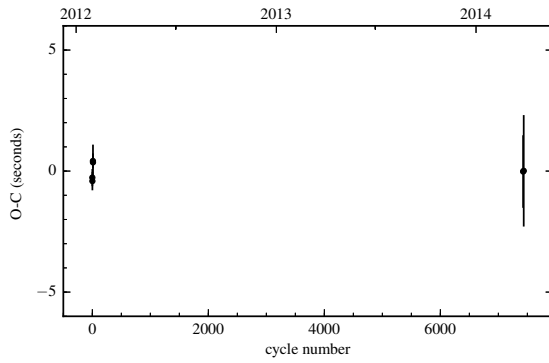
Figure B.13: O-C diagram of SDSS J0857+3318.
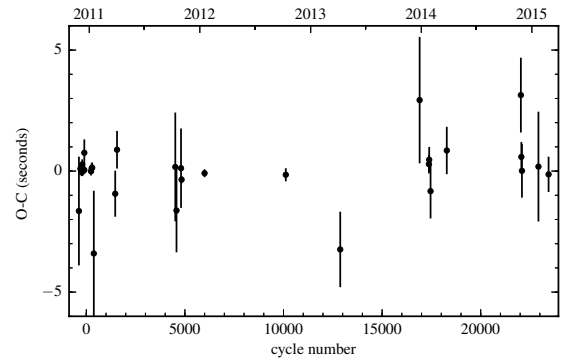
Figure B.14: O-C diagram of CSS 03170.
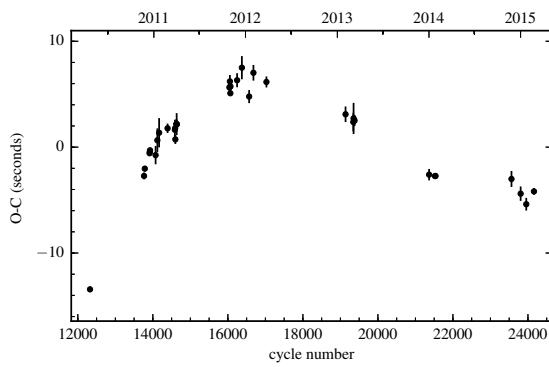
Figure B.15: O-C diagram of CSS 080502.
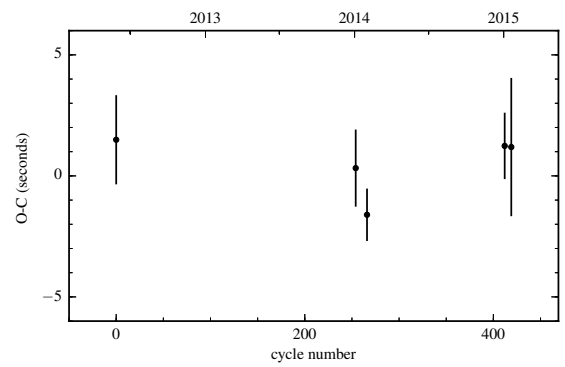
Figure B.16: O-C diagram of SDSS J0927+3329.
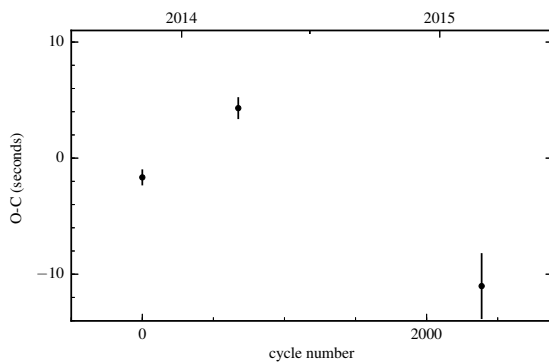
Figure B.17: O-C diagram of SDSS J0935+2700.
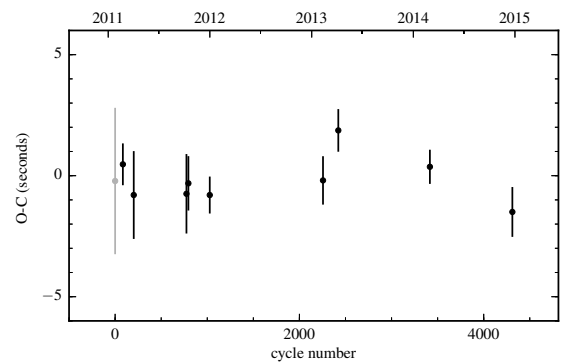
Figure B.18: O-C diagram of CSS 38094.
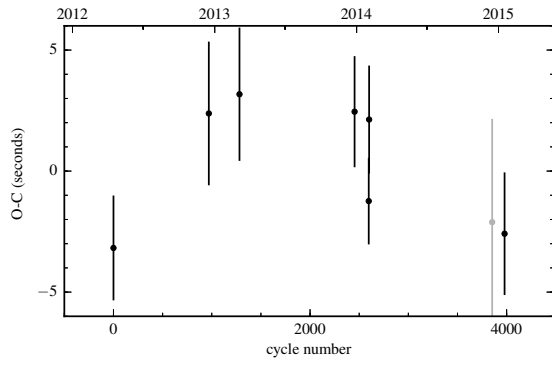
Figure B.19: O-C diagram of SDSS J0946+2030.
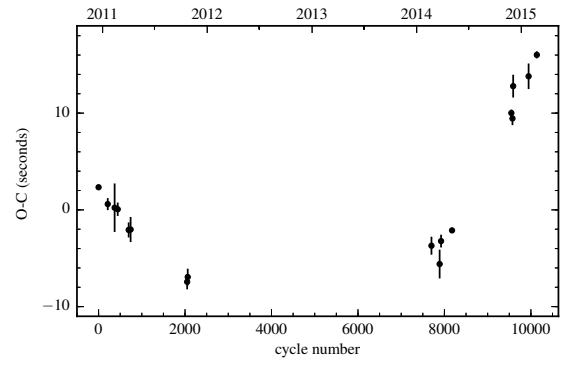
Figure B.20: O-C diagram of CSS 41631.
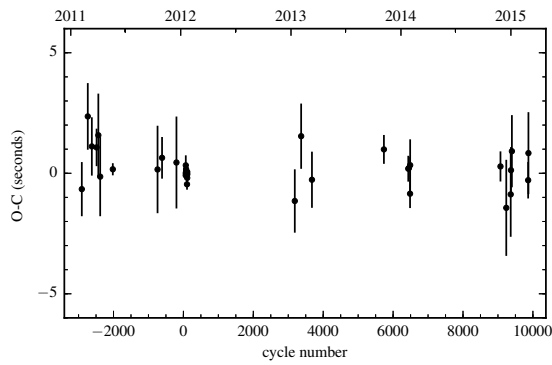
Figure B.21: O-C diagram of CSS 41177.
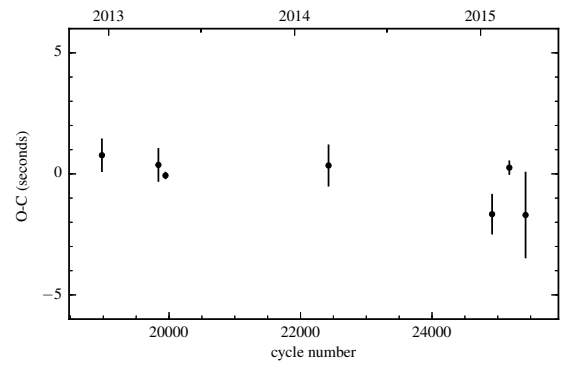
Figure B.22: O-C diagram of SDSS J1013+2724.
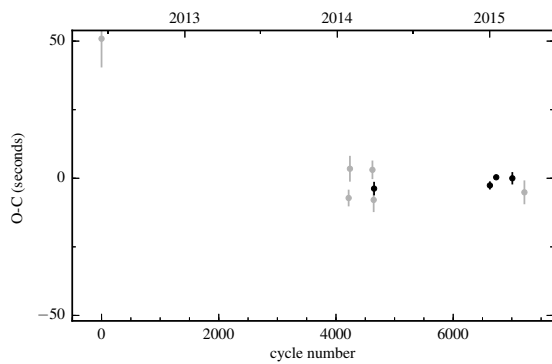
Figure B.23: O-C diagram of SDSS J1021+1744.
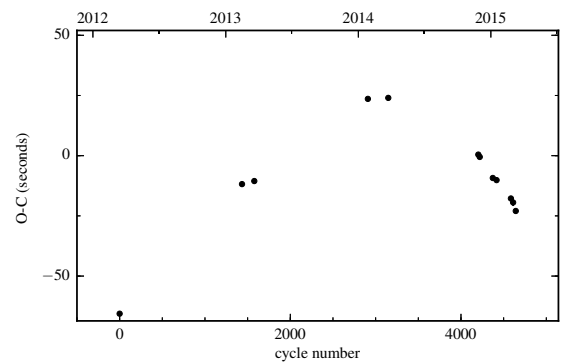
Figure B.24: O-C diagram of SDSS J1028+0931.
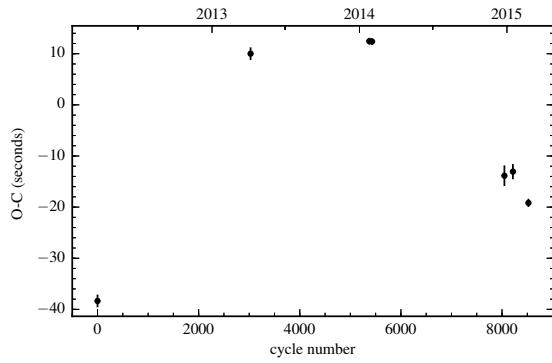
Figure B.25: O-C diagram of SDSS J1057+1307.
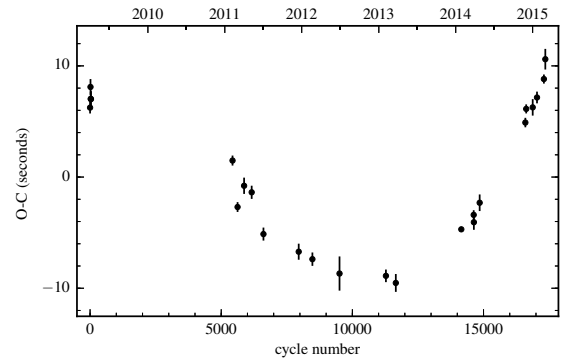
Figure B.26: O-C diagram of SDSS J1210+3347.
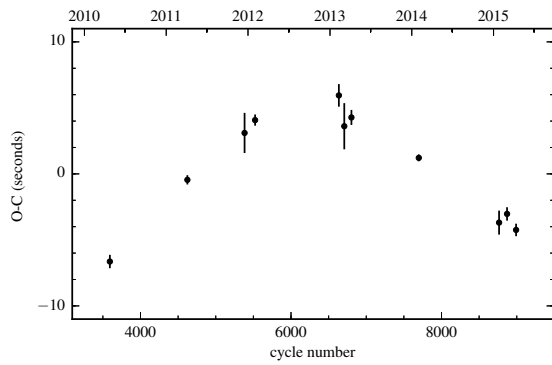
Figure B.27: O-C diagram of SDSS J1212-0123.
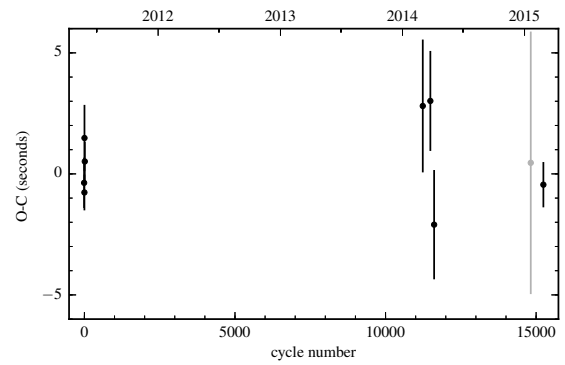
Figure B.28: O-C diagram of SDSS J1223-0056.
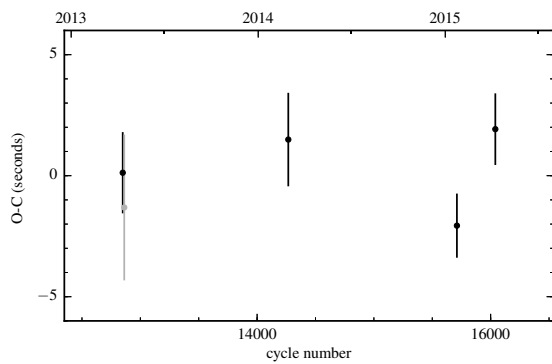
Figure B.29: O-C diagram of CSS 25601.
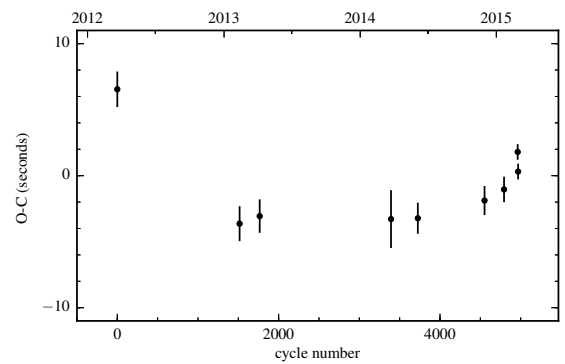
Figure B.30: O-C diagram of SDSS J1307+2156.
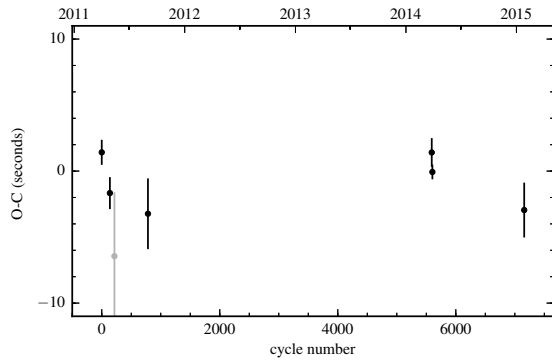
Figure B.31: O-C diagram of CSS 21616.
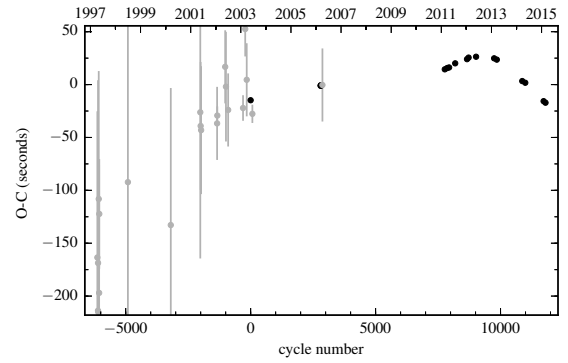
Figure B.32: O-C diagram of DE CVn.
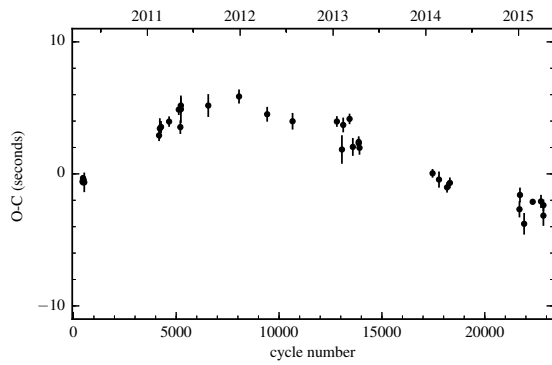
Figure B.33: O-C diagram of SDSS J1329+1230.
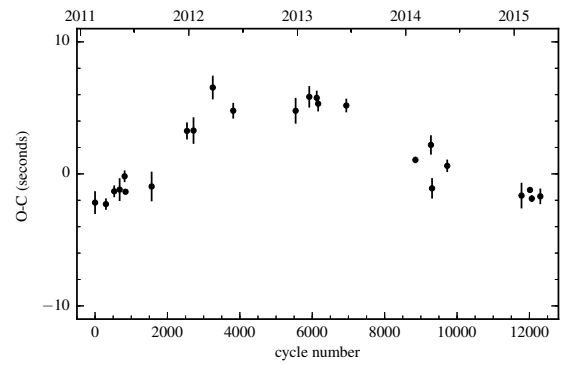
Figure B.34: O-C diagram of WD 1333+005.
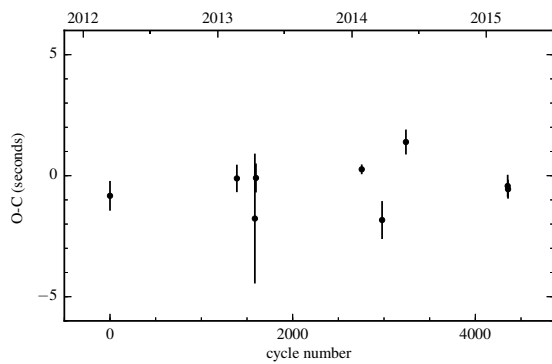
Figure B.35: O-C diagram of CSS 21357.
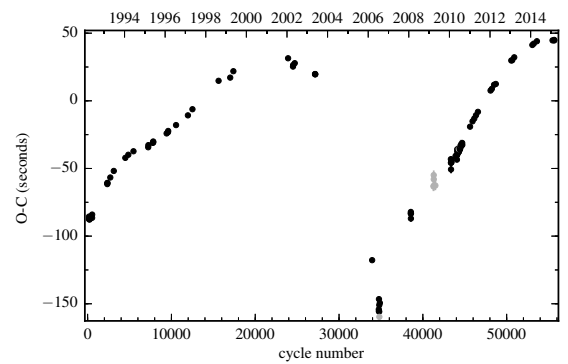
Figure B.36: O-C diagram of QS Vir.
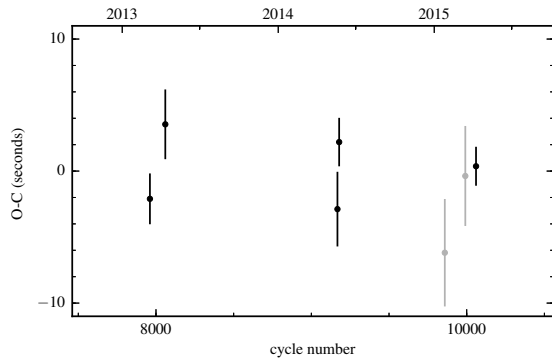
Figure B.37: O-C diagram of CSS 07125.
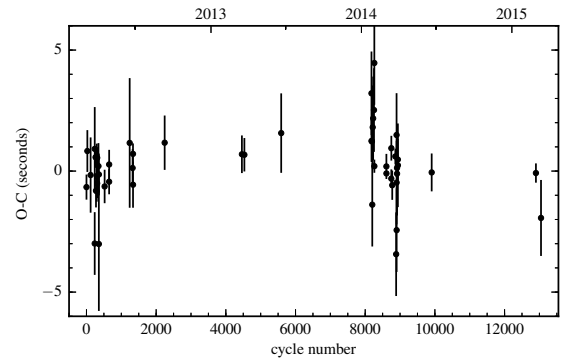
Figure B.38: O-C diagram of CSS 21055.
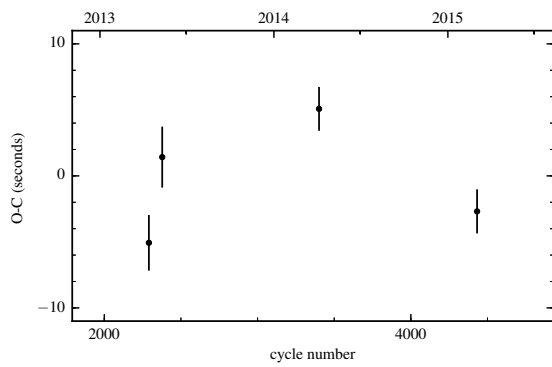
Figure B.39: O-C diagram of SDSS J1411+2117.
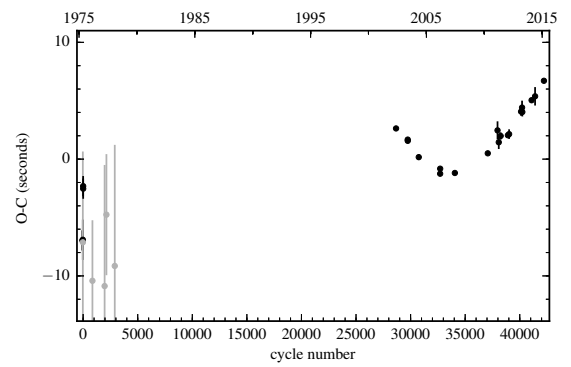
Figure B.40: O-C diagram of GK Vir.
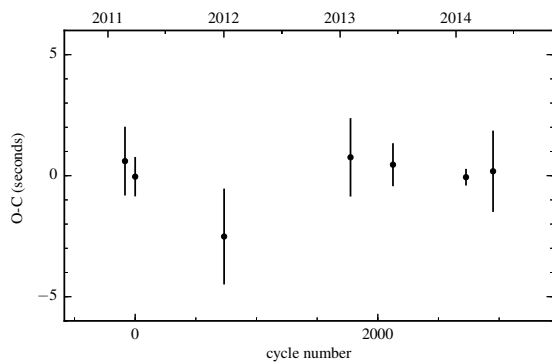
Figure B.41: O-C diagram of CSS 080408.
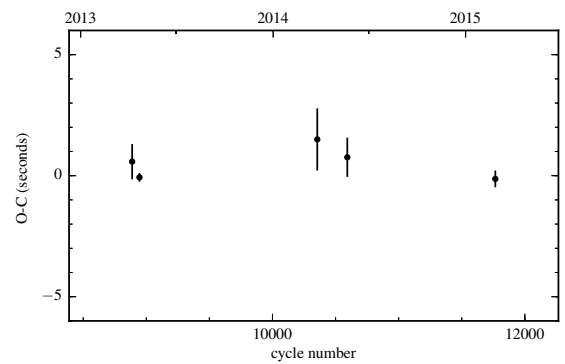
Figure B.42: O-C diagram of SDSS J1424+1124.
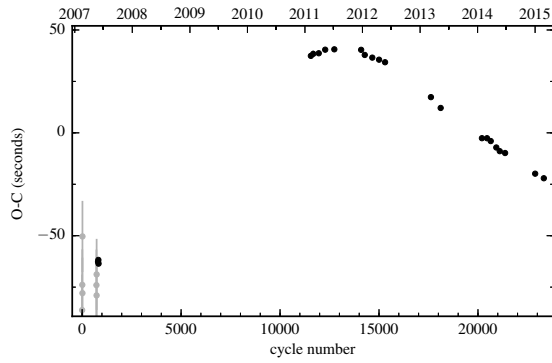
Figure B.43: O-C diagram of SDSS J1435+3733.
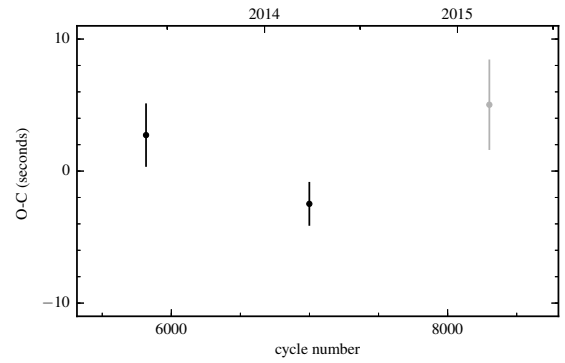
Figure B.44: O-C diagram of SDSS J1540+3705.
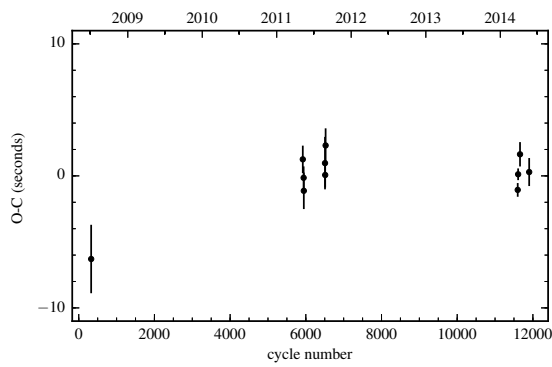
Figure B.45: O-C diagram of SDSS J1548+4057.
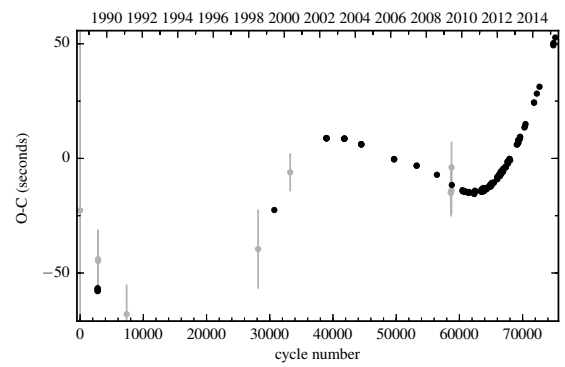
Figure B.46: O-C diagram of NN Ser.
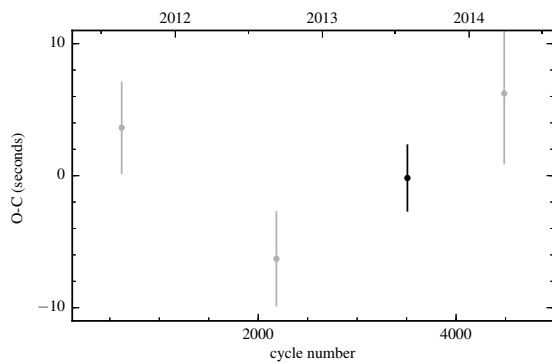
Figure B.47: O-C diagram of GALEX J1717+6757.
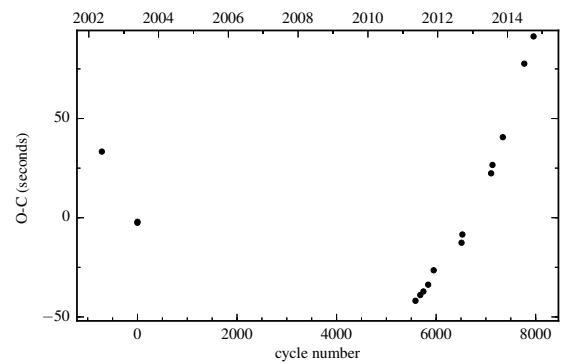
Figure B.48: O-C diagram of RX J2130.6+4710.
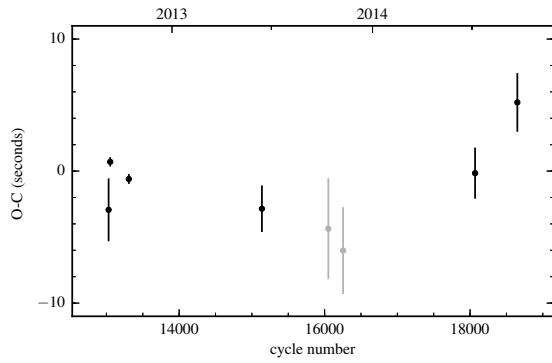
Figure B.49: O-C diagram of SDSS J2205-0622.
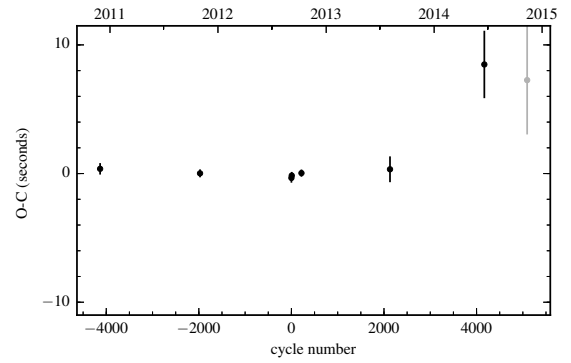
Figure B.50: O-C diagram of CSS 09704.
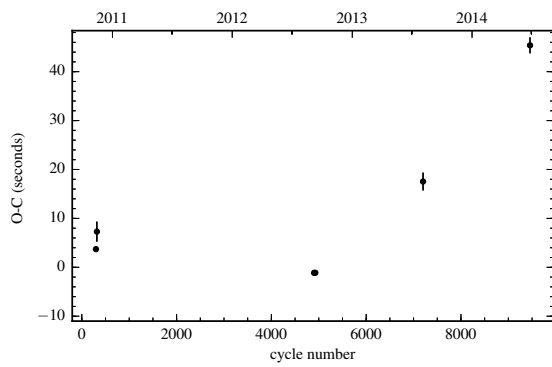
Figure B.51: O-C diagram of SDSS J2235+1428.
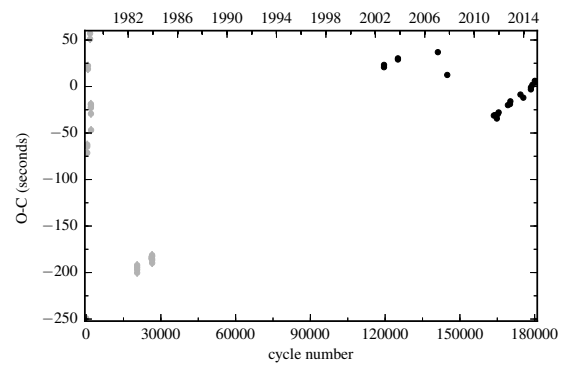
Figure B.52: O-C diagram of HT Cas.
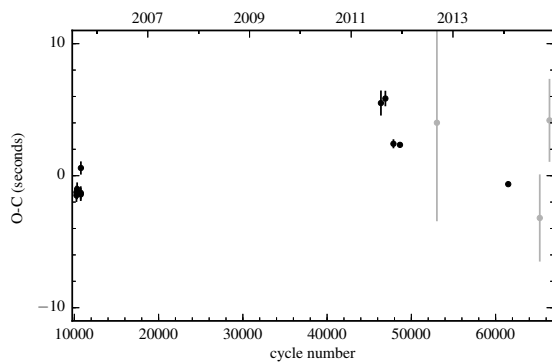
Figure B.53: O-C diagram of FL Cet.
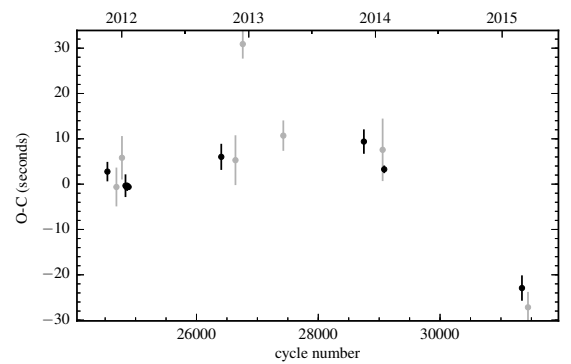
Figure B.54: O-C diagram of GY Cnc.
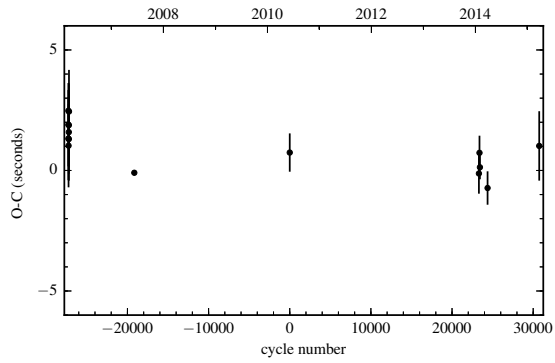
Figure B.55: O-C diagram of SDSS J1035+0551.
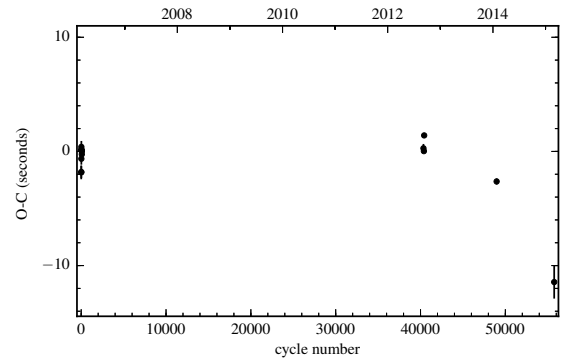
Figure B.56: O-C diagram of NZ Boo.
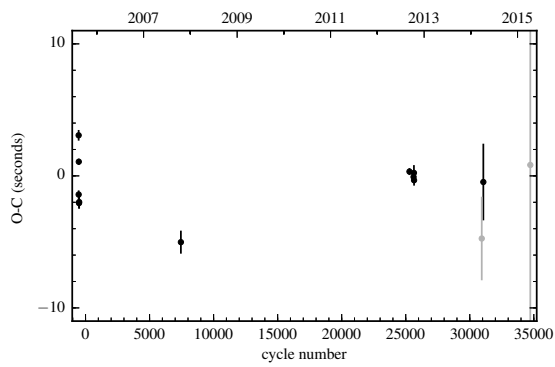
Figure B.57: O-C diagram of SDSS J1702+3229.
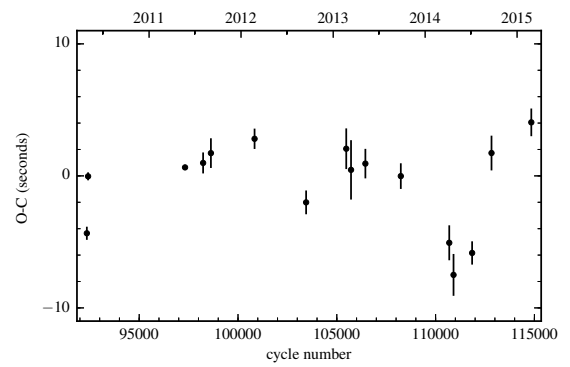
Figure B.58: O-C diagram of V2301 Oph.
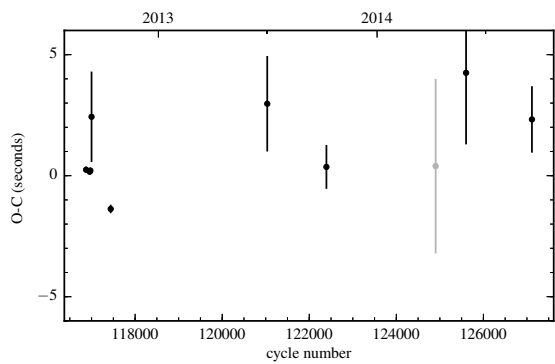
Figure B.59: O-C diagram of EP Dra.
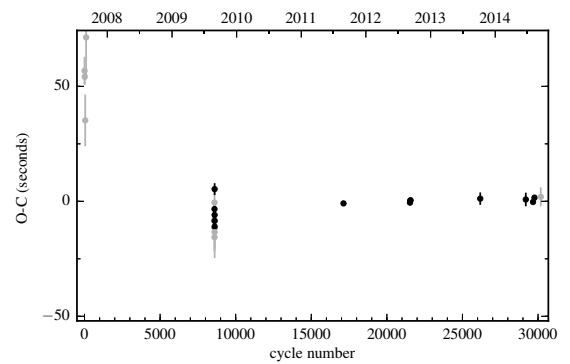
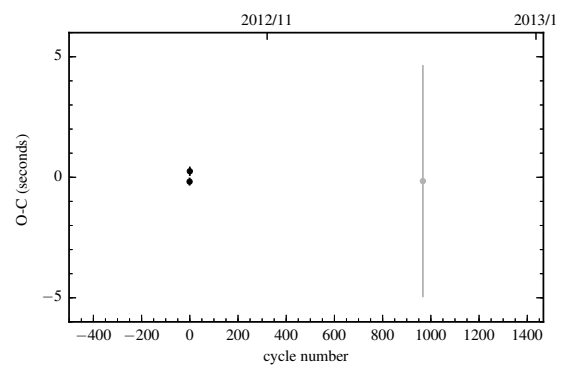**Figure B.60:** O-C diagram of V713 Cep.
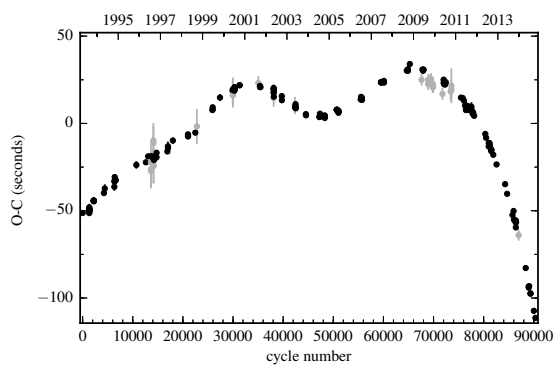
Figure B.61: O-C diagram of HU Aqr.

Figure B.62: O-C diagram of SDSS J2141+0507.

Bibliography

Aerts, C., Christensen-Dalsgaard, J., Kurtz, D. W., 2010, Asteroseismology

Almeida, L. A., Jablonski, F., 2011, in Sozzetti, A., Lattanzi, M. G., Boss, A. P., eds., IAU Symposium, vol. 276 of *IAU Symposium*, p. 495

Althaus, L. G., Serenelli, A. M., Benvenuto, O. G., 2001, MNRAS, 324, 617

Althaus, L. G., García-Berro, E., Isern, J., Córsico, A. H., Rohrmann, R. D., 2007, A&A, 465, 249

Althaus, L. G., Córsico, A. H., Isern, J., García-Berro, E., 2010, A&A Rev., 18, 471

Althaus, L. G., Miller Bertolami, M. M., Córsico, A. H., 2013, A&A, 557, A19

Antoniadis, J., et al., 2013, Science, 340, 448

Applegate, J. H., 1992, ApJ, 385, 621

Applegate, J. H., Patterson, J., 1987, ApJ, 322, L99

Backhaus, U., et al., 2012, A&A, 538, A84

Badenes, C., Maoz, D., 2012, ApJ, 749, L11

Badenes, C., Mullally, F., Thompson, S. E., Lupton, R. H., 2009, ApJ, 707, 971

Barstow, M. A., Bond, H. E., Holberg, J. B., Burleigh, M. R., Hubeny, I., Koester, D., 2005, MNRAS, 362, 1134

Bassa, C. G., van Kerkwijk, M. H., Koester, D., Verbunt, F., 2006, A&A, 456, 295

Bear, E., Soker, N., 2014, MNRAS, 444, 1698

Beavers, W. I., Lui, A., Herczeg, T. J., 1986, ApJ, 300, 785

Bento, J., et al., 2014, MNRAS, 437, 1511

Benvenuto, O. G., Althaus, L. G., 1998, MNRAS, 293, 177

Bergeron, P., Wesemael, F., Fontaine, G., 1991, ApJ, 367, 253

Bergeron, P., Wesemael, F., Lamontagne, R., Fontaine, G., Saffer, R. A., Allard, N. F., 1995, ApJ, 449, 258

Bergeron, P., Leggett, S. K., Ruiz, M. T., 2001, ApJS, 133, 413

Beuermann, K., Dreizler, S., Hessman, F. V., Deller, J., 2012, A&A, 543, A138

Beuermann, K., Dreizler, S., Hessman, F. V., 2013a, A&A, 555, A133

Beuermann, K., Dreizler, S., Hessman, F. V., Schwope, A. D., 2014, A&A, 562, A63

Beuermann, K., et al., 2010, AAP, 521, L60

Beuermann, K., et al., 2013b, A&A, 558, A96

Bildsten, L., Townsley, D. M., Deloye, C. J., Nelemans, G., 2006, ApJ, 640, 466

Bildsten, L., Shen, K. J., Weinberg, N. N., Nelemans, G., 2007, ApJ, 662, L95

Bloemen, S., et al., 2011, MNRAS, 410, 1787

Bois, B., Mochnacki, S. W., Lanning, H. H., 1988, AJ, 96, 157

Borges, B. W., Baptista, R., Papadimitriou, C., Giannakis, O., 2008, A&A, 480, 481

Bours, M. C. P., Marsh, T. R., Gänsicke, B. T., Parsons, S. G., 2015a, MNRAS, 448, 601

Bours, M. C. P., et al., 2014a, MNRAS, 438, 3399

Bours, M. C. P., et al., 2014b, MNRAS, 445, 1924

Bours, M. C. P., et al., 2015b, MNRAS, 450, 3966

Boyd, D., Denisenko, D., Koff, R., Miller, I., Staels, B., 2011, Journal of the British Astronomical Association, 121, 233

Bradley, P. A., 2001, ApJ, 552, 326

Breedt, E., Gänsicke, B. T., Marsh, T. R., Steeghs, D., Drake, A. J., Copperwheat, C. M., 2012, MNRAS, 425, 2548

Breedt, E., et al., 2014, MNRAS, 443, 3174

Breton, R. P., Rappaport, S. A., van Kerkwijk, M. H., Carter, J. A., 2012, ApJ, 748, 115

Bridge, C. M., et al., 2002, MNRAS, 336, 1129

Brinkworth, C. S., Marsh, T. R., Dhillon, V. S., Knigge, C., 2006, MNRAS, 365, 287

Brown, W. R., Kilic, M., Allende Prieto, C., Kenyon, S. J., 2010, ApJ, 723, 1072

Brown, W. R., Kilic, M., Hermes, J. J., Allende Prieto, C., Kenyon, S. J., Winget, D. E., 2011, ApJ, 737, L23

Brown, W. R., Kilic, M., Allende Prieto, C., Kenyon, S. J., 2012, ApJ, 744, 142

Brown, W. R., Kilic, M., Allende Prieto, C., Gianninas, A., Kenyon, S. J., 2013, ApJ, 769, 66

Burleigh, M. R., Barstow, M. A., 1999, A&A, 341, 795

Burleigh, M. R., Barstow, M. A., 2000, A&A, 359, 977

Burrows, A., et al., 1997, ApJ, 491, 856

Casewell, S. L., Dobbie, P. D., Napiwotzki, R., Burleigh, M. R., Barstow, M. A., Jameson, R. F., 2009, MNRAS, 395, 1795

Catalán, S., Isern, J., García-Berro, E., Ribas, I., 2008a, MNRAS, 387, 1693

Catalán, S., Isern, J., García-Berro, E., Ribas, I., Allende Prieto, C., Bonanos, A. Z., 2008b, A&A, 477, 213

Chandrasekhar, S., 1931, ApJ, 74, 81

Claret, A., 2000, A&A, 363, 1081

Claret, A., Bloemen, S., 2011, A&A, 529, A75

Claret, A., Hauschildt, P. H., Witte, S., 2012, A&A, 546, A14

Copperwheat, C. M., Marsh, T. R., Dhillon, V. S., Littlefair, S. P., Hickman, R., Gänsicke, B. T., Southworth, J., 2010, MNRAS, 402, 1824

Copperwheat, C. M., et al., 2012, MNRAS, 421, 149

Copperwheat, C. M., et al., 2013, MNRAS, 434, 661

Córsico, A. H., Romero, A. D., Althaus, L. G., Hermes, J. J., 2012, A&A, 547, A96

Costa, J. E. S., et al., 2008, A&A, 477, 627

Cropper, M., 1988, MNRAS, 231, 597

Cropper, M., 1990, Space Sci. Rev., 54, 195

Cropper, M., et al., 1989, MNRAS, 236, 29P

Dan, M., Rosswog, S., Guillochon, J., Ramirez-Ruiz, E., 2011, ApJ, 737, 89

de Bruijne, J. H. J., Allen, M., Azaz, S., Krone-Martins, A., Prod'homme, T., Hestroffer, D., 2015, A&A, 576, A74

Dhillon, V. S., et al., 2007, MNRAS, 378, 825

Dhillon, V. S., et al., 2011, MNRAS, 416, L16

Dhillon, V. S., et al., 2014, ArXiv e-prints

Dobbie, P. D., Napiwotzki, R., Burleigh, M. R., Williams, K. A., Sharp, R., Barstow, M. A., Casewell, S. L., Hubeny, I., 2009, MNRAS, 395, 2248

Doherty, C. L., Gil-Pons, P., Siess, L., Lattanzio, J. C., Lau, H. H. B., 2014, ArXiv e-prints

Doressoundiram, A., Roques, F., Boissel, Y., Arenou, F., Dhillon, V., Littlefair, S., Marsh, T., 2013, MNRAS, 428, 2661

Doyle, L. R., et al., 2011, Science, 333, 1602

Drake, A. J., et al., 2009, ApJ, 696, 870

Drake, A. J., et al., 2010, ArXiv e-prints

Drake, A. J., et al., 2014a, MNRAS, 441, 1186

Drake, J. J., Garraffo, C., Takei, D., Gaensicke, B., 2014b, MNRAS, 437, 3842

Dufour, P., Fontaine, G., Liebert, J., Williams, K., Lai, D. K., 2008, ApJ, 683, L167

Durant, M., et al., 2011, MNRAS, 410, 2329

Dvorak, R., 1986, A&A, 167, 379

Eastman, J., Siverd, R., Gaudi, B. S., 2010, PASP, 122, 935

Eggleton, P. P., 1983, ApJ, 268, 368

Eggleton, P. P., Fitchett, M. J., Tout, C. A., 1989, ApJ, 347, 998

Eisenstein, D. J., et al., 2006, ApJS, 167, 40

Falcon, R. E., Winget, D. E., Montgomery, M. H., Williams, K. A., 2010, ApJ, 712, 585

Faulkner, J., 1971, ApJ, 170, L99

Feline, W. J., Dhillon, V. S., Marsh, T. R., Watson, C. A., Littlefair, S. P., 2005, MNRAS, 364, 1158

Fontaine, G., Brassard, P., Bergeron, P., 2001, PASP, 113, 409

Foreman-Mackey, D., Hogg, D. W., Lang, D., Goodman, J., 2013, PASP, 125, 306

Fukugita, M., Ichikawa, T., Gunn, J. E., Doi, M., Shimasaku, K., Schneider, D. P., 1996, AJ, 111, 1748

Gänsicke, B. T., Beuermann, K., de Martino, D., 1995, A&A, 303, 127

Gänsicke, B. T., Long, K. S., Barstow, M. A., Hubeny, I., 2006, ApJ, 639, 1039

Gänsicke, B. T., et al., 2009, MNRAS, 397, 2170

Gelman, A., Carlin, J. B., Stern, H. S., Dunson, D. B., Vehtari, A., Rubin, D. B., 2014, Bayesian data analysis

Giammichele, N., Bergeron, P., Dufour, P., 2012, ApJS, 199, 29

Gianninas, A., Bergeron, P., Fontaine, G., 2006, AJ, 132, 831

Gianninas, A., Bergeron, P., Ruiz, M. T., 2011, ApJ, 743, 138

Gianninas, A., Strickland, B. D., Kilic, M., Bergeron, P., 2013, ApJ, 766, 3

Gianninas, A., Dufour, P., Kilic, M., Brown, W. R., Bergeron, P., Hermes, J. J., 2014a, ApJ, 794, 35

Gianninas, A., Hermes, J. J., Brown, W. R., Dufour, P., Barber, S. D., Kilic, M., Kenyon, S. J., Harrold, S. T., 2014b, ApJ, 781, 104

Gilks, W. R., Richardson, S., Spiegelhalter, D. J., 1996, Markov chain Monte Carlo in practice

Glenn, J., Howell, S. B., Schmidt, G. D., Liebert, J., Grauer, A. D., Wagner, R. M., 1994, ApJ, 424, 967

Goodman, J., Weare, J., 2010, Communications in Applied Mathematics and Computational Science, 5, 65

Goździewski, K., et al., 2012, MNRAS, 425, 930

Goździewski, K., et al., 2015, MNRAS, 448, 1118

Green, J. C., et al., 2012, ApJ, 744, 60

Green, R. F., Richstone, D. O., Schmidt, M., 1978, ApJ, 224, 892

Greiss, S., Gänsicke, B. T., Hermes, J. J., Steeghs, D., Koester, D., Ramsay, G., Barclay, T., Townsley, D. M., 2014, MNRAS, 438, 3086

Guinan, E. F., Ribas, I., 2001, ApJ, 546, L43

Haefner, R., Fiedler, A., Butler, K., Barwig, H., 2004, A&A, 428, 181

Hakala, P. J., Watson, M. G., Vilhu, O., Hassall, B. J. M., Kellett, B. J., Mason, K. O., Piirola, V., 1993, MNRAS, 263, 61

Hansen, B. M. S., et al., 2004, ApJS, 155, 551

Hansen, B. M. S., et al., 2013, Nature, 500, 51

Hardy, A., et al., 2015, ApJ, 800, L24

Harrop-Allin, M. K., Cropper, M., Hakala, P. J., Hellier, C., Ramseyer, T., 1999, MNRAS, 308, 807

Harrop-Allin, M. K., Potter, S. B., Cropper, M., 2001, MNRAS, 326, 788

Heber, U., 2009, ARA&A, 47, 211

Heerlein, C., Horne, K., Schwope, A. D., 1999, MNRAS, 304, 145

Hellier, C., 2001, Cataclysmic Variable Stars

Hermes, J. J., Montgomery, M. H., Winget, D. E., Brown, W. R., Kilic, M., Kenyon, S. J., 2012a, ApJ, 750, L28

Hermes, J. J., Kepler, S. O., Castanheira, B. G., Gianninas, A., Winget, D. E., Montgomery, M. H., Brown, W. R., Harrold, S. T., 2013a, ApJ, 771, L2

Hermes, J. J., Montgomery, M. H., Mullally, F., Winget, D. E., Bischoff-Kim, A., 2013b, ApJ, 766, 42

Hermes, J. J., et al., 2011, ApJ, 741, L16

Hermes, J. J., et al., 2012b, ApJ, 757, L21

Hermes, J. J., et al., 2013c, MNRAS, 436, 3573

Hermes, J. J., et al., 2013d, ApJ, 765, 102

Hermes, J. J., et al., 2014a, MNRAS, 444, 1674

Hermes, J. J., et al., 2014b, ApJ, 789, 85

Hinse, T. C., Lee, J. W., Goździewski, K., Haghighipour, N., Lee, C.-U., Scullion, E. M., 2012, MNRAS, 420, 3609

Hobbs, G. B., Edwards, R. T., Manchester, R. N., 2006, MNRAS, 369, 655

Holberg, J. B., Barstow, M. A., Bruhweiler, F. C., Cruise, A. M., Penny, A. J., 1998, ApJ, 497, 935

Holberg, J. B., Oswalt, T. D., Barstow, M. A., 2012, AJ, 143, 68

Horne, K., Wood, J. H., Stiening, R. F., 1991, ApJ, 378, 271

Horner, J., Marshall, J. P., Wittenmyer, R. A., Tinney, C. G., 2011, MNRAS, 416, L11

Horner, J., Hinse, T. C., Wittenmyer, R. A., Marshall, J. P., Tinney, C. G., 2012a, MN-RAS, 427, 2812

Horner, J., Wittenmyer, R. A., Hinse, T. C., Tinney, C. G., 2012b, MNRAS, 425, 749

Horner, J., Wittenmyer, R. A., Hinse, T. C., Marshall, J. P., Mustill, A. J., Tinney, C. G., 2013, MNRAS, 435, 2033

Howarth, I. D., 1983, MNRAS, 203, 301

Howell, S. B., 2006, Handbook of CCD Astronomy

Howell, S. B., Nelson, L. A., Rappaport, S., 2001, ApJ, 550, 897

Howell, S. B., Ciardi, D. R., Sirk, M. M., Schwope, A. D., 2002, AJ, 123, 420

Huang, S.-S., 1966, Annales d'Astrophysique, 29, 331

Hurley, J. R., Pols, O. R., Tout, C. A., 2000, MNRAS, 315, 543

İbanoğlu, C., Evren, S., Taş, G., Çakırlı, Ö., 2005, MNRAS, 360, 1077

Iben, Jr., I., Tutukov, A. V., 1984, ApJS, 54, 335

Iben, Jr., I., Tutukov, A. V., Yungelson, L. R., 1997, ApJ, 475, 291

Irwin, J. B., 1959, AJ, 64, 149

Istrate, A. G., Tauris, T. M., Langer, N., 2014a, A&A, 571, A45

Istrate, A. G., Tauris, T. M., Langer, N., Antoniadis, J., 2014b, A&A, 571, L3

Ivanova, N., et al., 2013, A&A Rev., 21, 59

Ives, D., Bezawada, N., Dhillon, V., Marsh, T., 2008, in Society of Photo-Optical Instrumentation Engineers (SPIE) Conference Series, vol. 7021 of *Society of Photo-Optical Instrumentation Engineers (SPIE) Conference Series*, p. 0

Jeans, J. H., 1902, Royal Society of London Philosophical Transactions Series A, 199, 1

Jenkins, C. R., 1987, MNRAS, 226, 341

Kalirai, J. S., Saul Davis, D., Richer, H. B., Bergeron, P., Catelan, M., Hansen, B. M. S., Rich, R. M., 2009, ApJ, 705, 408

Kaplan, D. L., 2010, ApJ, 717, L108

Kaplan, D. L., Bildsten, L., Steinfadt, J. D. R., 2012, ApJ, 758, 64

Kaplan, D. L., Bhalerao, V. B., van Kerkwijk, M. H., Koester, D., Kulkarni, S. R., Stovall, K., 2013, ApJ, 765, 158

Kaplan, D. L., et al., 2014, ApJ, 780, 167

Kawaler, S. D., Bradley, P. A., 1994, ApJ, 427, 415

Kilic, M., Brown, W. R., Allende Prieto, C., Agüeros, M. A., Heinke, C., Kenyon, S. J., 2011, ApJ, 727, 3

Kilic, M., Brown, W. R., Allende Prieto, C., Kenyon, S. J., Heinke, C. O., Agüeros, M. A., Kleinman, S. J., 2012, ApJ, 751, 141

Kilic, M., Brown, W. R., Gianninas, A., Hermes, J. J., Allende Prieto, C., Kenyon, S. J., 2014a, MNRAS, 444, L1

Kilic, M., Hermes, J. J., Gianninas, A., Brown, W. R., 2015, MNRAS, 446, L26

Kilic, M., et al., 2014b, MNRAS, 438, L26

Kippenhahn, R., Weigert, A., 1990, Stellar Structure and Evolution

Kleinman, S. J., et al., 2013, ApJS, 204, 5

Knigge, C., 2006, MNRAS, 373, 484

Knigge, C., Baraffe, I., Patterson, J., 2011, ApJS, 194, 28

Knox, R. A., Hawkins, M. R. S., Hambly, N. C., 1999, MNRAS, 306, 736

Koester, D., 1987, ApJ, 322, 852

Koester, D., 2009, A&A, 498, 517

Koester, D., 2010, Mem. Soc. Astron. Italiana, 81, 921

Koester, D., 2013, White Dwarf Stars, p. 559

Kowalski, P. M., Saumon, D., 2006, ApJ, 651, L137

Kraft, R. P., 1967, ApJ, 150, 551

Kroupa, P., Weidner, C., Pflamm-Altenburg, J., Thies, I., Dabringhausen, J., Marks, M., Maschberger, T., 2013, The Stellar and Sub-Stellar Initial Mass Function of Simple and Composite Populations, p. 115

Kulkarni, S. R., van Kerkwijk, M. H., 2010, ApJ, 719, 1123

Kundra, E., Hric, L., 2011, Ap&SS, 331, 121

Landau, L. D., Lifshitz, E. M., 1975, The classical theory of fields

Landolt, A. U., 1968, ApJ, 153, 151

Lanza, A. F., 2006, MNRAS, 369, 1773

Lanza, A. F., Rodono, M., Rosner, R., 1998, MNRAS, 296, 893

Lazarus, P., et al., 2014, MNRAS, 437, 1485

Leggett, S. K., Ruiz, M. T., Bergeron, P., 1998, ApJ, 497, 294

Leibundgut, B., Tammann, G. A., Cadonau, R., Cerrito, D., 1991, A&AS, 89, 537

Liebert, J., Bergeron, P., Holberg, J. B., 2005, ApJS, 156, 47

Littlefair, S. P., Dhillon, V. S., Marsh, T. R., Gänsicke, B. T., Southworth, J., Watson, C. A., 2006, Science, 314, 1578

Littlefair, S. P., Dhillon, V. S., Marsh, T. R., Gänsicke, B. T., Southworth, J., Baraffe, I., Watson, C. A., Copperwheat, C., 2008, MNRAS, 388, 1582

Littlefair, S. P., et al., 2014, MNRAS, 445, 2106

Loeb, A., Gaudi, B. S., 2003, ApJ, 588, L117

Lohr, M. E., et al., 2014, A&A, 566, A128

Mackay, D. J. C., 2003, Information Theory, Inference and Learning Algorithms

Marsh, T. R., 2001, MNRAS, 324, 547

Marsh, T. R., Pringle, J. E., 1990, ApJ, 365, 677

Marsh, T. R., Dhillon, V. S., Duck, S. R., 1995, MNRAS, 275, 828

Marsh, T. R., Gänsicke, B. T., Steeghs, D., Southworth, J., Koester, D., Harris, V., Merry, L., 2011, ApJ, 736, 95

Marsh, T. R., et al., 2014, MNRAS, 437, 475

Maxted, P. F. L., Marsh, T. R., Moran, C. K. J., 2002, MNRAS, 332, 745

Maxted, P. F. L., Marsh, T. R., Morales-Rueda, L., Barstow, M. A., Dobbie, P. D., Schreiber, M. R., Dhillon, V. S., Brinkworth, C. S., 2004, MNRAS, 355, 1143

Maxted, P. F. L., Napiwotzki, R., Dobbie, P. D., Burleigh, M. R., 2006, Nature, 442, 543

Maxted, P. F. L., O'Donoghue, D., Morales-Rueda, L., Napiwotzki, R., Smalley, B., 2007, MNRAS, 376, 919

Maxted, P. F. L., et al., 2013, Nature, 498, 463

Maxted, P. F. L., et al., 2014, MNRAS, 437, 1681

McGraw, J. T., Liebert, J., Starrfield, S. G., Green, R., 1979, in van Horn, H. M., Weidemann, V., eds., IAU Colloq. 53: White Dwarfs and Variable Degenerate Stars, p. 377

Meng, X., Chen, X., Han, Z., 2008, A&A, 487, 625

Mestel, L., 1968, MNRAS, 138, 359

Moffat, A. F. J., 1969, A&A, 3, 455

Montgomery, M. H., Williams, K. A., Winget, D. E., Dufour, P., De Gennaro, S., Liebert, J., 2008, ApJ, 678, L51

Mukadam, A. S., Montgomery, M. H., Winget, D. E., Kepler, S. O., Clemens, J. C., 2006, ApJ, 640, 956

Mullally, F., Winget, D. E., De Gennaro, S., Jeffery, E., Thompson, S. E., Chandler, D., Kepler, S. O., 2008, ApJ, 676, 573

Mustill, A. J., Marshall, J. P., Villaver, E., Veras, D., Davis, P. J., Horner, J., Wittenmyer, R. A., 2013, MNRAS, 436, 2515

Nelemans, G., Tout, C. A., 2005, MNRAS, 356, 753

Nelemans, G., Verbunt, F., Yungelson, L. R., Portegies Zwart, S. F., 2000, A&A, 360, 1011

Nelemans, G., Yungelson, L. R., Portegies Zwart, S. F., 2001, A&A, 375, 890

Nomoto, K., 1982, ApJ, 253, 798

Norton, A. J., Butters, O. W., Parker, T. L., Wynn, G. A., 2008, ApJ, 672, 524

O'Brien, M. S., Bond, H. E., Sion, E. M., 2001, ApJ, 563, 971

O'Donoghue, D., Koen, C., Kilkenny, D., Stobie, R. S., Koester, D., Bessell, M. S., Hambly, N., MacGillivray, H., 2003, MNRAS, 345, 506

O'Donoghue, D., et al., 2006, MNRAS, 372, 151

Orosz, J. A., et al., 2012a, Science, 337, 1511

Orosz, J. A., et al., 2012b, ApJ, 758, 87

Østensen, R. H., Bloemen, S., Vučković, M., Aerts, C., Oreiro, R., Kinemuchi, K., Still, M., Koester, D., 2011, ApJ, 736, L39

Paczyński, B., 1967, AcA, 17, 287

Paczyński, B., 1971, ARA&A, 9, 183

Paczyński, B., 1976, in Eggleton, P., Mitton, S., Whelan, J., eds., Structure and Evolution of Close Binary Systems, vol. 73 of *IAU Symposium*, p. 75

Paquette, C., Pelletier, C., Fontaine, G., Michaud, G., 1986, ApJS, 61, 197

Parsons, S. G., Marsh, T. R., Copperwheat, C. M., Dhillon, V. S., Littlefair, S. P., Gänsicke, B. T., Hickman, R., 2010a, MNRAS, 402, 2591

Parsons, S. G., Marsh, T. R., Gänsicke, B. T., Drake, A. J., Koester, D., 2011a, ApJL, 735, L30

Parsons, S. G., Marsh, T. R., Gänsicke, B. T., Tappert, C., 2011b, MNRAS, 412, 2563

Parsons, S. G., Marsh, T. R., Gänsicke, B. T., Schreiber, M. R., Bours, M. C. P., Dhillon, V. S., Littlefair, S. P., 2013a, MNRAS, 436, 241

Parsons, S. G., et al., 2010b, MNRAS, 407, 2362

Parsons, S. G., et al., 2012a, MNRAS, 420, 3281

Parsons, S. G., et al., 2012b, MNRAS, 426, 1950

Parsons, S. G., et al., 2012c, MNRAS, 419, 304

Parsons, S. G., et al., 2013b, MNRAS, 429, 256

Parsons, S. G., et al., 2014, MNRAS, 438, L91

Parsons, S. G., et al., 2015, MNRAS, 449, 2194

Patterson, J., 1981, ApJS, 45, 517

Perlmutter, S., et al., 1999, ApJ, 517, 565

Phillips, M. M., 1993, ApJ, 413, L105

Portegies Zwart, S., 2013, MNRAS, 429, L45

Postnov, K. A., Yungelson, L. R., 2014, Living Reviews in Relativity, 17, 3

Potter, S. B., et al., 2011, MNRAS, 416, 2202

Prialnik, D., 2000, An Introduction to the Theory of Stellar Structure and Evolution

Provencal, J. L., Shipman, H. L., Hog, E., Thejll, P., 1998, ApJ, 494, 759

Provencal, J. L., Shipman, H. L., Koester, D., Wesemael, F., Bergeron, P., 2002, ApJ, 568, 324

Provencal, J. L., et al., 2009, ApJ, 693, 564

Pyrzas, S., et al., 2009, MNRAS, 394, 978

Pyrzas, S., et al., 2012, MNRAS, 419, 817

Pyrzas, S., et al., 2015, MNRAS, 447, 691

Qian, S.-B., Liao, W.-P., Zhu, L.-Y., Dai, Z.-B., Liu, L., He, J.-J., Zhao, E.-G., Li, L.-J., 2010, MNRAS, 401, L34

Qian, S.-B., Liu, L., Zhu, L.-Y., Dai, Z.-B., Fernández Lajús, E., Baume, G. L., 2012, MNRAS, 422, L24

Qian, S.-B., et al., 2011, MNRAS, 414, L16

Ransom, S. M., et al., 2014, Nature, 505, 520

Rappaport, S., Verbunt, F., Joss, P. C., 1983, ApJ, 275, 713

Rebassa-Mansergas, A., Nebot Gómez-Morán, A., Schreiber, M. R., Gänsicke, B. T., Schwope, A., Gallardo, J., Koester, D., 2012, MNRAS, 419, 806

Rebassa-Mansergas, A., Schreiber, M. R., Gänsicke, B. T., 2013, MNRAS, 429, 3570

Rebolo, R., Zapatero Osorio, M. R., Martín, E. L., 1995, Nature, 377, 129

Reid, I. N., 1996, AJ, 111, 2000

Renzini, A., et al., 1996, ApJ, 465, L23

Richer, H. B., Fahlman, G. G., Rosvick, J., Ibata, R., 1998, ApJ, 504, L91

Richer, H. B., et al., 1997, ApJ, 484, 741

Richer, H. B., et al., 2008, AJ, 135, 2141

Riess, A. G., et al., 1998, AJ, 116, 1009

Ritter, H., Kolb, U., 2003, A&A, 404, 301

Robinson, E. L., et al., 1995, ApJ, 438, 908

Roeser, S., Demleitner, M., Schilbach, E., 2010, AJ, 139, 2440

Roques, F., et al., 2006, AJ, 132, 819

Salpeter, E. E., 1955, ApJ, 121, 161

Savoury, C. D. J., et al., 2011, MNRAS, 415, 2025

Schatzman, E., 1962, Annales d'Astrophysique, 25, 18

Schlafly, E. F., Finkbeiner, D. P., 2011, ApJ, 737, 103

Schlegel, D. J., Finkbeiner, D. P., Davis, M., 1998, ApJ, 500, 525

Schleicher, D. R. G., Dreizler, S., 2014, A&A, 563, A61

Schmidt, H., 1996, A&A, 311, 852

Schreiber, M. R., et al., 2010, A&A, 513, L7

Schwarz, R., Schwope, A. D., Vogel, J., Dhillon, V. S., Marsh, T. R., Copperwheat, C., Littlefair, S. P., Kanbach, G., 2009, A&A, 496, 833

Schwope, A. D., Thinius, B. D., 2014, Astronomische Nachrichten, 335, 357

Schwope, A. D., Thomas, H. C., Beuermann, K., 1993, A&A, 271, L25

Schwope, A. D., Mantel, K.-H., Horne, K., 1997, A&A, 319, 894

Schwope, A. D., Schwarz, R., Sirk, M., Howell, S. B., 2001, A&A, 375, 419

Schwope, A. D., Horne, K., Steeghs, D., Still, M., 2011, A&A, 531, A34

Seaton, M. J., 1979, MNRAS, 187, 73P

Shahbaz, T., Dhillon, V. S., Marsh, T. R., Casares, J., Zurita, C., Charles, P. A., 2010, MNRAS, 403, 2167

Shen, K. J., Bildsten, L., Kasen, D., Quataert, E., 2012, ApJ, 748, 35

Shipman, H. L., Provencal, J. L., Hog, E., Thejll, P., 1997, ApJ, 488, L43

Silvestri, N. M., Hawley, S. L., Oswalt, T. D., 2005, AJ, 129, 2428

Silvestri, N. M., et al., 2006, AJ, 131, 1674

Silvotti, R., et al., 2007, Nature, 449, 189

Steele, I. A., Bates, S. D., Gibson, N., Keenan, F., Meaburn, J., Mottram, C. J., Pollacco, D., Todd, I., 2008, in Society of Photo-Optical Instrumentation Engineers (SPIE) Conference Series, vol. 7014 of *Society of Photo-Optical Instrumentation Engineers (SPIE) Conference Series*

Steele, I. A., et al., 2004, in Oschmann, Jr., J. M., ed., Society of Photo-Optical Instrumentation Engineers (SPIE) Conference Series, vol. 5489 of *Society of Photo-Optical Instrumentation Engineers (SPIE) Conference Series*, p. 679

Steinfadt, J. D. R., Kaplan, D. L., Shporer, A., Bildsten, L., Howell, S. B., 2010, ApJL, 716, L146

Steinfadt, J. D. R., Bildsten, L., Kaplan, D. L., Fulton, B. J., Howell, S. B., Marsh, T. R., Ofek, E. O., Shporer, A., 2012, PASP, 124, 1

Sterken, C., 2005, in Sterken, C., ed., The Light-Time Effect in Astrophysics: Causes and cures of the O-C diagram, vol. 335 of *Astronomical Society of the Pacific Conference Series*, p. 181

Sterne, T. E., 1939, MNRAS, 99, 451

Stobie, R. S., et al., 1997, MNRAS, 287, 848

Szkody, P., et al., 2002, AJ, 123, 430

Tassoul, M., Fontaine, G., Winget, D. E., 1990, ApJS, 72, 335

Tauris, T. M., van den Heuvel, E. P. J., 2014, ApJ, 781, L13

Thorstensen, J. R., 2003, AJ, 126, 3017

Thorstensen, J. R., Lépine, S., Shara, M., 2008, AJ, 136, 2107

Toonen, S., Claeys, J. S. W., Mennekens, N., Ruiter, A. J., 2014, A&A, 562, A14

Tremblay, P.-E., Bergeron, P., Kalirai, J. S., Gianninas, A., 2010, ApJ, 712, 1345

Tremblay, P.-E., Bergeron, P., Gianninas, A., 2011a, ApJ, 730, 128

Tremblay, P.-E., Ludwig, H.-G., Steffen, M., Bergeron, P., Freytag, B., 2011b, A&A, 531, L19

Tremblay, P.-E., Ludwig, H.-G., Steffen, M., Freytag, B., 2013a, A&A, 552, A13

Tremblay, P.-E., Ludwig, H.-G., Steffen, M., Freytag, B., 2013b, A&A, 559, A104

Tremblay, P.-E., Kalirai, J. S., Soderblom, D. R., Cignoni, M., Cummings, J., 2014, ApJ, 791, 92

Tulloch, S. M., Dhillon, V. S., 2011, MNRAS, 411, 211

Tutukov, A., Yungelson, L., 1979, in Conti, P. S., De Loore, C. W. H., eds., Mass Loss and Evolution of O-Type Stars, vol. 83 of *IAU Symposium*, p. 401

Vallerga, J. V., McPhate, J. B., Martin, A. P., Gaines, G. A., Siegmund, O. H., Wilkinson, E., Penton, S., Beland, S., 2001, in Siegmund, O. H., Fineschi, S., Gummin, M. A., eds., UV/EUV and Visible Space Instrumentation for Astronomy and Solar Physics, vol. 4498 of *Society of Photo-Optical Instrumentation Engineers (SPIE) Conference Series*, p. 141

Valsecchi, F., Farr, W. M., Willems, B., Deloye, C. J., Kalogera, V., 2012, ApJ, 745, 137

van den Besselaar, E. J. M., et al., 2007, A&A, 466, 1031

van den Heuvel, E. P. J., 1976, in Eggleton, P., Mitton, S., Whelan, J., eds., Structure and Evolution of Close Binary Systems, vol. 73 of *IAU Symposium*, p. 35

van der Sluys, M. V., Verbunt, F., Pols, O. R., 2006, A&A, 460, 209

Van Grootel, V., Dupret, M.-A., Fontaine, G., Brassard, P., Grigahcène, A., Quirion, P.-O., 2012, A&A, 539, A87

Van Grootel, V., Fontaine, G., Brassard, P., Dupret, M.-A., 2013, ApJ, 762, 57

van Kerkwijk, M. H., Bergeron, P., Kulkarni, S. R., 1996, ApJ, 467, L89

Vennes, S., Christian, D. J., Thorstensen, J. R., 1998, ApJ, 502, 763

Vennes, S., et al., 2011, ApJ, 737, L16

Veras, D., Tout, C. A., 2012, MNRAS, 422, 1648

Verbunt, F., 1982, Space Sci. Rev., 32, 379

Verbunt, F., Rappaport, S., 1988, ApJ, 332, 193

Verbunt, F., Zwaan, C., 1981, A&A, 100, L7

Vernet, J., et al., 2011, A&A, 536, A105

Vrielmann, S., Schwope, A. D., 2001, MNRAS, 322, 269

Warner, B., 2003, Cataclysmic Variable Stars

Watson, C. A., Dhillon, V. S., Rutten, R. G. M., Schwope, A. D., 2003, MNRAS, 341, 129

Watson, M. G., 1995, in Buckley, D. A. H., Warner, B., eds., Magnetic Cataclysmic Variables, vol. 85 of *Astronomical Society of the Pacific Conference Series*, p. 179

Webbink, R. F., 1984, ApJ, 277, 355

Weidemann, V., 1977, A&A, 59, 411

Weidemann, V., 2000, A&A, 363, 647

Welsh, W. F., et al., 2012, Nature, 481, 475

Whelan, J., Iben, Jr., I., 1973, ApJ, 186, 1007

Winget, D. E., Kepler, S. O., 2008, ARA&A, 46, 157

Winget, D. E., Robinson, E. L., Nather, R. D., Fontaine, G., 1982, ApJ, 262, L11

Winn, J. N., 2010, ArXiv e-prints

Wittenmyer, R. A., Horner, J., Marshall, J. P., Butters, O. W., Tinney, C. G., 2012, MNRAS, 419, 3258

Wittenmyer, R. A., Horner, J., Marshall, J. P., 2013, MNRAS, 431, 2150

Wolszczan, A., 1994, Science, 264, 538

Wolszczan, A., Frail, D. A., 1992, Nature, 355, 145

Wood, B. D., Forbes, J. E., 1963, AJ, 68, 257

Wood, J. H., Marsh, T. R., 1991, ApJ, 381, 551

Wood, M. A., 1992, ApJ, 386, 539

Wood, M. A., 1995, in Koester, D., Werner, K., eds., White Dwarfs, vol. 443 of *Lecture Notes in Physics, Berlin Springer Verlag*, p. 41

Woodgate, B. E., et al., 1998, PASP, 110, 1183

Woodley, K. A., et al., 2012, AJ, 143, 50

Woods, T. E., Ivanova, N., van der Sluys, M. V., Chaichenets, S., 2012, ApJ, 744, 12

York, D. G., et al., 2000, AJ, 120, 1579

Zorotovic, M., Schreiber, M. R., 2013, A&A, 549, A95

$\star \star \star$

Vita

I was born on the 3rd of November 1986 in the Netherlands. I attended the Sint Michael-school in Brachterbeek, and later the Bisschoppelijk College in Echt as my primary and secondary schools.

In 2005 I moved to Nijmegen to study Physics & Astronomy at the Radboud University. My bachelor thesis focused on identifying weak X-ray sources in the galactic plane using the ASCA and IPHAS surveys, and was done together with Hannah Duckwitz in the group of Paul Groot. I continued studying to obtain a master's degree in astronomy, a part of which was a one-year research project with Gijs Nelemans and Silvia Toonen. This project was about single-degenerate supernova Type Ia progenitors, and in particular focused on how the retention efficiency of the accreting white dwarfs effects the theoretical supernova Ia rates and delay-time distributions obtained from the binary population synthesis code SeBa. The results were published in the Astronomy & Astrophysics Journal and, together with my course work, earned me a cum laude M.Sc. degree.

I then decided to switch back to observational astronomy, and got a PhD position in the Astronomy & Astrophysics group at the University of Warwick, under the supervision of Tom Marsh. As discussed in this thesis, I studied and modelled close white dwarf binary stars, for which I obtained observations ranging from far-ultraviolet HST spectroscopy to high-speed photometry with ULTRACAM and ULTRASPEC. This allowed me to obtain observational experience by using telescopes and instruments on La Palma, Spain, in Chile and in Thailand. The results of these projects have led to four first-author publications in the Monthly Notices of the Royal Astronomical Society, and have been presented at national and international conferences in London, Manchester, St. Andrews, Kraków, Galway and Montréal.

Throughout my B.Sc., M.Sc. and Ph.D. studies I have been a teaching assistant for a number of astronomy and physics courses for B.Sc. students, as well as a lab demonstrator for undergraduate students. I have also been involved in outreach through open astronomy evenings with local telescopes and the STFC Astronomy Roadshow.

<p align="center">★ ★ ★</p>